STATIC AND DYNAMIC PROPERTIES OF CHARGE DENSITY WAVE CONDUCTORS AND OTHER LOW DIMENSIONAL MATERIALS

by

Michael Frederic Hundley

Dissertation submitted in partial satisfaction
of the requirements for the degree of

DOCTOR OF PHILOSOPHY

in Physics, in the Graduate Division of
the University of California at Berkeley

May, 1988

STATIC AND DYNAMIC PROPERTIES OF CHARGE DENSITY WAVES CONDUCTORS AND OTHER LOW DIMENSIONAL MATERIALS

Michael Frederic Hundley

STATIC AND DYNAMIC PROPERTIES OF CHARGE DENSITY WAVE CONDUCTORS AND OTHER LOW DIMENSIONAL MATERIALS

Michael Frederic Hundley

Department of Physics
University of California at Berkeley

ABSTRACT

The electronic transport properties of a number of unusual low dimensional materials are examined in this report. Emphasis is placed on the dynamical properties of the quasi-one-dimensional charge density wave (CDW) conductors $NbSe_3$ and $K_{0.3}MoO_3$. Additionally, we examine the transport properties of the heavy Fermion compound URu_2Si_2, self-similar gold percolation networks, and the layered high temperature superconductor $La_{1.85}Sr_{0.15}CuO_4$.

We investigate the transport properties of $NbSe_3$ samples in applied magnetic (H) fields. The experimental results indicate that the anomalous H-field effects exhibited by $NbSe_3$ are due to H-field induced normal-to-CDW carrier conversion. The data further suggest that the conventional CDW impurity-pinning mechanism breaks down in large H-fields.

We also examine the effects of applied temperature

gradients on the Shapiro step spectrum displayed by $NbSe_3$ samples. The results indicate that thermal gradients act to reduce CDW phase velocity coherence, while applied ac electric fields act to increase CDW coherence. Additionally, a simple model is presented which successfully accounts for the effects of temperature gradients on $NbSe_3$ crystals. These thermal gradient techniques are also used to study CDW domain structure and impurity length scale effects in switching samples of pure and iron doped $NbSe_3$.

We demonstrate that extremely thin samples of the CDW material $K_{0.3}MoO_3$ display high quality narrow band noise (NBN) spectra when driven by dc electric fields. In combined ac and dc driving fields $K_{0.3}MoO_3$ crystals also exhibit unusual interference phenomena whenever the internal NBN and the external ac frequencies coincide. These results are analyzed in terms of a simple classical CDW dynamical model.

In addition, we examine the transport properties of URu_2Si_2, a heavy Fermion compound which appears to undergo a Fermi surface-based density wave transition at 17.5 K. We also study the temperature dependent frequency-scaling ac conductivity of a novel class of gold films which can be characterized by a fractal dimensionality. Lastly, we examine the transport properties of the planar ceramic oxide $La_{1.85}Sr_{0.15}CuO_4$ to characterize this material's normal and superconducting states.

For Jaima

TABLE OF CONTENTS

Acknowledgments

I wish to first thank my research advisor, Professor Alex Zettl, who directed this thesis project. None of this work would have been possible without the excellent facilities and equipment that exist in the novel materials transport laboratory which he has single-handedly developed during the past five years. He has also taught me a great deal about how to perform a wide variety of electronic transport measurements. I also thank Professors John Clarke and Neil Bartlett for their assistance they have given me as members of my thesis committee, and Professors Alan Portis and Leo Falicov for their participation as members of my qualifying exam committee. My thanks also go to Harvey Mudd College Professor Jim Eckert who first introduced me to the excitement and challenges of experimental condensed matter physics as well as to the intriguing properties of charge density wave materials.

I also wish to thank Phil Parilla who I collaborated with in performing a number of the experiments discussed in this report. Many of the ideas presented here were immensely improved through my discussions with Phil. I am also indebted to my other fellow Lab mates, Mark Sherwin, Ulrich Walter, Mike Crommie, Lincoln Bourne, Bill Creager, Storrs Hoen, and R.P. Hall, for innumerable useful discussions -- sometimes relating to physics -- and for helping to

create a pleasant working atmosphere in the laboratory.

I also wish to thank my parents, Janna and Richard Hundley, for their interest in my work and their continuing support (both financial and moral) throughout my academic career.

Most of all, I wish to thank Jaima Jackson for her support, companionship, editorial advice and legal assistance during my graduate career. I can say with certainty that neither my graduate studies nor my work on this report would have gone as smoothly as they did without her help.

This research was funded in part by NSF Grants DMR 84-00041 and 83-51678 and a research grant from the General Motors Research Corporation.

Vita

October 2, 1961:	Born in Los Angeles, California
May, 1983:	B.S. Degree, Harvey Mudd College, Claremont, California
May, 1985:	M.A. Degree, University of California at Berkeley
September 1983 to May, 1988:	Teaching and Research Assistant, Department of Physics, University of California at Berkeley
June, 1983 to August, 1983:	Research Consultant, IBM Research Laboratory, San Jose, California

Publications

1. M.F. Hundley and A. Zettl. Shapiro step spectrum and phase-velocity coherence in $NbSe_3$ in a uniform temperature gradient. Phys. Rev. B **33**, 2883 (1986).

2. R.P. Hall, M.F. Hundley, and A. Zettl. Switching and phase-slip centers in charge-density-wave conductors. Phys. Rev. Lett. **56**, 2399 (1986).

3. P. Parilla, M.F. Hundley, and A. Zettl. Magnetic-field-induced carrier conversion in a charge-density wave conductor. Phys. Rev. Lett. **57**, 619 (1986).

4. M.F. Hundley, P. Parilla, and A. Zettl. Charge-density-wave magnetodynamics in $NbSe_3$. Phys. Rev. B **34**, 5970 (1986).

5. R.P. Hall, M.F. Hundley, and A. Zettl. A phase-slip model of switching. Physica **143**B, 152 (1986).

6. A. Zettl, M.F. Hundley, and P. Parilla. Magnetotransport studies in charge density wave conductors. Syn. Met. **19**, 807 (1987).

7. R.P. Hall, M.F. Hundley, and A. Zettl. An RF-induced dynamic coherence length in $NbSe_3$. Syn. Met. **19**, 813 (1987).

8. M.F. Hundley and A. Zettl. Magnetothermopower of $NbSe_3$. Solid State Commun. **61**, 587 (1987).

9. M.F. Hundley, L.C. Bourne, A. Zettl, C. Rossel, and M.B. Maple. On the 17.5 K transition in URu_2Si_2: thermopower and elasticity. Solid State Commun. **62**, 603 (1987).

10. M.F. Hundley, A. Zettl, A. Stacy, and M.L. Cohen. Transport properties of the superconducting oxide $La_{1.85}Sr_{0.15}CuO_4$. Phys. Rev. B **35**, 8800 (1987).

11. M.F. Hundley and A. Zettl. Charge-density-wave switching in an applied temperature gradient. Solid State Commun. **65**, 791 (1988).

12. M.F. Hundley and A. Zettl. Domain structure and impurity length scale effects in switching charge density wave conductors. Phys. Rev. B (in press).

13. M.F. Hundley and A. Zettl. Noise and Shapiro Step Interference in the charge-density-wave conductor $K_{0.3}MoO_3$. Solid State Commun. (submitted).

14. M.F. Hundley and A. Zettl. Noise and ac-dc interference phenomena in the charge density wave conductor $K_{0.3}MoO_3$. Phys. Rev. B (submitted).

15. R.P. Hall, M.F. Hundley and A. Zettl. Switching and charge-density-wave transport in $NbSe_3$. I: DC characteristics. Phys. Rev. B (submitted).

16. M.F. Hundley, P. Parilla, and A. Zettl. Model of temperature gradient effects in charge density wave conductors. (to be published).

17. M.F. Hundley and A. Zettl. Temperature dependent ac conductivity of thin percolation films. (to be published).

Chapter 1: Introduction

The study of low dimensional solids has developed into a rapidly expanding research field during the past two decades. Prior to 1970, the interest in low dimensional materials was solely theoretical in nature.[1,2] The situation changed considerably in the early 70's when advances in both organic and inorganic synthesis techniques made it possible to produce conductors with highly anisotropic electronic structures. These breakthroughs have lead to an extensive study by the physics community of both single-particle and collective mode electronic transport in a wide variety of low dimensional materials.[3]

A particularly intriguing class of low dimensional materials is that of quasi-one-dimensional (Q1D) inorganic[4,5] and organic conductors.[6] These materials undergo a Peierls transition[1] to a semiconducting ground state at moderate temperatures due to the strong electron-phonon interactions present in one dimensional electronic systems. The Peierls transition also gives rise to the formation of a periodic modulation in the electronic charge density, commonly referred to as a charge density wave (CDW).

In 1976 Monceau, *et al.* discovered that the linear-chain compound $NbSe_3$ exhibits non-linear dc electrical conductivity when a small electric field is applied across the crystal chain axis.[7] Subsequent transport measurements[8]

on $NbSe_3$ could not be explained in terms of single-particle transport phenomena, and X-ray[9] and NMR[10] measurements clearly indicate that this anomalous transport is actually due to the collective mode sliding of the entire CDW. To date, this exciting collective mode phenomenon has been observed in roughly half a dozen inorganic CDW materials.[4,5] While we now have a rough understanding of the main features of CDW transport, many unanswered questions concerning both the subtle and not-so-subtle nature of CDW dynamics still exist.

In an attempt to answer a number of questions concerning CDW dynamics we shall examine the electrical transport properties of two inorganic CDW materials, $NbSe_3$ and $K_{0.3}MoO_3$. In particular, we shall investigate the effects of externally applied magnetic fields and temperature gradients on the transport properties of $NbSe_3$, and, in so doing, gain an understanding of carrier conversion processes and CDW domain structure in CDW crystals. We shall also study the transport properties of $K_{0.3}MoO_3$ in combined ac and dc electric fields and compare the results to those exhibited by other CDW compounds.

In addition to examining CDW dynamical behavior, we will also study the transport properties of a number of other low dimensional/anisotropic materials which do not exhibit dynamical CDW ground states. We examine the transport properties of the heavy Fermion compound URu_2Si_2 which

appears to have an intermediate spin or charge density wave state in addition to a low temperature superconducting state. We will also investigate the frequency and temperature dependent conductivity of a novel class of thin gold percolation films. Due to their self-similar nature, these films can be characterized by a non-integer, fractal dimension, and as a result, they display intriguing electronic transport properties. Lastly, we shall study the transport properties of the anisotropic, moderately "high T_c" compound $La_{1.85}Sr_{0.15}CuO_4$ to better characterize this material's normal and superconducting states.

This report is organized in the following manner: in Chapter 2 a brief introduction to CDW formation, dynamics, dynamical models, and materials is presented. A discussion concerning the motivation for this research, with a particular emphasis on the questions we are attempting to answer, appears in Chapter 3. These introductory chapters are followed by the presentation and analysis of the experimental results in Chapters 4-8. In Chapter 4 we examine the effects of externally applied magnetic fields and temperature gradients on $NbSe_3$. This is followed by an investigation in Chapter 5 of noise and ac-dc interference phenomena in $K_{0.3}MoO_3$. In Chapter 6 the transport properties of the heavy Fermion compound URu_2Si_2 will be studied, followed by an examination of the frequency and temperature dependent conductivity of gold percolation films in Chapter

7. The transport properties of the anisotropic ceramic-oxide superconducting compound $La_{1.85}Sr_{0.15}CuO_4$ are examined in Chapter 8. Lastly, a summary of the findings presented here as well as concluding remarks and possible directions for future research are presented in Chapter 9.

Chapter 2: An introduction to charge density waves

In 1955, Peierls[1] and Fröhlich[2] independently suggested that one-dimensional metals should be susceptible to a periodic lattice distortion that would lead to the formation of a periodic modulation in the electronic charge density, known today as a charge density wave (CDW). In this chapter we examine the special properties that make low-dimensional solids unstable towards a periodic lattice distortion, the consequences of this distortion, and the dynamical properties of sliding CDWs.

This chapter is organized as follows: the underlying mechanisms responsible for CDW formation, a brief chronological history of the field, and the dynamical behavior of collective CDW motion are presented in Sec. 2.1. This is followed by a brief review in Sec. 2.2 of the phenomenological models which attempt to account for CDW dynamical behavior. Lastly, in Sec. 2.3 we examine in detail the structural properties of the two CDW conductors whose static and dynamic properties are the subject of this report ($NbSe_3$ and $K_{0.3}MoO_3$). This chapter is intended only as a brief overview of CDW systems; for a more complete treatment, the reader is directed to the extensive review articles and conference proceedings listed in the reference section.[3-6]

2.1 CDW formation and dynamics

As we shall see, charge density waves form at low temperatures in low dimensional conductors. When we speak of "low dimensional" conductors, we are referring not to the overall crystal structure, which is obviously three dimensional, but instead to the underlying atomic arrangements which constrain conduction electrons to preferentially travel in only one or two dimensions. In the quasi-one-dimensional (Q1D) materials, the metallic atoms (the transition metal atoms in the transition metal trichalcogenides) are arranged in infinite chains, with the nearest neighbor separation along the chain comparable to the inter-atomic spacing in the metallic atom's pure crystal phase. The separation between neighboring chains is far larger than this due to intervening non-metallic atoms (the chalcogenide atoms in the transition metal trichalcogenides). Hence, a Q1D crystal structure consists of infinite conducting chains with very little inter-chain coupling. Similarly, quasi-two-dimensional materials are composed of conducting planes with only a small degree of inter-plane coupling.

To see why electronically low-dimensional conductors are susceptible to a periodic lattice distortion, as first suggested by both Peierls and Fröhlich, we examine the response of a nearly free electron gas (NFEG) to a periodic

potential of the form

$$V = \Delta\, e^{iQx}\,, \tag{2.1}$$

where Δ ($<< E_F$) and Q are the potential's amplitude and wave vector, respectively.[7] This perturbation couples together the states |k> and |k+Q> in such a way as to open an energy gap $E_g = 2\Delta$ in the electronic energy spectrum at $k = \pm Q/2$. Peierls[1] and Fröhlich[2] independently pointed out that this potential can be provided by the lattice ions, and for $Q = 2k_F$ the energy gap will lead to a reduction in the overall electronic lattice energy. Peierls concluded that the Fermi surface of all Q1D materials should be gapped, and hence all such materials should be insulators or semiconductors.[1]

We examine the electron-phonon interaction in low dimensional conductors to understand both where the static, periodic potential originates in these materials as well as why metallic low dimensional materials exist at room temperature. A phonon of wave vector q will perturb the electrons within a lattice in such a way as to produce a relative change in the electronic charge density which can be given by $\delta\rho = -\chi(q)V(q)$; here, V(q) is the periodic mean-field potential induced by the phonons and $\chi(q)$ is the electronic susceptibility. The mean-field phonon potential arises from the periodic ion displacement which embodies a phonon; this potential is given by

$$V(q) = gU_o e^{iqx} , \qquad (2.2)$$

where U_o is the displacement amplitude and g is the electron-phonon coupling constant ($\Delta \equiv gU_o$). The electronic susceptibility in a metal is given by the Lindhard susceptibility function,[8]

$$\chi(q) = \sum_k \frac{f(k) - f(k+q)}{E(k+q) - E(k)} , \qquad (2.3)$$

where f(k) is the temperature-dependent Fermi-Dirac distribution, E(k) is the electronic energy at k, and we sum over all occupied electronic states.

In three dimensions the Lindhard susceptibility is a relatively uninteresting function of q. This is not the case in one dimension, where $\chi(q)$ shows a large, sharp peak at $q = 2k_F$. As T drops to zero, $\chi(2k_F)$ grows, until, at T = 0, it displays a logarithmic singularity. This $2k_F$ singularity in the electronic susceptibility occurs due to the effects of a periodic potential on a nearly free electron gas, as discussed earlier. The singularity in the Lindhard susceptibility occurs due to the nature of the denominator in Eqn. 2.3; as the summation is carried out near $k = -k_F$, the denominator goes to zero at $q = 2k_F$. This stems from the

fact that in a purely one-dimensional compound, the Fermi surface at $k < 0$ can be translated ($k \Rightarrow k+q$) onto the Fermi surface at $k > 0$ by a single wave vector $q = 2k_F$ (the Fermi surface is said to nest). In materials with a higher dimensionality (Q1D or Q2D compounds) perfect nesting does not occur along the entire Fermi surface. Nonetheless, a large susceptibility can still occur at $2k_F$ if a significant fraction of the Fermi surface can be nested by a single wave vector. Hence, the nearly free electron gas is strongly influenced by the $2k_F$ phonon mode in low dimensional metals.

At $T > 0$, the peak in the electronic susceptibility gives rise to a large $2k_F$ modulation in the charge density. This charge modulation in turn produces a force on the oscillating ions which tends to increase their relative displacements. The additional force on the ions is given by $F = -2g^2\chi U_o$. Hence, this force (which is functionally equivalent to that of a simple harmonic oscillator) acts to reduce the $2k_F$ phonon frequency $\omega(2k_F)$. This is turn forms a Kohn anomaly in the phonon dispersion relationship. By including the effects of the electron-phonon interactions, the $2k_F$ phonon frequency becomes[7]

$$\omega^2(2k_F) = \omega_o^2 - \frac{2g^2\chi(2k_F)}{M} \quad , \qquad (2.4)$$

where ω_o is the $2k_F$ phonon frequency in the absence of any

electron-phonon interactions, and M is the ionic mass. As the temperature drops, $\chi(2k_F)$ rises until, at $T = T_c^{MF}$, $\chi(2k_F) = M\omega_o^2/2g^2$ and the $2k_F$ phonon frequency drops to zero. Hence, at and below T_c^{MF} a $Q = 2k_F$ periodic lattice distortion is frozen into the system. This periodic lattice distortion is accompanied by a permanent, periodic modulation of the charge density, otherwise known as a charge density wave.

The onset of the periodic lattice distortion, now referred to as a Peierls transition, leads to the formation of a gap $E_g = 2\Delta$ at the Fermi surface. Because the gap occurs at E_F, the total electronic energy is reduced. This is offset by an increase in the total elastic energy due to the permanent lattice distortion. By minimizing the total crystal energy (lattice plus electrons), the energy gap becomes[7]

$$\Delta = 2\ E_F\ e^{-1/\lambda}\ , \qquad (2.5)$$

where $\lambda = D(E_F)g^2/M\omega_o^2$ is a dimensionless coupling constant, and $D(E_F)$ is the density of states at the Fermi energy. By calculating $\chi(2k_F)$ as a function of temperature, T_c^{MF} and $\Delta(T=0)$ are found to be related by the familiar BCS relation,

$$2\Delta = 3.52\ k_B T_c^{MF}\ , \qquad (2.6)$$

where k_B is the Boltzmann constant.

This mean-field analysis is not entirely correct because it neglects the effects of inter-chain coupling and three dimensional ordering. Roughly speaking, T_c^{MF} is the temperature at which ordering along individual chains begins to take place. According to a calculation by Lee, Rice, and Anderson,[9] true three dimensional ordering does not take place until $T_c \approx T_c^{MF}/4$. Hence, the true transition temperature is T_c, and not T_c^{MF}.

Because a gap opens at E_F, the Peierls transition converts a low dimensional metal into a semiconductor or insulator. Fröhlich pointed out that the periodicity of the CDW $\lambda = \pi/k_F$ need not be directly related to the lattice periodicity.[2] Hence, the energy of a one-dimensional CDW should be independent of its position relative to the lattice (the CDW is said to be incommensurate with the lattice in this case). Fröhlich, who, in the days before BCS, was searching for a superconductivity mechanism, proposed therefore that the CDW should be able to slide relative to the lattice with no resistance. This Fröhlich mode would consist of a displacement of the electrons which form the CDW, leading to a macroscopic current, while the ions would fluctuate around their average positions. This ionic motion would add no current to the mode, but the ion's inertia would substantially increase the dynamical CDW effective mass.

While very intriguing, the possibilities of a Peierls transition and the Fröhlich mode were unrealized before the early 1970's because no known quasi-one or two dimensional materials then existed. The situation changed considerably with advances in organic and inorganic synthesis techniques that occurred in the first half of the 1970's. The new synthesis techniques made it possible to make solids with highly anisotropic electronic structures. The linear chain platinum salt $K_2Pt(CN)_4Br_{0.3}$ (KCP) was the first Q1D material in which a Peierls transition was identified.[10] A family of organic charge-transfer salts, which are best exemplified by tetrathiafulvanium-tetracyanoquinodimethanide (TTF-TCNQ), were also found to undergo a Peierls transition.[11] A group of quasi-two-dimensional materials, the transition metal dichalcogenides, were also found to contain a two dimensional CDW.[12] Research on these systems centered on studying the structural changes brought on by the Peierls transition. Although these materials showed no sign of a dc Fröhlich mode (recent conductivity studies indicate that TTF-TCNQ may display collective CDW motion),[13] reflectivity measurements indicated that, in the case of KCP and TTF-TCNQ, the CDW phason mode[14] has a characteristic frequency in the far-infrared region.[15]

In 1976 Monceau, *et al.* discovered that the linear chain conductor $NbSe_3$ displays non-linear dc conductivity in both CDW states (T_{c1} = 144 K, T_{c2} = 59 K; due to this

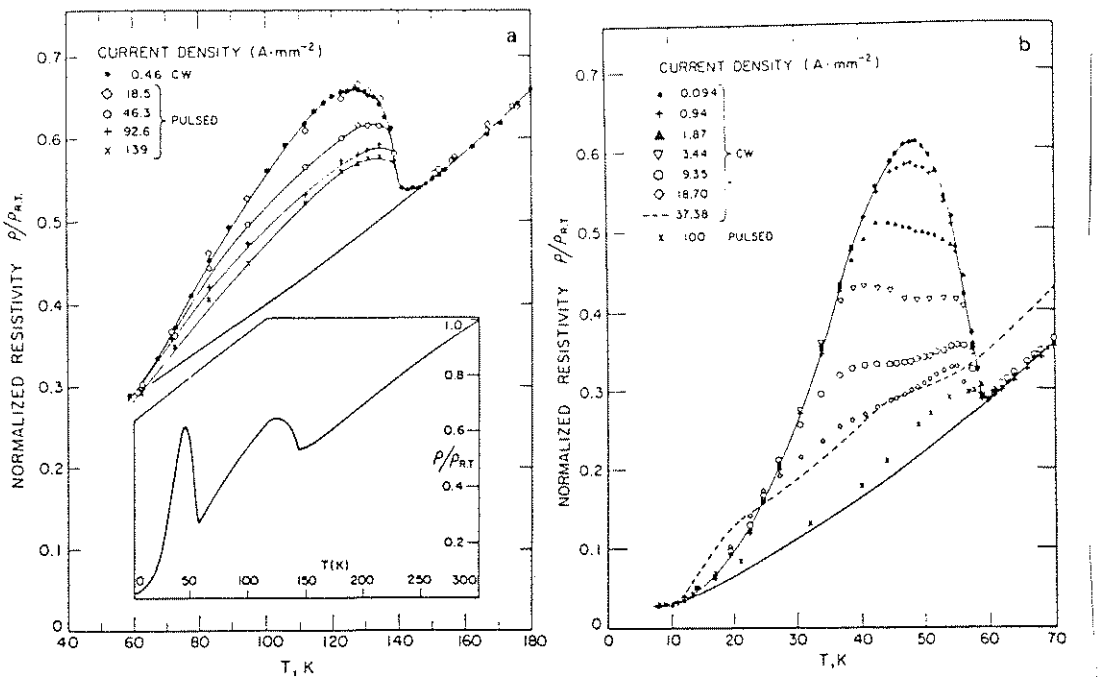

Figure 2-1 $NbSe_3$ resistivity below the upper (a) and lower (b) Peierls transitions; ρ is measured at various dc current densities. The inset in (a) shows the low field resistivity between room temperature and 4.2 K (from Ref. 16).

material's multi-chain structure, the two Peierls transitions only partially gap the Fermi surface).[16] As indicated in Fig. 2-1, the two resistance anomalies are progressively suppressed with increasing bias voltage. In the limit of large dc fields, the resistivity appears to saturate to a value consistent with no CDW transition. This phenomenon was initially attributed to CDW electric field breakdown via single particle zener tunneling across a small energy gap.[16] However, subsequent X-ray diffraction experiments[17] clearly indicated that the CDW does not break down in the non-Ohmic regime, indicating that Zener tunneling was not responsible for the non-linear conductivity.

In 1979 Bardeen suggested that the experimental results were due to the Fröhlich sliding CDW mode.[18] Subsequently, differential resistance measurements indicated that a strongly temperature-dependent electric threshold field E_T exists which separates a low field, Ohmic, conductivity state from a high field, non-Ohmic conductivity state (see Fig. 2-2).[19,20] More recently, NMR experiments clearly indicate that the non-linear dc conductivity exhibited by $NbSe_3$ is due to collective CDW motion.[21] A non-zero threshold field and the absence of a superconducting Fröhlich mode apparently occur in these materials because the CDW is pinned to the lattice by impurities.[22] This has been verified by experiments which indicate that E_T increases when impurity or doping concentrations are increased.[23] Presumably, the

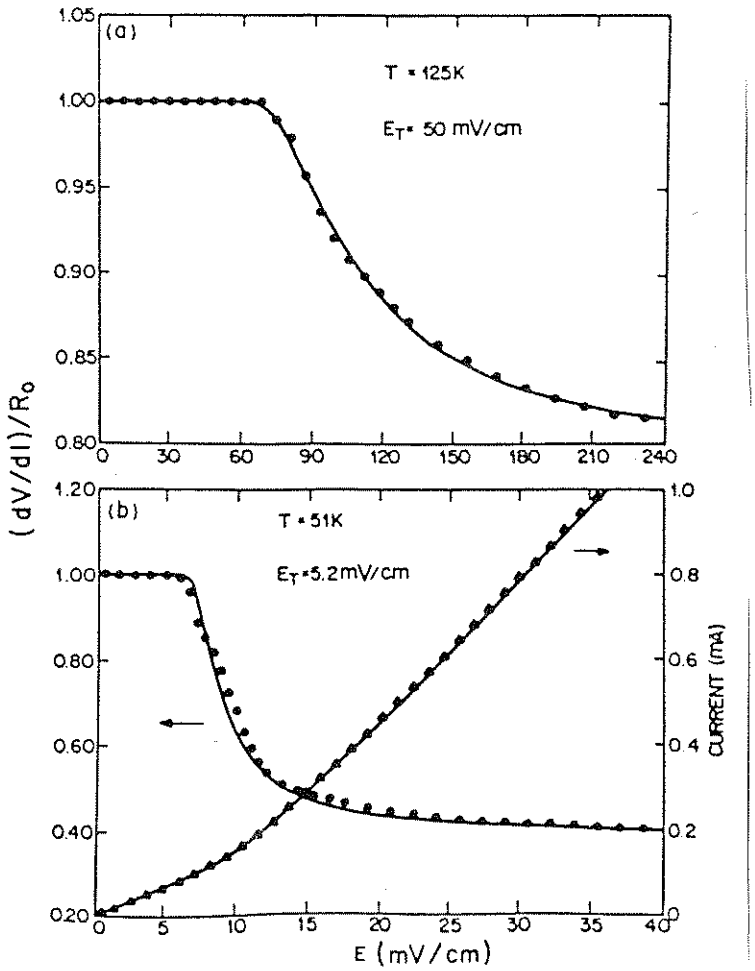

Figure 2-2 Differential resistance and current-voltage characteristics of $NbSe_3$ in the upper (a) and lower (b) CDW states. The solid lines are fits to an empirical expression proposed by Fleming (from Ref. 20).

organic CDW materials (KCP and TTF-TCNQ) do not usually exhibit CDW motion because of excessive impurity pinning.

There now exist seven known Q1D CDW materials which display non-linear collective-mode conductivity. They include three compounds from the transition metal trichalcogenides ($NbSe_3$, monoclinic and orthorombic TaS_3, and type III NbS_3),[24,25] the blue bronzes ($X_{0.3}MoO_3$, X = K, Rb),[26] and the halogenated transition metal tetrachalcogenides [$(TaSe_4)_2I$ and $(NbSe_4)_{3.33}I$].[27,28] We now briefly discuss the dynamical properties associated with sliding CDW motion (for a more extensive treatment, see Refs. 3-6).

2.1.1 Frequency-dependent CDW response

The charge density wave materials which display non-linear dc conductivity also exhibit strongly frequency-dependent conductivity at unusually low frequencies. The frequency-dependent conductivity of $NbSe_3$ and TaS_3 are shown in Fig. 2-3.[29,30] In both cases, the real part of the conductivity increases with increasing frequency starting at 1 to 10 MHz, and saturates to a maximum value at roughly 1 to 10 GHz; in the microwave region ($> 10^3$ GHz) the conductivity falls to zero. The imaginary part of the conductivity is also strongly frequency dependent. The general frequency dependence of the data presented in Fig. 2-3 is suggestive of a simple, overdamped harmonic oscillator

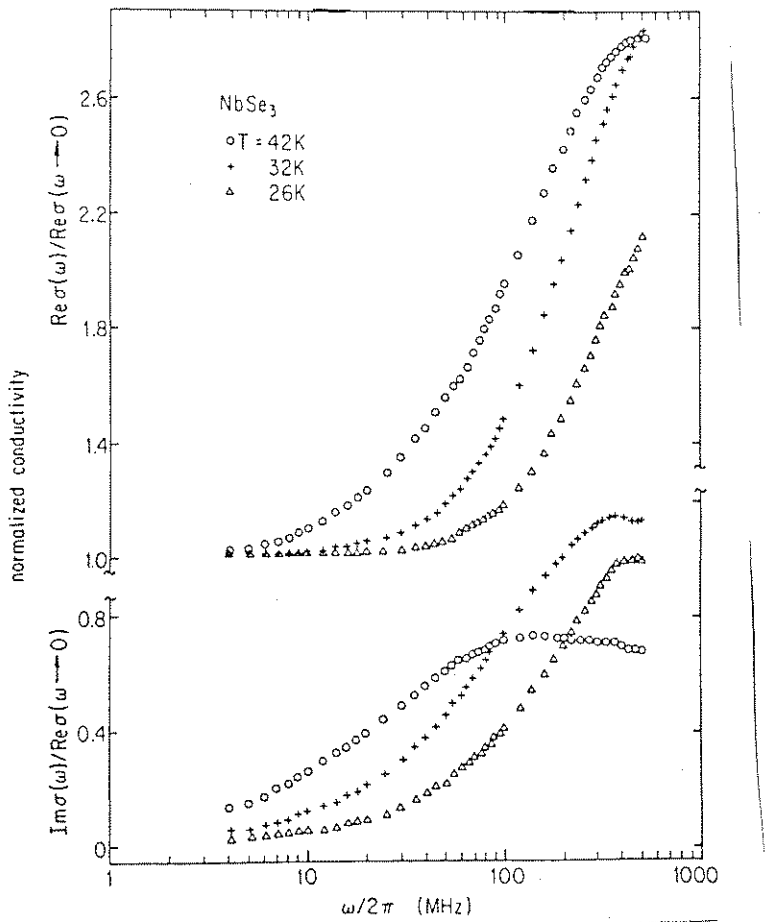

Figure 2-3a Real and imaginary parts of the frequency dependent conductivity of $NbSe_3$ below 1 GHz (from Ref. 29).

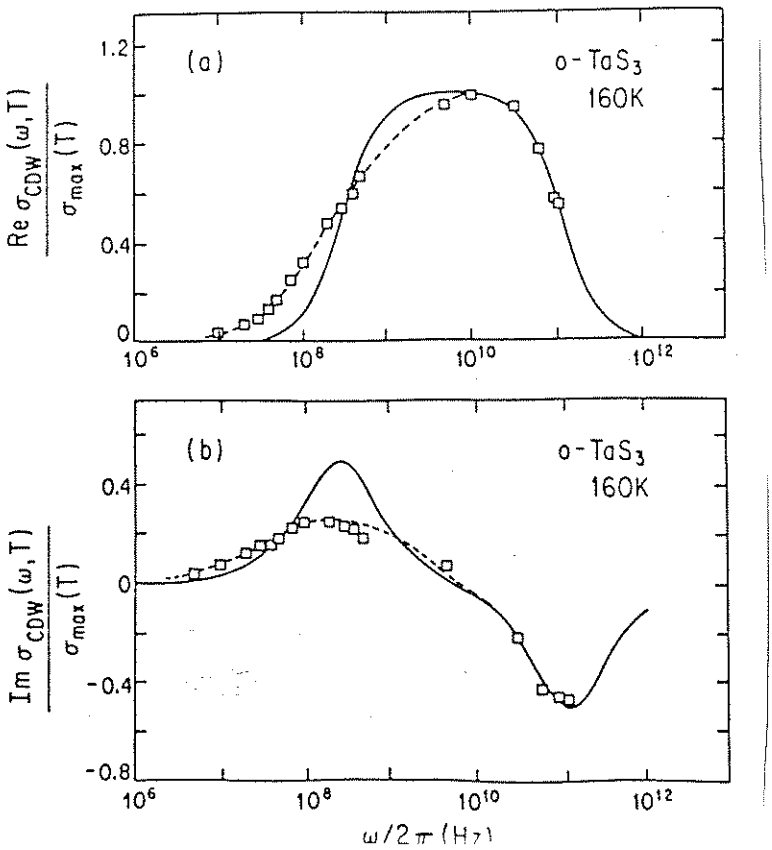

Figure 2-3b Normalized real and imaginary parts of the frequency dependent conductivity of TaS_3. The solid and dashed lines are fits to a simple, driven-dampened harmonic oscillator model assuming a single relaxation time (solid lines) and a distribution of relaxation times (dashed lines) (from Ref. 30).

with a characteristic crossover frequency ω_{co}. It has been found that ω_{co} increases with increasing impurity concentration in precisely the same way that the threshold electric field does.[31] This indicates that the peak present in the real part of the frequency-dependent conductivity is due to collective excitations of the charge density wave phason mode.

In addition to the giant phason mode evident in Fig. 2-3, completely gapped CDW materials also exhibit a small, strongly frequency- and temperature-dependent low frequency (< 10 MHz) dielectric relaxation mode. This mode was first seen in $K_{0.3}MoO_3$,[32] and more recently in $(TaSe_4)_2I$.[33] This mode is well described by a Debye relaxation equation with a broad distribution of relaxation times.[32] Recent theoretical work indicates that this conductivity mode stems from interactions between the CDW and normal electron.[34]

2.1.2 Periodic current oscillations

By far the most intriguing aspect of CDW dynamics is the noise phenomena which accompany the collective dc motion of a sliding CDW. For $E > E_T$, a CDW exhibits a large amount of broad band (1/f) noise and coherent ac current oscillations in addition to the dc CDW response. The coherent current oscillations typically appear in the MHz frequency range. Both of these noise-related phenomena were first observed by Fleming and Grimes in 1979.[19] A typical

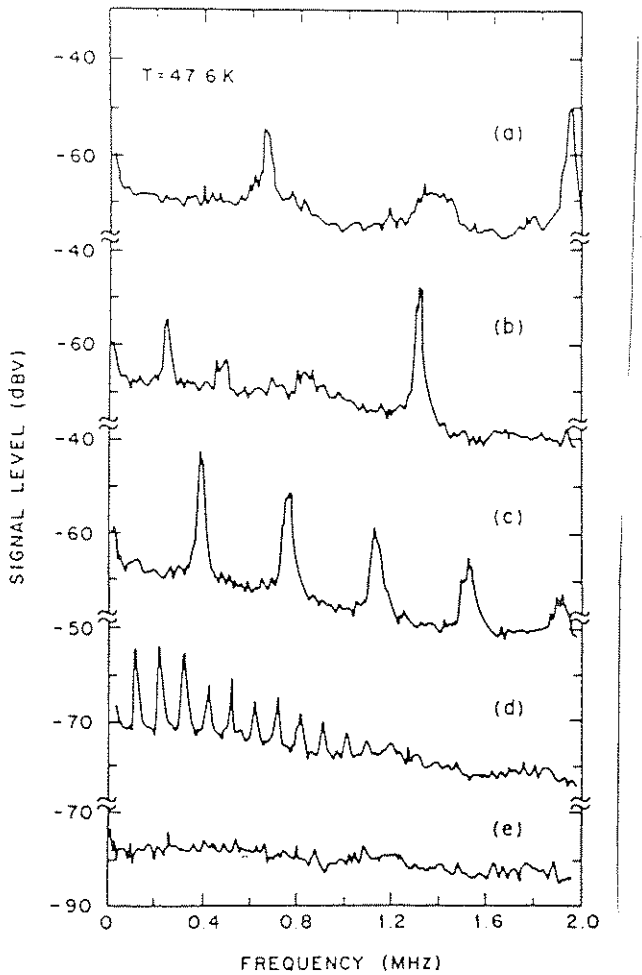

Figure 2-4 Noise spectra produced by a depinned $NbSe_3$ crystal for a variety of bias currents: (a) I = 270 μA, (b) I = 219 μA, (c) I = 154 μA, (d) I = 123 μA, and (e) I = 0 (from Ref. 19).

set of coherent current oscillation spectra are shown in Fig. 2-4. These current oscillations are now referred to as narrow band noise (NBN). A typical NBN spectrum consists of a strong fundamental noise peak at f_{NBN} and a set of harmonics at $f = nf_{NBN}$, where $n = 1,2,3,\ldots$. The data in Fig. 2-4 indicates that f_{NBN} is a strong function of bias current and that the harmonic amplitude decreases with increasing n. Narrow band noise spectra have been obtained from samples of $NbSe_3$,[19] TaS_3,[35] $(TaSe_4)_2I$,[27] $(NbSe_4)_{3.33}I$,[28] and $K_{0.3}MoO_3$.[26]

On both theoretical and experimental grounds it has been found that the narrow band noise frequency is linearly related to the CDW velocity v_{CDW}, and hence the CDW current density J_{CDW}, by[36]

$$J_{CDW} = a\, f_{NBN} , \tag{2.7}$$

where a is a material-, sample-, and temperature-dependent constant. Although considerable debate as to the origin of the narrow band noise has existed ever since its initial discovery,[37] recent research strongly indicates that this phenomena is a bulk effect caused by the sliding charge density wave interacting with the underlying periodic potential supplied by pinning impurities.[38]

2.1.3 Ac-dc interference phenomena

Due to the internal narrow band noise ac signal present in depinned CDW crystals, intriguing interference phenomena can occur in the presence of combined ac and dc electric fields. These effects are analogous to microwave-induced Shapiro steps in Josephson junctions.[39] Shapiro steps were first observed in $NbSe_3$ by Monceau, *et al.*[36] A typical Shapiro step spectrum exhibited by a mode-locked $NbSe_3$ sample is shown in Fig. 2-5. In the case of CDW conductors, steps in the current-voltage characteristic and peaks in the differential resistance occur whenever the bias-dependent NBN frequency is related to the externally applied frequency f_{ex} by

$$p\, f_{ex} = q\, f_{NBN} \quad , \tag{2.8}$$

where p and q are integers.

The Shapiro steps occur due to the mode locking of the CDW to the external ac signal. As the dc bias is increased in an ac-dc interference experiment, the internal ac frequency f_{NBN} will, as suggested by Eqn. 2.7, also increase. Suppose that at a bias field E_{lock} the two frequencies coincide ($f_{NBN} = f_{ex}$). It is energetically favorable for the internal ac signal to stay locked to the external ac signal over a small range of dc bias fields, $E = E_{lock} \pm \delta E$. Hence, while the CDW is mode-locked to the external signal, the CDW narrow band noise frequency and hence the CDW velocity does not change as the bias is varied. As a result, the normal

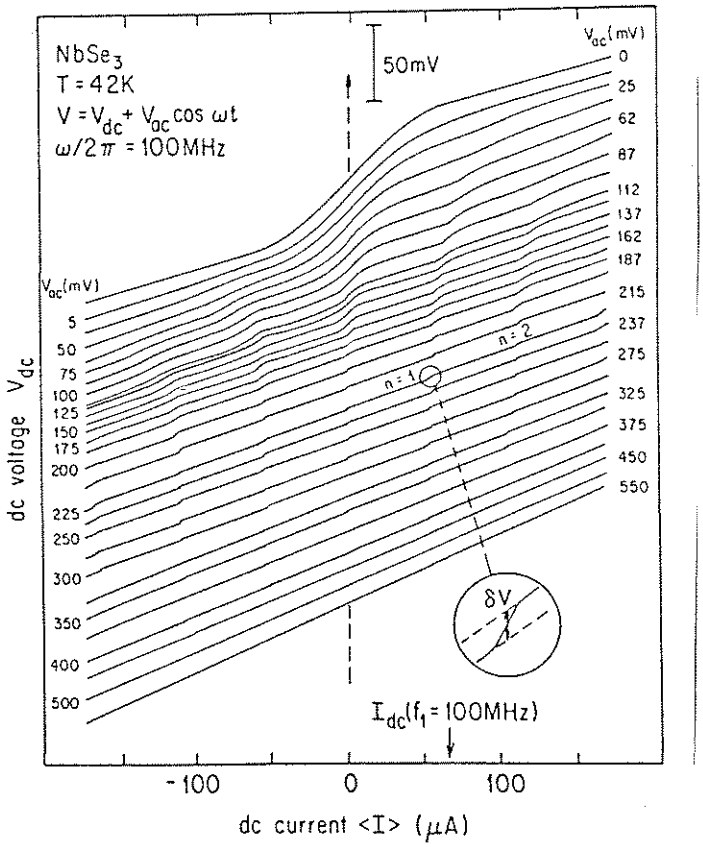

Figure 2-5a Shapiro steps in the current-voltage characteristic of an $NbSe_3$ crystal (from Ref. 40).

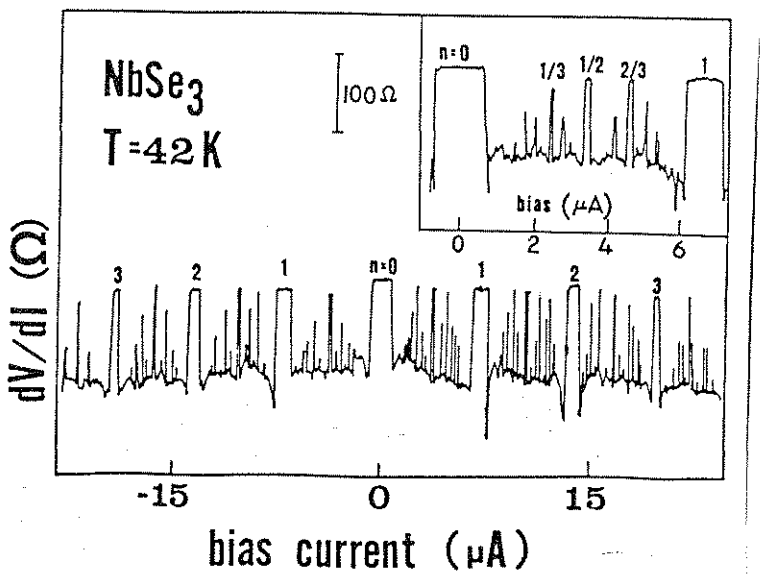

Figure 2-5b Shapiro steps in the differential resistance traces of an $NbSe_3$ crystal. The order n = p/q of the more prominent Shapiro steps are indicated in the figure (from Ref. 42).

electrons must carry the extra current necessitated by the changing bias, and, in the case of complete mode locking, the sample differential resistance must increase to the low field ($E < E_T$) value. It is this mode locking of the CDW to the external ac signal that gives rise to the anomalies in Fig. 2-5.

The mode-locking phenomena has been extensively studied in $NbSe_3$ crystals.[36,40-42] It has also been observed in samples of TaS_3,[43] and $K_{0.3}MoO_3$.[44] Inductive anomalies in the bias-dependent ac conductivity of $NbSe_3$ and $K_{0.3}MoO_3$ have also been reported.[41,45]

2.1.4 Switching

In the majority of CDW samples which display non-linear dc conductivity the change in the conductivity at and above E_T occurs in a relatively smooth, continuous fashion. Far above E_T, the conductivity appears to again saturate to an ohmic value (See Fig. 2-2). In some samples the CDW depinning can occur so abruptly in the current-voltage characteristic that a discontinuity appears at threshold.[46] In these samples the conductivity appears to "switch" directly from the low field to the high field state. Samples which display this phenomenon are referred to as switching samples. The temperature-dependent current-voltage characteristics of a switching $NbSe_3$ sample are shown in Fig. 2-6. Switching was first seen in $NbSe_3$,[46] and has

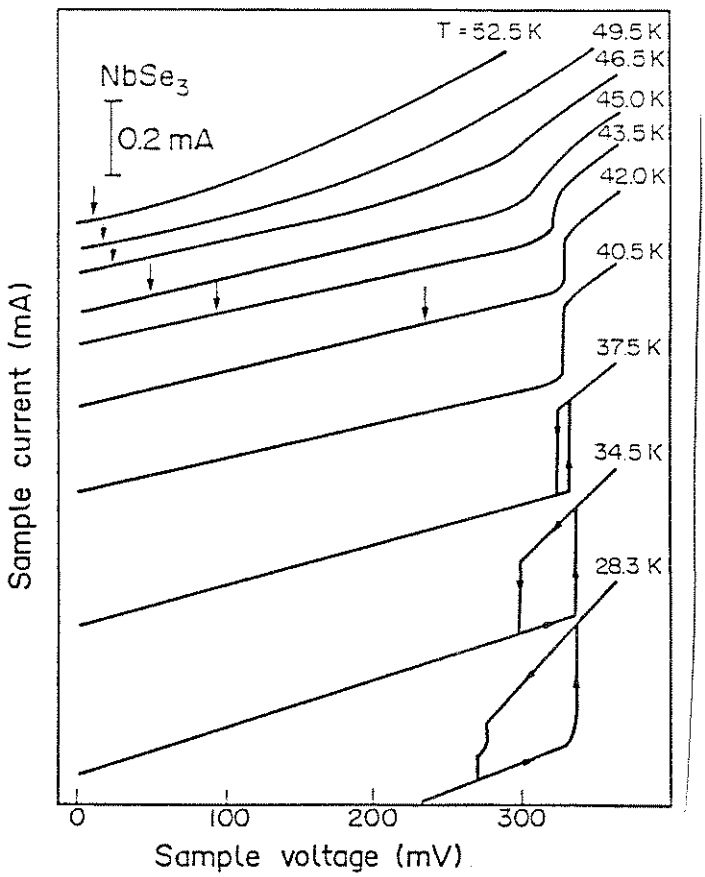

Figure 2-6 Current-voltage characteristic of a switching $NbSe_3$ crystal. The initial depinning fields are indicated by the arrows (from Ref. 48).

subsequently been observed in samples of TaS_3,[47] $K_{0.3}MoO_3$,[26] and $(NbSe_4)_{3.33}I$.[28]

The dynamical switching state in CDW conductors is characterized by unusually large, temperature-independent threshold fields,[48] inductive ac response,[49] hysteresis and metastable states,[50] negative differential resistance,[51] and period doubling routes to chaos.[52] Recently it has been suggested that switching stems from the presence of phase-slip pinning centers in switching crystals that create large CDW phase polarization and localized CDW amplitude collapse.[53]

2.2 Dynamical models

A number of phenomenological models have been proposed to account for the dynamical properties discussed in the previous section. The proposed models include a single particle classical description,[54] a quantum mechanical tunneling model,[55] and a number of deformable medium theories based on the Fukuyam-Lee-Rice Hamiltonian.[56] All of these dynamical models assume that the unusual ac and dc response associated with CDW materials is due to collective motion of the charge density wave.

By far the simplest dynamical CDW model is the single particle classical model proposed by Grüner, Zawadowski, and Chaikin.[54] In this model, the CDW is treated as a rigid object with a mass m^* and a charge e moving in a sinusoidal

potential; the CDW internal degrees of freedom are completely neglected in this approach. This model has been surprisingly successful in qualitatively and semi-quantitatively describing the essential frequency and electric field dependent features of CDW transport.[2] The single particle equation of motion is[54]

$$\frac{d^2x}{dt^2} + \Gamma\frac{dx}{dt} + \frac{\omega_o^2}{Q}\sin(Qx) = \frac{eE}{m^*}, \qquad (2.9)$$

where x is the CDW center-of-mass coordinate, E is the applied electric field, Q is the periodic pinning potential wave vector, ω_o is the characteristic CDW resonance frequency, and $\Gamma = 1/\tau$ is a damping constant with a characteristic relaxation time τ. Recent theoretical work concerning the pinning effects of impurities on a sliding CDW suggests that the CDW pinning potential roughly resembles a sinusoidal function with a periodicity equal to the CDW wavelength ($Q = 2\pi/\lambda$).[57] Hence, there is some underlying physical justification for expecting Eqn. 2.9 to model CDW dynamical behavior.

Equation 2.9 successfully accounts for CDW non-linear dc conductivity past a electric threshold field, the bias-dependent narrow band noise, harmonic ($q = 1$) mode-locking, frequency-dependent conductivity (a fit using

Eqn. 2.9 is included in Fig. 2-3b), and impurity-dependent pinning effects.[3] While these effects are well accounted for by the single particle model, it cannot account for all aspects of CDW dynamics. In particular, it cannot account for the metastable effects that CDW materials exhibit,[58] switching phenomena, broad band noise, subharmonic ($q > 1$) Shapiro steps, and the detailed functional form of σ_{dc} near threshold. These deficiencies are presumably due to the simple form of this model's equation of motion. Some of these deficiencies could be alleviated by using a more realistic form for the pinning potential. In particular, the model can predict the existence of subharmonic Shapiro steps if a pinning potential with higher harmonic content, such as that suggested by the work of Tütto and Zawadowski,[57] is used. The other deficiencies exhibited by this model can be attributed to its neglect of the CDW internal degrees of freedom. Hence, there are a number of fundamental problems with this simple model, but it is nonetheless a useful pedagogical tool for understanding the basic properties of CDW transport.

A more complete description of CDW dynamics is realized in the Fukuyam-Lee-Rice Hamiltonian; this phase Hamiltonian includes the effects of non-uniform and random impurity pinning as well as the internal CDW degrees of freedom. The Hamiltonian is given by[56]

$$H = \frac{\kappa}{2}\int d^3x \; |\nabla\phi|^2 + W_o\rho_a \sum_i \cos[2k_F x_i + \phi(x_i)]$$

$$+ \int \frac{e\rho}{2k_F}\,\phi\, E \; dx \quad , \qquad (2.10)$$

where κ is the CDW elasticity constant, W_o is the impurity potential, ρ is the local charge density, ρ_a is the average charge density, and $\phi(x)$ is the local CDW phase. The three terms in Eqn. 2.10 are related to the CDW phase elasticity, CDW-impurity interactions, and the interaction between the CDW and externally applied electric fields, respectively. This expression assumes that the CDW amplitude is independent of position and time. Equation 2.10 is in general quite difficult to solve, and numerous simplifying assumptions have been made to determine its theoretical prediction.[3] A number of other models which include CDW internal degrees of freedom have also been proposed; these include a Frenkel-Kontorova model and a hydrodynamical model.[56] These models can successfully account for many aspects of CDW dynamics.[56]

Bardeen has taken a considerably different approach in attempting to account for dynamical CDW behavior. In the quantum model of charge density wave dynamics, CDW transport phenomena are assumed to occur due to the macroscopic quantum tunneling of the CDW across small pinning gaps.[55] These gaps presumably stem from the presence of pinning impurities within a CDW crystal. This approach was first suggested

because of the close similarity between the CDW electric-field dependent conductivity and that of zener tunnel junctions. In addition to accurately fitting the electric field dependent CDW conductivity, this model can account for narrow band noise oscillations, ac-dc interference phenomena, and the scaling relationship that exists between the ac and dc conductivity of a CDW material.[3]

At the present time it is difficult to say whether or not a quantum mechanical approach is superior to the previously discussed classical models. As yet, no experimental observation exist which can be explained only by a quantum description. It was believed at one point in time that the results of harmonic mixing experiments strongly supported a quantum description,[59] but recent analysis of the Fukuyam-Lee-Rice model suggests that the harmonic mixing data are actually better described classically.[60] Further, the failure to see any photon-assisted tunneling in combined ac and dc field experiments,[61] one of the most intriguing and important predictions of the quantum model,[55] strongly suggests that a quantum description of CDW dynamics may be inappropriate.

2.3 CDW materials

The static and dynamic properties of two quasi-one-dimensional charge density wave conductors, $NbSe_3$ and $K_{0.3}MoO_3$, are extensively examined in Chapters 4 and 5 of

this report. In the subsections to follow we briefly examine the structural and electronic properties of these two compounds.

2.3.1 $NbSe_3$

The crystal structure of $NbSe_3$ is depicted in Fig. 2-7. The basic building block consists of trigonal prismatic units with niobium atoms in the center of selenium prisms.[62,63] These prisms are stacked end-to-end, forming infinite chains, with the chain axis corresponding to the crystalline b axis. The crystal structure in the a-c plane, perpendicular to the chain axis, is shown in Fig. 2-8. The niobium chains are linked together along the c axis by inter-chain niobium-selenium bonds. Hence, $NbSe_3$ forms in ribbons along the b and c directions. The electrical conductivity along the c axis is roughly ten times smaller than along the b axis. Hence, $NbSe_3$ is only a moderately anisotropic compound.

As depicted in Fig. 2-8, the crystal structure in the a-c plane is fairly complicated. The unit cell consists of a pair each of three inequivalent prismatic chains. These three chains are distinguished by the distance between the selenium pairs in their respective prism bases. The type III chains have strong Se-Se pairing (the Se-Se separation is 2.37 Å), while the type I chains have intermediate pairing (2.49 Å), and the type II chains have relatively weak pairing

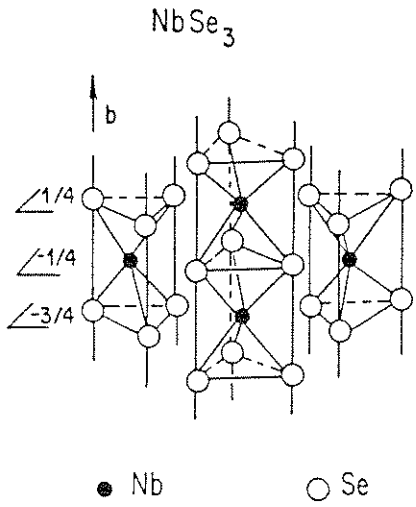

Figure 2-7 The trigonal prismatic chain structure of $NbSe_3$. The b axis corresponds to the niobium chain axis in $NbSe_3$ (from Ref. 62).

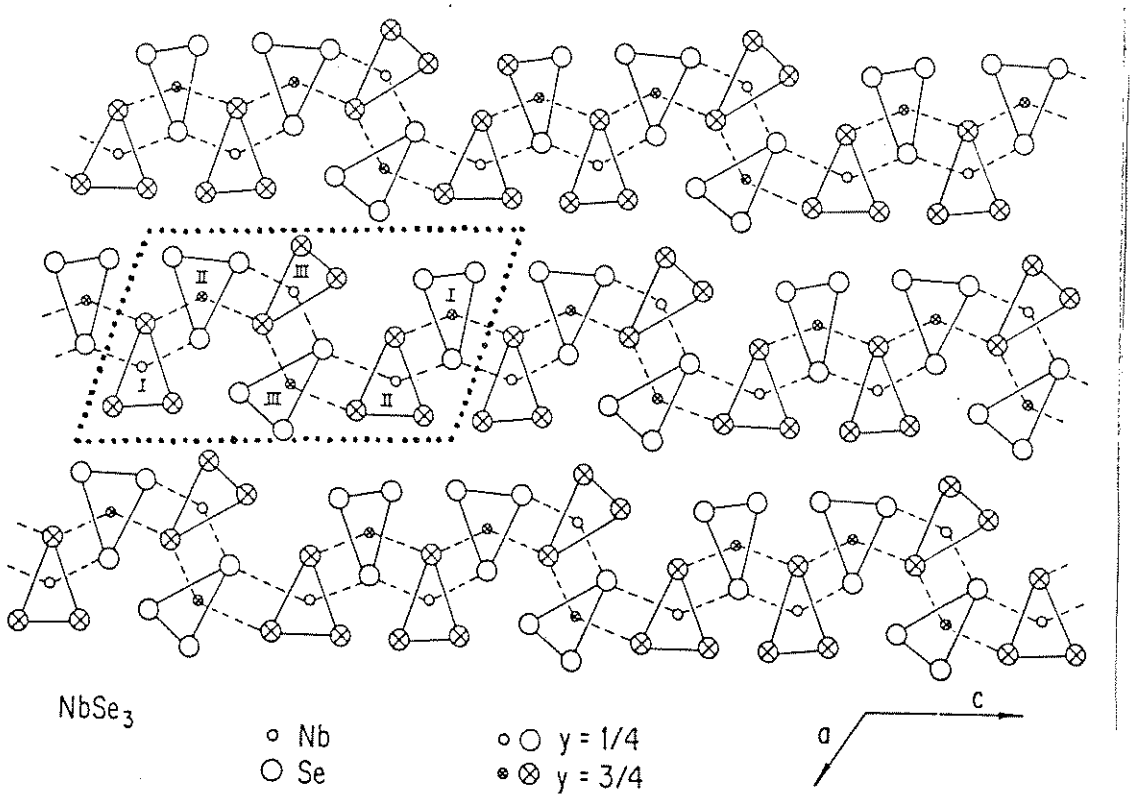

Figure 2-8 Projection of the $NbSe_3$ crystal structure in the a-c plane, perpendicular to the CDW chain (b) axis. The monoclinic unit cell, containing a pair each of the three chain types, is highlighted by the dotted lines (from Ref. 63).

(2.91 Å).[62,63]

The inequivalent nature of the three basis chains present in $NbSe_3$ strongly affects the band filling in this material. It has been suggested that the relatively strong Se pairing in type I and III chains gives rise to a covalent bond between their two base selenium sites, while the large separation in the type II chains requires independent, ionic bonding at the base sites. As a result, the electronic band structure filling for $NbSe_3$ has been roughly estimated as follows (note that Se is valence -2 while Nb is valence +5):[64,65] the five valence electrons of each niobium atom contribute 30 electrons to each unit cell. The four chains with strong Se-Se pairing (two type I and two type III chains) take up 16 of these electrons, while the two type II chains, with weak Se-Se interactions, account for 12 of the remaining electrons. Hence, there are 30 - 28 = 2 conduction electrons shared amongst the four conducting Nb sites (in this simple approach it is assumed that the Nb atoms in the type II chains do not take part in the conduction process). This gives 0.5 electrons per Nb site, corresponding to a quarter-filled conduction band.

$NbSe_3$ undergoes two Peierls transitions that lead to the formation of a pair of CDWs.[17,66] The first transition at T_{c1} = 144 K creates an incommensurate CDW with a wave vector of Q_1 = (0, 0.243, 0);[17] the second transition at T_{c2} = 59 K forms a second, independent CDW with a wave vector of

Q_2 = (0.5, 0.259, 0.5). The resistance anomalies shown in Fig. 2-1 are directly associated with these Peierls transitions. Clearly, $NbSe_3$ stays metallic at all temperatures. A number of band structure calculations[67,68] and NMR measurements[21,69] suggest that the first CDW transition takes place on the more highly one-dimensional type III chains. Hence, the upper Peierls transition only destroys a portion of the Fermi surface (the type I and type II chains are ungapped), and $NbSe_3$ stays metallic below T_{c1}. Shima's band structure calculations[67] indicate that the electronic dispersion of the type I and II chains create three independent Fermi surfaces. Two of these nest, and presumably account for the lower Peierls transition. The third, a small ellipsoidal structure, is believed to be unaffected by either CDW transition, and thus accounts for the metallic nature of $NbSe_3$ below 59 K.

2.3.2 $K_{0.3}MoO_3$

Although potassium blue bronze ($K_{0.3}MoO_3$) was first synthesized[70] in 1964 and subsequent research indicated that a metal-semiconductor transition occurs at 180 K,[71] it was not until $K_{0.3}MoO_3$ was "re-discovered" in 1981 that this material's low-dimensional character was carefully examined.[72] Optical reflectivity[73] and dc electrical resistivity[72] measurements indicate $K_{0.3}MoO_3$ is a quasi-one-dimensional metal above 180 K; additionally, X-ray

analysis clearly shows that the 180 K phase transition is a Peierls transition that results in the formation of an incommensurate charge density wave.[74] Potassium blue bronze has also been found to exhibit non-linear transport phenomena and narrow band noise oscillations due to collective CDW motion.[26]

As shown in Fig. 2-9, the crystal structure of $K_{0.3}MoO_3$ consists of infinite chains composed of MoO_6 octahedra.[75] The infinite chains extended along the crystallographic b axis, with the potassium atoms separating neighboring chains. There are three inequivalent types of MoO_6 octahedra which are differentiated by their relative positions within the unit cell. This is most clearly shown in an a-c plane projection of the crystal structure, which is depicted in Fig. 2-10.[76] The basic unit contains ten of these octahedra (four each of octahedra types 2 and 3, and two of type 1). The type 2 and 3 octahedra are linked via their respective edges and form infinite chains. The neighboring units are weakly linked via corner sharing of an oxygen site in the type 3 octahedra. This corner sharing results in the formation of infinite slabs in the [101] direction (in terms of the I-centered unit cell). The intervening potassium atoms act to strongly separate the neighboring planes. Hence, $K_{0.3}MoO_3$ consists of infinite chains along the b axis, which also form a weakly linked planar structure along the [101] direction. The room temperature conductivity along the

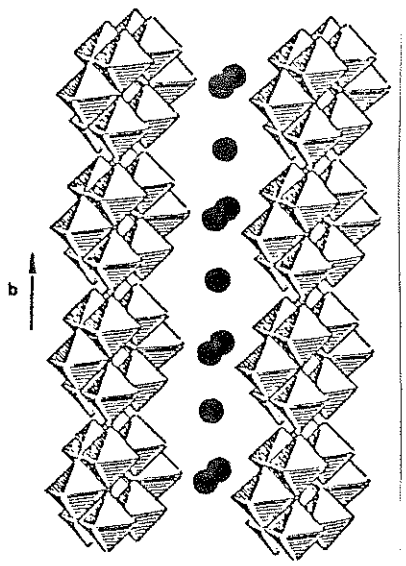

Figure 2-9 Crystal structure of $K_{0.3}MoO_3$ showing the infinite MoO_6 octahedral chains along the b axis, separated by intervening potassium atoms (denoted by black dots) (from Ref. 75).

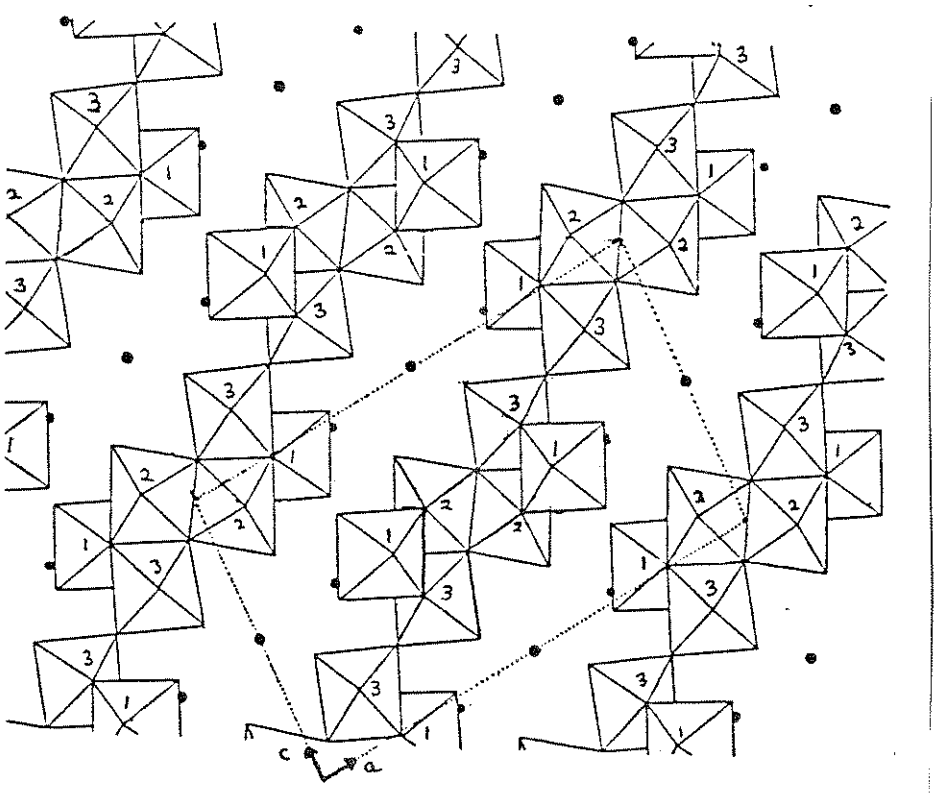

Figure 2-10 Projection of the $K_{0.3}MoO_3$ crystal structure in the a-c plane, perpendicular to the CDW chain axis. The I-centered monoclinic unit cell is highlighted by the dotted lines. The potassium atoms are denoted by black dots and the type of each MoO_6 octahedron is indicated by a number (1, 2, or 3) (from Ref. 76).

chain axis is roughly 80 times larger than along the planar direction, and more than 1000 times larger than along the direction perpendicular to these layers.[75] Hence, $K_{0.3}MoO_3$ is electronically far more one dimensional than $NbSe_3$.

The temperature-dependent resistance of $K_{0.3}MoO_3$ is depicted in Fig. 2-11 as a function of 1/T. Above 180 K $K_{0.3}MoO_3$ behaves metallically, while below this temperature the resistivity clearly follows an activated behavior indicative of a low temperature semiconducting state.[72,77] Hence, $K_{0.3}MoO_3$ undergoes a metal to semiconductor transition at T_c = 180 K. X-ray diffraction measurements indicate that this transition is accompanied by the formation of both a periodic lattice distortion and an incommensurate charge density wave.[74] The observed wave vector is Q = (0,0.74,0.5).[74] The size of the energy gap as determined from dc conductivity data indicates that $2\Delta \approx 8k_BT_c$, in rough agreement with Eqn. 2.6, assuming $T_c \approx T_c^{MF}/4$.[75]

The resistivity data in Figs. 2-1 and 2-11 indicate that the respective Peierls transitions which take place in $K_{0.3}MoO_3$ and $NbSe_3$ affect the two materials in subtly different ways. First, due to its more highly one dimensional nature, $K_{0.3}MoO_3$ undergoes a Peierls transition at a higher temperature than does $NbSe_3$. Secondly, the two transitions which occur in $NbSe_3$ do not completely destroy the Fermi surface in this material, thus allowing $NbSe_3$ to exhibit metallic behavior at all temperatures, while the

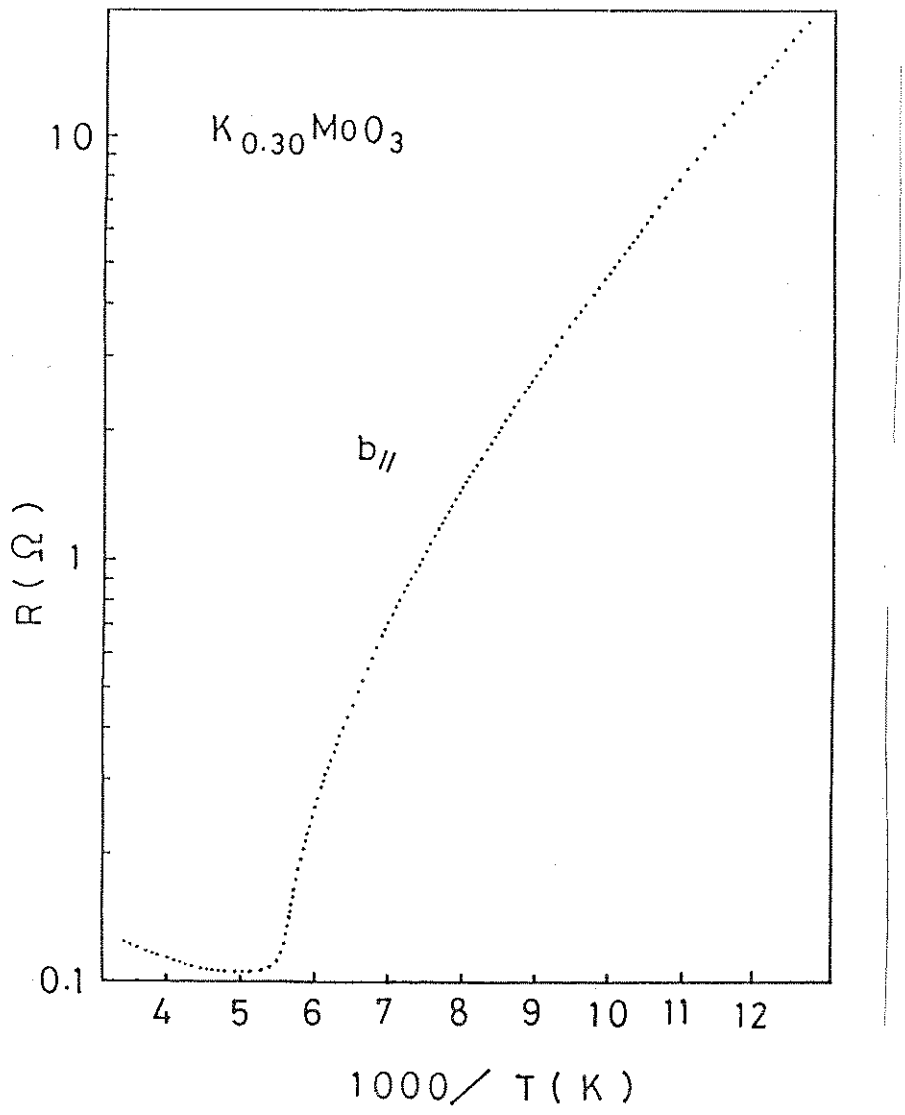

Figure 2-11 The temperature-dependent resistance of potassium blue bronze ($K_{0.3}MoO_3$) in the low-field limit. The resistance was measured along the chain axis (from Ref. 77)

single 180 K transition in $K_{0.3}MoO_3$ completely gaps the conduction band, converting $K_{0.3}MoO_3$ into a semiconductor below 180 K.

Chapter 3: Motivation for this experimental study

The objectives of this research project, with an emphasis on the questions we wish to answer, will be presented in this chapter. The project goals were twofold, first, to examine the collective mode static and dynamic properties of the charge density wave (CDW) conductors $NbSe_3$ and $K_{0.3}MoO_3$, and second, to investigate the single-particle transport properties of three anisotropic materials (URu_2Si_2, gold percolation films, and $La_{1.85}Sr_{0.15}CuO_4$). The motivating factors concerning the CDW research appear in Sec. 3.1, while those factors concerning the work on the non-CDW materials appears in Sec. 3.2.

3.1 Charge density wave materials

Although CDW collective mode dynamics has been studied extensively since 1976, there still exist many unanswered questions concerning the nature of this phenomena. The motivational factors for the four aspects of research performed on CDW materials in this research project appear in the following subsections.

3.1.1 Magnetic field effects on $NbSe_3$

In 1985 Coleman *et al.*[1] reported unusual magnetoresistance effects in the lower CDW state ($T < 59$ K)

of $NbSe_3$. They concluded that these effects could not stem from conventional magnetic field effects. Instead, they suggested that the anomalous magnetoresistance could be due to magnetic field-induced variations in either the number or mobility of the normal electrons. They also speculated that the anomalous magnetoresistance implies that there exists a spin density wave component to the CDW in $NbSe_3$. Subsequent theoretical calculations supported the notion that the strong magnetoresistance stems from normal-to-CDW carrier conversion.[2]

Unfortunately, it was impossible to determine, based solely on the magnetoresistance data, if this theoretical conjecture was correct. Hence, a portion of this research project consisted of performing careful static and dynamic transport measurements on $NbSe_3$ crystals in externally applied magnetic fields. This work was undertaken to determine whether or not carrier conversion occurs in $NbSe_3$, and also to see if applied magnetic fields have any effect on CDW dynamics.

3.1.2 Temperature gradient effects on $NbSe_3$

When this research project was initiated in 1984 there existed considerable controversy as to the nature of the mechanisms responsible for the narrow band noise (NBN) oscillations which accompany dc CDW motion. The two vying schools of thought believed that narrow band noise was either

a bulk[3] or a contact[4] effect. At that time, seemingly contradictory evidence existed to support both notions. To determine which process is responsible for the NBN oscillations, researchers took advantage of the strong temperature dependence of the parameters which determine the fundamental NBN frequency by examining the NBN spectra produced by CDW crystals in the presence of longitudinally applied temperature gradients.[5]

These initial investigations did not completely clear up the NBN controversy. For this reason, we embarked on a detailed examination of the temperature gradient effects on NBN and related phenomena in $NbSe_3$. Because no theory concerning the temperature gradient effects on bulk-generated NBN existed, we also developed a simple model of the ΔT effects on bulk-generated NBN spectra to determine if bulk-based NBN production was consistent with the experimental temperature gradient observations.

3.1.3 CDW switching in a temperature gradient

In most cases, CDW depinning is evident in a current-voltage (I-V) relationship as a smooth, continuous change from the pinned, linear state to the higher conductance sliding, non-linear state. In some CDW crystals, the CDW depins in a sharp, hysteretic manner creating an abrupt discontinuity in the I-V curve; this phenomenon is referred to as switching.[6] It has been suggested that this

effect is due to the presence of ultra-strong pinning centers within switching crystals that strongly alter the CDW depinning process.[7]

When this research project began, little was known about the internal arrangement of these ultra-strong impurity sites. Further, while all switching I-V curves show discontinuous depinning, there exist large sample-to-sample variations in the number of switches and the degree of hysteresis that a particular sample's I-V curve can exhibit. To determine the underlying causes of these variations, and to map out the structure of CDW switching domains, we have performed a careful study of temperature gradient effects on switching $NbSe_3$ samples.

3.1.4 Noise phenomena in $K_{0.3}MoO_3$

Although $K_{0.3}MoO_3$ was first synthesized in 1964,[8] it was not until 1982 that it was realized that this material undergoes a Peierls transition at 180 K.[9] $K_{0.3}MoO_3$ was subsequently found to exhibit sliding collective mode non-linear dc conductivity.[10] While this material displays narrow band noise oscillations, these oscillations are typically of very low quality, indicating that the sliding CDW state is generally very incoherent.[11] As a result, $K_{0.3}MoO_3$ samples do not usually display the many phenomena associated with NBN oscillations. To determine if strongly coherent CDW response, and the noise and interference

phenomena related with it, can occur in $K_{0.3}MoO_3$, we have carefully examined ultra-thin samples of this material in combined ac and dc driving fields.

3.2 Non-CDW materials

Although not all low-dimensional conductors display charge density wave ground states, their electronic transport properties can still be very different from those exhibited by conventional, isotropic materials. In the following subsections we examine the special properties of three such novel systems which motivated their study in this research project.

3.2.1 The heavy Fermion compound URu_2Si_2

In addition to displaying heavy Fermion properties (high effective charge carrier mass) and a low temperature superconducting ground state, URu_2Si_2 also shows evidence for an intermediate density wave state.[12] Heat capacity and resistivity measurements suggest that a Fermi surface based transition occurs at 17.5 K in URu_2Si_2. At the time this research project was instigated, the precise nature of this instability was unclear. Hence, we have performed careful electronic transport measurements on URu_2Si_2 to determine the nature of the 17.5 K transition.

3.2.2 Gold percolation films

With the rapidly expanding interest in fractal geometry[13] which occurred during the early 1980's, there has been a considerable effort recently to find real-world fractal systems and study their transport properties. With this goal in mind, IBM researchers fabricated special thin gold fractal percolation films in 1982.[14] Initial room temperature, low frequency conductivity measurements suggested that electron transport in this fractal percolation system was considerably different from that predicted by scaling percolation theories.[15] We have extended these measurements to higher frequencies (1 GHz) and down to 4.2 K in order to more clearly determine the dynamical properties of these films.

3.2.3 The high T_c compound $La_{1.85}Sr_{0.15}CuO_4$

With the discovery of high temperature superconductivity in the alloyed lanthunum-copper-oxides $La_{2-x}M_xCuO_4$ (M = Ba, Ca, Sr) by Bednorz and Müller,[16] a mammoth research effort began throughout the world to understand the physics of this new class of materials. When this research project began, very little was known about the electronic properties of lanthanum-copper-oxides. Hence, we initiated a careful study of the transport properties of $La_{1.85}Sr_{0.15}CuO_4$ to more fully characterize this material's normal and superconducting state properties.

Chapter 4: Static and dynamic properties of the charge density wave conductor $NbSe_3$

In this chapter the results from measurements of the sliding and pinned transport properties of $NbSe_3$ shall be presented. These experimental results are presented and their implications discussed in three sections: magnetic field effects (4.1), temperature gradient effects in non-switching crystals (4.2), and charge density wave (CDW) switching behavior in a temperature gradient (4.3).

4.1 Magnetic field effects in $NbSe_3$

A growing number of synthetic inorganic quasi-one-dimensional metals have been observed to be unstable towards $2k_F$ Peierls distortions, resulting in a CDW ground state. Of particular interest in these systems is the dynamic nature of the CDW condensate itself, and a great deal of experimental and theoretical effort has been devoted to the understanding of the resulting collective-mode transport.[1] A simple Peierls distortion of the crystal lattice is associated (in a 1-D system) with a complete destruction of the Fermi surface (FS), through formation of a temperature dependent gap in the (single particle) excitation spectrum. Indeed, virtually all low-dimensional conductors which are known to display "sliding" CDW conduction undergo metal-insulator transitions. Below the transition

temperature T_P, a semiconducting state is realized, with T = 0 gaps on the order of $2\Delta_o \approx 1000$ K.

A notable exception to this behavior is $NbSe_3$, which undergoes two CDW transitions (T_{P1} = 144 K, T_{P2} = 59 K), neither of which completely destroys the entire FS: $NbSe_3$ remains metallic (or semimetallic) at all temperatures.[2,3] Interestingly, $NbSe_3$ was the first material to display CDW conduction, and has been the most widely studied in terms of CDW dynamics. In general, the observed CDW behavior in $NbSe_3$ is qualitatively similar to that observed in true CDW semiconductors (e.g. TaS_3, $(TaSe_4)_2I$, $K_{0.3}MoO_3$), and hence in $NbSe_3$ the "normal" carriers (resulting from the remaining portions of the FS below T_P) are often assumed to represent a non-interacting parallel conduction mechanism.

Recently, Coleman *et al.* reported unusual magnetoresistance effects in the lower CDW state (T < 59 K) of $NbSe_3$ when a magnetic field was applied perpendicularly to the crystal chain (b) axis.[4] Their temperature-dependent magnetoresistance data are depicted in Fig. 4-1. The presence of the magnetic field appears to greatly enhance the resistance anomaly present below T_{c2} = 59 K. At the relatively high temperature of 25 K, a relative increase in the resistivity, $[\rho(H) - \rho(0)]/\rho(0)$, on the order of 5 was observed at H = 227 kG. A magnetoresistance of this magnitude and at these relatively high temperatures cannot be attributed to conventional magnetoresistance mechanisms.[5]

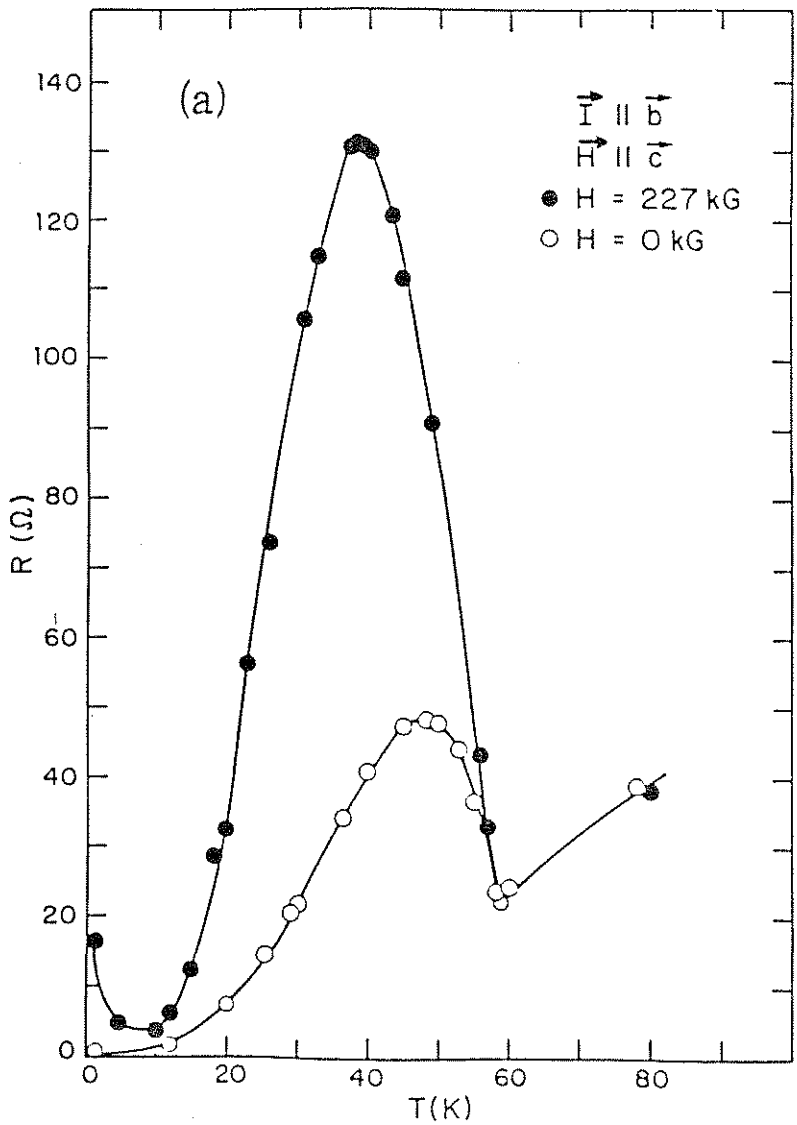

Figure 4-1a The resistance of $NbSe_3$ as a function of temperature measured at H = 0 (open circles) and H = 227 kG (solid circles). The resistance anomaly below T_{c2} = 59 K is clearly enhanced (from Ref. 4).

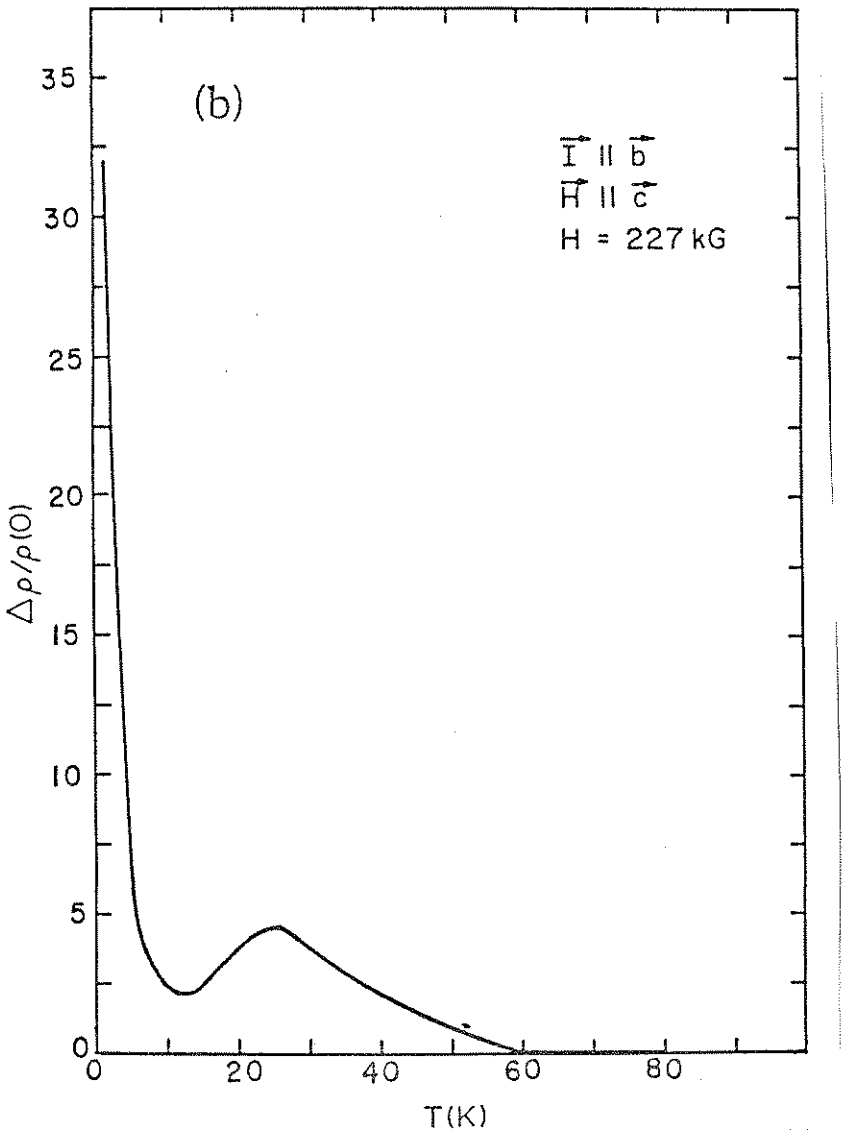

Figure 4-1b The magnetoresistance $[\rho(H)-\rho(H=0)]/\rho(H=0)$ as determined form the data in Fig. 4-1a (from Ref. 4).

Coleman *et al.* also observed a reduction in the CDW depinning threshold field E_T when it was measured in the presence of a perpendicularly applied magnetic field. They concluded that the large enhancement of the resistance anomaly was not caused by the dynamics of the CDW, but rather by the effect of the magnetic field on either the number or the mobility of the normal electrons. They further speculated that such a strong coupling between carriers and the applied H field implies a spin density wave (SDW) component to the density wave ground state.

Subsequent work by Balseiro and Falicov[6] has demonstrated that strong magnetic fields may lead to a destruction of electron hole pockets in imperfectly nested anisotropic conductors, leading to an H-enhanced gap at the Fermi level for a system with an intrinsically stable density wave ground state (either CDW or SDW). The mechanism of Balsiero and Falicov (which includes the effects of band broadening and tunneling between bands) would imply that, in $NbSe_3$, the H field induces a direct conversion of normal carriers to CDW (condensed) carriers, thus effectively modifying the CDW order parameter Δ, and enhancing the one dimensional character of this material.

In this section we present the results from three different sets of experiments which were performed in order to better characterize these magnetic field effects, and in so doing, determine their underlying causes. The results of

narrow band noise and resistivity measurements are presented in Sec. 4.1.1,[7] magnetothermopower results are presented in Sec. 4.1.2,[8] and magnetodynamical ac conductivity measurements are presented in Sec. 4.1.3.[9] These data are all consistent with the conjecture that direct magnetic-field-induced normal to CDW carrier conversion is responsible for the anomalous magnetoresistance exhibited by $NbSe_3$.

4.1.1 Magnetic field induced carrier conversion in $NbSe_3$

We have performed careful noise and resistivity measurements on $NbSe_3$ in H fields up to 75 kG, in an attempt to observe directly a possible H-induced increase in CDW carrier concentration n_c.[7] We find H-induced changes in the narrow band noise spectrum which indicate clearly that n_c increases with increasing H, the effect becoming greater at lower temperatures where the magnetoresistance increases. The observed changes in n_c correlate well to the percentage of FS destroyed by the magnetic field, as determined by the ohmic and nonlinear dc conductivity.

In these experiments, single crystals of $NbSe_3$, with typical cross-sectional areas of $A = 2.2 \times 10^{-7}$ cm^2 and lengths of $L = 0.5$ mm, were mounted in a two probe configuration with the chain (b) axis of the crystal perpendicular to the H field. A dc current was applied through the sample, and the

voltage across the sample was amplified and detected with either a dc voltmeter or high frequency spectrum analyzer. For applied electric fields E exceeding the threshold E_T for the onset of CDW conduction, and with H = 0, a clear narrow band noise spectrum was observed, with a dominant fundamental and numerous higher harmonics. Application of H fields up to 75 kG were found to have no marked effect on the amplitude or quality of the narrow band noise spectrum, but for fixed dc bias, the fundamental noise frequency f was highly H-field dependent.

In a simple model,[10,11] the narrow band noise frequency is related to the excess CDW current I_{CDW} through

$$I_{CDW} = n_c e\, v_d A = n_c e\, f \lambda, \qquad (4.1)$$

where $I_{CDW} = I - V/R_o$ with I the total sample current, V the time averaged sample voltage, and R_o the low field (ohmic) sample resistance. v_d is the CDW drift velocity, A the sample cross sectional area, and λ is a constant length which reflects the periodicity of the CDW pinning potential; previous H = 0 NBN measurements indicate that λ is the CDW wavelength.[1] Eqn. 4.1 indicates that for fixed n_c, I_{CDW} is directly proportional to f, and the ratio I_{CDW}/f directly reflects n_c.

Fig. 4-2 shows I_{CDW} vs. f for $NbSe_3$ at T = 37.4 K, for H = 0 and for an applied field H = 75 kG. For H = 0, the

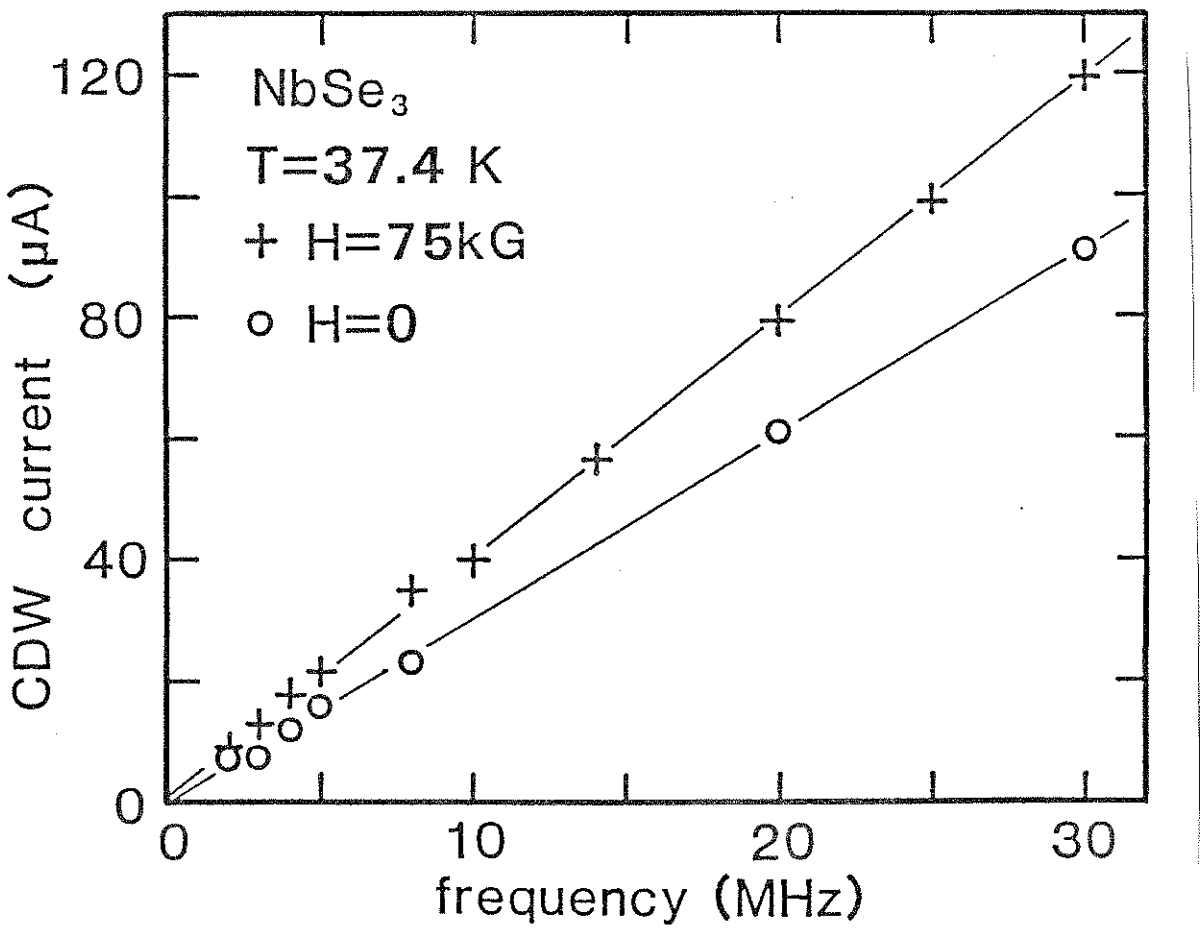

Figure 4-2 I_{CDW} vs. narrow band noise frequency in $NbSe_3$ with and without an applied magnetic field.

linear relationship is in accord with Eqn. 4.1 and consistent with previous narrow band noise studies in $NbSe_3$.[11-13] With H = 75 kG, a linear dependence of f upon I_{CDW} is again observed, but with a different slope. Fig. 4-2 demonstrates clearly that the ratio I_{CDW}/f *increases* in the presence of an applied magnetic field. With e, λ, and A independent of H in Eqn. 4.1, Fig. 4-2 demonstrates that *the effect of a magnetic field in $NbSe_3$ is to directly enhance the CDW carrier concentration*. At 37 K, the effect of an H = 75 kG field is to increase the CDW carrier concentration by approximately 30%, a fairly dramatic change. As will be shown below, the H-field induced carrier conversion (normal to CDW electrons) appears to account entirely for the spectacular (low electric field) magnetoresistance in $NbSe_3$, and hence the present experiments rule out normal-carrier-mobility effects as being the source of the magnetoresistance.

Data such as that shown in Fig. 4-2 were taken at various values of magnetic field strength and temperature in the lower CDW state. Fig. 4-3 shows the slope I_{CDW}/f vs. H for T fixed at 37.4 K. Up to H = 75 kG, a virtually linear dependence of I_{CDW}/f (and hence n_c) on H is obtained, with $d[I_{CDW}/f]/dH = 1.8 \times 10^{-3}$ μA/MHz kG. With λ = 14 Å, this corresponds to an H-field induced carrier conversion rate $dn_c(H)/dH = 3.6 \times 10^{18}$ carriers/kG cm^3.

Fig. 4-4 shows the relative increase in CDW carrier

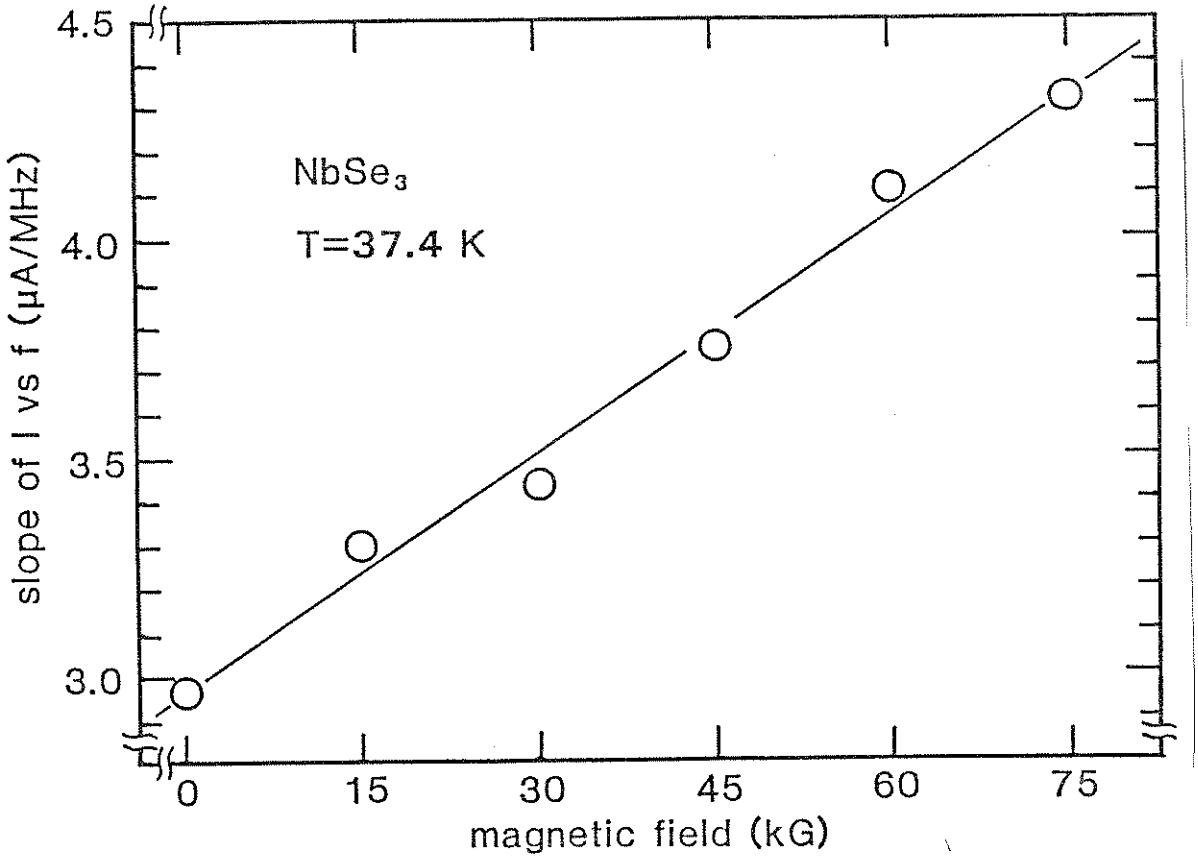

Figure 4-3 $I_{CDW}/f \approx n_c$ vs. H in $NbSe_3$. An increasing magnetic field results in an increase in the CDW carrier concentration. Up to H = 75 kG, the carrier conversion rate is linear in H.

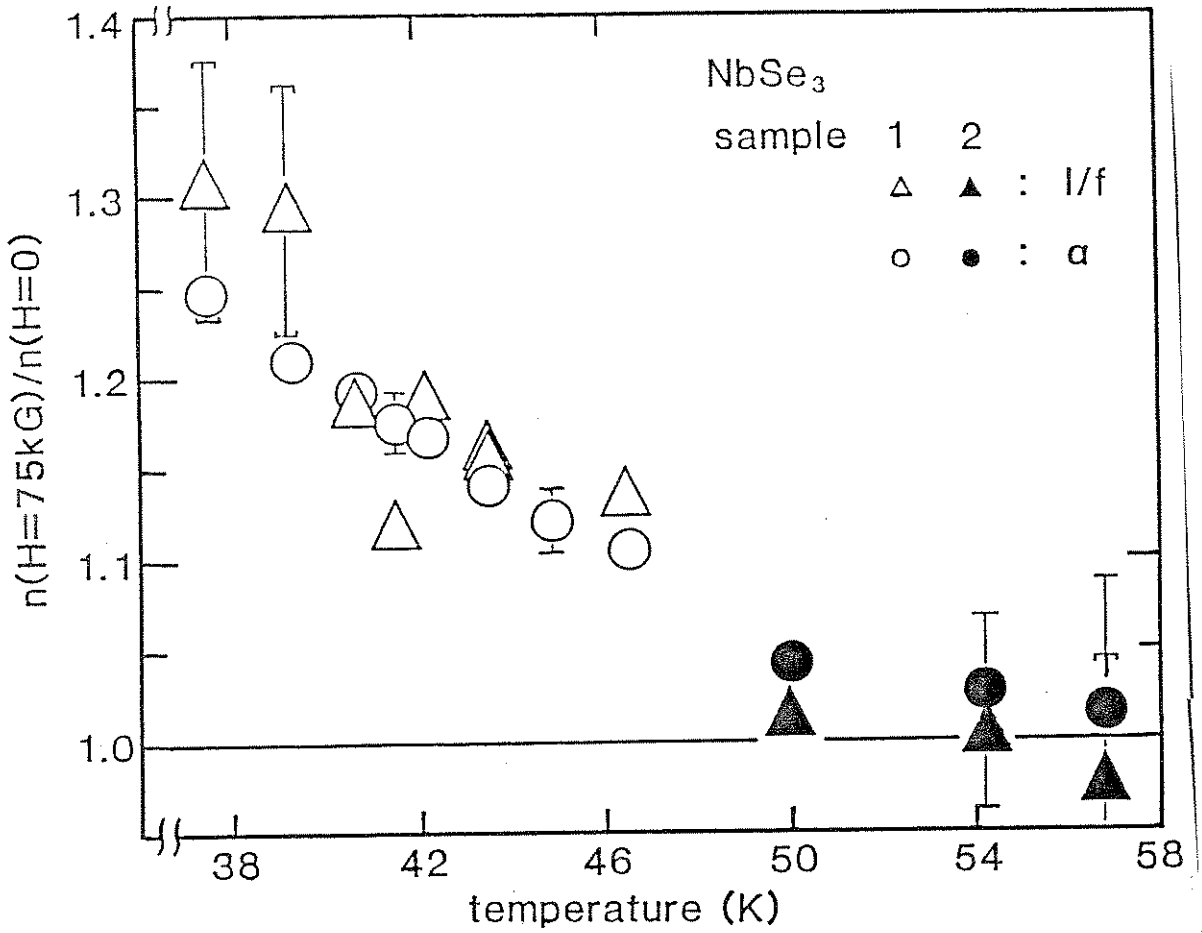

Figure 4-4 Relative increase in CDW carrier concentration due to 75 kG field in $NbSe_3$, as a function of temperature. The triangles refer to n_c as determined directly from noise spectra, while the circles refer to the fraction of Fermi surface destroyed as determined from resistivity data (see text).

concentration, induced by an H = 75 kG field, as a function of temperature in the lower CDW state. Near the CDW transition temperature T_p = 59 K, no increase in n_c is observed, while $n_c(H=75kG)/n_c(H=0)$ increases dramatically with decreasing temperature. Fig. 4-4 effectively defines the new CDW order parameter $\Delta(H,T)$. Previous studies[12,13] have demonstrated that the temperature dependence of $\Delta(H=0,T)$ is borne out directly in measurements of $I_{CDW}/f \approx n_c$. In the mean field approximation, the CDW carrier concentration is related to the order parameter by[14]

$$\frac{n_c(T)}{n_c(T=0)} \approx \Delta(T), \qquad (4.2)$$

valid for T close to T_p (note that this result supersedes earlier derivations which erroneously suggested that $n_c \approx \Delta^2$ near T_p.[15] Lee and Rice discuss the reasons for the discrepancy in Ref. 14). For $T << T_p$, $\Delta(T)$ may again be related to $n_c(T)$,[14] and, as in superconductors, at T=0, $n_c(T)$ equals unity; i.e., all carriers are condensed in the CDW state, *if* the system displays perfect Fermi surface nesting.

The magnetic-field enhancement of n_c (and hence the enhancement of the CDW order parameter) shown in Fig. 4-4 for the narrow band noise study, may be compared to the percentage of FS removed by the CDW transition and the

applied H-field. In addition to measurements of the narrow band noise just described, we have performed pulsed low and high electric field I-V studies on $NbSe_3$ in the presence and absence of magnetic fields. Consistent with the results of Coleman *et al.*,[4] we find that although the low field (Ohmic) resistance R_o of the crystal is strongly influenced by H, the high electric field (saturated) resistance R_{sat} is independent of H. The fraction of FS removed by the CDW transition and H field may be expressed as[16]

$$\alpha(H,T) = \frac{\sigma_c(H,T)}{\sigma_o(H,T) + \sigma_c(H,T)}, \tag{4.3}$$

with

$$\sigma_o(H,T) = \frac{1}{R_o(H,T)}, \tag{4.4}$$

$$\sigma_c(H,T) = \frac{1}{R_{sat}(H,T)} - \sigma_o(H,T). \tag{4.5}$$

With H = 0, approximately 60% of the remaining FS is destroyed by CDW formation at T_P = 59 K;[16] with H = 75 kG this percentage is significantly greater, and temperature dependent. The circles in Fig. 4-4 represent the fractional increase in α due to application of a 75 kG magnetic field. The ratio $\alpha(H = 75\ kG,T)/\alpha(H = 0,T)$ is seen to be in good agreement with carrier concentration increases deduced from the narrow band noise studies. It should, however, be noted

that Eqn. 4.3 represents only a crude approximation to the fraction of FS removed; a more quantitative evaluation of α would require detailed information concerning the band structure of $NbSe_3$ above and below the 59 K Peierls transition.

In summary, narrow band noise measurements indicate that the anomalous magnetoresistance effects exhibited by $NbSe_3$ are well accounted for by a straightforward enhancement of the CDW order parameter $\Delta(H,T)$ induced by the applied magnetic field. This finding is consistent with the theoretical predictions of Falicov and Balsiero,[6] and indicates that the anomalous magnetoresistance can be accounted for without requiring that there be a spin density wave component to the CDW in $NbSe_3$. A more quantitative comparison of our results for $\Delta(H,T)$ with this theory would necessitate a detailed knowledge of the semimetallic band structure of $NbSe_3$.

4.1.2 Magnetothermopower of $NbSe_3$

In this section magnetothermopower (TEP) measurements on the lower CDW state of $NbSe_3$ in magnetic fields up to 75 kG in strength are presented. At temperatures below the 59 K CDW transition, application of a large magnetic field transverse to the crystal chain axis causes the longitudinal thermopower to become increasingly positive. At temperatures below 20 K, the thermopower appears to saturate at high

magnetic fields. These results indicate that the magnetic field causes $NbSe_3$ to become more hole-like. That is, the magnetic field removes normal electron-like states from the Fermi surface, leaving the holes less compensated and resulting in a positive increase in the thermopower. The "disappearing" electrons condense into the ground state CDW condensate where they give no contribution to the thermopower. These results will be interpreted in terms of a magnetic field induced one-dimensionalization of the electronic band structure of $NbSe_3$, and an associated normal-to-CDW carrier conversion.

The experimental thermopower measurements were performed on single crystals of $NbSe_3$ grown by the usual vapor-transport method. The crystals were of reasonable quality as determined from dc electric threshold field measurements ($E_T \approx 30$ mV/cm at 48 K). The thermopower was measured using a slow ac heating method.[17] Single-crystal samples with gold leads attached to the ends with silver paint were suspended (in vacuum) between a pair of crystalline quartz blocks. Both quartz blocks were wrapped with independent manganin heater wires which could be used to ramp a temperature gradient of varying magnitude and direction across the sample. The temperature gradient was monitored with a chromel-constantan reference thermocouple, which was relatively insensitive to magnetic field.[18] For all the data presented in this communication, the magnetic

field was directed perpendicularly to the chain (b) axis of the $NbSe_3$ crystals.

Figure 4-5 shows the thermopower of $NbSe_3$ at temperatures below 100 K, for selected values of applied magnetic field up to 75 kG. For H = 0, these results are consistent with those of previous studies.[19,20] Above T_{c2} = 59 K, the TEP is independent of H. On the other hand, below T_{c2}, application of H results in a positive increase in the TEP, with the effect becoming larger with decreasing temperature. At T = 25 K, for example, a 75 kG H field changes the TEP from zero to +60 μV/K. Below 15 K, the TEP in the high H-field limit appears to saturate at a maximum value of roughly +80 μV/K.

Figure 4-6 shows the thermopower plotted as a function of H in the temperature range 11 K to 56 K. Just below the Peierls transition temperature T_{c2}, the magnetic field affects the TEP by only a small amount (ΔS = 3 μV/K at H = 75 kG). As the temperature is lowered, the H-induced change in the thermopower becomes larger, and follows a roughly quadratic dependence on H. The dashed lines in Fig. 4-6, drawn for the 42 K, 33 K, and 29 K data, are quadratic fits normalized to the high and low H field values. The dependence of the thermopower on H increases by roughly one order of magnitude between 49 K and 29 K [d^2S/dH^2 (49 K) = 7.1×10^{-4} μV/K kG^2, d^2S/dH^2 (29 K) = 6.9×10^{-3} μV/K kG^2). Below 30 K the thermopower appears to lose its quadratic

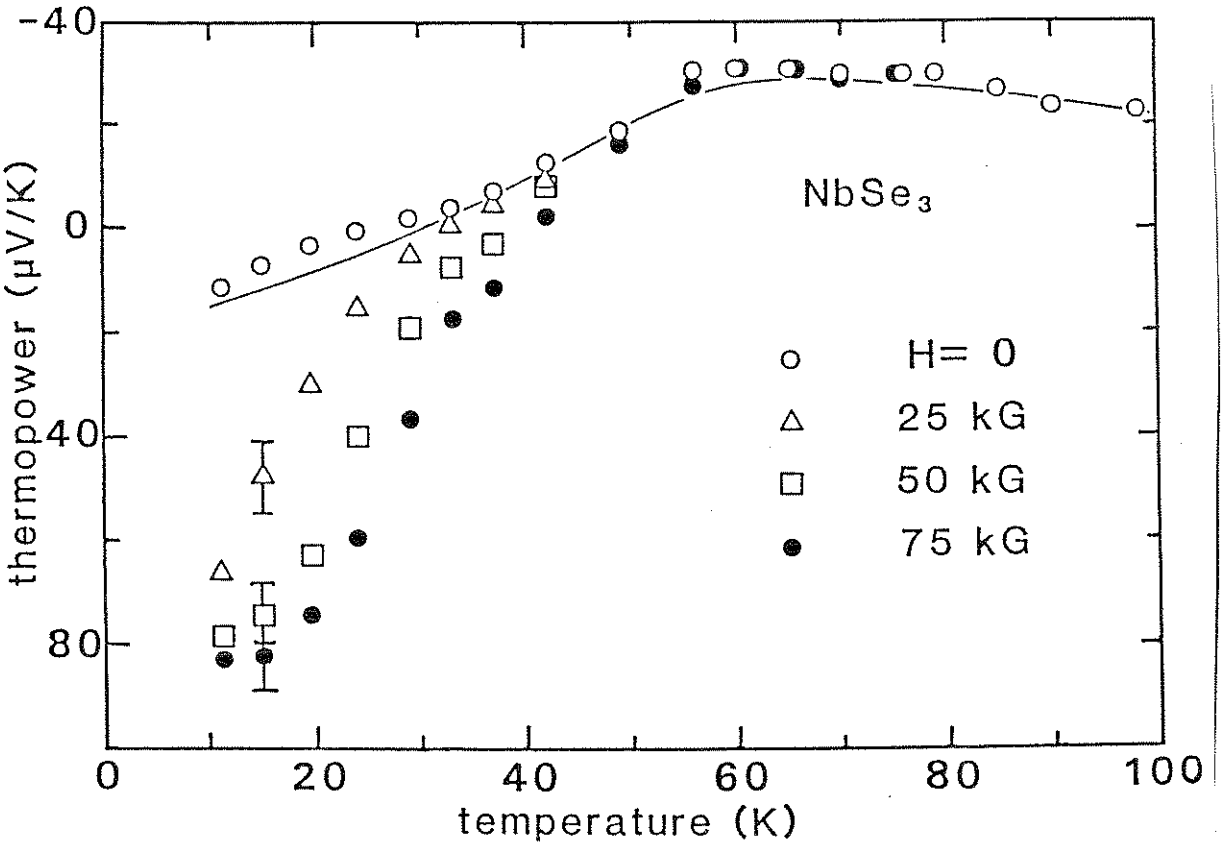

Figure 4-5 Magnetothermopower versus temperature in $NbSe_3$. The lower CDW state exists below T<59 K. The solid line is H=0 data from ref. 19.

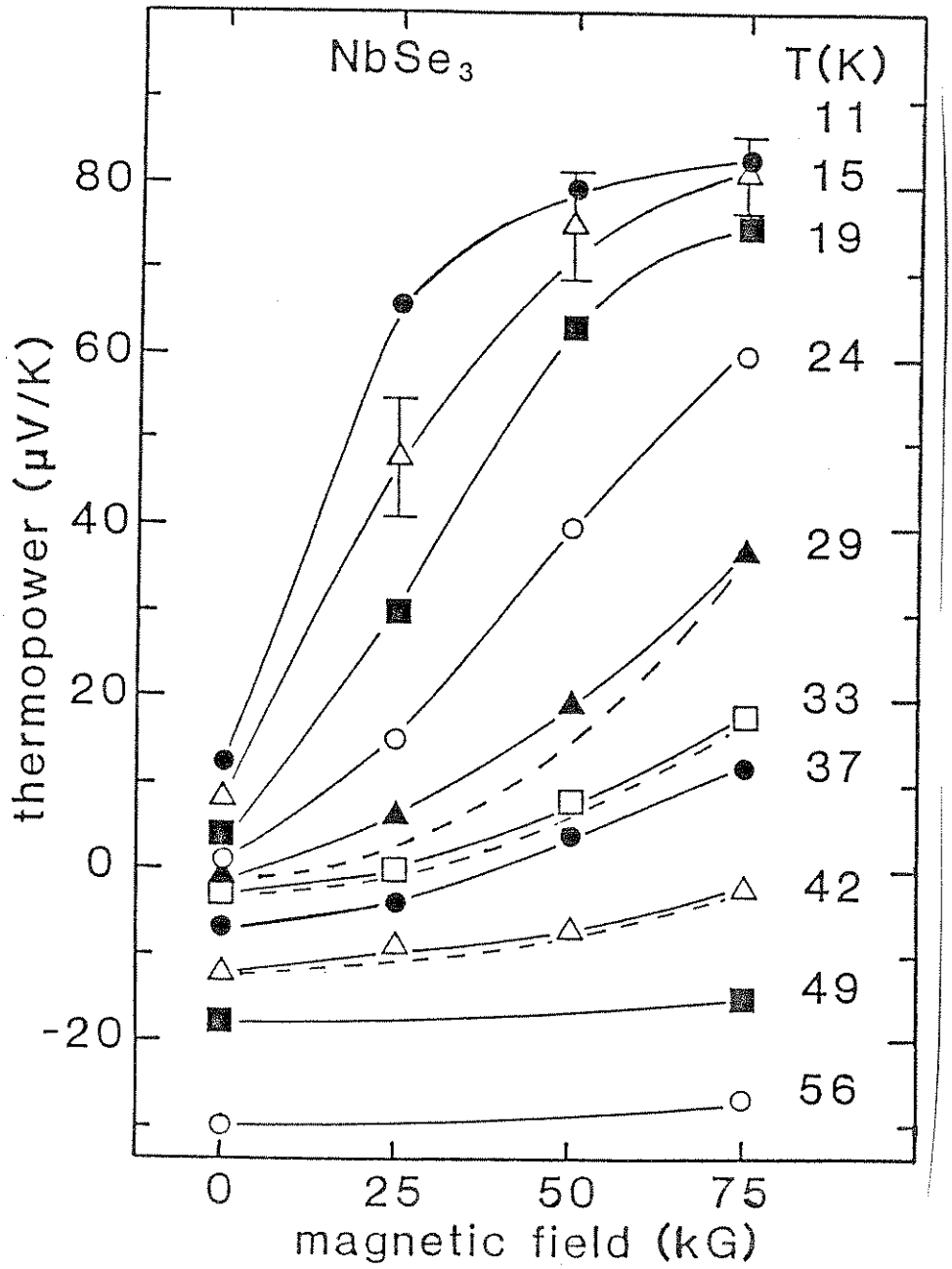

Figure 4-6 Magnetothermopower versus magnetic field strength up to 75 kG at temperatures below the 59 K Peierls transition. The solid lines are guides to the eye. The dashed lines are quadratic fits to the 29 K, 33 K, and 42 K data.

dependence on H, becoming approximately linear in field strength.

Finally, at temperatures below 20 K the TEP appears to saturate at high H, to roughly +80 μV/K. The saturation value is approached approximately as $1/H^2$. The general trend we thus observe is that at low magnetic fields and high temperatures the TEP is quadratic in H, while at high magnetic fields and low temperatures the TEP saturates in an inverse quadratic manner. At moderate temperatures and H fields there is a crossover between these two behaviors; this is well illustrated by the T = 24 K data of Fig. 4-6.

In analyzing these results we consider two possible mechanisms for the magnetic field thermopower enhancement. The strong magnetothermopower effect could be due to novel magnetic field interactions with the imperfectly nested remnants of the Fermi surface, or the effect could be a result of more conventional magnetic field interactions with the conduction electrons, as occurs in noble metals. Before examining this question in detail, a few comments on thermopower in general are in order. The thermopower of a conductor is due to two contributions. First is the contribution of charge carriers (electrons, or electrons and holes if we consider a two band system) as they diffuse across the sample in response to the applied temperature gradient. This portion of the thermoelectric power is expected to be roughly linear in temperature, and to have a

sign that reflects the sign of the majority carrier. Secondly, in tandem with carrier diffusion is the diffusion of phonons across the sample. At high temperatures such phonons give no contribution to the thermopower, because they cannot effectively couple to the charge carriers. At low temperatures, well below the Debye temperature, phonons can effectively scatter off holes or electrons, thereby imparting momentum to them; in essence the stream of phonons drag the charge carriers along, resulting in a "phonon drag" contribution to the TEP. At moderate to low temperatures, such phonon drag contributions can dominate the TEP.

Experimental and theoretical work has demonstrated that both charge diffusion and phonon drag components of the TEP can be affected by magnetic fields. In aluminum alloys, for example, the drift contribution has been observed to change sign with increasing H and saturate at high H.[21] Using a simple model of electron diffusion magnetothermopower, Blatt et. al. suggest that the TEP always saturates at high H fields, irrespective of the H-dependence of the magnetoresistance.[22] In noble metals, the phonon drag contribution to the TEP can be substantially enhanced by the application of an external magnetic field;[23] similar results are obtained in aluminum and indium.[24]

Although magnetothermopower effects such as those just described cannot be entirely ruled out for $NbSe_3$, they do not appear to form a significant contribution to the behavior

observed in Figs. 4-5 and 4-6. Even with H=0, $NbSe_3$ shows no substantial phonon drag behavior, and H-induced changes in the TEP shown in Figs. 4-5 and 4-6 are much larger than those normally associated with H field phonon drag enhancements. In the diffusion magnetothermopower theory of Blatt et. al., the TEP can be expressed as[22]

$$\Delta S = \frac{\pi^2 k_B^2 T}{3\,|e|}\left[\frac{\Delta\rho/\rho}{1+\Delta\rho/\rho}\right] D \qquad (4.6)$$

where $\Delta\rho/\rho$ is the magnetoresistance and D is a fitting parameter. From Eqn. 4.6, $\Delta S(H)$ saturates at high H fields for $\Delta\rho/\rho >> 1$. This expression is in strong disagreement with the TEP results for $NbSe_3$. For example, in Fig. 4-6 the low temperature saturation of the TEP near H = 75 kG occurs for $\Delta\rho/\rho \approx 2.2$, in contrast to the expected condition $\Delta\rho/\rho >> 1$. Detailed fits of Eqn. 4.6 to the data of Fig. 4-6 also indicate $D \approx 300\ eV^{-1}$ near 17 K, an unreasonably large value.[22] Hence, neither conventional phonon drag or diffusion thermopower can account for the observed magnetothermopower in $NbSe_3$.

We now consider the special CDW properties of $NbSe_3$ and the associated TEP. The usual interpretation of the H = 0 TEP of $NbSe_3$ is that the lower Peierls transition at T_{c2} takes place on predominantly electron-like portions of the Fermi surface.[19] As a result, the material becomes hole-like

with decreasing T below T_{c2}, resulting in an increasingly positive TEP. From Fig. 4-5 it appears that the effect of a magnetic field is to further enhance the process of electron state destruction, resulting in a positive enhancement of the (normal carrier) TEP.

The electron-like carriers removed from the conduction band probably condense into the CDW, thereby enhancing the CDW carrier concentration and order parameter, as has been suggested by other transport studies.[4,7,8] The condensed CDW carriers carry no entropy, and hence the CDW contributes nothing to the TEP.[25] Our magnetothermopower data is thus at least qualitatively consistent with the view that transverse H fields in $NbSe_3$ essentially improve the one-dimensionality of the system, and convert normal carriers left over from the imperfectly nested Fermi surface and higher bands into condensed carriers.

A more quantitative analysis of our data is complicated by the nature of the thermoelectric effect. In a two band model, the thermopower becomes a weighted average given by[26]

$$S = \frac{\sigma_e S_e + \sigma_h S_h}{\sigma_e + \sigma_h} \qquad (4.7)$$

where $\sigma_{e(h)}$ is the electron (hole) contribution to the dc electrical conductivity, and $S_{e(h)}$ is the electron (hole) diffusion thermopower neglecting the other band in the

material. In the semiclassical model, the diffusion thermopower can be expressed in terms of the conductivity as[27]

$$S = \frac{-\pi^2}{3} \frac{k_B^2 T}{|e|} \left(\frac{\sigma'}{\sigma} \right)_{E_F} \tag{4.8}$$

where the derivative is made with respect to energy and is evaluated at the Fermi energy E_F. The dc electrical conductivity may be expressed in terms of Fermi surface parameters by[28]

$$\sigma = \frac{1}{3} e^2 \tau_F v_F^2 N(E_F) , \tag{4.9}$$

where τ_F is the relaxation time, v_F is the mean Fermi velocity averaged over the Fermi surface, and $N(E_F)$ is the density of states at the Fermi energy. In combining Eqns. 4.8 and 4.9 we see that the TEP depends on the density of states, carrier velocity and relaxation time, as well as the energy derivatives of these quantities, evaluated at E_F. Together with Eqn. 4.7, the two band TEP is a highly convoluted function of six Fermi surface parameters and their derivatives. Hence, obtaining semi-quantitative information from our TEP data necessitates some approximations.

Of specific interest is the H-dependent concentration of normal electronic states in the lower CDW state of $NbSe_3$. We may estimate this quantity by assuming that the dominant effect of H is to change σ_e; σ_h, S_h, and S_e are to first order taken as independent of H. This leads to an H-dependent (normal) electron concentration

$$\frac{n_e(H)}{n_e(0)} \approx \left(\frac{S(0) - S_e}{S(H) - S_e}\right)\left(\frac{S_h - S(H)}{S_h - S(0)}\right) . \qquad (4.10)$$

Figure 4-7 shows, as a function of temperature, $n_e(H)/n_e(0)$ as determined from Eqn. 4.10, using estimated values for S_h and S_e of 80 μV/K and -30 μV/K, respectively, and the experimentally determined values of S(H). Figure 4-7 indicates that the effect of an H field in the lower CDW state of $NbSe_3$ is to reduce the free electron carrier concentration n_e. We emphasize, however, that the results in Fig. 4-7 are only qualitatively correct owing to the limited validity of Eqn. 4.10. An obvious difficulty with the data in Fig. 4-7 is that it indicates that at H = 75 kG and below T ≈ 20 K, virtually all free electron states have been eliminated. This would appear inconsistent with the nearly linear increase in CDW carrier concentration with H up to H = 75 kG as indicated by the narrow band noise measurements presented in Fig. 4-3. This effect appears related to the saturation in the magnetothermopower at low T and large H,

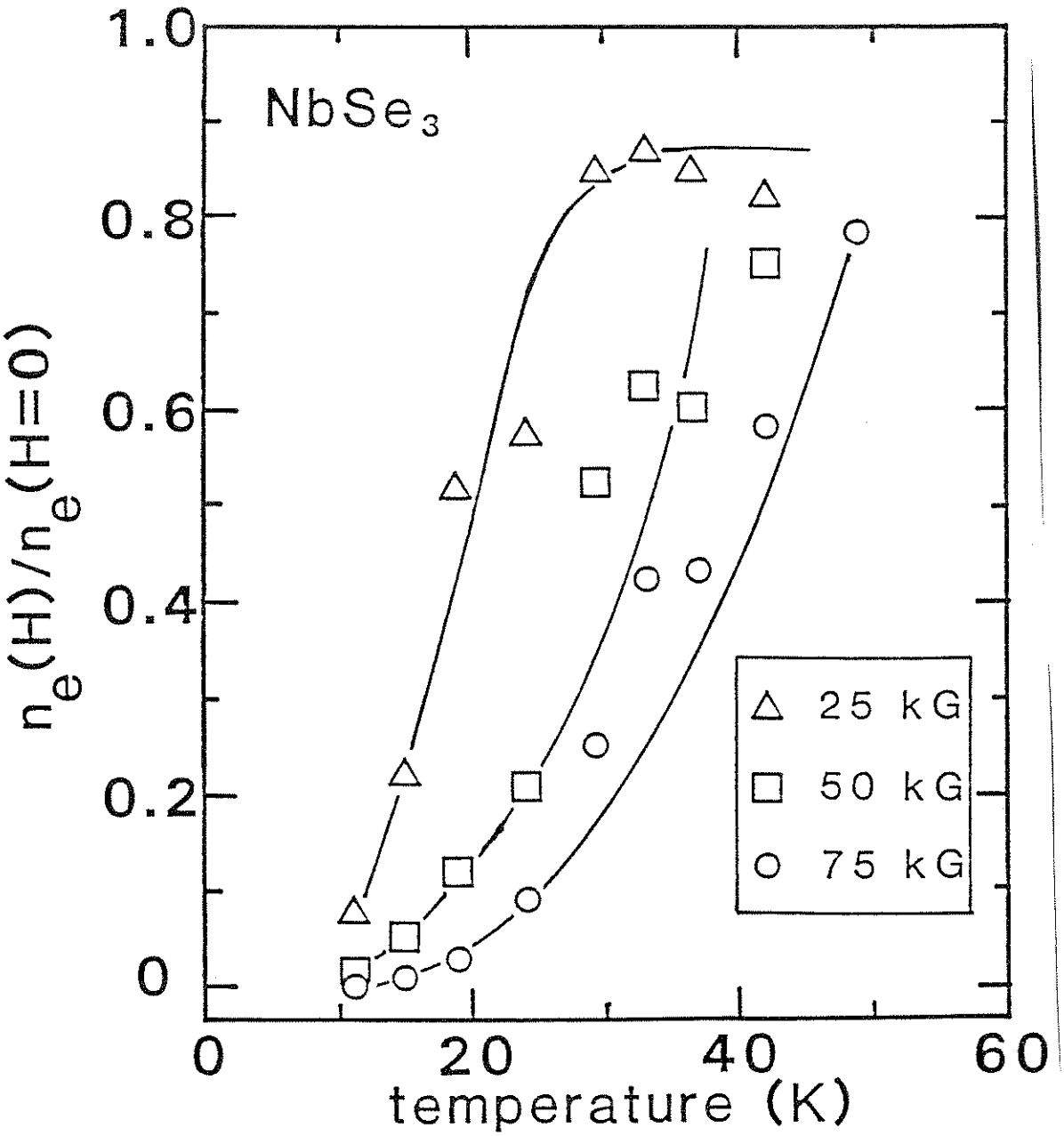

Figure 4-7 Normalized conduction electron concentration versus temperature in the lower CDW state, as determined from Eqn. 4.10. The solid lines are guides to the eye.

despite the nearly quadratic increase in magnetoresistance.

In summary, the strong H-dependence of the TEP of $NbSe_3$ in the lower CDW state is suggestive of an H-induced destruction of electron states at the Fermi level, resulting in a more hole-like and more electrically insulating state.

4.1.3 Charge density wave magnetodynamics in $NbSe_3$

The results presented in the previous two sections are consistent with a magnetic field induced one dimensionalization of the band structure in $NbSe_3$ at temperatures below T_{c2}. Those measurements were concerned only with the effects of an external magnetic field on the CDW concentration and did not determine the effects the field had on the dynamics of the sliding CDW. Research by Coleman *et al.*[4] indicate that an externally applied magnetic field reduces the electric depinning field E_T. Hence, it seems that the CDW dynamics are also strongly effected by the presence of an external magnetic field.

In this section the magnetodynamics of $NbSe_3$ are examined. In particular, we present measurements of the complex ac conductivity $\sigma(\omega)$ of $NbSe_3$ in the lower CDW state, in the frequency range 4 MHz to 1 GHz, and for applied H fields in the range 0 - 75 kG.[9] The data indicate that, in the presence of magnetic field, $\sigma(\omega)$ remains overdamped, and the conductivity lost at low frequency due to the magnetoresistance is fully recovered in the high frequency

limit. At both low and high frequencies, the dielectric response is consistent with an H-induced conversion of normal to CDW carriers. The characteristic ac "crossover frequency" ω_{co} increases with increasing H, whereas the dc threshold field E_T decreases with increasing H; this suggests a possible breakdown in the conventional impurity pinning mechanism which dictates the dc and ac responses.

These experiments were performed on single crystals of $NbSe_3$ grown by conventional vapor-transport methods, with typical minimum threshold fields E_T = 30 mV/cm at 48 K. The crystals were mounted in a 2-probe configuration with silver paint contacts, and formed the termination of a micro-coaxial cable. $\sigma(\omega)$ was measured parallel to the chain (b) axis, and H was applied perpendicular to b. Both the real and imaginary parts of $\sigma(\omega)$, $Re\sigma(\omega)$ and $Im\sigma(\omega)$, were determined by a computer-controlled network analyzer (HP 87454A), using an ac sinusoidal excitation amplitude more than two orders of magnitude smaller than E_T. Our experimental set-up allowed simultaneous measurement of the electric field dependent dc conductivity $\sigma_{dc}(E)$, and observation of the narrow band noise spectrum for $E > E_T$.

Figure 4-8 shows $\sigma(\omega)$ for $NbSe_3$ at 25 K, both with and without an applied H-field. From the general behavior of $\sigma(\omega)$, it is apparent that the CDW continues to behave overdamped in the presence of H. Important features of the data are found at the frequency extremes. In the low

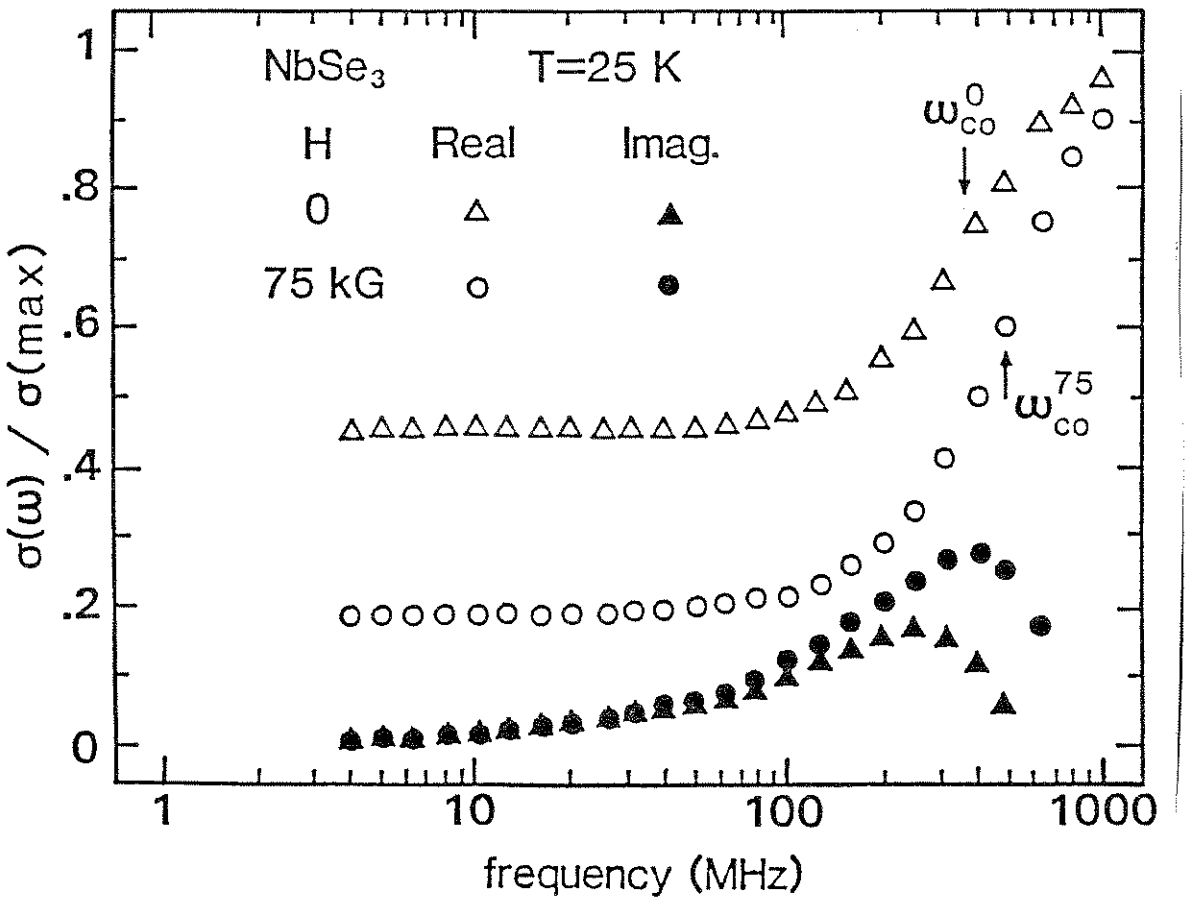

Figure 4-8 Complex ac conductivity of $NbSe_3$ with and without a 75 kG H-field. The crossover frequencies are indicated by vertical arrows.

frequency limit there is a large H-induced reduction in Reσ, consistent with the sample's ohmic dc magnetoresistance. In the high frequency limit, Reσ becomes H-independent, and both Re$\sigma(\omega, H = 0)$ and Re$\sigma(\omega, H = 75$ kG) appear to approach the same saturation value [strictly speaking, the ac conductivity does not saturate at high frequencies (1-10 GHz), but instead reaches a broad maximum corresponding to $\sigma_{dc}(E \rightarrow \infty)$. At still higher frequencies (30-100 GHz), inertial effects lead to a decrease in Re$\sigma(\omega)$ with increasing ω].[29] Simultaneous (pulsed) measurements of $\sigma_{dc}(E)$ confirmed that this saturation value corresponds to $\sigma_{dc}(E \rightarrow \infty)$, independent of H. The crossover frequency, ω_{co}, may be defined as that frequency for which Re $\sigma(\omega)$ has attained one-half its maximum value. ω_{co} is identified for the two data sets in Fig. 4-8. At 25 K, $\omega_{co}(H = 0)/2\pi = 350$ MHz, while $\omega_{co}(H = 75$ kG$)/2\pi =$ 480 MHz, an increase over the H = 0 value of approximately 37%. Fig. 4-8 shows that Im$\sigma(\omega)$ is also affected by the application of a magnetic field. At low frequencies no H-induced change was detected (within our experimental resolution of Im$\sigma(\omega)/\omega = \pm$ 1pF) in Imσ, while at high frequencies Im$\sigma(\omega, H = 75$ kG) clearly exceeds Im$\sigma(\omega, H = 0)$. At $\omega/2\pi = 300$ MHz, for example, application of the H = 75 kG field increases Imσ by a factor of 1.7. In addition, the peak in Imσ, which corresponds roughly to the crossover frequency in Reσ, increases with increasing H.

Experimental data, such as that presented in Fig. 4-8,

were obtained for the same $NbSe_3$ crystal at other temperatures in the lower CDW state. The same basic features described above were observed. Fig. 4-9 shows the characteristic crossover frequency extracted from such data, as a function of temperature. It is apparent that ω_{co}(H = 75 kG) always exceeds ω_{co}(H = 0), with the relative increase becoming larger at lower temperature where the ohmic magnetoresistance increases. Just below the transition temperature T_p = 59 K, no appreciable difference was found in ω_{co} for H = 0 and H = 75 kG.

The main features of our experimental results appear consistent with an H-field induced conversion of normal to CDW carriers. At low frequencies, only the normal carriers contribute to Reσ, and, as observed in Fig. 4-8, Reσ is significantly reduced by application of H. At high frequencies, Reσ has significant contributions from both CDW and normal carriers. Previous microwave and radio frequency studies[16,30] have shown that in $NbSe_3$ the high frequency conductivity attains a saturation maximum which corresponds to the (normal) conductivity expected in the absence of CDW formation. This indicates that, with H = 0, the CDW carriers have the same high frequency ac response as do the normal carriers, and the high frequency conductivity thus depends only on the total carrier concentration $n = n_n + n_c$, with n_n the normal carrier concentration and n_c the CDW carrier concentration. In Fig. 4-8, the high frequency conductivity

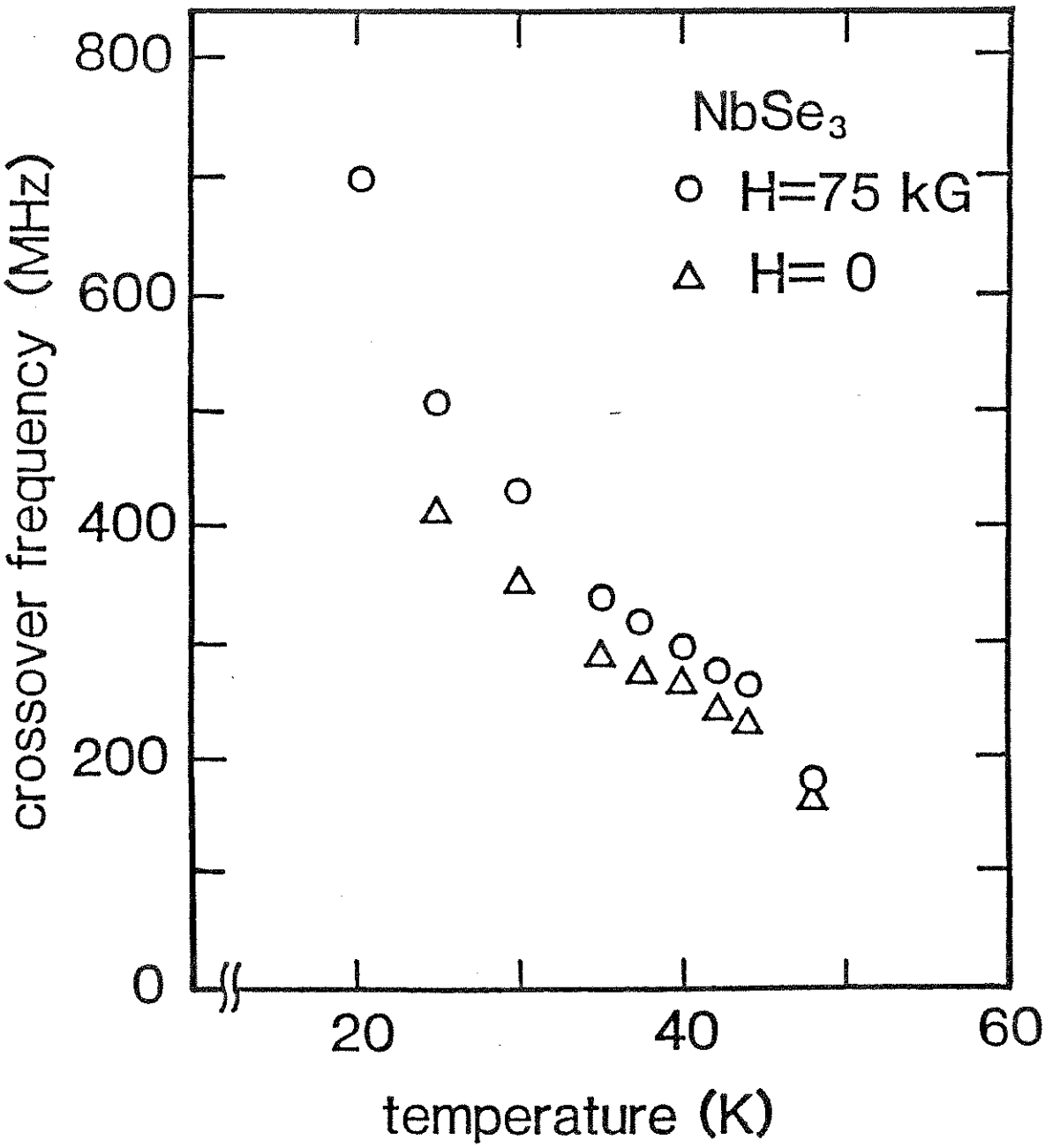

Figure 4-9 Crossover frequency ω_{co} versus temperature in the lower CDW state of $NbSe_3$. At fixed temperature, an H-field increases ω_{co}.

$Re\sigma(\omega)$ is again observed to be equal to that expected in the absence of CDW formation [determined equivalently by extrapolating the ohmic temperature dependent resistance from high temperature to low, or by direct measurement of the dc conductivity $\sigma_{dc}(E \rightarrow \infty)$], indicating a conserved total carrier concentration in the presence of H, and an insensitivity to H of the high frequency behavior of normal and CDW conduction states. For example, if the ohmic dc magnetoresistance were strictly due to a normal carrier mobility effect (assumed frequency independent), then $Re\sigma(\omega,H = 0)$ and $Re\sigma(\omega,H = 75$ kG) in Fig. 4-8 would differ only by a frequency independent constant, in sharp contrast to the experimentally observed convergence in the data at high frequencies.

A shift in carriers between normal and CDW states can also be inferred from $Im\sigma(\omega)$ in Fig. 4-8. Normal electrons do not contribute to $Im\sigma$ in the frequency range being considered here (well below the metallic plasma frequency), and hence $Im\sigma$ is dominated by the contribution from CDW carriers. As seen in Fig. 4-8, $Im\sigma$ increases with increasing H, in particular near the ac crossover frequency. As discussed below, the low frequency behavior of $Im\sigma$ is also consistent with CDW carrier enhancement.

The increase in ω_{co} with increasing H, as shown in Fig. 4-9, is in striking contrast to the observed decrease in E_T. We have carefully measured $E_T(H)$, for the same $NbSe_3$ crystal

as was used for the data of Figs. 4-8 and 4-9, by applying a pulsed dc conductivity technique, and by observation of the onset of narrow band noise for applied steady state dc fields. For any given H-field, the two methods yielded identical values of E_T. The open circles in Fig. 4-10 show the ratio $E_T(H)/E_T(H = 0)$ for $NbSe_3$ at selected H-field values and temperatures. For a given field H, the relative reduction in E_T becomes greater at lower temperatures, consistent with previous studies.[4] Figure 4-10 also contrasts the $E_T(H)$ behavior to that of $\omega_{CO}(H)$; the two parameters have dramatically opposite H-field dependences.

A number of models of CDW transport have been advanced, including rigid particle classical motion,[10] quantum tunneling,[31] and deformable medium theories based on the Fukuyama-Lee-Rice Hamiltonian.[32] In a very simple classical description set forth by Grüner, Zawadowski, and Chaikin,[10] the CDW is treated as a charged rigid object in a periodic pinning potential. Although this model has some severe deficiencies, it allows us to readily identify important H-dependent CDW parameters. In the model, the limiting dc conductivity of the CDW condensate is given by $\sigma_{dc,CDW}(E \rightarrow \infty) = n_c e^2 \tau_c / m^*$, while the ac conductivity is

$$\mathrm{Re}\,\sigma_{CDW}(\omega) = \frac{n_c e^2 \tau_c}{m^*} \frac{1}{1 + (\omega_o^2 \tau_c / \omega)^2}, \qquad (4.12)$$

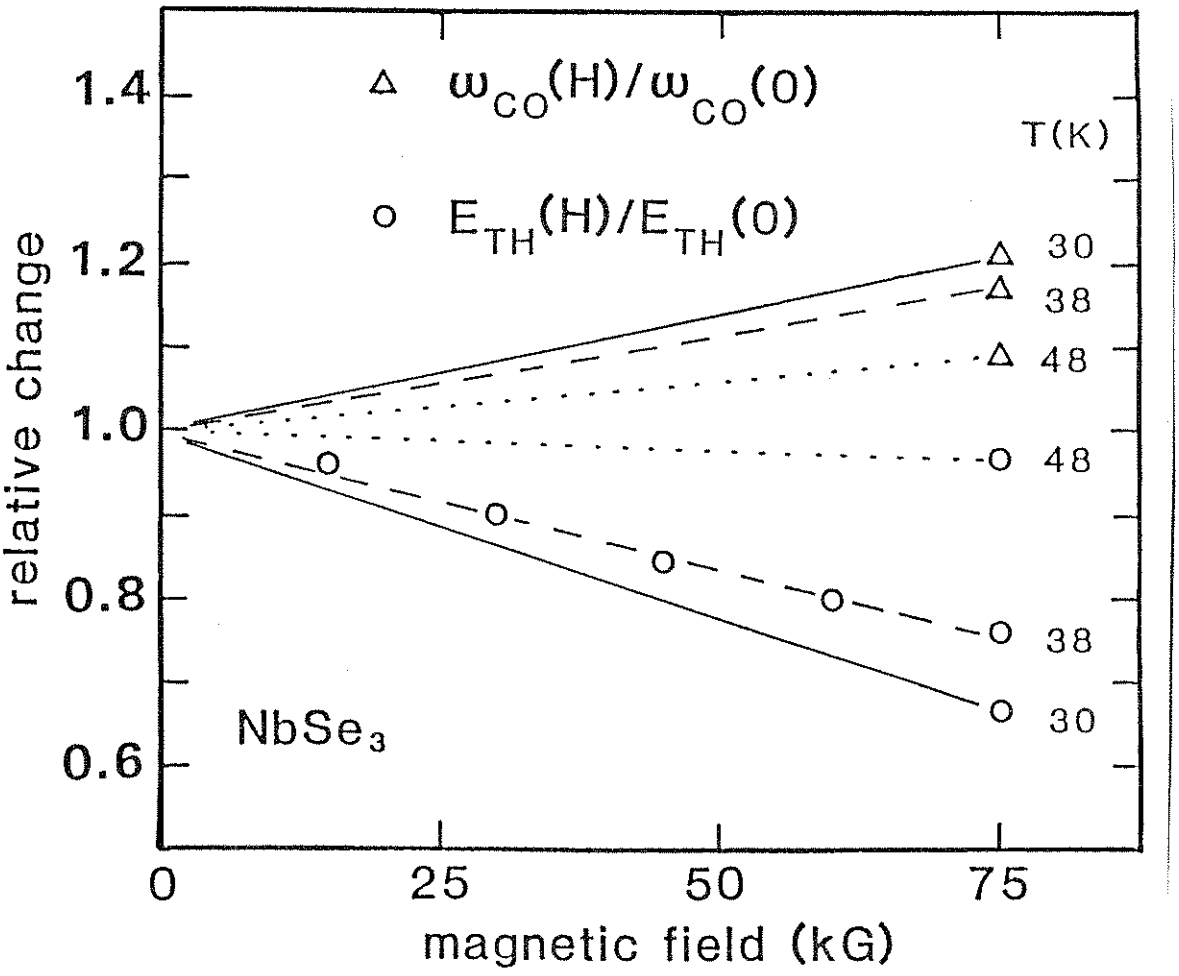

Figure 4-10 Normalized crossover frequency and threshold electric field versus H in $NbSe_3$.

$$\mathrm{Im}\,\sigma_{CDW}(\omega) = \frac{n_c e^2 \tau_c}{m^*} \frac{(\omega_o^2 \tau_c/\omega)}{1 + (\omega_o^2 \tau_c/\omega)^2}, \qquad (4.13)$$

where τ_c is the CDW characteristic scattering time, m^* is the effective mass of electrons condensed in the CDW state, and ω_o is the CDW pinning frequency. $\omega_o^2\tau_c$ is identified with the ac crossover frequency. We assume the total sample conductivity to be given by $\sigma_{tot} = \sigma_{CDW} + \sigma_{normal}$, where σ_{normal} represents the contribution of the normal carriers. Allowing for normal to condensed carrier conversion, the independence of σ_{tot} on H in the high frequency or high electric field limit implies

$$\frac{n_c e^2 \tau_c}{m^*} + \frac{n_n e^2 \tau_n}{m} = \frac{ne^2\tau}{m} = \text{constant}, \qquad (4.14)$$

where constant here means an H-independent quantity. With τ_n, n, and m independent of H, we find τ_c/m^* = constant, independent of H.

In the low frequency limit, Eqn. 4.13 yields a dielectric constant

$$\varepsilon = \frac{4\pi \mathrm{Im}\,\sigma(\omega)}{\omega} = \frac{4\pi n_c e^2}{m^* \omega_o^2} \quad . \tag{4.15}$$

Experimentally, we find no H-field effect on the very low frequency dielectric constant, hence $\omega_o^2 m^* \propto n_c$, or, equivalently, $m^*/\tau_c \propto n_c/\omega_o^2\tau_c$. With constant m^*/τ_c, and the experimentally determined ratio $\omega_o^2\tau_c(H = 75\ kG)/\omega_o^2\tau_c(H = 0) = 1.2$ (measured at T = 30 K), we find $n_c(H = 75\ kG)/n_c(H = 0) = 1.2$ at T = 30 K. This H-induced increase in CDW carrier concentration is in good agreement with that determined from the narrow-band noise studies presented in Sec. 4.1.1, where $n_c(H = 75\ kG)/n_c(H = 0) \approx 1.3$ at T = 37.4 K.

Unfortunately, the above analysis does not allow for independent determination of $m^*(H)$, $\tau_c(H)$, and $\omega_o(H)$. In Bardeen's tunneling theory,[31] the dc and ac conductivities scale over a wide range of electric field and frequency, such that $\omega = 2\pi e^* LE/h$, with $e^*/e \approx m/m^*$ and L a CDW correlation length. Although the ac and dc conductivities for the $NbSe_3$ sample used for Fig. 4-8 did not show excellent scaling between $\sigma_{dc}(E)$ and $\mathrm{Re}\sigma(\omega)$ at all temperatures investigated in the lower CDW state (although proper scaling was observed at selected temperatures), a rough correspondence between E and ω could always be established by matching $\mathrm{Re}\sigma(\omega)$ at the crossover frequency to $\sigma_{dc}(E \rightarrow \infty)/2$, both with and without

applied magnetic field. At T = 30 K, ω/E was found to correspond to 3 MHz/mV (H = 0), and ω/E = 3.1 MHz/mV (H = 75kG). Assuming L to be H-independent, this leads to m^*(H = 75 kG)/m^*(H = 0) = 0.97. This implies that H does not appreciably change m^* (or τ_c), and hence the H-induced increase in $\omega_{co} = \omega_o^2\tau_c$ is primarily due to an effective increase in ω_o, the CDW pinning frequency.

The increase in ω_o with increasing H is in sharp contrast to the observed decrease in E_T with increasing H. Rigid particle, tunneling, and elastic medium models based on impurity pinning all predict that the ac and dc behaviors go hand in hand. In the rigid particle model, for example, the threshold field E_T and the characteristic CDW pinning frequency ω_o are related by

$$E_T = \frac{m^*}{Qe}\omega_o^2 \quad , \tag{4.16}$$

where $Q = 2\pi/\lambda_{pin}$ is the wave vector corresponding to the periodicity of the CDW pinning potential. Eqn. 4.16 would predict that increases in impurity concentration generated by chemical doping or sample irradiation should increase both ω_o and E_T, and indeed this is observed experimentally in $NbSe_3$ and TaS_3.[33,34] In the context of impurity pinning (which clearly dominates at H = 0), our results would suggest that application of H effectively reduces "dc impurity pinning" but enhances "ac impurity pinning". The analysis presented

in this section indicates that within the confines of simple impurity pinning models, the *increase* in ω_{co} follows directly from the magnetic field induced *increase* in n_c, while the *decrease* in E_T cannot be accounted for by any of the models which describe CDW dynamics; in fact, these models would predict that E_T should increase when n_c increases. We therefore conclude that important H-sensitive interactions, previously ignored by CDW theories, come into play when an H-field is present in $NbSe_3$. Such an effect could have its origin in interactions between CDW carriers and normal electrons, or unusual CDW-phonon scattering at intermediate frequencies. Indeed, recent work on $NbSe_3$, TaS_3, and $K_{0.3}MoO_3$ have shown important couplings between the limiting CDW and normal carrier conductivities.[35] Whether these effects are related to the H-field phenomena reported here remains to be seen.

Finally, we remark that the only theory which discusses the anomalous magnetoresistance effects in $NbSe_3$, that of Balsiero and Falicov,[6] does not address the dynamics of the CDW condensate. An extension of this theory, which incorporates condensate magnetodynamics, may help clarify the role of impurity pinning in the presence of applied magnetic fields.

4.1.4 Conclusions

The three sets of measurements presented in this

section clearly indicate that normal-to-CDW carrier conversion occurs when $NbSe_3$ crystals are subjected to an external magnetic field applied perpendicularly to the CDW chain axis. This static effect can be qualitatively accounted for by the theory of magnetic field enhanced one-dimensionalization as first proposed by Balseiro and Falicov.[6]

The data presented in Sec. 4.1.3 concerning CDW dynamics indicate that an external magnetic field affects the sliding CDW in ways which cannot be accounted for by assuming only that n_c is an increasing function of H. Hence, it appears that the conventional impurity pinning mechanisms responsible for CDW dynamics are also altered by an externally applied magnetic field.

4.2 Temperature gradient effects in $NbSe_3$

In this section we explore the temperature gradient effects on narrow band noise and related phenomena in $NbSe_3$. The so-called narrow band noise (NBN) exhibited by CDW materials is a periodic voltage oscillation which accompanies the dc motion of a sliding CDW. A large amount of research performed on many different CDW materials indicates that the fundamental NBN frequency f_{NBN} is directly related to the CDW drift velocity v_c and the current density J_{CDW} by[11-13,36-38]

$$J_{CDW} = n_c e v_c = n_c e \lambda_{pin} f_{NBN} , \qquad (4.17)$$

where n_c is the CDW carrier concentration, and λ_{pin} is the characteristic length of the CDW pinning potential. In the past, considerable controversy has existed as to whether this NBN is a bulk[39-41] or a contact[42,43] effect. Recent experiments, though, have definitively demonstrated that the narrow band noise is generated in the bulk.[44,45] It is now believed that these periodic noise oscillations stem from the interactions between a phase velocity coherent CDW domain, moving at a dc velocity v_c, and randomly distributed impurity pinning centers.[39-41] A quantum scattering theory which considers this interaction suggests that the resulting pinning potential is roughly approximated by a sinusoid with a wavelength $\lambda_{pin} = \lambda_{CDW}$.[46] Although early NBN studies suggested that $\lambda_{pin} = \lambda_{CDW}/2$,[47] re-analysis[48] and experiments

on more highly coherent samples[37,38,49] indicate that $\lambda_{pin} = \lambda_{CDW}$, in good agreement with Tütto and Zawadowski's impurity interaction theory.[46] Because the NBN is produced via a bulk process, the NBN spectrum produced by a crystal directly reflects the relative phase velocity coherence of the sliding CDW within the material.

An interesting experimental technique for the study of noise phenomena in $NbSe_3$ has been the external application of temperature gradients. This technique exploits the temperature dependences of the local parameters -- the CDW energy gap Δ, the CDW depinning field E_T, and the low-field resistivity -- which characterize the CDW phase velocity and hence the NBN frequency. Original studies of the NBN spectrum in relatively short $NbSe_3$ samples in a temperature gradient demonstrated that the quality and amplitude of the noise are not degraded by the gradient, but rather reflect the average temperature of the specimen.[53] Subsequent experiments on longer samples indicate that the application of a temperature gradient can result in single[42,51] or multiple splittings[52,53] of the NBN fundamental. Although at first the single-splitting results were thought to be evidence for contact-induced NBN production,[42,51] the observation of multipally-split NBN spectra clearly rule this out, and suggest that the NBN is instead a bulk phenomenon.[52,53]

In the two subsections to follow we further examine

both experimental and theoretical aspects of the temperature gradient effects on the NBN produced by $NbSe_3$ crystals. In Sec. 4.2.1 we examine the temperature gradient effects on mode locking in this material,[54] while in Sec. 4.2.2 a simple phase slip model of temperature gradient NBN effects in CDW conductors is presented.[55]

4.2.1 Shapiro step spectrum and phase-velocity coherence in $NbSe_3$ in a uniform temperature gradient

When a CDW crystal in placed in the presence of combined dc and ac electric driving fields (or currents), interference occurs between intrinsic oscillations of the crystal and the applied ac field,[11] leading to "Shapiro" steps in the dc current voltage (I-V) characteristics of the specimen.[56] The Shapiro step phenomenon in $NbSe_3$ has both a rich harmonic[56] and subharmonic[57,58] structure, and both incomplete and complete mode-locking have been observed[59].

In this section the effects of an applied temperature gradient upon mode locking in $NbSe_3$ crystals is examined.[54] We find that under uniform temperature gradient conditions, sharp Shapiro step interference still occurs, although there results a well-defined break-up of the isothermal Shapiro step spectrum. Analysis of the Shapiro step structure allows us to identify, for a given set of electric field and temperature gradient parameters, the volume fraction of the sample synchronized to, and hence oscillating at, the

frequency of the applied ac field. We also find that, while an increasing temperature gradient tends to split a sample into separate domains, an increasing rf signal tends to bring together domains which were initially split by a gradient. By varying the rf signal amplitude and temperature gradient strengths, we determine critical values for the temperature gradient and ac amplitude at which the sample breaks from a single, macroscopically phase coherent domain, to two distinct domains, each comprising approximately one-half the sample volume.

Our experimental set-up employed single crystals of $NbSe_3$ suspended (in vacuum) between two large copper mounting posts anchored to peltier heater chips. Electrical contact to the sample was made by conductive silver paint. Our two-probe mounting configuration allowed the temperature of the sample ends to be independently varied, and thermometry was accomplished through a diode sensor and several miniature differential thermocouples. Shapiro steps were induced by driving the sample with a dc current and a superimposed radio frequency (rf) current. An additional low-frequency (280 Hz) low-amplitude current modulation provided a suitable signal for lock-in detection of the (dc) differential resistance dV/dI.

Figure 4-11 shows a series of dV/dI traces for a $NbSe_3$ sample of length l = 0.5 mm, with successively increasing temperature gradients. Here the temperature of the cold end

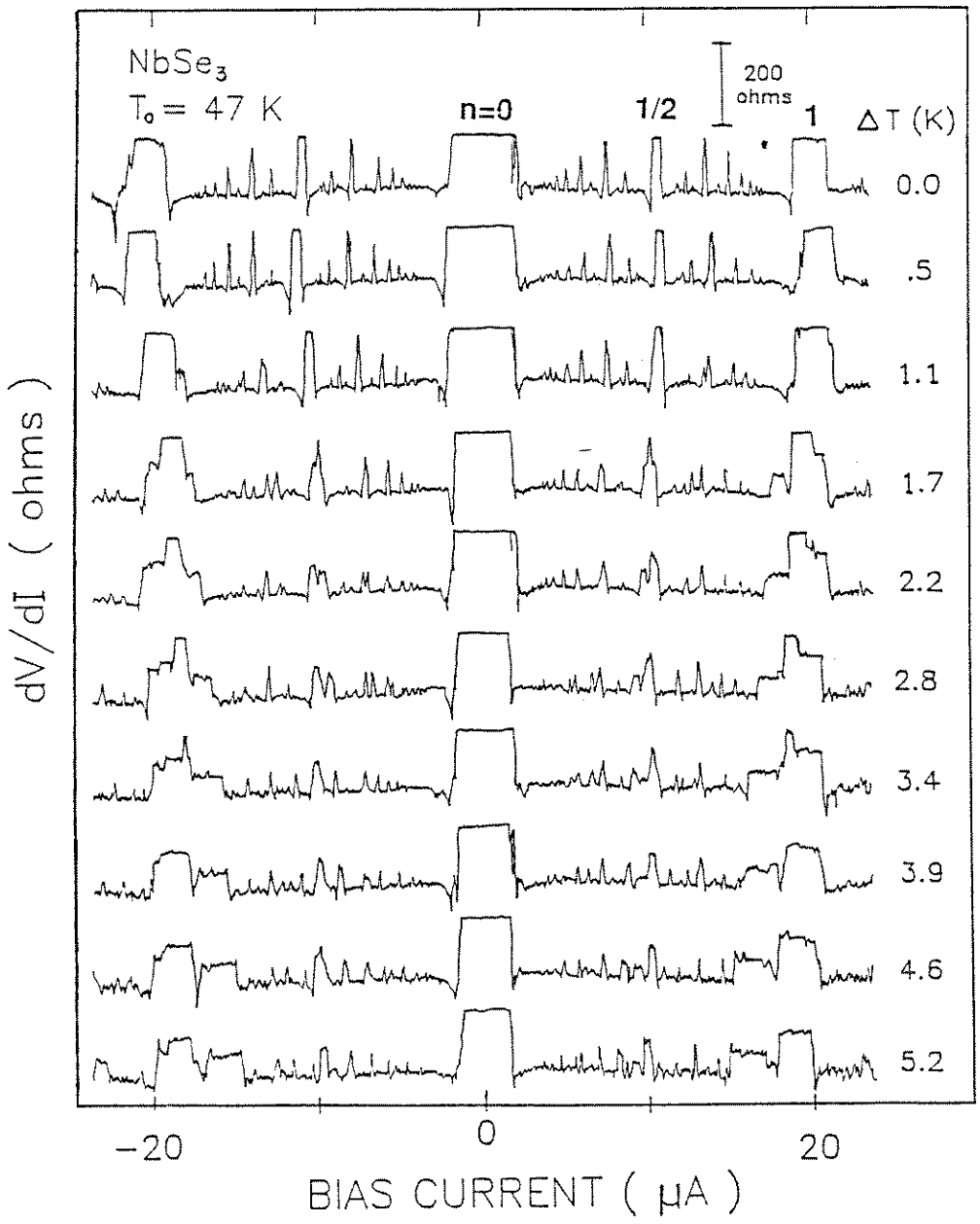

Figure 4-11 Shapiro step spectrum of $NbSe_3$ for various values of an applied uniform temperature gradient. ΔT is the total temperature difference across the sample, while T_o is the (fixed) temperature of the cold end of the sample. $\omega/2\pi$ = 10 MHz, V_{rf} = 111 mV.

of the sample, T_o, was fixed at 47 K, while the temperature of the "hot" end, T_1, was varied between 47 K and 52.2 K. We define $\Delta T = T_1 - T_o$. The top trace in Fig. 4-11 corresponds to isothermal conditions, and a rich Shapiro step spectrum, consistent with previous studies,[57,58] is observed. We note that in this high-quality sample the fundamental (n = 1) interference peak (at 20 μA bias) displays complete mode locking, as do several subharmonic interference peaks (n is the step index, to be discussed below). With increasing ΔT, the Shapiro step spectrum is observed to remain well-defined (i.e. no smearing), but a general break-up or splitting of both harmonic and subharmonic interference peaks occurs. The bottom trace of Fig. 4-11, for example, is best described as a superposition of two distinct Shapiro step spectra, although neither of the two "subspectra" displays complete mode locking (see below). By direct spectrum analyzer detection of the narrow-band noise spectrum (no rf current), it was confirmed that the break-up of the Shapiro step spectrum is associated with a corresponding splitting of the narrow-band noise spectrum. No minimum ΔT was observed for the onset of splitting of the noise spectrum.

In the presence of a temperature gradient, the break-up of the Shapiro step spectrum can be reversed by increasing substantially the rf current amplitude. This is shown in Fig. 4-12, which displays several dV/dI traces for the same $NbSe_3$ crystal with a constant $\Delta T = 1$ K. V_{rf} is the rf

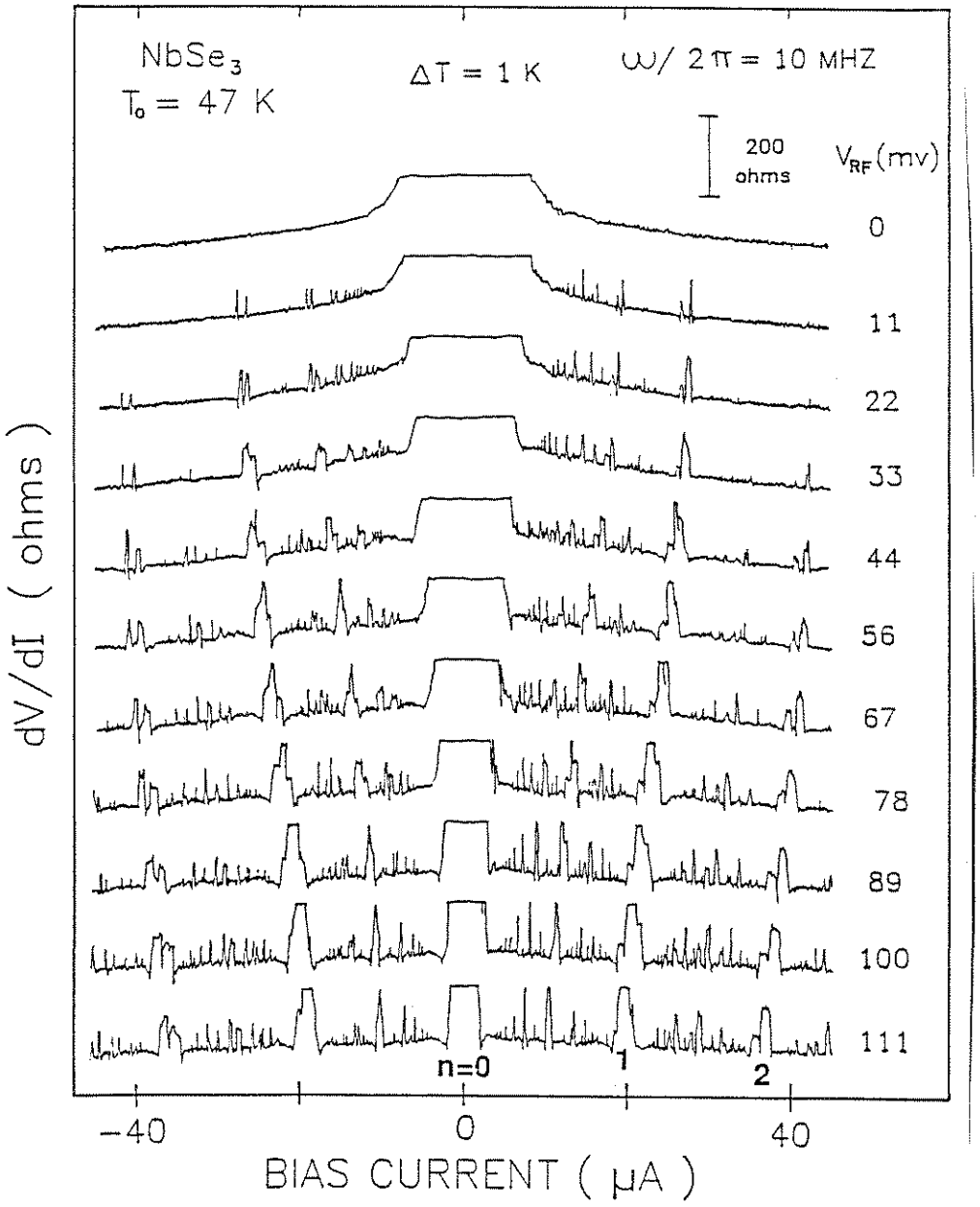

Figure 4-12 Shapiro step spectrum of $NbSe_3$ for various values of the rf electric field drive. The temperature gradient is fixed at 20 K/cm.

voltage amplitude across the sample measured at zero dc bias. At low rf amplitude, a dual or split Shapiro step spectrum is observed. With increasing rf field amplitude the Shapiro step magnitude increases (see Ref. 56), and a smooth merging of the main interference peaks occurs. The merging is, however, a sensitive function of the order of the harmonic or subharmonic interference peak. For example, in the bottom trace of Fig. 4-12, the n = 1 interference peaks (at 20 μA bias) have almost fully coalesced, as have the n = 1/2 (at 10 μA bias) subharmonic peaks, whereas higher order subharmonic and harmonic peaks (e.g. n = 3/2 at 25 μA bias; n = 2 at 35 μA bias) remain distinct. These higher order peaks can, however, be forced to merge by further increasing the rf drive amplitude.

We now analyze these results. In Shapiro step experiments, interference occurs whenever $\omega_j = n\ \omega_{ex}$, where the step index n = p/q with p and q integers.[56-58] Two parameters are of particular importance in the discussion of Shapiro step interference. The first is the actual height h of the interference peak recorded on a dV/dI plot, measured from the effective baseline, or saturated dV/dI value. h determines what portion (volume fraction) of the CDW is locked to the external rf drive. If dV/dI on the interference steps attains the ohmic differential resistance value R_o, then $h = h_{max}$ and locking is complete; the entire CDW condensate assumes a unique and fixed phase velocity, and

only normal (uncondensed) electrons contribute to the differential resistance. It has been demonstrated that in the complete mode-locked state, all internal phase velocity fluctuations (sources of broad-band noise) are absent.[59] In incomplete locking, $h < h_{max}$, and only a portion of the CDW condensate is synchronized or mode locked to the external rf drive. The relative Shapiro step height is an indirect measure of the CDW volume locked to the external rf signal. To see that this is the case, consider a simple one-dimensional CDW crystal composed of N independent serially arranged domains; each domain consists of a normal resistance R_n, reflecting the normal electrons in the domain, in parallel with a CDW differential resistance R_{CDW}. When a domain is locked to an external rf signal, $R_{CDW} = \infty$, while $R_{CDW} = R_c$ for a conduction saturated domain when it is not locked to that signal. If j of the N domains are locked,

$$h = \frac{j R_n^2}{R_c + R_n} . \qquad (4.18)$$

Hence, $h/h_{max} = j/N$, and the relative Shapiro step height indirectly measures the volume fraction of CDW locked to the rf signal. In the data presented in Figs. 4-11 and 4-12, slight increases in the dc bias field result in an increase in I_{CDW} due to these unlocked regions.

The second parameter of interest is the actual Shapiro step magnitude δV, which would be directly observed on a dc I-V plot as the increase in the sample voltage due to a Shapiro step. In a current driven differential resistance experiment, δV is given by the integrated area of the interference peak, $\delta V = h\Delta I$, where ΔI is the current bias range over which locking persists.

We interpret the breakup of the Shapiro step spectrum in Fig. 4-11 as reflecting a breakup of the sample into macroscopic domains, each with a different intrinsic frequency for a particular value of dc bias current. The difference in intrinsic frequency arises mainly from the strong temperature dependence of the ratio I_{CDW}/ω_i, which decreases sharply with increasing temperature above 45 K.[13,50] As we discuss below, the temperature gradient appears to break the sample into two distinct macroscopic domains, which we identify as the "hot" and "cold" domains. As dc bias current is swept through the sample with an applied temperature gradient, one expects first locking with the hot domain (with a higher intrinsic frequency for a given I_{CDW}), and then locking with the cold domain. This effect is clearly demonstrated in Fig. 4-11, where the gradient induces new interference structure at lower bias currents. The interference peaks identified with the cold domain also shift to slightly lower bias currents with increasing temperature gradient, due to an increase in the average temperature of

the cold domain. We focus for the moment on the detailed structure of the dominant (n = 1) interference peak associated with the ΔT = 2.8 K trace of Fig. 4-11. The external rf frequency is fixed at $\omega_{ex}/2\pi$ = 10 MHz. As the bias current approaches 16.9 μA, the intrinsic oscillation frequency of the hot domain, ω_{ih}, becomes sufficiently close to ω_{ex} such that mode locking takes place between this domain and the external rf drive. From h/h_{max} = 0.33 in this mode-locked region, we find that the hot domain comprises 33% of the sample volume. As the dc bias current I is increased to 18.4 μA, ω_{ih} remains locked to ω_{ex}. At this current bias, the intrinsic frequency of the cold domain, ω_{ic}, is sufficiently close to ω_{ex} that the cold domain also becomes locked to ω_{ex}. With both the hot and cold domains mode-locked to ω_{ex}, h = h_{max} and complete mode locking results. At a bias current I = 19.4 μA, the hot domain becomes unlocked from ω_{ex}(it apparently no longer remains energetically favorable for ω_{ex} to "pull" ω_{ih} so far from its unperturbed value), and between 19.4 μA and 20.6 μA, only the cold domain remains locked. In the later mode-locked region, h/h_{max} determines the volume of the cold domain: 67% of the sample volume. As an independent check, we note that the volumes of the hot and cold domains sum to 100% of the total sample volume.

The mode-locking process described above for ΔT = 2.8 K is essentially unaltered for different values of the

temperature gradient, except that the locking range of the hot domain moves successively to lower (higher) bias currents with increasing (decreasing) ΔT, and the locking ranges of the hot and cold domains no longer overlap if ΔT exceeds 3.9K. However, the respective volumes of the hot and cold domains remain at 33% and 67% of the sample volume, independent of the magnitude of the temperature gradient (up to dT/dL = 10.4 K/cm). While this slight asymmetry may be simply due to enhanced domain boundary formation at a grain boundary or other relatively weak defect within the crystal structure, it may instead stem from the fundamental nature of the temperature gradient domain splitting process.[55] This process favors having the boundary between the domains exist closer to the hot end of the sample rather than equi-distant between the two ends (see Sec. 4.2.2).

The Shapiro step magnitude associated with oscillations in different domains is given from classical mixing theory as[13]

$$\delta V = 2\alpha V_T(\omega = 0) \left| J_n\left(\frac{\Omega V_{rf}}{\omega_{ex} V_T(\omega = 0)}\right)\right| , \qquad (4.19)$$

where J_n is the Bessel function of order n, $V_T(\omega = 0)$ is the threshold voltage for the onset of CDW conduction with no rf, Ω is a scaling parameter, and α describes both the completeness and range of mode lock of the interference

phenomenon. Fig. 4-13a shows δV associated with the n = 1 interference peaks of Fig. 4-11, as a function of ΔT. The step magnitudes have been decomposed into contributions from the cold domain, hot domain, and mixed domain (appropriate when the two domains are locked together). The break-up of the sample into two distinct domains is demonstrated clearly in Fig. 4-13a. Also shown in this figure is the sum δV_{tot} of all three contributions to δV. In the temperature range of interest, the parameters V_T and Ω are only weakly temperature dependent, and hence δV_{tot} reflects directly the parameter α. δV_{tot} is seen to remain approximately constant as ΔT is increased from zero to 5.2 K, and hence the data of Fig. 4-13a consistently accounts for the entire CDW condensate volume throughout the range of applied temperature gradient.

The "merging" effect shown in Fig. 4-12 appears to be a manifestation of rf-induced phase homogenization[58,59] within the sample volume. Increasing the rf amplitude greatly increases the coupling between domains, making a temperature gradient less effective in separating hot and cold domains in the Shapiro step spectrum. The sensitivity of the Shapiro step splitting on the harmonic (or subharmonic) order n reflects the relatively weak coupling of the external rf to the CDW condensate at high p and q values, consistent with the limited range of mode lock (under isothermal conditions) for the higher order interference.[57,58]

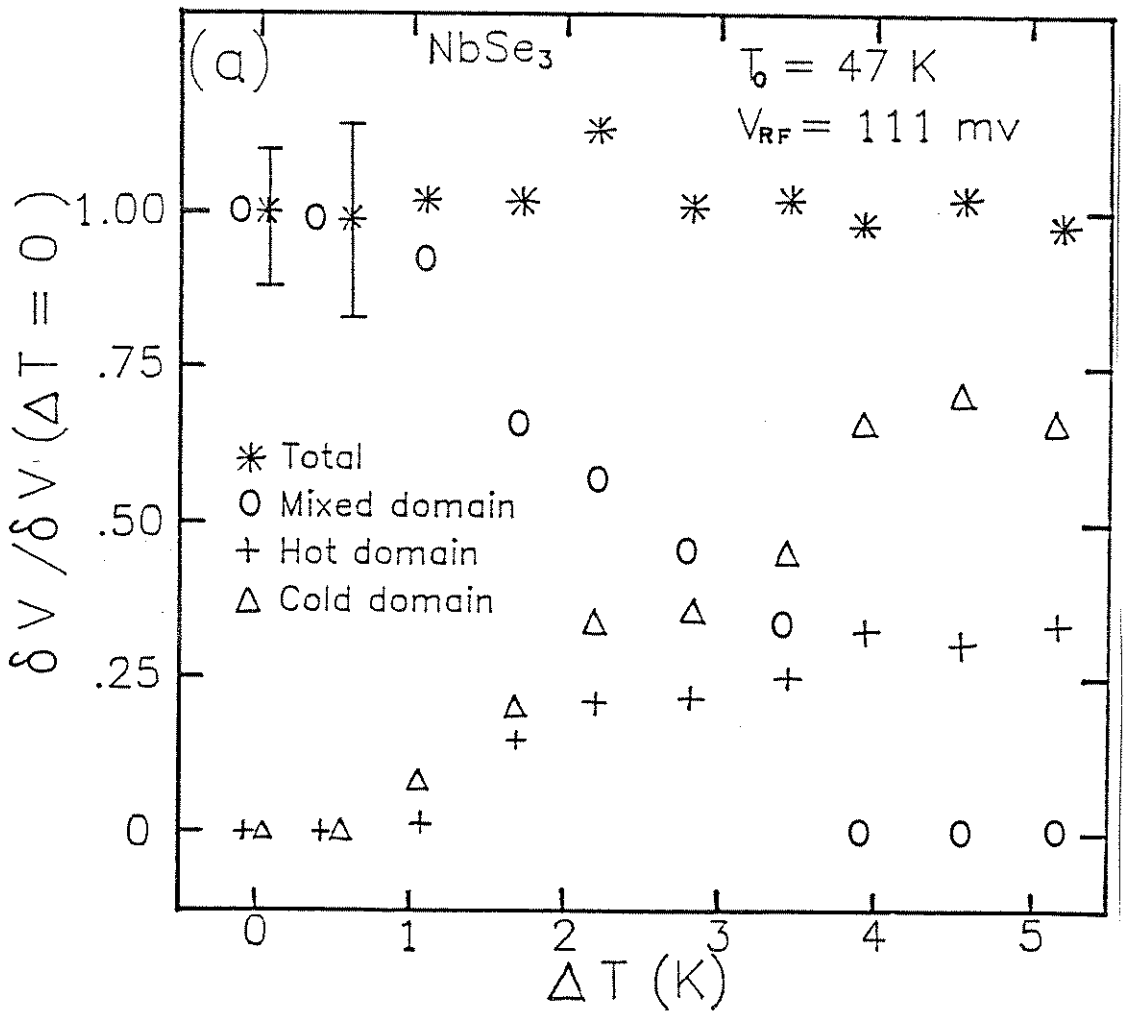

Figure 4-13a Shapiro step magnitude δV associated with different macroscopic domains in the CDW crystal.

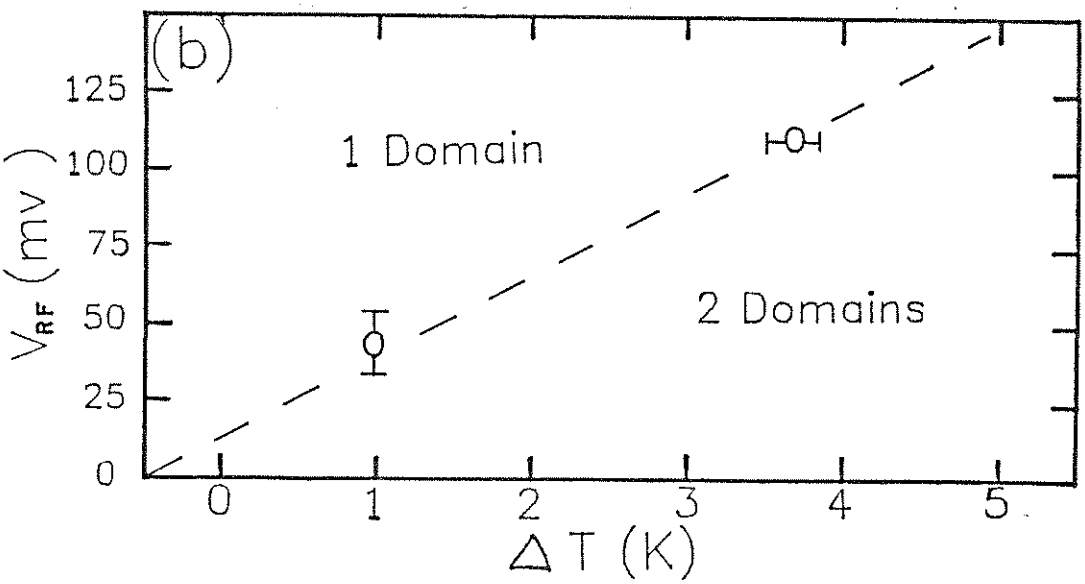

Figure 4-13b Phase portrait of critical temperature gradient and rf field amplitude which divide the sample between consisting of a single macroscopic domain and two independently coherent domains.

From Figs. 4-12 and 4-13a we may extract critical values of ΔT and rf amplitude V_{rf} at which the sample breaks up from one coherent domain to two independently coherent domains. For fixed V_{rf}, we define ΔT_{crit} as the temperature difference above which no common locking (complete mode lock) can be achieved, while for fixed ΔT, $V_{rf\ crit}$ is that value of rf amplitude above which a common locking of the hot and cold domains is obtained. The resulting phase diagram is displayed in Fig. 4-13b. It is apparent that the dynamic coherence length ξ_D is a strong function of both ΔT and V_{rf}. For very short samples, we expect the phase plot of Fig. 4-13b to be modified; in particular, a finite X-axis (ΔT) intercept is expected when the intrinsic dynamic phase coherence length greatly exceeds the sample length. This effect would be consistent with temperature gradient experiments on the behavior of the narrow-band noise spectrum for short samples.[50,51]

In summary, an applied temperature gradient acts to split apart an isothermal Shapiro step into multiple steps. Under a fixed thermal gradient, the isothermal Shapiro step spectrum can be effectively recovered by increasing the amplitude of the external rf signal. This suggests that these two parameters (ΔT and V_{rf}) oppose each other in terms of their relative effects upon a CDW domain's phase velocity coherence. When the Shapiro step peaks are split, the data clearly indicate that the sample breaks into separate

domains, with each domain oscillating at a frequency determined by its local conditions. Hence, these data support the notion that the NBN oscillations are a bulk phenomenon.

4.2.2 Model of temperature gradient effects in charge density wave conductors

In this section a description of a simple conceptual model which account for temperature gradient effects on the moving charge density wave in $NbSe_3$ is presented.[55] This model, valid in the high field limit, qualitatively and semi-quantitatively succeeds in explaining why a CDW sample breaks up into multiple, serially arranged phase velocity coherent domains due to the presence of an applied thermal gradient. The presentation of this model is organized in the following manner: first, a description of the underlying principles involved in temperature gradient domain splitting is presented, followed by the derivation of the relevant energy strain equations. The qualitative and quantitative predictions of this theory are then compared to experimental observations and measurements.[50-54]

We first assume that a moving CDW must form phase velocity coherent domains. This is clearly necessary due to the elastic strain term ($|\nabla\phi|^2$) in the CDW phase Hamiltonian.[32] If the CDW velocity were position-dependent, this elastic strain energy would increase in time, and

eventually destroy a moving CDW. Only by forming phase velocity coherent domains can a CDW minimize this strain energy and, in so doing, slide without destroying itself. Hence, with no thermal gradient, the CDW velocity is the same throughout a domain; when a longitudinal temperature gradient is applied across the length of a sample, variations in the local temperature-dependent parameters which determine the CDW velocity (E_T, ρ, σ_{CDW}, n_c, and Δ) will cause elastic strain to build up within a domain as the CDW adjusts itself to keep the domain velocity constant. When this strain energy exceeds a critical value, the domain will split, forming two sub-domains, with the new domain velocities matching the local conditions more closely and hence lowering the total CDW strain energy. These two domains move at different velocities and must be linked by a section of collapsed CDW; we call this interface a *phase slip center.*

The model that describes these temperature gradient effects is based on the minimization of the total CDW strain energy. The two energies involved are the elastic strain energy, U_s, and the total phase slip center energies, U_{ps}. U_s will be a decreasing function of the number of domains N, while U_{ps} will linearly increase with N. Hence, the number of domains into which a sample will break is determined by finding the minimum energy configuration ($U_{tot} = U_s + U_{ps}$). Note that this model breaks down when the individual domain length L_d is less than the CDW phase coherence length ξ_{FLR}.[32]

With $L_d < \xi_{FLR}$, a phase velocity coherent domain would become unstable.

We first consider the elastic strain energy term U_s; this strain energy builds up within a CDW domain due to the change in local parameters which determine the CDW velocity brought on by the application of a thermal gradient. The parameters which determine the CDW velocity include the threshold electric field E_T, the low field resistivity ρ_o, the CDW conductivity σ_c, the local CDW energy gap Δ, and the local CDW carrier concentration n_c. These parameters are all strongly temperature dependent, and by changing them, the local CDW velocity will in turn be changed in the absence of CDW elasticity. Since the CDW is a coupled wave it must move at a constant velocity. Any variation in velocity along the CDW would give rise to a huge increase in elastic strain energy, destroying the moving CDW. Since this does not happen, the CDW in a domain must move at a constant velocity chosen so as to minimize the domain strain energy.

The local strain energy density $u_s(x)$ will depend upon the difference between the domain velocity V_o and the local velocity in the absence of coupling CDW elasticity $V_c(x)$:

$$u_s(x) = f\{V_o - V_c(x)\} , \qquad (4.20)$$

where x is the position coordinate within the CDW. As a first step towards obtaining an expression for $u_s(x)$ we

derive an expression for $V_c(x)$. We use a simple two fluid model of CDW dynamics with the normal and CDW channels of conduction acting in parallel. The voltage across a domain is simply the voltage across the normal channel,[50]

$$V = I_n R_o = (I_o - I_c) R_o \ , \tag{4.21}$$

where R_o is the low field resistance, and I_o, I_n, and I_c are the total, normal, and CDW currents, respectively. The electric field within a domain is given by

$$E = \frac{\rho_o (I_o - I_c)}{A} \ , \tag{4.22}$$

where A is the sample cross-sectional area. Based both on experimental and theoretical grounds, the CDW velocity is related to the CDW current by[10-13,36-38]

$$I_c = n_c e V_c A \ . \tag{4.23}$$

By substituting Eqn. 4.23 into 4.22, we obtain the following expression for the electric field:

$$E = \frac{\rho_o (I_o - n_c e V_c A)}{A} \ . \tag{4.24}$$

To solve for the CDW velocity V_c, an additional expression relating the electric field and the CDW velocity is required. In $NbSe_3$ the nonlinear CDW conductivity σ_{CDW} is well described by the empirical expression[60]

$$\sigma_{CDW}(E) = \sigma_c \left(1 - \frac{E_T}{E}\right) \exp\left(-\frac{E_o}{E - E_T}\right), \qquad (4.25)$$

where E_T is the threshold field, E_o is a fitting parameter, and σ_c $(= 1/\rho_\infty - 1/\rho_o)$ is the additional sample conductivity due to the depinned CDW in the limit $E >> E_o, E_T$. In the limit of large electric field $(E >> E_o)$ this expression simplifies to

$$\sigma_{CDW} = \sigma_c \frac{(E - E_T)}{E} . \qquad (4.26)$$

Henceforth we will make use of this simple expression rather than Eqn. 4.25. Thus, these calculations will be valid only in the limit $E >> E_o$. In this high field limit the CDW velocity becomes

$$V_c = \frac{\sigma_{CDW} E}{n_c e} = \frac{\sigma_c}{n_c e}\left(E - E_T\right) . \qquad (4.27)$$

By combining Eqns. 4.24 and 4.27, the CDW velocity and domain electric field can be solved for simultaneously:

$$V_c = \frac{\sigma_c}{n_c e} \frac{(I_o \rho_o / A - E_T)}{(1 + \sigma_c \rho_o)} , \qquad (4.28)$$

and

$$E = \rho_o \frac{(I_o / A + \sigma_c E_T)}{(1 + \sigma_c \rho_o)} ; \qquad (4.29)$$

note that the term $1 + \sigma_c \rho_o$ is just the ratio between the total and normal charge carriers n_t / n_n. Using relevant parameters for $NbSe_3$,[1,2,12,16,60,61] the CDW velocity as predicted by Eqn. 4.28 is plotted as a function of temperature in Fig. 14-4; the velocity is an increasing function of temperature up to roughly 57 K. As a result, a sample in a thermal gradient will have slow moving domains near its cold end and faster moving domains near its hot end. Above 57 K, the CDW velocity drops sharply because the threshold field diverges near $T_{c2} = 59$ K.

The CDW is a deformable medium and it is therefore possible for the local CDW to move at a velocity unequal to that given by Eqn. 4.28. As a consequence, deformations in the CDW phase must occur in order for an entire domain to move at a constant velocity V_o. Elastic strain energy will build up as a result of these phase deformations.

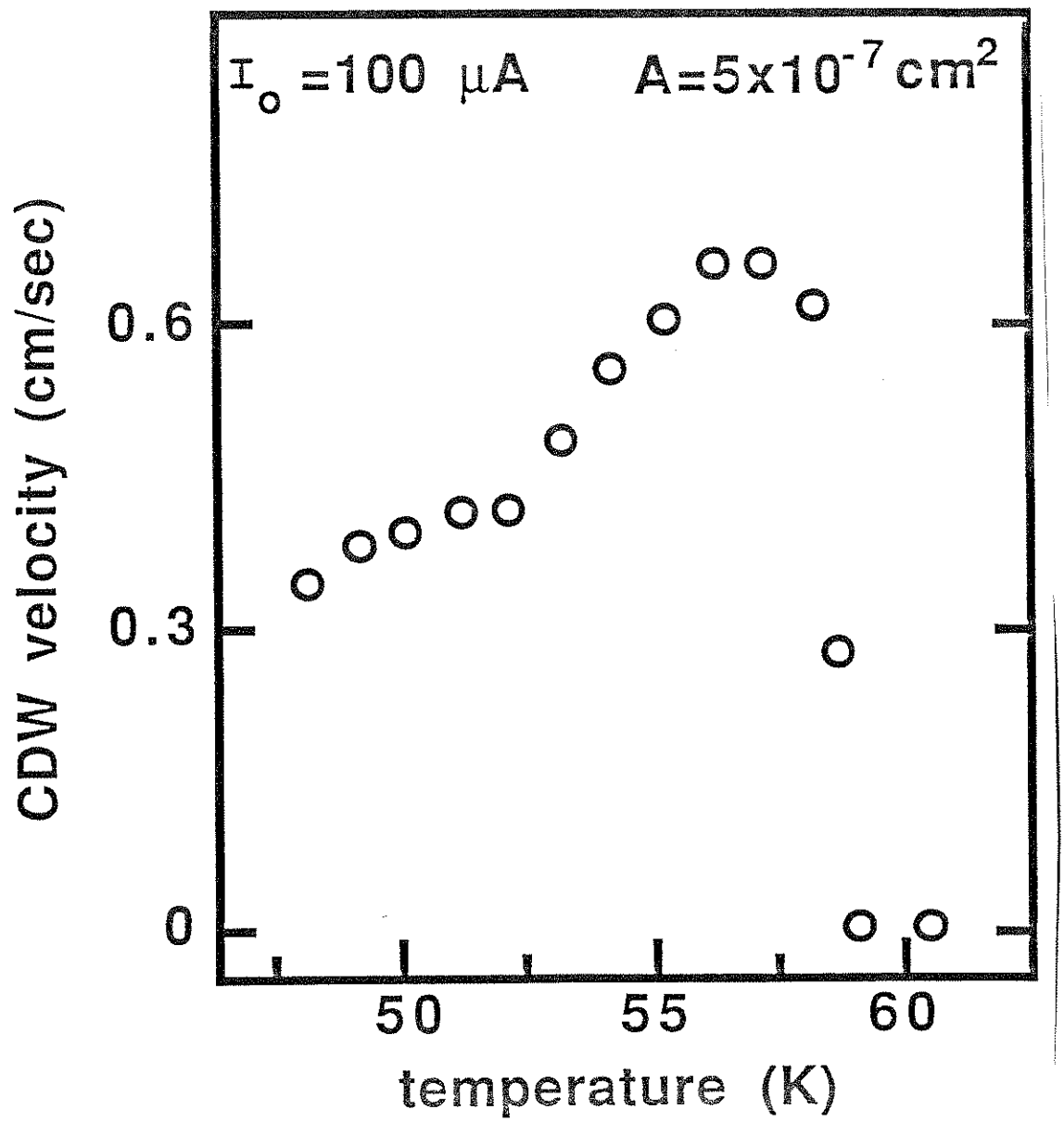

Figure 4-14 V_{CDW} as given by equation 4.28 as a function of sample temperature. Note that the bias current falls below the threshold current at temperatures above 58 K.

Consider, as a classical analog to a continuous, deformable CDW, a series of charged objects connected by springs residing in a viscous medium. Each interconnecting spring has an equal force constant κ, while each ball holds a different electrical charge. With an electric field directed along the chain, the assembly will move, reaching some terminal velocity V_o due to the viscous medium surrounding the chain. Since each mass has a different charge on it, each ball would reach a different terminal velocity in the absence of the interconnecting springs. If the *i*th ball has an isolated terminal velocity V_i greater than V_o, the ball will push up against the neighboring springs until the spring forces slow the ball to V_o. (for our purposes we are uninterested in any oscillatory behavior and will only consider the dc velocity). Similarly, if $V_i < V_o$, then the ball will be pushed and pulled by the neighboring springs until it moves at V_o. This pushing and pulling would occur for every ball in the chain, with the force acting on a given mass dependent on the velocity difference $V_i - V_o$. In the rest frame of the moving chain, the *i*th ball initially has a velocity $V_i - V_o$ and a kinetic energy of $T=(m/2)(V_i-V_o)^2$. When this ball reaches equilibrium this kinetic energy will be converted into spring potential energy. The total strain energy for the entire chain will be

$$U = \frac{1}{2} \sum_i m_i \, (V_i - V_o)^2 \, , \qquad (4.30)$$

where V_i is a function of E, m_i, q_i and the viscosity of the external medium. The dc chain velocity V_o would be that velocity which minimizes the total chain energy as given by Eqn. 4.30.

A discrete chain is clearly analogous to a deformable CDW, with the only major difference between them being that of the continuous nature of a CDW. To more correctly calculate the CDW strain energy we must consider a continuous elastic medium moving at a velocity V_o. An infinitesimal slice at position x would move, in the absence of neighboring slices, at $V_c(x)$. The kinetic and potential energy densities for this medium are[62]

$$t = \frac{m^*}{2} n_c \left(\frac{d\phi}{dt} \frac{1}{q} \right)^2 \, , \qquad (4.31)$$

and

$$u = \frac{\kappa}{2} n_c \, |\nabla\phi|^2 \, , \qquad (4.32)$$

where q is the CDW wave vector ($q = 2k_f$), ϕ is the CDW phase, κ is a phenomenological elastic constant, and m^* is the CDW effective mass. Following the analysis for the case of a discrete chain, the CDW slice at position x will initially

have a kinetic energy density in the CDW rest frame of

$$t(x) = \frac{m^*(x)}{2} n_c \{V_c(x) - V_o\}^2 , \qquad (4.33)$$

where we have used the relation $qV = (d\phi/dt)$. When the system comes to equilibrium, this extra kinetic energy density will be converted into potential energy in the form of local CDW phase distortions. The equilibrium phase distortion at x will be

$$\nabla\phi(x) = \sqrt{\frac{m^*(x)}{\kappa}} |V_c(x) - V_o| \qquad (4.34)$$

$$\approx \frac{\Delta\phi}{\Delta x} .$$

The total elastic strain energy density is equal to the initial excess kinetic energy

$$u_s(x) = \frac{m^*(x)}{2} n_c(x) \{V_c(x) - V_o\}^2 . \qquad (4.35)$$

The total domain strain energy then becomes

$$U_s = \int u_s \, d^3x = \frac{A}{2} \int u_s(x) \, dx , \qquad (4.36)$$

where the integration is performed over the length of the domain.

It is important to note that the expression for the local CDW velocity $V_c(x)$ (Eqn. 4.28) will not conserve current when the effects of the thermal gradient are considered. This arises because Eqn. 4.35 was not obtained in a self-consistent manner; V_c, the local expected CDW velocity, is itself a function of the domain velocity V_o due to the feedback which occurs when the constraint of current conservation within a domain ($I_o = I_n + I_c$) is considered. Hence, $V_c(x)$ in Eqn. 4.35 must be replaced by $V_c(x,V_o)$, giving the following expression for the strain energy density

$$u_s(x) = \frac{m^*(x)}{2} n_c(x) \{V_c(x,V_o) - V_o\}^2 . \qquad (4.37)$$

To calculate $V_c(x,V_o)$ in Eqn. 4.37, we follow the derivation used to obtain Eqns. 4.28 and 4.29, but with the condition that the CDW moves at a velocity V_o. Hence, we calculate what the local velocity should be when the domain moves at V_o. By applying Eqn. 4.24 with $V_c \Rightarrow V_o$, the local electric field becomes

$$E = \frac{\rho_o (I_o - n_c e V_o A)}{A} . \qquad (4.38)$$

We now apply Eqn. 4.27 with the E field as determined by Eqn. 4.38, and find that the local expected CDW velocity becomes

$$V_c(x,V_o) = \frac{\sigma_c}{n_c e}\{E - E_T\}$$
$$= \frac{\sigma_c(x)}{n_c e}\left[I_o\rho_o/A - n_c(x)eV_o\rho_o(x) - E_T(x)\right]. \qquad (4.39)$$

The velocity difference $V_c(x,V_o)-V_o$ takes on the following simple form when the original local velocity $V_c(x)$ as given by Eqn. 4.28 is used:

$$V_c(x,V_o) - V_o = (1 + \sigma_c\rho_o)\ (V_c(x) - V_o)\ ; \qquad (4.40)$$

hence, the current conserving velocity difference is simply multiplied by the weighting factor $1 + \sigma_c\rho_o = n_t/n_n$. The self-consistent energy density then becomes

$$u_s(x) = \frac{m^*(x)}{2}\, n_c(x)\ (1 + \sigma_c\rho_o)^2 (V_c(x) - V_o)^2\ , \qquad (4.41)$$

with $V_c(x)$ as given by Eqn. 4.28. Finally, by integrating Eqn. 4.41 over the entire CDW volume we have for the complete sample strain energy:

$$U_s = \frac{A}{2} \sum_i \int_{L_{d,i}} dx\, m^*(x)\, n_c(x)\, [1 + \sigma_c(x)\rho_o(x)]^2 [V_c(x) - V_{o,i}]^2, \tag{4.42}$$

where the summation is performed over all N domains and each integration is performed over the length $L_{d,i}$ of each domain, with

$$V_c(x) = \frac{\sigma_c(x)}{n_c(x)e} \left(\frac{I_o \rho_o(x)/A - E_T(x)}{1 + \sigma_c(x)\rho_o(x)} \right) . \tag{4.28}$$

Note that the temperature gradient effects come into play via the positional -- and hence temperature -- dependence of the parameters in these equations. In practice, the strain energy for an N domain CDW is found by calculating the strain energy for each domain and summing the energies; the velocity for a given domain $V_{o,i}$ is chosen so as to minimize that domain's strain energy.

To determine the total CDW potential energy $U_{tot} = U_s + U_{ps}$ we must also calculate the phase slip center energy U_{ps}. At the interface between domains the CDW must collapse in a phase slip process due to the discontinuity in the CDW velocity. The energy required to destroy the CDW via the

formation of a domain wall with a thickness on the order of the CDW amplitude correlation length ξ is[63]

$$U_w \approx A\xi N^2(E_F)\Delta \ , \qquad (4.43)$$

where $N(E_F)$ is the electron density of states at the Fermi energy and Δ is the CDW gap energy. It is always energetically favorable to have the CDW collapse instead along a line of phase vortices which move transverse to the CDW chain axis.[63] The energy of a phase vortex is essentially equivalent to that of a domain wall but scaled to a much smaller volume[64]

$$U_{pv} \approx \eta N^2(E_F)\Delta\xi^3 \ , \qquad (4.44)$$

where η ($\approx$0.1 to 0.01) is the CDW anisotropy parameter. With typical sample parameters (ξ = 100 Å, η = 0.1, and A = 100 μm^2) the ratio between these two energies is $U_w/U_{pv} = 10^7$. Clearly ,the phase slip center will consist of some form of phase vortices rather than a complete domain wall. Due to the small size of the phase vortex (it has a volume of ξ^3), large variation in the phase slip energy may exist if the phase slip were to occur on or near an impurity site where the relevant parameters [Δ and $N(E_F)$] could be far below the clean, bulk value. Hence, Eqn. 4.44 should be considered at

best as an approximate upper limit to the phase slip energy.

The thermal gradient effect upon a CDW can be calculated by combining the total strain energy as given by Eqn. 4.42 with the total phase slip energy as given by Eqn. 4.44 and minimizing the total energy with respect to the number N of domains. A number of qualitative results can be gleaned from these equations and can be directly compared to experimental observations. The most important result is that the phase strain energy, and hence the total number of domains, scale with the magnitude of the thermal gradient ∇T; this is in excellent agreement with the experimental observations that N grows with increasing ∇T.[53] The theoretical framework described here shows that N is an increasing function of ∇T because large gradients cause a correspondingly large spread in $V_c(x)$ to exist within a domain; this will raise U_s and hence cause domain splitting to occur.

The strain energy equation (Eqn. 4.42) also predicts that the number of domains should scale linearly with the sample length [with a temperature difference ΔT, the local strain density u_s scales as ΔT, and the total domain strain density scales as $(\Delta T)L$]; this is in complete agreement with the results of experiments on $NbSe_3$ where very short samples are not split by large gradients[50] while long samples are easily split by relatively small gradients.[51-54] Closely associated with this predicted length scaling is the

prediction that domain splitting should scale with sample cross-sectional area ($U_s \propto A$). That is, given two samples of equal length, bias field and applied thermal gradient, the thicker samples, being comprised of a larger volume of CDW, should more readily split into multiple domains than a thinner one. This prediction agrees with experiments where it has been found that extremely thin samples, as with extremely short samples, tend not to split in gradients which would split a thicker sample.[48]

Equations 4.42 and 4.28 indicate that by increasing the sample current I_o the number of domains should also rise. This arises from the corresponding growth in the CDW velocity that will occur when the bias current is increased. The increase in the domain velocity will in turn give rise to an increase in the strain energy density because the local velocity mismatch will grow. This prediction is in agreement with studies where samples un-split at low biases under a given thermal gradient can be split if the bias current is increased.[48]

Shapiro step experiments in the presence of an applied thermal gradient sometimes indicate that the CDW splits into domains of unequal length (see Sec. 4.2.1).[54] The model gives a simple explanation for this effect. The expression for the phase slip energy (Eqn. 4.44) indicates that this energy drops with rising temperature since $\Delta(T)$ falls to zero as T approaches T_c from below. Hence, given a sample which

has split into more than one domain, it is energetically favorable for the phase slips to occur as close as possible to the hot end of the sample. Clearly there is a limit to how close a phase slip can get to the hot end since there will in turn be a slight increase in the energy of the longer domain. Past a critical shift in phase slip location, the cold domain will grow in strain energy by more than the phase slip energy will drop. This could explain the result in the Shapiro step-thermal gradient experiment presented in Sec. 4.2.1 where a sample broke up into a hot and cold domain with the cold domain comprising 67 % of the total crystal.

The model also provides an insight into why depinned CDW samples which appear to be split into multiple domains with no thermal gradient are not further split by the application of a gradient.[48] In these samples, the sizes of the zero gradient domains are quite small, and, as a result, thermal strain energy sufficient to split them cannot develop. Effectively, an internal chemical gradient, analogous to a thermal gradient, already exists in the sample and as a result moderate thermal gradients cannot split apart the already split domains.

Qualitatively, the model of domain splitting due to thermal gradient induced phase deformation appears to agree with experimental results quite well. To quantitatively test the model, the strain energy as a function of sample domain number has been numerically calculated using Eqns. 4.28,

4.42, and 4.44 for a sample of $NbSe_3$ with the cold end at T_o = 48 K and the hot end at $T_o + \Delta T$ (this corresponds to the experimental conditions in Sec. 4.2.1 and Ref. 50). The relevant temperature-dependent parameters where obtained from published $NbSe_3$ data. Specifically, values for σ_c and ρ_o were taken from plots of ρ vs. T,[2] while values for $n_c(T)$ [$\propto \Delta(T)$][14] and $\Delta(T)$ were obtained from plots of Δ vs. T [65] (with $\Delta(T=0)$ = 35 meV and $n_c(T=0) = 3.3 \times 10^{21}$ cm^{-3}).[1,12,16,61,66] The exact nature of the temperature dependence of the CDW effective mass m^* is still in debate; microwave data indicates that it may be relatively independent of temperature with a value of $m^* \approx 100\ m_e$, and this value was used in the calculations presented here.[61]

The numerically calculated sample strain potential energy is plotted as a function of ΔT for N = 1, 2, and 3 in Fig. 4-15. The strain energy rises with increasing thermal gradient and falls with increasing domain number (note that the maximum in U_S at $\Delta T \approx 8$ K occurs because E_T diverges above T = 53 K, and, as a result, the "hot" portion of the simulated crystal becomes pinned above $\Delta T \approx 8$ K). The calculated strain energy, phase slip energy, and total CDW potential energy for a particular ΔT value are plotted as a function of domain number in Fig. 4-16. Again, the strain energy is a decreasing function of the number of domains. By assuming a value for the phase slip energy (U_{ps} = 4 meV) the total phase slip energy is determined [$(N-1)U_{ps}$], and the

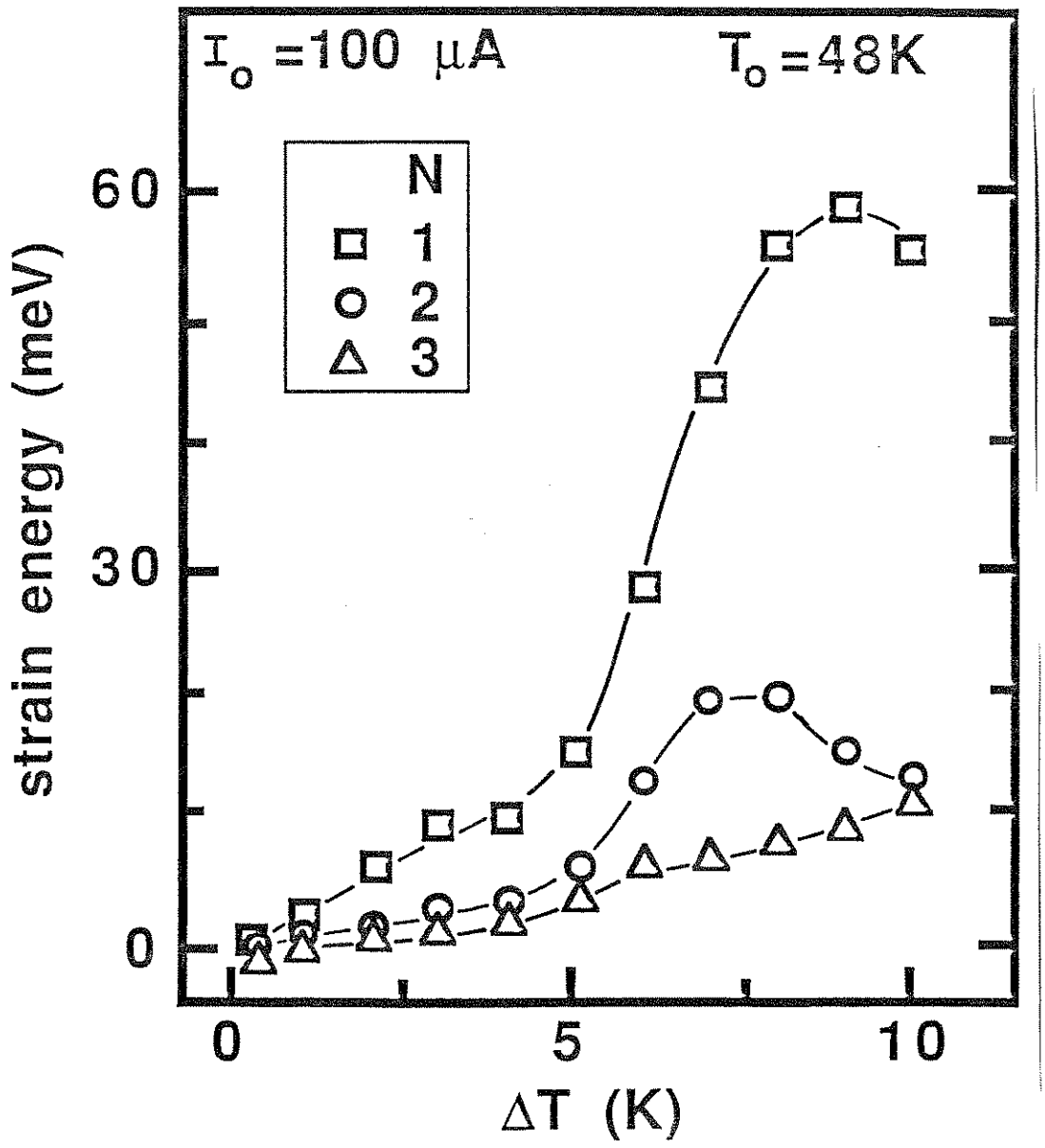

Figure 4-15 Calculated sample strain energy plotted as a function of thermal gradient assuming the sample consists of one (squares), two (circles), and three (triangles) phase velocity coherent domains. Sample parameters are A = 5×10^{-7} cm^2 and L = 1 mm.

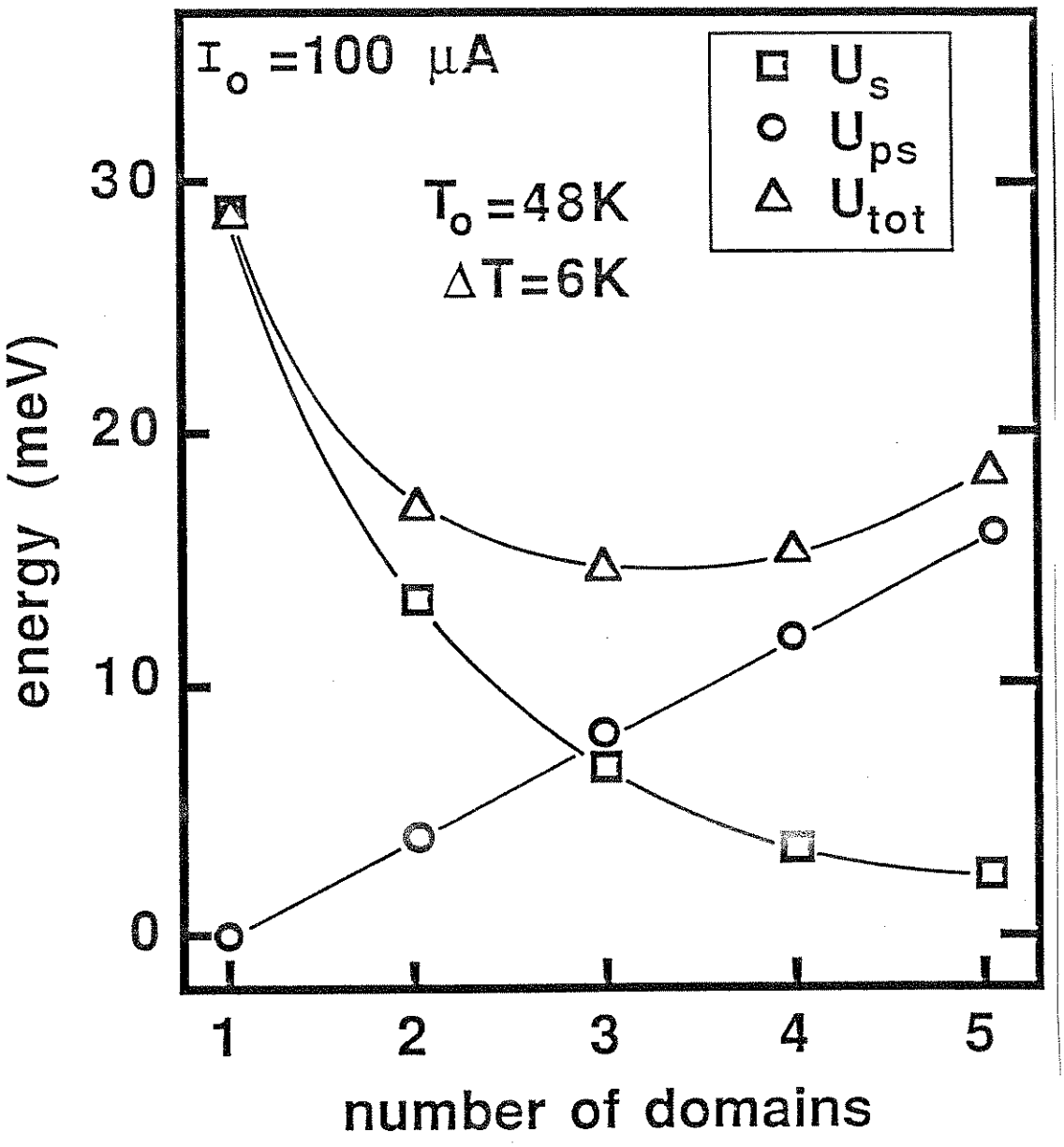

Figure 4-16 Calculated Strain energy (squares), total phase slip energy (circles), and total CDW energy (triangles) plotted as a function of the number of domains for a sample with A = 5×10^{-7} cm^2 and L = 1 mm. In this configuration, the minimum energy state occurs for N = 3.

minimum energy configuration can be found. In Fig. 4-16, the minimum total energy occurs with N = 3. This number increases as ΔT, L, I_o, or A are raised, in agreement with empirical observations.[48,50-54] Hence, the calculations show that the predicted number of domains correctly scale with the gradient size, the sample dimensions, and the bias current.

These numerical results all qualitatively agree with experiment but the strain energies appear much smaller, by a factor of roughly 10 to 100, than the estimated phase slip center energy as given by Eqn. 4.44. Typical domain kinetic energies are on the order of 100 meV, while the strain potential energies are on the order of 10 meV. Rough estimates of the phase slip energy via Eqn. 4.44 yield values on the order of 100 to 1000 meV. If this were the case, the strain energy that arises from a thermal gradient would never be large enough to cause domain splitting. The exact nature of the phase slip process is quite complicated and it is possible that the estimate given by Eqn. 4.44 is far higher than the real values when local impurities and lattice irregularities are taken into account. The phase slip energy will be drastically reduced if the phase slip occurs near sample irregularities of this sort since the relevant parameters, $N(E_F)$, ξ and Δ, will in turn drop. Furthermore, since the phase slip center will form in a location that can minimize its energy, it appears reasonable that the energy of a phase slip could be much less than that predicted by Eqn.

4.44.

In conclusion, a simple model based on phase distortion and phase slip processes has been proposed to account for thermal gradient effects in CDW conductors. This model is in good qualitative agreement with the temperature gradient effects seen in samples of $NbSe_3$. Numerical studies indicate that phase slippage must occur in areas of a sample where local crystal irregularities exist so as to drastically reduce the phase slip energy. This point could be clarified further by a more detailed examination of the phase slip process in samples containing randomly positioned impurities.

4.3 Domain structure and impurity length scale effects in switching charge density wave conductors

The intriguing nonlinear electrical conductivity observed both in $NbSe_3$ and other quasi-one-dimensional materials has been extensively studied during the past decade.[1] Research has proven that the nonlinear conductivity exhibited by these materials stems from the depinning and subsequent Fröhlich motion of the charge-density-wave (CDW) condensate. This sliding motion occurs when an applied electric field E exceeds the CDW pinning threshold field E_T. The sliding CDW gives rise to nonlinear conductivity and a decrease in the crystal's differential dc resistance. The depinning is usually evident in the current-voltage (I-V) relationship as a smooth, continuous change from the pinned, linear state to the higher conductance sliding, nonlinear state; at fields well past E_T the CDW conductance saturates and the differential resistance becomes field independent.

Not all samples display a smooth depinning process in their I-V characteristics. In some samples of $NbSe_3$, the CDW depins in a sharp, hysteretic manner which gives rise to a strong discontinuity in the I-V curve. This phenomenon was first observed in the low temperature state of $NbSe_3$ and is referred to as *switching*.[67] The dynamic switching state is characterized by a temperature independent depinning field,[68] hysteresis,[69] negative differential resistance,[70] period-doubling routes to chaos,[71] and inductive ac

response.[72] Switching has also been observed in many other CDW materials which show nonlinear transport. These materials include TaS_3,[73] $K_{0.3}MoO_3$,[74] and $(NbSe_4)_{3.33}I$.[75] It has been found that switching can also be induced by iron doping $NbSe_3$[76] or by irradiating either TaS_3 or $K_{0.3}MoO_3$.[77] This suggests that switching is caused by the interaction of impurities with the CDW.

Recent work has indicated that switching in both $NbSe_3$ and Fe_xNbSe_3 is associated with the separation of the CDW into distinct, serially arranged macroscopic phase-velocity coherent domains.[78] These domains were found to be separated by localized phase-slip centers which are presumed to consist of ultra-strong impurity sites.[79] According to a phase-slip switching model,[79-81] switching occurs when the CDW amplitude at an ultra-strong pinning site collapses due to the strong phase polarization which builds up there in the presence of a dc bias field. This phase and amplitude dynamical model has been successful in accounting for the physical behavior displayed by switching CDW crystals.[80,81]

While all switching samples show abrupt and discontinuous CDW depinning, there is a wide diversity in the I-V character of switching samples of $NbSe_3$. The I-V characteristics of switching crystals can be loosely classified into two categories. In what we call type I samples, the CDW depins largely via a single predominant switch although other, much smaller switches might also be

present in the I-V curve. These large type I switches generally show a large amount of hysteresis which is accompanied by the formation of switching sublevels within the hysteresis loop.[69] Type II samples depin via a number of much smaller, roughly equal-sized switches and display only small amounts of hysteresis. No sublevels are evident in the I-V characteristics of type II samples. While the physical ideas which are embodied in the phase-slip switching model successfully describe the underlying mechanisms which cause switching, it is far from obvious that the model can account for the large diversity observed in the I-V characteristics of switching CDW crystals.

In this section we examine the results from a study of switching in both $NbSe_3$ and Fe_xNbSe_3 that was performed in order to clarify the differences between type I and type II switching behavior in these materials.[82,83] To determine the underlying differences between these two classes of switching behavior, we employ two techniques that probe the distribution, structure, and relative coherence of switching domains. In the first technique, thermal gradients are applied across the length of switching samples. The resulting effects upon the switches in an I-V curve indirectly indicate the coherence and internal structure of switching domains. In addition, the locations of these domains are mapped out by using a non-invasive domain localization voltage probe technique. By using these

techniques we determine that the drastically varied switching behavior observed in different crystals of these materials is a direct result of dissimilarities in the distribution of the ultra-strong impurities contained within them. This behavior is consistent within the framework of the phase-slip model of switching.[80,81]

The remainder of this section is organized in the following manner. A description of the method of approach is presented in Sec. 4.3.1, and the experimental results are presented in Sec. 4.3.2. This is followed by an analysis in Sec. 4.3.3. Finally, we briefly summarize our findings and present concluding remarks in Sec. 4.3.4.

4.3.1 Methods

Both thermal gradient and domain localization techniques were employed to examine the internal domain structure and coherence of switching domains in $NbSe_3$ and Fe_xNbSe_3. The intra-domain structure in switching CDW crystals can be investigated by applying longitudinal temperature gradients across the samples.[82] This powerful method has proven to be useful in the study of phase-velocity coherent domains in *non*-switching CDW samples (see Sec. 4.2); in those experiments the gradient causes the CDW to break up into separate and distinct current carrying domains.[50-54] This technique exploits the temperature dependence of the parameters which characterize the CDW condensate.

4.3.1.1 The CDW condensate: thermal gradients and domain localization

A CDW is a modulation of the electronic charge density $\rho(x)$ which can be represented by

$$\rho(x) = \rho_a + \rho_c \cos[2k_F x + \phi(x)] \qquad (4.45)$$

where ρ_a is the average electronic density, ρ_c is the amplitude of the density wave, k_F is the Fermi wave vector, and $\phi(x)$ is the position-dependent phase of the CDW; motion or distortion of the wave is accounted for by the phase variable $\phi(x)$. In the presence of a bias current I which exceeds the depinning threshold current I_T the CDW will slide with a velocity $v(x)$ related to the time derivative of the phase. This phase velocity depends on the parameters which characterize the CDW,

$$v(x) \propto \frac{d\phi(x)}{dt} = f(\rho_o(T(x)), n_c(T(x)), E_T, I) \ , \qquad (4.46)$$

where ρ_o is the low field resistivity, n_c is the CDW electron density, and E_T is the CDW threshold electric field. In Eqn. 4.46 we explicitly indicate that both ρ_o and n_c are functions of temperature while E_T is *independent* of temperature in a

switching crystal.[68] The CDW phase velocity is independent of the position coordinate x within a CDW domain because of the form of the phase distortion term in the CDW Hamiltonian[32]

$$H_{elastic} = \frac{1}{2} \kappa \int |\nabla\phi|^2 \, d^3x \qquad (4.47)$$

where κ is the CDW phase elasticity coefficient. If $d\phi/dt$ were a function of position, the phase gradient $\nabla\phi$ would steadily increase with time and result in the destruction of the CDW. Hence, a stable sliding CDW must form phase-velocity coherent domains.

When a temperature gradient is applied across the length of a sample [$T(x)=T_o+(\nabla T)x$, $0<x<L$] Eqn. 4.46 would suggest that the local phase velocity must become a function of position. This is at odds with the requirement that the CDW phase velocity be constant in order to keep the phase distortions from destroying the sliding CDW. To insure that the sliding CDW is stable in a thermal gradient, subtle local phase distortions must occur which cause the entire domain to move at a velocity v_o. These distortions will act to slow down CDW regions where otherwise $v(x)>v_o$ and speed up CDW regions where otherwise $v(x)<v_o$. Hence, the phase velocity of a domain becomes constant at the expense of creating phase distortions along the length of the domain. These phase

distortions raise the energy of the CDW as indicated by Eqn. 4.47. The degree to which the CDW energy increases will depend upon how much the domain velocity v_o and $v(x)$ differ. This velocity mismatch will depend on the applied temperature difference ΔT as well as the sample length L. As a result, it is possible that the energy increase due to the presence of the thermal gradient can be minimized if the domain were to split into a number of subdomains. With many smaller subdomains the domain velocity "mismatches" and the resulting phase distortions can be reduced. Hence, under certain conditions it can be energetically favorable for a CDW domain in the presence of a temperature gradient to break into a number of subdomains. Each domain will move at a different velocity corresponding to its local average temperature. In this situation, the interface between neighboring subdomains must act as a phase-slip center because of the discontinuity in the CDW domain velocities. The CDW amplitude must periodically collapse at these phase-slip centers in order to link neighboring subdomains together.

It is energetically very costly to create a phase-slip center unless large impurities exist within a domain. Hence, uniform and coherent switching domains will not in general be broken down into subdomains by a thermal gradient (this is the behavior of type II samples). In the opposite case of domains which are non-uniform and contain many large impurity centers the CDW will, under the action of a temperature

gradient, readily split into subdomains so as to lower the overall energy of the system (this is the behavior of type I samples).

In the case of type I samples, once the subdomains are decoupled from the neighboring sections of the CDW they will behave according to their own local average temperature. This decoupling process can be observed by measuring the current driven I-V characteristics of a crystal. The *switching* threshold current I_T will be

$$I_T(T) = \frac{aE_T}{\rho_o(T)} , \qquad (4.48)$$

where a is the sample cross sectional area and we explicitly indicate that ρ_o is a function of temperature while E_T is not. In the temperature region studied here, ρ_o is an increasing function of temperature ($\rho_o \sim T$) in both $NbSe_3$ and Fe_xNbSe_3, and the threshold current will therefore drop with increasing temperature ($I_T \sim 1/T$). Hence, in the presence of a thermal gradient each decoupled subdomain will depin at a threshold current which is determined solely by its local temperature.

The thermal gradient effects on a sample's current-driven I-V characteristics therefore indicate whether or not the zero gradient domains are internally uniform and coherent. If a domain is internally uniform (i.e., there are

no ultra-strong impurities contained within it) the switch should be unaffected by the temperature gradient. On the other hand, if a domain contains a number of ultra-strong impurities, the switch caused by its zero gradient depinning will decompose into a number of smaller subswitches in the presence of a thermal gradient. These subswitches will each depin according to their local temperatures and will therefore be separated in the resulting I-V curve. Hence, by observing the thermal gradient effects on a switching I-V curve one can indirectly determine the uniformity, internal structure, and relative coherence of a zero gradient switching domain.

4.3.1.2 Materials and experimental techniques

Samples used in this research consisted of single crystals of high purity $NbSe_3$ and Fe_xNbSe_3 that were produced by the conventional vapor-transport method. The amount of iron which was incorporated into the Fe_xNbSe_3 was much smaller than the nominal doping level ($x \approx 0.03$); it was below the 1% sensitivity of microprobe analysis.[79] Typical crystal cross-sectional dimensions for both $NbSe_3$ and Fe_xNbSe_3 were 5μm x 3μm. Crystal lengths varied from 0.3mm to 1.5mm.

The experimental configuration consisted of single switching crystals suspended in vacuum between either two large copper mounting posts anchored to peltier heater chips

or between a pair of sapphire blocks with manganin heater wire wound about their bases. Electrical contacts were made at the ends of the crystal with silver conductive paint. Thermometry was accomplished by a diode sensor and several miniature differential thermocouples. All I-V curves presented in this paper were measured using a current driven configuration.

The domain localization technique was employed to more directly map out the switching domains in these materials. In this technique, current domains are observed via non-perturbative measurements of local dc conductivities.[78,79] The method uses a three terminal probe. A pair of current leads, terminals 1 and 3, are attached to either end of a crystal using silver conductive paint. The third probe, terminal 2, is a non-perturbing voltage sensing lead composed of fine 2.54 μm thick wollaston (Rh-Pt) wire which can be lightly pressed against the sample. The location of this probe could be varied along the entire length of the sample with its absolute position determinable to within an accuracy of ±5 μm. By measuring the I-V characteristics of various sections of a given switching sample, the number and location of the switching domains can be directly determined. Fine wollaston wire was used so as to minimize any mechanical and current distribution perturbations and, when in the presence of a temperature gradient, thermal perturbations at the point where the

probing wire touches the sample.

4.3.2 Experimental results

In the subsections that follow we apply both the thermal gradient and the domain localization techniques to switching samples of $NbSe_3$ and Fe_xNbSe_3. The results from experiments on type I $NbSe_3$ are presented first. This is followed by the results from experiments on type II $NbSe_3$ and Fe_xNbSe_3.

4.3.2.1 Type I $NbSe_3$

The zero gradient I-V characteristics of a typical type I switching sample of $NbSe_3$ at temperatures between 24.6K and 29.3K are presented in Fig. 4-17. The data clearly show that the switch depinning threshold current, I_T, is a decreasing function of temperature in the switching regime. This particular crystal shows negative differential resistance at 29K and clear switching below 27K. Below 26K the CDW depinning proceeds via two independent switches, labeled S_1 and S_2 in the figure. The first switch, S_1, is much larger than switch S_2. This suggests that in isothermal conditions the crystal consists of two macroscopic current-carrying domains. These two domains are probably separated by a phase-slip center. The two switches become hysteretic below 25.5K, and no additional switches are observed at temperatures less than 24K.

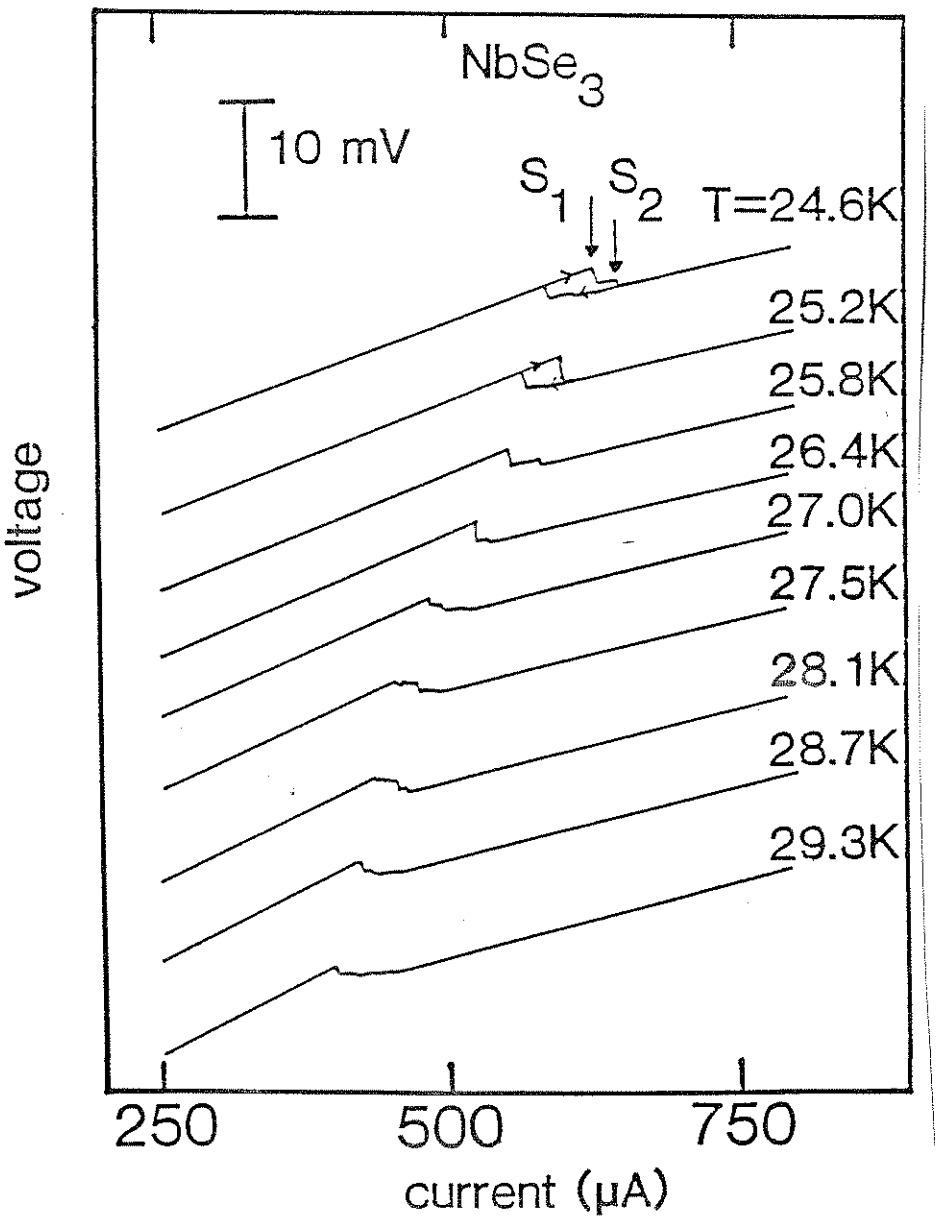

Figure 4-17 Zero gradient current driven I-V characteristics for a type I $NbSe_3$ switching crystal at temperatures between 24 K and 29 K. At low temperatures two distinct hysteretic switches, S_1 and S_2, occur and are identified by the vertical arrows.

The effects of a temperature gradient on two type I switching crystals with widely different lengths are shown in Fig. 4-18. The data in Fig. 4-18a shows the effects of a temperature gradient on the I-V characteristics of the same 300 μm long sample examined in Fig. 4-17, while Fig. 4-18b shows the thermal gradient I-V characteristics of a different type I switching sample which is 1.5 mm in length. We first consider the results presented in Fig. 4-18a. In this case, the temperature of one end of the sample was held fixed at T_o=24 K while the other end was warmed to a higher temperature, $T_o+\Delta T$, ranging between 24 K and 28 K. The curves in Fig. 4-18a are labeled by the temperature difference ΔT. The data in Fig. 4-18a demonstrates that applied thermal gradients have a strong effect upon the switching characteristics of type I $NbSe_3$. As the temperature gradient is increased, the dominant switch, S_1, appears to break up into a series of smaller switches. These subswitches are labeled S_1', S_1'', S_1''', and S_1'''' in the ΔT=2.3 K trace in Fig. 4-18a. As the gradient is increased in strength the lowest threshold switch, S_1' seems to depin at progressively lower threshold currents. In the process of moving to lower threshold currents, switch S_1' appears to break apart, shedding the smaller switches S_1'', S_1''', etc., and in so doing becomes smaller in size. The smaller switches continue to move to lower threshold currents as the gradient is increased. The smaller switch S_2 appears

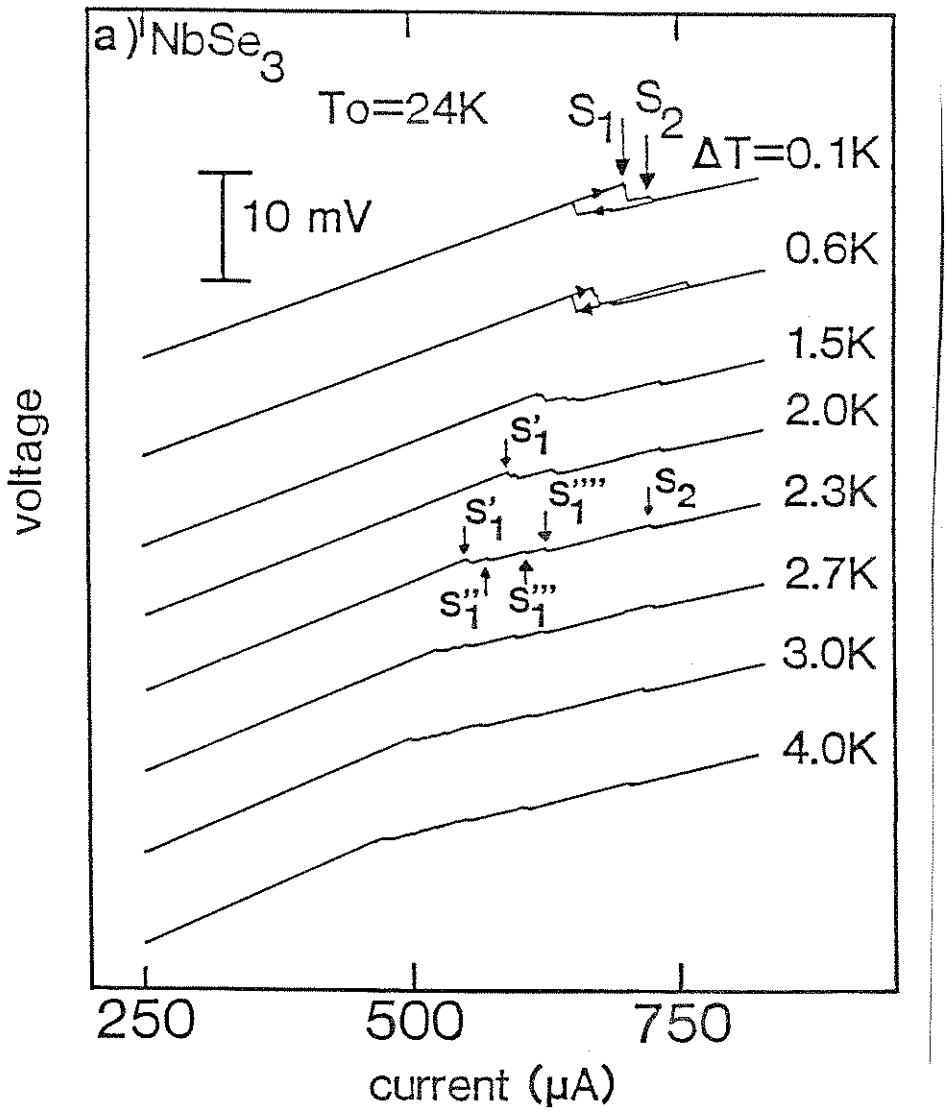

Fig. 4-18a Current driven I-V characteristics for the same type I $NbSe_3$ sample used in Fig. 4-17, but in the presence of a temperature gradient. The cold end of the sample is held at T_0=24 K while the hot end is at $T_0+\Delta T$. With increasing ΔT, switch S_1 breaks up into a series of smaller switches S_1', S_1'', etc., as identified in the ΔT=2.3K trace.

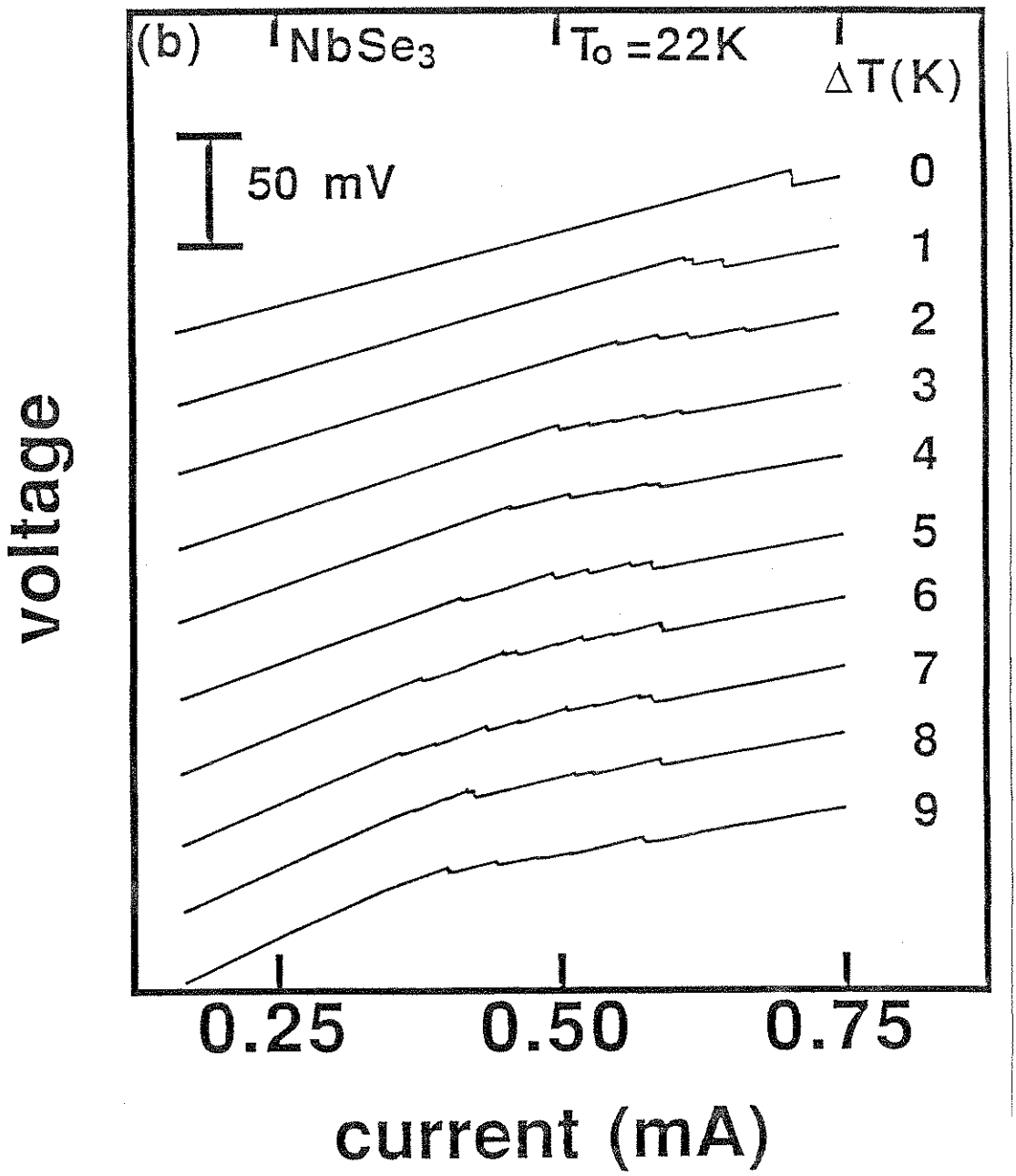

Fig. 4-18b Thermal gradient I-V characteristics of a type I switching sample that is five times as long as that used in Fig. 4-18a.

essentially unaffected by the temperature gradient.

The thermal gradient effects on the I-V characteristics of the crystal of length L_s=1.5mm are shown in Fig. 4-18b. In this case the temperature of one end of the sample was held fixed at T_o=22 K while the other end was heated to a temperature of $T=T_o+\Delta T$, ranging between 22 K and 31 K. With $\Delta T=0$ this sample depins via a single extremely large switch with a magnitude of ΔV=10 mV, some three times larger than that of switch S_1 in Fig. 4-18a. The thermal gradient acts to break the isothermal switch into a series of small subswitches which continue to spread apart in the I-V curve as the gradient is increased. As in Fig. 4-18a, the number of switches rises as the gradient increases in magnitude, reaching a maximum value of roughly eight at ΔT=7 K. Above ΔT=8K the minimum-threshold switch begins to depin in a non-switching fashion, indicating that the hot end of the sample is outside of the switching temperature regime (for this sample $T_{switch} \leq 30$ K). The general behavior observed in both of these samples is not unique: the thermal gradient switch break-up has been observed in all type I switching samples which we have examined.

We associate the temperature gradient behavior of Figs. 4-18a and 4-18b with the underlying domain structure of these type I samples. The I-V characteristics in the presence of a thermal gradient clearly show that the zero gradient domains which give rise to switch S_1 in Fig. 4-18a and the extremely

large switch in Fig. 4-18b are actually composed of a number of subdomains. These numerous subdomains can only be seen in the I-V curve when stress, here in the form of a temperature gradient, is applied to the sample. For the 0.3mm long sample used for Fig. 4-18a this is demonstrated more clearly in Fig. 4-19a, where the depinning threshold current of switch S_1' is plotted as a function of temperature [assuming $T(\text{domain } S_1') = T_o + \Delta T$], along with the temperature dependence of the threshold current of the zero gradient switch S_1 as deduced from Fig. 4-17. Similar data for the 1.5mm long sample of Fig. 4-18b are shown in Fig. 4-19b. In both cases the two thresholds match closely throughout their respective temperature ranges. These data indicate that the domains which give rise to the large switches in the isothermal I-V curves in Figs. 4-18a and 4-18b are actually composed of a number of subdomains. In the absence of a thermal gradient these subdomains appear to depin in unison, creating a large zero gradient switch. As a thermal gradient is applied and increased in strength, the subdomains decouple and depin according to their own local temperature. As discussed in the previous section, $I_T \sim 1/T$ and, as a result, the hotter subdomains must depin at progressively lower currents as the gradient is increased.

By examining the way in which the large zero gradient switches decompose as the temperature gradient is increased in strength it appears that these subdomains must actually be

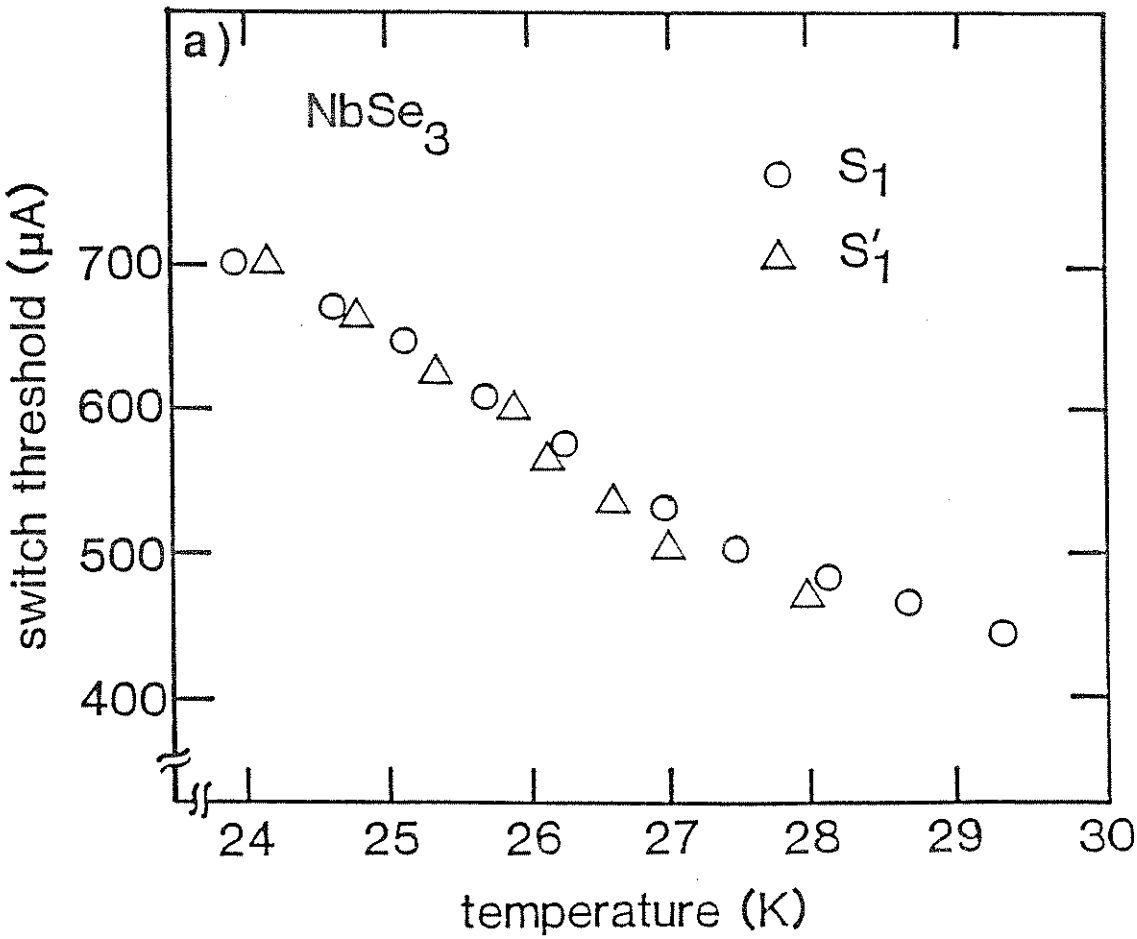

Fig. 4-19a Threshold current versus temperature for switching to occur in the same type I $NbSe_3$ crystal used in Figs. 4-17 and 4-18a. The open circles refer to switch S_1 of Fig. 4-17 (zero gradient) while the triangles refer to the first switch S_1' of Fig. 4-18a (with a gradient). The temperature used when plotting $I_T(S_1')$ is $T_0+\Delta T$. The close correspondence of the two data sets indicate that S_1' is associated with a switching current domain very near the "hot" end of the sample.

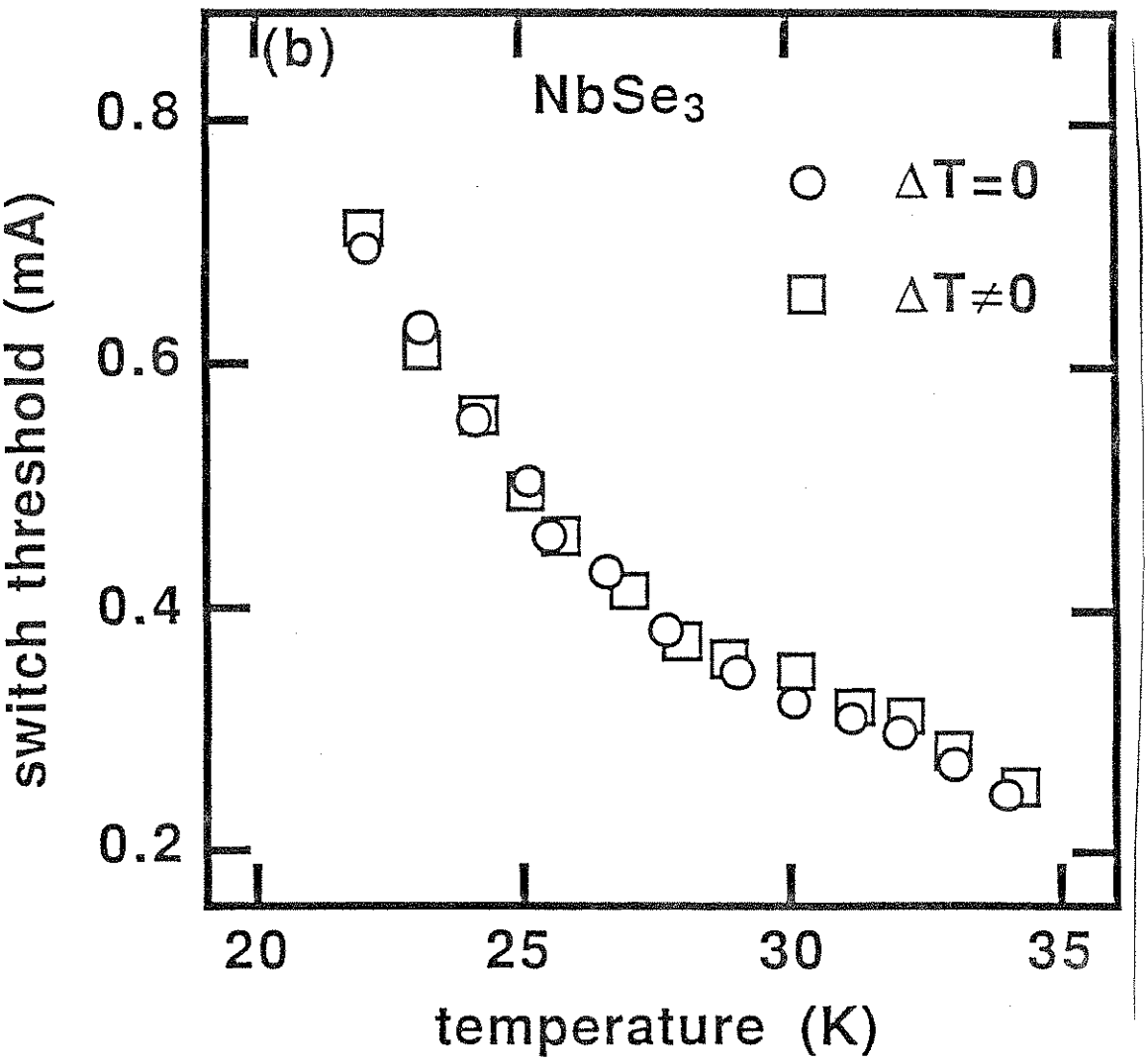

Fig. 4-19b Switching threshold current versus temperature corresponding to the data presented in Fig. 4-18b. The open circles refer to the threshold in the absence of a thermal gradient. The squares show the minimum switching threshold in the presence of a temperature gradient, assuming $T=T_o+\Delta T$.

strongly coupled together, making them depin in a synchronized fashion when $\Delta T = 0$. This becomes evident when we consider three important aspects of the small thermal gradient data in Figs. 4-18a and 4-18b. First, the number of subswitches increases as the gradient is increased; this indicates that the neighboring subdomains are linked together since, with no such linkage, the subdomains would all depin at different threshold currents even in the presence of small gradients (this would cause the zero gradient switch to become smoothly "smeared" in the limit of low thermal gradients). Second, the subswitches appear to break off from the larger switch one at a time as the larger switch decomposes in a thermal gradient. This larger switch continues to move to lower thresholds as it sheds the subswitches. As the gradient increases the "main" switch becomes as small as the decoupled subswitches and stops devolving further. This suggests that the coupled subdomains depin together in the absence of a thermal gradient; the depinning of this large "train" of switching subdomains creates a large type I switch. As a gradient is applied, single subdomains break off from the main group, giving rise to the isolated switches in the I-V curve. As the gradient is increased further, more and more subdomains decouple until all of them are depinning independently. The third piece of evidence which suggests that the grouped subdomains depin in a synchronized fashion is that the data in Figs. 4-19a and

4-19b match the zero gradient thresholds even in small gradients sufficient to split the sample into only two domains. Hence, the train of coupled subdomains near the hot end of the sample do not act as if they were depinning at their average temperature (somewhere between T_o and $T_o+\Delta T$), but rather at the hot end temperature of $T_o+\Delta T$. This indicates that the subdomain at the hot end, with $T=T_o+\Delta T$, must be depinning first, and in turn triggering all the other subdomains which are coupled to it. This seems plausible in light of the fact that the "hot" subdomain may have a smaller threshold current than all the other subdomains since $I_T \sim 1/T$. Thus, the temperature gradient I-V curves in Figs. 4-18a and 4-18b suggest that large type I switching domains actually consist of a number of subdomains which depin in a synchronized manner as long as no thermal gradients are present across the length of the crystal.

In order to verify the existence of these subdomains, we attempted to perform domain localization experiments on type I switching samples. This technique has been successfully used to map out the domain structure in switching Fe_xNbSe_3 crystals.[78] Unfortunately it is impossible to apply the "non-perturbing" voltage probe to type I switching samples without drastically altering the I-V characteristics. The character of the depinning switch is measurably changed regardless of how finely the probing wire is laid across the sample. Generally, a type I sample, which

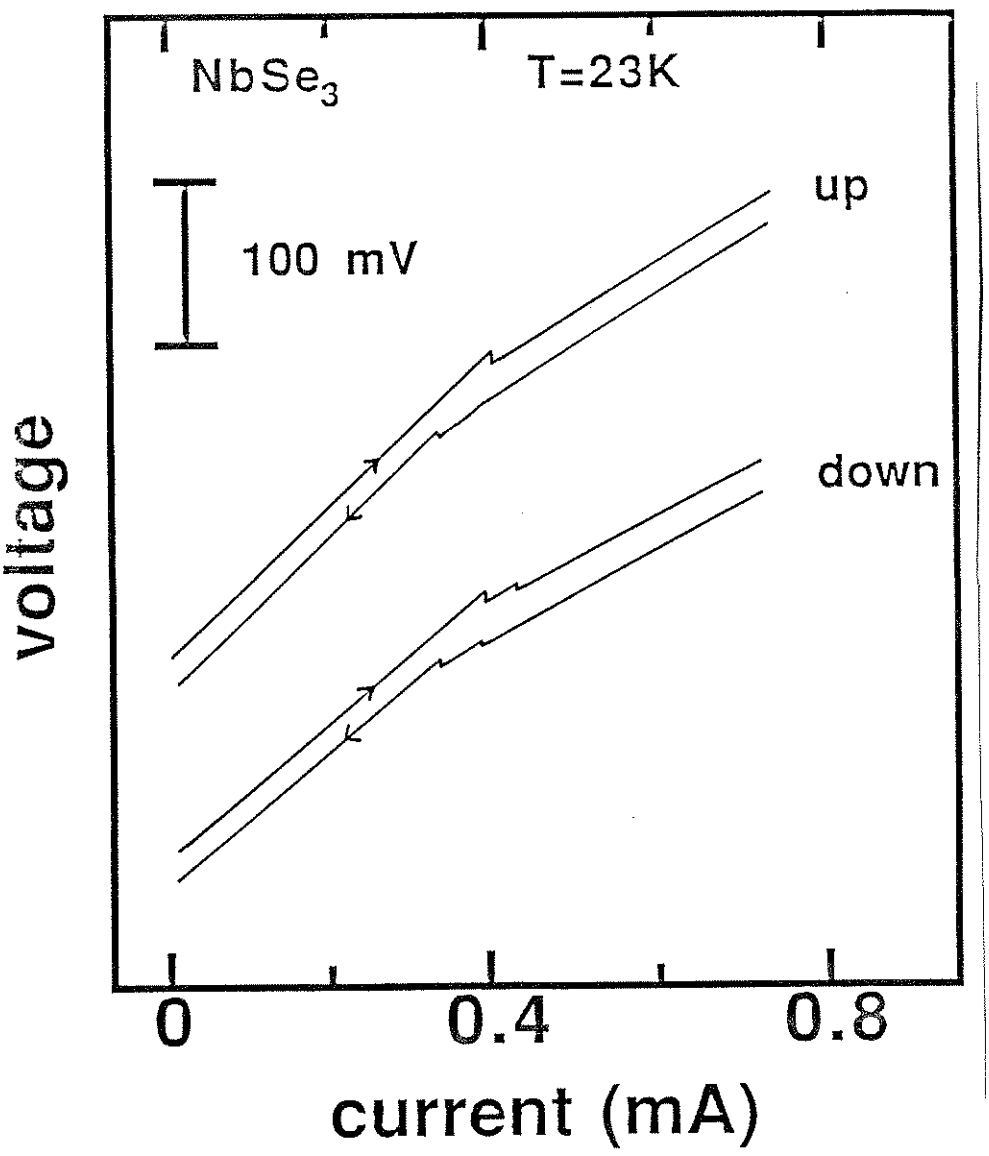

Figure 4-20 Change in I-V characteristics of a type I switching sample when a fine movable voltage probe is touching ("down") and not touching ("up") the crystal. The perturbing 0.1 mil wollaston wire was placed in the middle of the sample, half way between both end contacts. All traces have been vertically offset for clarity.

normally depins via a single large switch in the absence of the movable voltage probe, will depin via a number of much smaller switches due to the physical perturbation supplied by the probe wire in contact with it. This effect is shown in Fig. 4-20, where a type I sample which depins by way of a single switch displays two switches under the influence of the voltage probe. No temperature gradient is applied in either case. Hence, switching samples which are perturbed by a thermal gradient are also extremely sensitive to the slight mechanical stress brought on by the external probe.

The thermal gradient and probe pressure effects on type I switching samples indicate that they are composed of many small switching domains. In the absence of external perturbations, these subdomains depin in a synchronized fashion, manifesting themselves in an I-V trace as a single, large switch. Only by perturbing the system can the coupling between subdomains be reduced sufficiently to show this underlying subdomain structure. Attempts at domain localization show that the inter-domain coupling is also very sensitive to external mechanical perturbations. The existence of many subdomains in type I samples suggests that switch-causing ultra-strong impurities are closely spaced within type I samples.

4.3.2.2 Type II $NbSe_3$

The effects of an applied temperature gradient on a type II $NbSe_3$ switching sample of length L_s=1.40 mm are shown

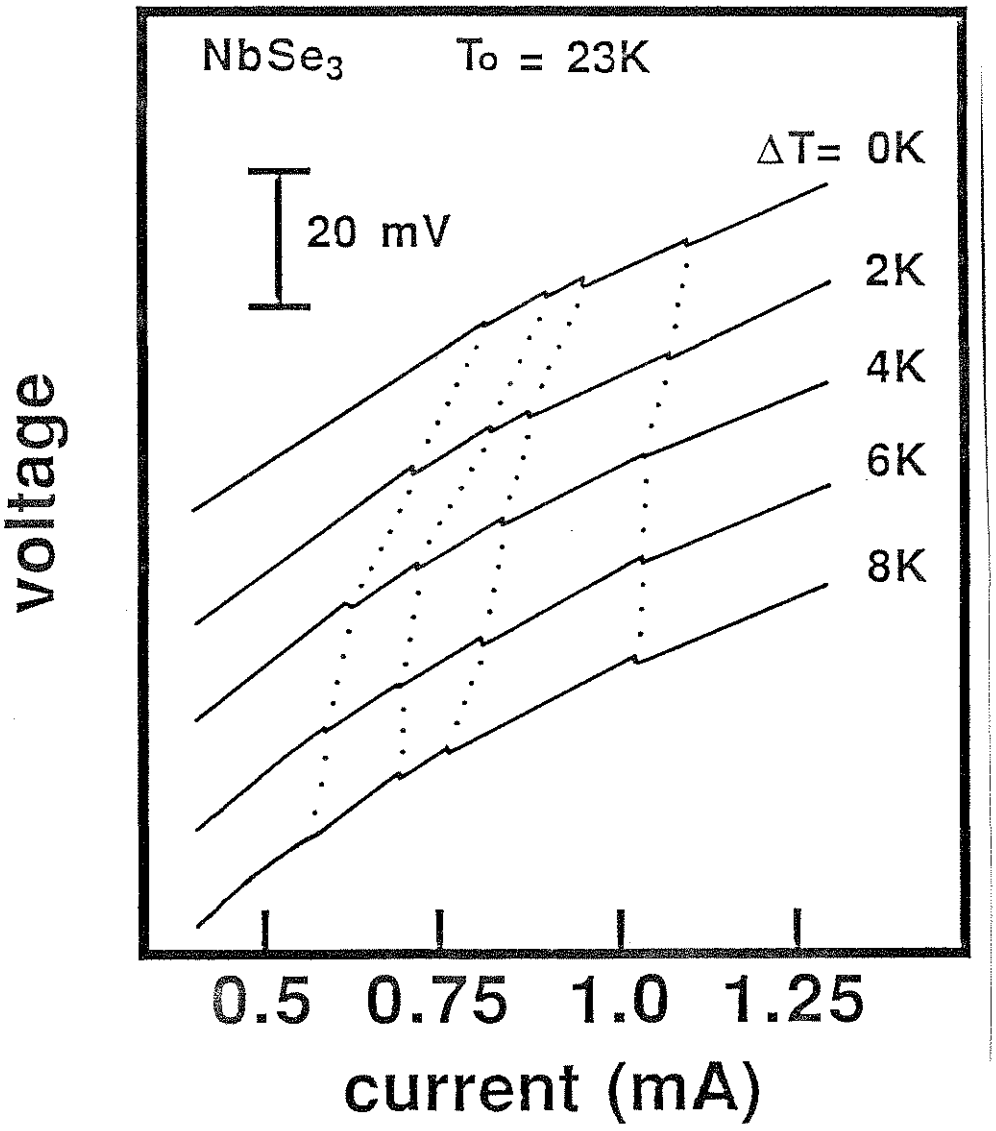

Figure 4-21 Current driven I-V characteristics in a temperature gradient for a type II $NbSe_3$ crystal. In this sample the original four switches do not divide into smaller switches when the gradient is applied. The dotted lines are guides to the eye showing the progression of switching onsets as the gradient is varied.

in Fig. 4-21. The zero gradient trace indicates that this sample depins by way of four separate switches in an isothermal configuration. As displayed in Fig. 4-21, thermal gradients do not break down these switches into a larger number of small switches. The thermal gradient only acts to move the switching onsets to lower threshold currents, as expected when each local switching domain is raised in temperature. Note that the applied gradient was sufficient to heat the first depinning domain out of the switching regime.

These data indicates that type II switching domains cannot be decoupled into subdomains even in gradients sufficient to cause decoupling in type I samples. As an example, the data in Fig. 4-18b indicates that this type I sample is divided into roughly 10 domains by a 5 K/mm gradient, while the data shown in Fig. 4-21 indicates that this type II sample consists of only four subdomains even in thermal gradients as large as 10 K/mm. Similar results have been obtained when studying other type I and type II samples. Hence, it would appear that type II zero gradient switching domains are not composed of further subdomains, in contrast to the type I samples discussed previously.

We have performed domain localization measurements on this type II sample. The localization results for the same sample as was used for Fig. 4-21 are presented in Figs. 4-22a-c. Unlike type I samples, type II switching crystals

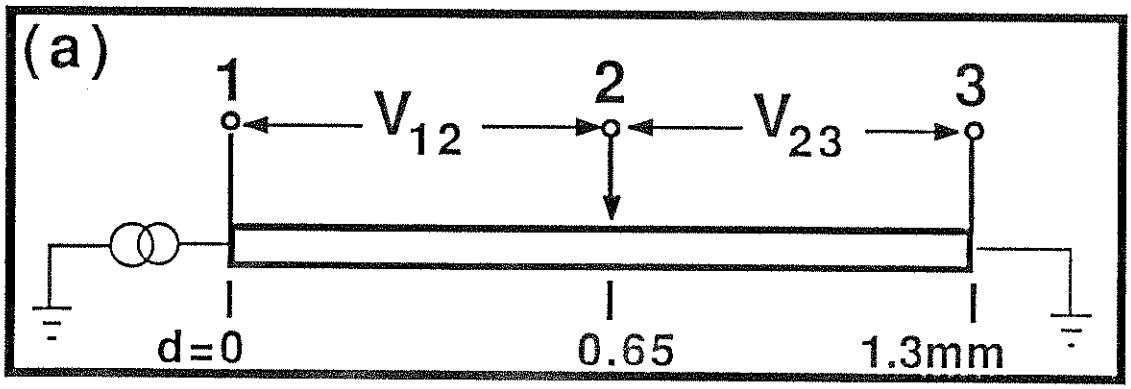

Fig. 4-22a Voltage probe configuration for I-V traces shown in Fig. 4-22b.

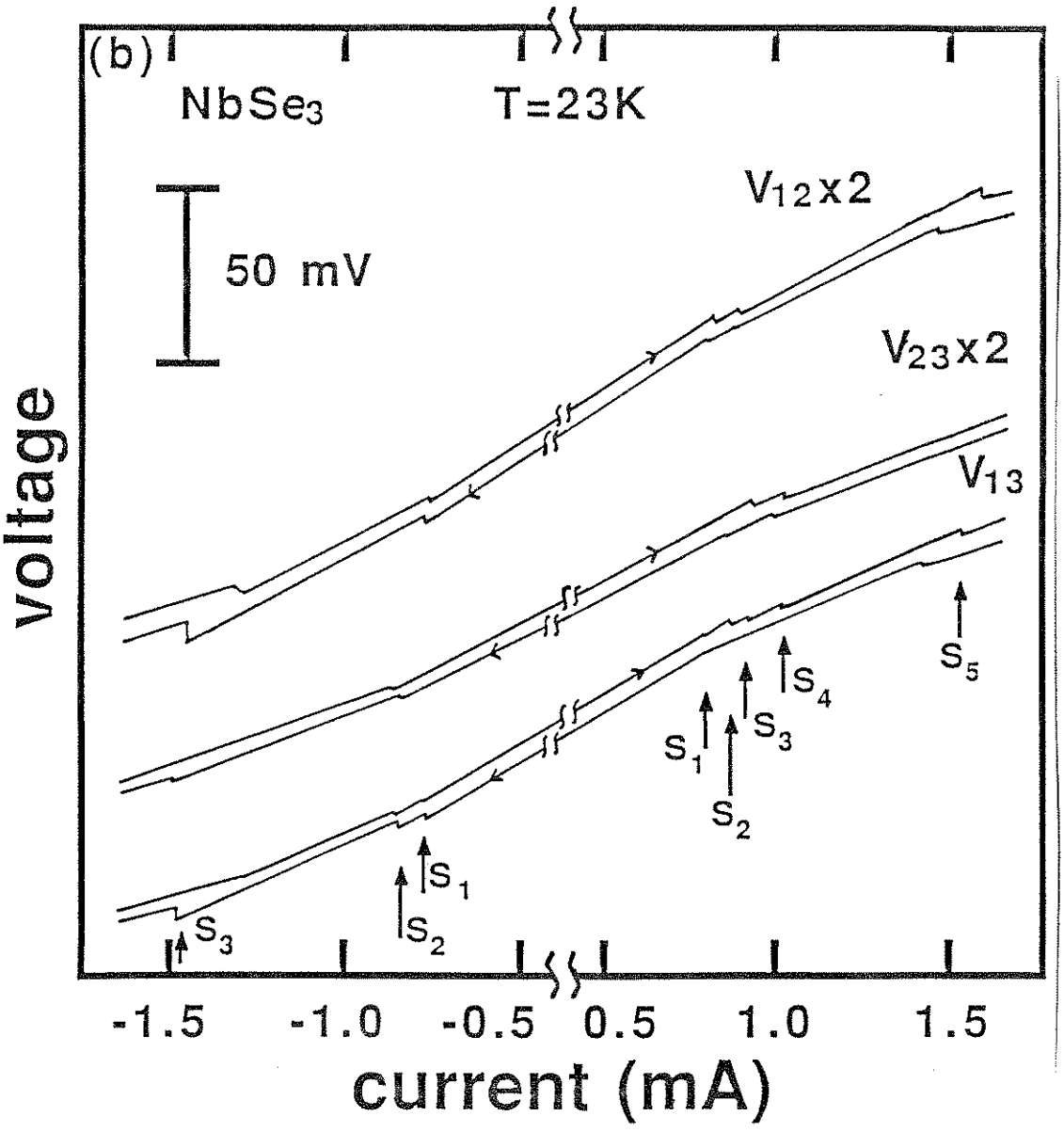

Fig. 4-22b Simultaneously recorded current driven I-V traces for different segments of a type II $NbSe_3$ switching crystal at T=23K. The traces for increasing and decreasing bias sweeps have been vertically offset for clarity.

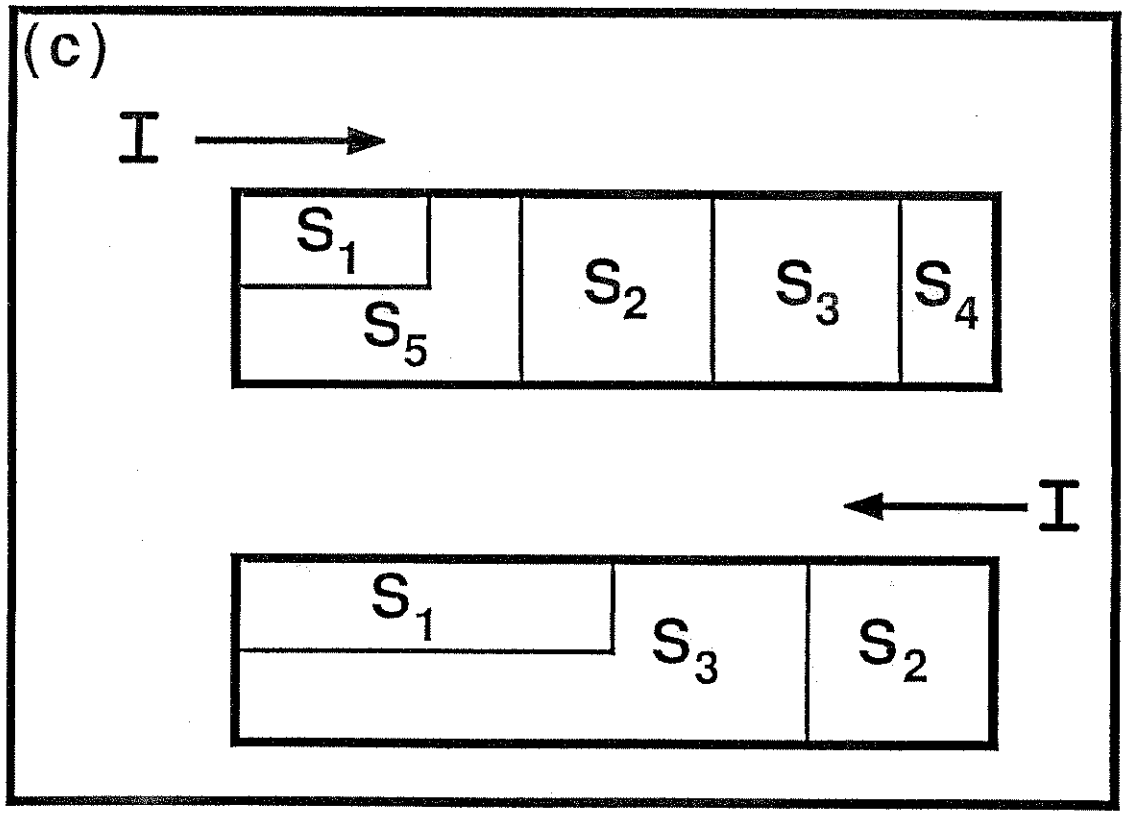

Fig. 4-22c The arrangement of the switching domains in the sample studied in Fig. 4-22b as determined by the domain localization technique. The current direction is indicated in both diagrams. The switches are labeled S_i, where the index indicates the depinning order.

are essentially unaffected by the mechanical stress that results from the placement of the movable voltage probe. The I-V measurements obtained with the movable contact positioned in the middle of the sample (as indicate in Fig. 4-22a) are depicted in Fig. 4-22b. The position of the many switching domains contained within this sample can be roughly determined by examining the I-V characteristics on either side of the adjustable contact. In order to more precisely determine the location and arrangement of these domains, eight sets of I-V curves were measured with the middle contact position ranging between contact 1 and 3. The domain arrangement determined experimentally is depicted in Fig. 4-22c. These results show a very strong current polarity dependence on the switching characteristics. With the current flowing in one direction the CDW depins by way of five switches, while when flowing in the opposite direction the CDW depins via only three switches. Note that the location of the interfaces between switching domains are also different for the two current polarities. Hence, different ultra-strong pinning sites are activated and cause switching to occur when the current flow direction is reversed. The diagram in Fig. 4-22c also indicates that the switching domains need not be serially arranged. In general, switching domains occur side-by-side transversely only if they are located adjacent to a current contact. This suggests that non-serially arranged switching domains may be a result of

irregular current injection near a current contact. The domain arrangement of Fig. 4-22c remained unchanged when a thermal gradient was applied across the sample.

The absence of temperature gradient decoupling effects in type II samples suggests that there are no subdomains in these crystals and that neighboring domains do not couple together when depinning. This is also borne out by the fact that the movable voltage probe acts in a non-perturbing manner when positioned on a crystal. Thus, type II crystals consist of a relatively small number of large switching domains which are internally homogeneous. These large domains presumably do not couple together in a synchronized depinning process due to the presence of a chemical gradient within the samples. Because the crystal is already separated into multiple domains, an applied thermal gradient is unable to break the sample into more subdomains. The chemical gradient which causes this behavior may be in the form of large variations in either the local impurity or lattice defect concentrations. In either case the data suggest that type II samples contain fewer, more widely spaced ultra-strong impurities than do type I samples.

4.3.2.3 Fe_xNbSe_3

Switching in iron doped $NbSe_3$ differs subtly from that observed in the pure material. In addition to occurring at higher temperatures, the size of the switching voltage

discontinuity ΔV in Fe_xNbSe_3 is usually not as large as in pure $NbSe_3$.[79] In type I $NbSe_3$ the switching voltage discontinuity can be as large as $\Delta V \approx 10$ mV while it is generally no more than 1 mV in Fe_xNbSe_3. Iron doped switching samples depin via single or multiple switches, show only small amounts of hysteresis, and never display any hysteretic switching sublevels. Thus, switching in Fe_xNbSe_3 belongs to the type II classification.

The results from both temperature gradient and domain localization experiments on $NbSe_3$ clearly show that these techniques can be used to infer the distribution of switching impurities within a crystal. For this reason we have applied these techniques to switching samples of Fe_xNbSe_3. In light of the fact that the incorporation of iron tends to cause switching in $NbSe_3$, these techniques should provide a means of indirectly determining the distribution of iron in this material. In particular, this study was carried out to determine if the iron is incorporated in a uniformly distributed manner or if it tends to cluster in a highly localized fashion.

The thermal gradient effects on a sample of Fe_xNbSe_3 which depins by way of a single switch is shown in Fig. 4-23. The thermal gradient only moves the switching onset to lower threshold currents and does not cause the switch to break down into a series of smaller switches. The same results have been obtained on other samples of Fe_xNbSe_3 which depin

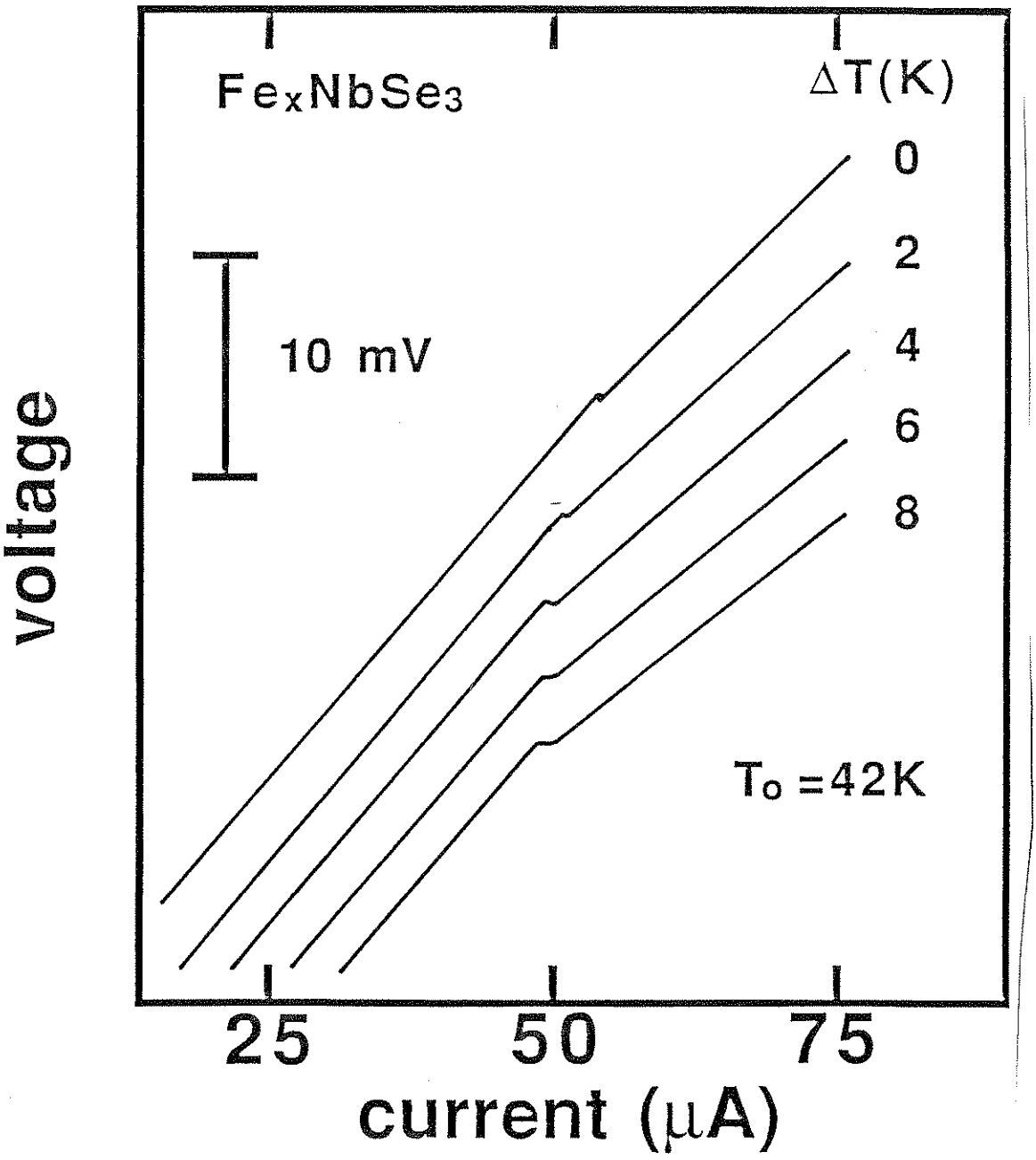

Figure 4-23 Thermal gradient effects on Fe_xNbSe_3. The cold end of the sample was held fixed at T_o=42 K while the hot end was heated to $T_o+\Delta T$.

via more than one switch. These results suggest that iron doped samples consist of widely spaced impurities and large switching domains.

To more directly determine the domain structure of this sample we performed a domain localization experiment similar to the one described above for type II $NbSe_3$. A typical set of I-V traces are shown in Fig. 4-24b, with the movable probe positioned as indicated in Fig. 4-24a. Localization traces indicate that five-eighths of the sample consists of a switching domain (the hatched region in Fig. 4-24a). The remainder of the sample does not cause a discontinuity in the sample voltage when it depins (both of these domains depin at roughly the same threshold current). These results are similar to those of previous studies of Fe_xNbSe_3.[78] In all cases, Fe_xNbSe_3 is far less affected by the movable voltage probe than are samples of type I $NbSe_3$.

These results show that iron doped switching samples contain large switching domains, indicating that the switch-causing impurities in Fe_xNbSe_3 are widely separated. This suggests that the iron is not uniformly incorporated into the doped $NbSe_3$. Switching in Fe_xNbSe_3 is characterized by large switching domains, no domain coupling, and no external perturbation effects.

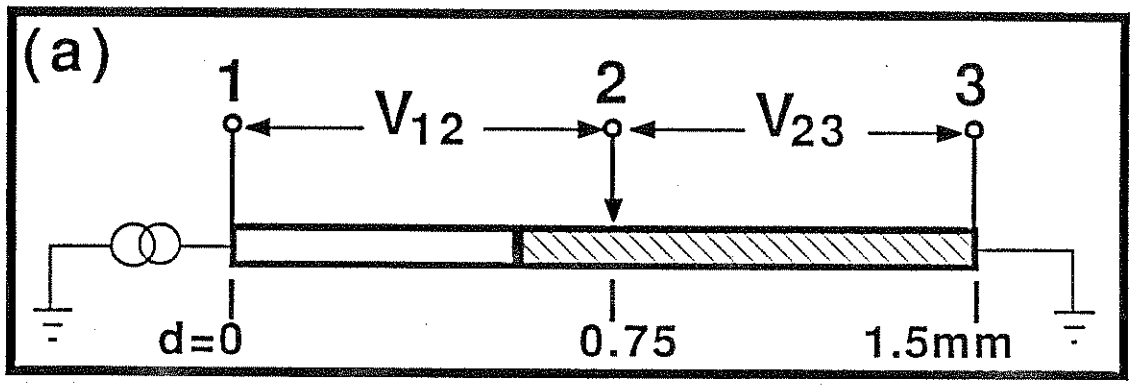

Fig. 4-24a Voltage probe configuration for I-V traces shown in Fig. 4-24b.

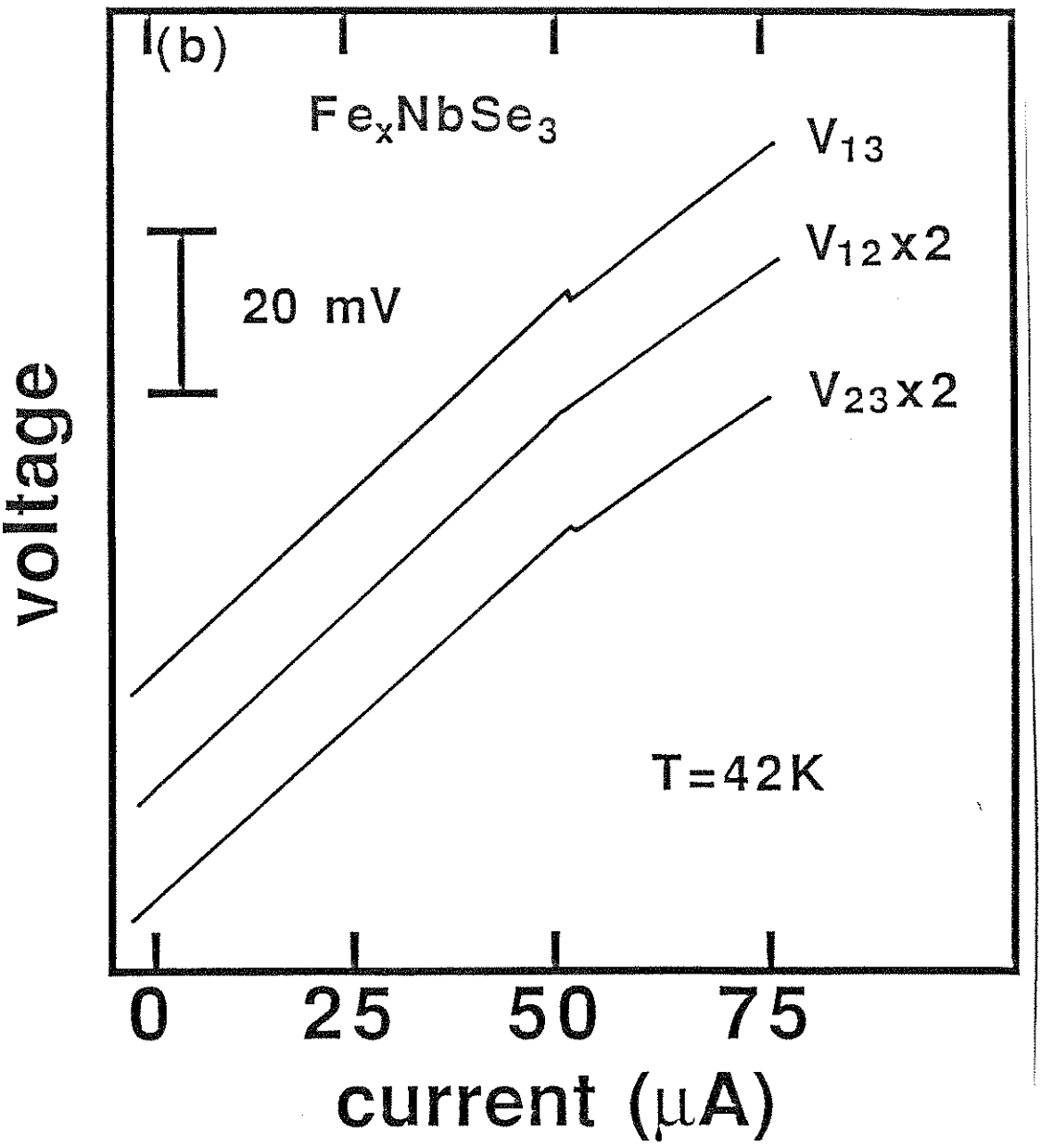

Fig. 4-24b Simultaneously recorded current driven I-V traces for different segments of a Fe_xNbSe_3 crystal at T_o=42 K. In this instance the non-perturbing contact was located near the interface between the two CDW domains.

4.3.3 Analysis

The data presented here is in agreement with earlier work which indicated that the sliding CDW in switching samples breaks up into separate and distinct phase-velocity coherent domains.[78,79] Each switching domain depins at a unique threshold field and moves at a unique field-dependent velocity. This means that discontinuities in the CDW velocities must exist at the interface between adjacent switching domains. This requires that a phase-slip center must exist in the region between the neighboring domains in order to tie together the CDW phase across this interface. CDW amplitude dynamics must play an important role in this phase-slip process. We consider the Fukuyama-Lee-Rice CDW dynamic phase Hamiltonian[32]

$$H = \frac{\kappa}{2}\int d^3x \; |\nabla\phi|^2 + W_o\rho_a \sum_i \cos[2k_F x_i + \phi(x_i)] + \int \frac{e\rho}{2k_F}\,\phi E \; dx \qquad (4.49)$$

where κ is the CDW elastic constant, W_o is the impurity potential, and ρ is the charge density. The three terms in Eqn. 4.49 are related to the CDW phase elasticity, the CDW interaction with impurities at x_i, and the CDW interaction with an external electric field E, respectively. This expression intentionally neglects any fluctuations in the CDW

amplitude, assuming instead that the amplitude is always constant. This Hamiltonian cannot describe the CDW in the vicinity of a phase-slip center because it is invalid in the limit of large phase polarization $\nabla\phi$. To see this, consider a moving CDW domain d_1 ($v_1>0$) adjacent to a nonmoving domain d_2 ($v_2=0$). The CDW phase will become highly polarized and distorted in the interface region between d_1 and d_2 as the CDW phase piles up there. This phase pile-up and distortion will effect the system in two ways. First, the large phase polarization in the interface region will force the CDW amplitude to collapse there. This comes about because the phase polarization effectively changes the CDW wave vector. The CDW amplitude is determined by balancing the lattice energy cost of the Peierls distortion against the electronic energy gained from forming the CDW; the CDW amplitude must diminish when the CDW wave vector is distorted away from $Q=2k_F$. Hence, the CDW amplitude must collapse due to the strong build-up of phase distortion in the interface region between the two domains. When the amplitude is collapsed the CDW phase can jump by a factor of 2π so as to reduce the phase distortion, thus completing a cycle of the phase-slip process.[81] The large phase polarization will also act as a pinning force on the moving CDW domain; only because of the periodic collapse of the CDW amplitude in the interface region can the domain continue to slide. Thus, the CDW velocity discontinuities in switching crystals suggest that

amplitude dynamics as contained in the phase-slip process are very important in switch depinning.

To insure that the phase-slip process is the primary cause of switching, we must again consider a pair of neighboring domains d_1 and d_2, where in this case domain d_1 is only weakly pinned while the small domain d_2 is pinned so strongly that it cannot be depinned by an electric field. When an electric field is applied to this domain system the phase in d_1 will become polarized in the direction of d_2. Because the CDW in d_2 is pinned, domain d_1 will not depin in the usual fashion even when the bias field exceeds its weak pinning threshold field. As the bias is increased further the phase polarization in the interface between the two domains will increase until $\nabla\phi$ is so large that the CDW amplitude in the interface must collapse. At this point the polarization pinning forces holding d_1 back disappear and the domain can depin; it will switch to a high field state because the bias necessary to cause the amplitude collapse is far higher than the weak pinning threshold field. At the same time, the phase in the interface region is free to change so as to relieve the phase polarization stress. The phase will slip by a factor of 2π to relieve the stress while still minimizing the impurity potential energy of domain d_2. After this phase-slip process the CDW amplitude will reform (because the phase difference has been reduced by 2π), and the CDW polarization will again increase, leading to another

sequence of the phase-slip process. Thus, switching can be accounted for by the phase-slip process which must occur between adjacent CDW sections which move at dissimilar velocities. Switching occurs because of the coupling between neighboring domains which is in the form of phase polarization. This phase polarization acts to create a large pinning force on weakly pinned domains which only disappears when the polarization requires the CDW amplitude to collapse. Once the amplitude collapses the CDW switches to a high field state and the CDW phase slips by 2π. The CDW amplitude subsequently reforms and the phase-slip process is repeated.[79-81]

The phase-slip switching mechanism requires there to be small regions where the CDW is strongly pinned to the lattice. This is corroborated by the fact that switching can be induced in $NbSe_3$ by iron doping, or in $K_{0.3}MoO_3$ by irradiation damage. These results suggest that the presence of impurities within a crystal play an important role in creating switch-causing phase-slip centers. The most energetically efficient phase-slip process consists of the formation of phase vortices.[42] In this type of phase-slip process the CDW velocity discontinuities are relieved by a stream of phase vortex cores which run perpendicular to the direction of CDW motion. The energy of a single phase vortex is[79]

$$E_{\text{phase-slip}} = N_o \Delta^2 \xi^3 [1 + \alpha \ln(L_o/\xi)] \qquad (4.50)$$

where $\alpha \equiv \kappa/(N_o \Delta^2 \xi^2)$, N_o is the density of states at the Fermi surface, Δ is the CDW energy gap, κ is the CDW elastic constant, L_o is the CDW phase coherence length, and ξ is the amplitude coherence length. The first term in Eqn. 4.50 corresponds to the energy of the vortex core while the second term relates to the phase distortion in the vicinity of the vortex. This phase-slip energy is far greater than the impurity pinning strength of conventional weak or strong impurities. Hence, the phase-slip centers in switching CDW crystals must be created by the presence of far stronger impurities which we call ultra-strong impurities.[78,79] These ultra-strong impurities could consist of extremely large strong impurity concentrations; they might also be a result of dislocation lines or, in the case of Fe_xNbSe_3, phase inclusions. Regardless of their exact physical nature, ultra-strong impurities so strongly pin the CDW near them that they create phase-slip centers which in turn cause weakly pinned neighboring sections of CDW to undergo switch depinning.

The development of a complete model of CDW switching dynamics necessitates a system Hamiltonian which includes both CDW phase and amplitude dynamics. Such a Hamiltonian has not yet been established. Here we consider a simple

dynamical model[80,81] of switching based on the physical mechanisms involved in the phase-slip process discussed above.[84] The model can be understood by considering a weakly pinned CDW domain d_1 adjacent to a small section of CDW d_2 which contains an ultra-strong impurity. In addition to the usual weak pinning forces, domain d_1 will also be pinned by a polarization force due to the coupling between the two domains. This force will depend on the phase difference $\phi_1-\phi_2$ as well as the CDW amplitude Δ_2 at the ultra-strong impurity. This CDW amplitude will also depend on this phase difference $\phi_1-\phi_2$; Δ_2 will decrease as the phase polarization increases. Lastly, the phase ϕ_2 in the impurity domain d_2 is completely pinned by the ultra-strong impurity situated within it. Hence, ϕ_2 is constant when Δ_2 is non-zero; when Δ_2 drops to zero because of phase polarization, ϕ_2 can hop by a factor of 2π to relieve the phase polarization forces on both domains. A discrete set of hydrodynamical equations which embody these physical mechanisms are given by[80,81]

$$\frac{d\phi_1}{dt} = e - \sin\phi_1 - \alpha\Delta_2(\phi_1-\phi_2) \tag{4.51}$$

$$\phi_2 = \begin{cases} \phi_2 & \Delta_2>0 \\ \phi_2+2\pi & \Delta_2=0 \end{cases} \tag{4.52}$$

$$\Gamma\frac{d\Delta_2}{dt} = 1 - \Delta_2 - \left(\frac{\phi_1-\phi_2}{\theta}\right)^2 \tag{4.53}$$

where e ($\geq$0) is the applied electric field, α is the phase mode elasticity coefficient ($\alpha=2/\varepsilon$ where ε is the Fukuyama-Lee pinning parameter[32]), Γ is the amplitude mode relaxation rate relative to that of the phase mode, and θ is the amplitude mode elasticity coefficient. These equations successfully predict hysteretic CDW switching behavior.[80] In addition, numerical calculations which include the effects of an applied ac field in addition to a dc field indicate that these equations also successfully predict period doubling routes to chaos, inductive ac response, and mode locking.[81] Thus, the phase-slip model of switching as expressed in Eqns. 4.51-53 provides a simple yet realistic dynamical model of CDW switching. Switching occurs in this model due to the large phase polarization and subsequent amplitude collapse which arises from the extreme phase pinning at an ultra-strong impurity site.

With the fundamental physical principles of switching in mind, we now analyze the experimental results presented in section III in order to determine the way in which the switch-causing ultra-strong impurities are distributed in switching crystals. We also wish to establish the effect this distribution has on the I-V characteristics of switching samples.

The thermal gradient effects on the type I sample depicted in Fig. 4-18a indicates that a temperature

difference as small as 2K is sufficient to break a phase-velocity coherent switching domain into four subdomains over a distance of only 300 μm. This length is far smaller than the sample length required for a thermal gradient to divide this type of domain in a non-switching sample of $NbSe_3$.[50-54] The much larger effect in type I switching samples clearly indicates that CDW impurity pinning is non-uniform within type I switching domains. These apparently coherent switching domains must actually consist of a number of coupled subregions with an average length of not more than 60 μm. These subregions are separated by ultra-strong pinning centers which give rise to switching behavior. In a non-switching crystal, the absence of ultra-strong impurities allow large velocity-coherent domains to stay coupled in the presence of relatively large thermal gradients.

The conventional switching behavior of type II samples is well accounted for by the phase slip model of switching described by Eqns. 4.51-53.[81] Subdomain coupling and avalanche depinning as observed in type I switching samples can be accounted for by an extension of this model.[85] We consider a long chain of neighboring domains $d_1 d_2 \ldots d_n$. Each domain is separated from its neighbors by an ultra-strong pinning site US_i which pins the CDW phase in the interface (US_i lies between domains d_i and d_{i+1}). By extending the dynamical phase-slip equations (Eqns. 4.51-53) we have the

following set of differential equations which describe the dynamics of this chain of subdomains:

$$\frac{d\phi_i}{dt} = e - V_i \sin \phi_i - \Delta_{i-1}\alpha_{i-1}(\phi_i - \psi_{i-1}) - \Delta_i \alpha_i (\phi_i - \psi_i) \quad (4.54)$$

$$\psi_i = \begin{cases} \psi_i & \Delta_i > 0 \\ \psi_i + 2\pi & \Delta_i = 0 \end{cases} \quad (4.55)$$

$$\Gamma \frac{d\Delta_i}{dt} = 1 - \Delta_i - \left(\frac{\phi_i - \psi_i}{\theta_i}\right)^2 - \left(\frac{\phi_{i+1} - \psi_i}{\theta_i}\right)^2 \quad (4.56)$$

where e (≥ 0) is the applied electric field, V_i is the weak impurity strength in domain d_i, α_i is the phase elasticity coefficient associated with the impurity US_i, Γ is the amplitude relaxation rate relative to that of the phase mode, and θ_i is the amplitude elasticity coefficient at the site US_i; the phase of domain d_i is ϕ_i, while the phase and amplitude of the site US_i are given by ψ_i and Δ_i respectively. Eqn. 4.54 indicates that the phase in domain d_i is pinned by polarization forces stemming from the ultra-strong impurities on either side of it. Similarly, Eqn. 4.56 indicates that the CDW amplitude at an impurity site US_i, Δ_i, is affected by the phase polarization between it and the two weakly pinned domains which it lies between. In the absence of coupling, each subdomain would have an intrinsic switching threshold field E_i; for simplicity we

assume that domain d_1 depins first ($E_1<E_{i\neq1}$). In the presence of an electric field $E<E_1$ directed from d_1 to d_n, the CDW in each domain becomes polarized in the direction of the field. As indicated by Eqn. 4.54, there will be three pinning forces acting on each domain d_i: $F_i=f_w+f_{i-1}+f_i$, where f_w is due to weak impurities while f_i and f_{i-1} are due to the CDW phase contraction and elongation at the ultra-strong pinning sites in front of and behind the domain, respectively. When E exceeds E_1, Δ_1 will go to zero and domain d_1 depins. The periodic collapse of the CDW at US_1 will periodically eliminate one half of the phase distortion pinning force acting on d_2 (f_1 will go to zero). This reduction of the pinning force acting on the CDW in domain d_2 may allow it to also depin. If this occurs, the same coupling process can depin domain d_3, then d_4 and so on. Thus, a domain d_i can be triggered to depin when domain d_{i-1} depins if the initial depinning field E_1 is sufficient to overcome the reduced pinning force $F_i=f_w+f_i$. This process of synchronized, triggered depinning is a direct result of the coupling that occurs between neighboring domains when the CDW amplitude collapses at the ultra-strong pinning site which lies between them.

To quantitatively show that the phase-slip model can account for synchronized depinning we have numerically integrated a subset of Eqns. 4.54-56. This subset consists of two weakly pinned domains and two ultra-strong impurity

sites arranged serially in the following manner: d_1-US_1-d_2-US_2. The equations which describe the dynamics of this system are

$$\frac{d\phi_1}{dt} = e - V_1 \sin \phi_1 - \Delta_1 \alpha_1 (\phi_1 - \psi_1) \tag{4.57}$$

$$\frac{d\phi_2}{dt} = e - V_2 \sin \phi_2 - \Delta_1 \alpha_1 (\phi_2 - \psi_1) - \Delta_2 \alpha_2 (\phi_2 - \psi_2) \tag{4.58}$$

$$\psi_1 = \begin{cases} \psi_1 & \Delta_1 > 0 \\ \psi_1 + 2\pi & \Delta_1 = 0 \end{cases} \tag{4.59}$$

$$\Gamma \frac{d\Delta_1}{dt} = 1 - \Delta_1 - \left(\frac{\phi_1 - \psi_1}{\theta_1}\right)^2 - \left(\frac{\phi_2 - \psi_1}{\theta_1}\right)^2 \tag{4.60}$$

$$\psi_2 = \begin{cases} \psi_2 & \Delta_2 > 0 \\ \psi_2 + 2\pi & \Delta_2 = 0 \end{cases} \tag{4.61}$$

$$\Gamma \frac{d\Delta_2}{dt} = 1 - \Delta_2 - \left(\frac{\phi_2 - \psi_2}{\theta_2}\right)^2 \tag{4.62}$$

where ϕ_1 (ϕ_2) is the phase of domain d_1 (d_2), and ψ_1 (ψ_2) and Δ_1 (Δ_2) are the phase and amplitude of impurity site US_1 (US_2) respectively. For simplicity we assume that the parameters which characterize the weakly pinned domains are exactly the same while the strengths of the two ultra-strong pinning sites are different. This is manifested in the model by the two different amplitude elasticity constants θ_1 and θ_2 (stronger pinning leads to a softer amplitude mode and a smaller elasticity constant). The two weakly pinned domains have the same pinning potentials (V_1=V_2) as well as the same

phase elasticity constants ($\alpha_1=\alpha_2=0.2$, corresponding to a Fukuyama and Lee pinning parameter of $\varepsilon=10$). In addition we assume that both the phase and amplitude modes have the same relaxation rates ($\Gamma=1$). The calculated I-V characteristics of this CDW system are depicted in Fig. 4-25 with two sets of amplitude elasticity constants. In Fig. 4-25a the impurity in US_2 is weaker than that in US_1 ($\theta_1=10\pi$, $\theta_2=15\pi$). The I-V curve clearly shows that this set of parameters leads to two independent, unsynchronized depinnings. The depinning of d_1 is unable to trigger d_2 because the amplitude mode in US_2 is far stiffer than the amplitude mode of US_1. In Fig. 4-25b the impurities in both ultra-strong pinning sites are the same ($\theta_1=10\pi$, $\theta_2=10\pi$). In this case synchronized depinning does occur. Domain d_2 is able to depin when domain d_1 depins because both ultra-strong pinning sites are of similar strength. In general, domain d_2 is triggered to depin by the depinning of d_1 as long as $\theta_2 \leq \theta_1$. Hence, the phase-slip model of switching can successfully account for both synchronized and unsynchronized subdomain switch depinning.

The triggered depinning process involves a simple linear coupling, and as a result, a chain of synchronized domains will be highly susceptible to the effects of external perturbations. Considering again the chain of n subdomains, if the coupling between domains d_i and d_{i+1} were to break down, all the domains $d_{j>i}$ would no longer take part in synchronized depinning. The fragile nature of the avalanche

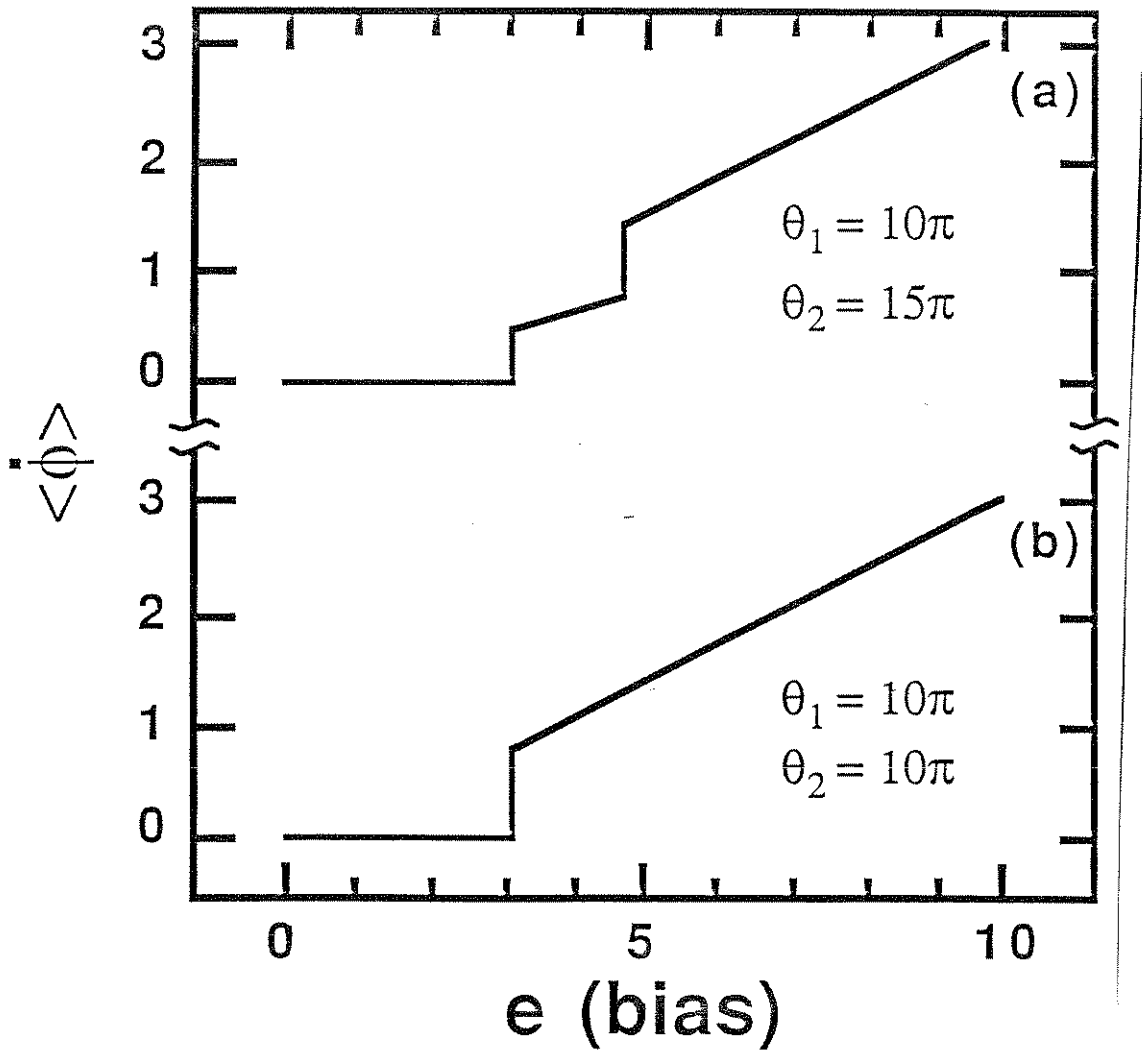

Figure 4-25 I-V characteristics obtained by integrating the two domain phase-slip equations (Eqns. 4.57-62) using two different values for the amplitude elasticity coefficient of the second phase-slip center: (a) $\theta_2=15\pi$, and (b) $\theta_2=10\pi$. In both cases the other parameters are $V_1=V_2=1.0$, $\theta_1=10\pi$, $\alpha_1=\alpha_2=0.2$, and $\Gamma=1.0$.

process indicates why type I samples are so highly affected by external perturbations. In particular, a thermal gradient destroys the long coupled chain of subdomains which cause large type I switches because it changes the depinning conditions along the length of the crystal. As a result, a given subdomain may no longer be triggered to depin by its neighbor's depinning. Similarly, type I switches are highly perturbed when a fine wire is lightly pressed to a sample because the resulting mechanical stress can have a strong effect on the coupling between adjacent subdomains. The data in Fig. 4-20 suggests that the presence of the perturbing wire in the middle of that crystal destroys the coupling between subdomains near the wire. The sublevels which have been observed in hysteretic type I switches must also arise from the fragile coupling which exists between subdomains.[69] Sublevels are created when coupling intermittently breaks down between subdomains along a type I chain of coupled subdomains. This intermittent break may result from subtle temperature or electric field fluctuations.

Type II $NbSe_3$ and Fe_xNbSe_3 samples show no synchronized depinning effects. In particular, the switches that occur in these materials are unperturbed by either thermal gradients or the mechanical stress brought on by a movable voltage probe. This indicates that there is actually no coupling between neighboring domains in these materials. Hence, neighboring domains are completely independent and depin

according to their local conditions. It is important to note that the CDW pinning strengths of the impurities which cause switching in type II $NbSe_3$ are similar to those found in type I samples. This is evident from the fact that the switching threshold fields are roughly the same in these two classes of switching $NbSe_3$. Thus, the lack of domain coupling in type II samples cannot be attributed to stronger pinning in those crystals.

A typical type II switching domain is much larger than the small subdomains which give rise to switching in type I $NbSe_3$. This is evident in the results presented in the previous section; in samples of roughly equal length, a type I $NbSe_3$ crystal was composed of ten switching domains while the type II sample consisted of four domains. This indicates that the separation between the ultra-strong impurities has a direct bearing on whether or not neighboring domains can couple together when depinning. To clarify the situation, we define a length scale L_{us} which is the average distance between neighboring ultra-strong impurities; in addition, L_c is defined as the critical separation beyond which adjacent domains do not interact. Within this framework type I samples are characterized by $L_{us}<L_c$. In this case coupling does occur between adjacent domains and this causes synchronized depinning and the many effects associated with it (i.e., large switches, sublevels, ΔT switch break up). Both type II samples of $NbSe_3$ and all samples of Fe_xNbSe_3

correspond to $L_{us}>L_c$. In this case there can be no switch domain coupling. As a result, the switches in these samples are unaffected by external perturbations.

There are two possible explanations for why the coupling mechanism can break down when $L_{us}>L_c$. First, it may be that when created in the crystal growth process, closely spaced impurities have equivalent pinning strengths, while the strengths of widely separated impurities differ considerably. Secondly, it is also possible that the coupling effects on a domain decrease as the domain becomes larger; the reduction in the pinning force on a large domain due to the periodic collapse of the CDW at the interface with a depinned neighbor might not be a large enough effect to allow synchronized depinning. A combination of these two effects is probably influential in undermining the coupling mechanism between large type II domains. Regardless of the underlying mechanisms, the behavior of many type I and type II $NbSe_3$ samples indicates that the critical ultra-strong impurity separation is roughly $L_c \approx 200\mu m$.

4.3.4 Conclusion

The widely varying I-V characteristics observed in $NbSe_3$ switching samples can be accounted for by differences in the distribution of the ultra-strong impurities which cause switching. When the impurities are closely spaced, coupling can occur between adjacent switching domains. This

allows a depinning wave to move along the length of the crystal, creating a large switch in the I-V curve. The mechanism which links neighboring domains is fragile and is easily destroyed by the application of external perturbations. Conversely, widely spaced impurities do not allow adjacent domains to interact. With no inter-domain coupling, these materials depin via a number of small switches which are unaffected by external perturbations. Hence, we propose that the drastically different behavior observed in type I and type II switching samples is simply a manifestation of the different distributions of ultra-strong impurities contained within them.

Iron doped $NbSe_3$ displays only small switches which are unaffected by external perturbations. These samples show no synchronized depinning behavior. This indicates that the impurities in Fe_xNbSe_3 are widely spaced. No coupling occurs between adjacent domains and each switching domain behaves independently of the other domains.

These results have important implications for the physical arrangement of the impurities which cause switching. In the case of iron doped $NbSe_3$, these impurities are not plentiful. This suggests that the iron dopant is not uniformly distributed throughout a crystal. With regard to pure $NbSe_3$, the ultra-strong impurities can be quite plentiful, giving rise to type I behavior, or extremely sparse, resulting in type II behavior. The closest

separation between adjacent impurities inferred from thermal gradient experiments is $L_{us} \approx 40$ μm which is roughly in line with the density of grain boundaries and twinning defects observed in $NbSe_3$.[86] Further research employing TEM and advanced microprobe analysis is needed to determine the precise nature of the impurities which cause switching in $NbSe_3$.

Chapter 5: Noise and ac-dc interference phenomena in the charge density wave conductor $K_{0.3}MoO_3$

5.1 Introduction

The study of the dynamical properties of the sliding charge density wave (CDW) state in quasi-one-dimensional materials began in 1976 when Monceau, *et al.* first discovered that the CDW in $NbSe_3$ could be depinned by applying a small dc electric field along the crystal chain axis.[1] Since this initial discovery, a great deal of work has been performed by many researchers in an attempt to understand the transport properties of the dynamic CDW state.[2] One of the most intriguing properties associated with CDW conduction is that of the so-called narrow band noise (NBN) oscillations which accompany the dc motion of a sliding CDW. NBN oscillations have been observed in all sliding CDW conductors.[2] The fundamental NBN frequency f_{NBN} directly scales with the charge density wave current density J_{CDW}:[3]

$$J_{CDW} = a\, f_{NBN}\,, \tag{5.1}$$

where a is a sample and temperature dependent constant. Although debate[4] continues, there is much evidence to suggest that the NBN oscillations are a bulk phenomenon, possibly originating from the CDW's interaction with the potential provided by pinning impurities.[5]

A number of unusual interference effects occur[6,7] in a charge density wave material when it is driven by combined ac and dc driving fields of the form

$$V = V_{dc} + V_{ac}\cos(\omega t) \quad . \tag{5.2}$$

The effects reflect a direct interaction between the depinned CDW oscillating at a frequency f_{NBN} and the external fields oscillating at a frequency $\omega/2\pi$.

For values of V_{ac} comparable to or larger than the CDW depinning threshold voltage V_T, the CDW can become *mode-locked* to the external signal over an appreciable range of dc bias voltage. This results in the formation of so-called Shapiro steps in the current-voltage (I-V) characteristics of the sample; the steps also appear in the sample's differential resistance.[6-8] Shapiro step interference occurs whenever the externally applied frequency $\omega/2\pi$ is related to the internal NBN frequency f_{NBN} by

$$p\,\frac{\omega}{2\pi} = q\,f_{NBN} \quad , \tag{5.3}$$

where p and q are integers.[9] The index n of a specific step is defined as n=p/q. For integer values of n, the Shapiro step forms due to the interaction between the NBN fundamental f_{NBN} (q=1) and the nth harmonic of the external signal; this

is referred to as a harmonic Shapiro step. For non-integer values of n, the Shapiro step is referred to as a subharmonic step. Shapiro steps have been extensively studied in $NbSe_3$,[6-10] and to a lesser extent in TaS_3.[11]

For small values of V_{ac} ($V_{ac}<<V_T$) mode locking of the entire CDW condensate does not readily occur. Nonetheless, the sample ac conductivity is strongly affected by interference between the internal and external frequencies. The complex ac conductivity $\sigma(\omega)$ is determined by measuring the in-phase and out-of-phase response of the sample at the frequency $\omega/2\pi$ when a driving field of the form given by Eqn. 5.2 is applied, with $V_{ac} << V_T$. As the test frequency $\omega/2\pi$ or the dc bias V_{dc} is swept, interference in $\sigma(\omega)$ occurs when the conditions of Eqn. 5.3 are satisfied. Whenever $\omega/2\pi = f_{NBN}$, a dramatic "inductive" resonance occurs; this effect has been studied extensively in highly coherent $NbSe_3$ [7,10] and less extensively in $K_{0.3}MoO_3$.[12]

$K_{0.3}MoO_3$ (Potassium blue bronze) undergoes a Peierls transition at T_p=180 K which gives rise to the formation of a depinnable incommensurate CDW.[13] In addition to displaying nonlinear conductivity and NBN, this material also exhibits a low frequency (< 10 MHz) dielectric relaxation mode whose characteristic frequency is highly temperature dependent.[14,15] The mechanisms responsible for the creation of this mode are thought to be closely related to those which cause many metastable effects.[16] In the microwave region

(>100 MHz), $K_{0.3}MoO_3$ also exhibits a conductivity mode analogous to that seen in other CDW materials.[17]

Usually, $K_{0.3}MoO_3$ samples display very weak NBN spectra, indicating that the sliding state in this material is generally very incoherent.[13] In contrast, the semi-metallic CDW material $NbSe_3$ shows highly coherent behavior. Samples of these two materials are usually very different in size. $NbSe_3$ grows in fine needle-like whiskers with typical dimensions of 1 mm x 5 μm x 1 μm (volume=$5x10^{-9}$ cm^3), whereas blue bronze samples are far larger, with typical dimensions of 1mm x 0.5 mm x 0.25 (volume=$1.25x10^{-4}$ cm^3). Hence, a typical blue bronze sample which displays weak NBN is also five orders of magnitude larger in volume than a typical highly coherent $NbSe_3$ crystal. This suggests that NBN generation is in general a finite size effect in CDW materials, as has been suggested for $NbSe_3$.[5] For this reason, we examine extremely thin samples of $K_{0.3}MoO_3$ here, with typical volumes of 10^{-8} to 10^{-7} cm^3, in order to observe strong CDW coherence effects. We find that these samples do indeed display a highly coherent dynamic CDW response.

We find that extremely thin, optically transparent single crystals of $K_{0.3}MoO_3$ display NBN spectra of exceptional quality.[18] When examined in the presence of combined ac and dc driving fields, the crystals exhibit both strong mode locking in differential resistance (dV/dI) traces and large resonance anomalies in the complex frequency

dependent conductivity.[18,19] We have measured the Shapiro step spectrum as a function of both applied ac amplitude and frequency (10 to 100 kHz), and find reasonable agreement between the data and a simplified classical single-particle CDW equation of motion.[20] The analysis suggests that the external fields couple to the *low frequency dielectric relaxation mode*[14] rather than to the high frequency pinned phason mode. We have also investigated the ac-dc interference effects on the complex ac conductivity $\sigma(\omega)$ ($\omega/2\pi < 1$ MHz). Large and narrow inductive dips occur when the external frequency equals the narrow band noise frequency. We show that this resonance phenomenon appears analogous to that present in the response of a phase shifted resonant harmonic oscillator. The highly coherent response of the samples examined in this study provides a means of accurately measuring the CDW current density to NBN frequency ratio; we find that the empirically determined value implies a pinning potential periodicity equal to the CDW wavelength.

The remainder of this chapter is organized as follows: A description of both sample preparation techniques and experimental methods are presented in Sec. 5.2. Experimental results are given in Sec. 5.3, followed by an analysis in Sec. 5.4. Lastly, we briefly summarize our findings and present concluding remarks in Sec. 5.5.

5.2 Sample preparation and experimental techniques

Single crystals of $K_{0.3}MoO_3$ were obtained using an

electrochemical growth technique[21] which produces high quality crystals with typical dimensions of 2 mm x 1 mm x 1 mm. Extremely thin, optically transparent samples were prepared by first cleaving a large crystal down to a thickness of roughly 200 μm. The cleaved face was then glued to a sapphire substrate with a cryano-acrylic adhesive ("super glue"). The mounted crystal was then cleaved still further using the "scotch tape" method, until a transparent piece was obtained. By following this procedure, we have been able to obtain samples with uniform thicknesses ranging from 0.1 μm to 1 μm and areas of up to 1 mm^2. The sample used to study ac-dc interference effects in blue bronze was determined to be 0.2 μm thick by using a Tencor Instruments step height analyzer; the sample's complete dimensions were 0.625 mm x 0.5 mm x 0.2 μm (volume=6.25×10^{-8} cm^3), with the b axis directed along the largest dimension. Electrical contacts were made to this sample via evaporated indium pads and silver conducting paint. The two probe room temperature resistivity was found to be $\rho_{RT} = 3.5 \times 10^{-4}$ Ω cm. All measurements presented in this chapter were made by using a two-probe current-driven configuration. For comparative purposes, all data presented in this chapter are from the same $K_{0.3}MoO_3$ sample. We have obtained qualitatively similar results on all sub-micron blue bronze samples that we have examined.

Current-driven narrow band noise spectra were measured

with an HP 8558B spectrum analyzer. Shapiro steps were obtained by simultaneously driving the sample with both a dc and an ac ($\omega/2\pi$ = 10 to 100 kHz) current. The differential resistance dV/dI was measured via a low frequency bridge with lock-in detection of a low frequency (280 Hz) modulation signal.

The complex ac conductivity $\sigma(\omega)$ (both frequency and dc bias dependent) was measured at frequencies between 100 Hz and 1 MHz by a computer controlled HP 4192A impedance analyzer. The ac amplitude was always kept well below the CDW depinning voltage so that the ac signal would act only as a probe of the sample's conductivity. The evaporated indium contacts were found to be of high quality by analyzing the sample response in the complex impedance plane.[14]

Our experiments were performed at 77K to facilitate a comparison of the data with other previously published results. The extremely fragile crystals were slowly cooled in a helium gas flow system to prevent fracturing them during the cool-down process. The helium gas flow system also provided stable temperature control.

5.3 Experimental results

The NBN spectrum produced by a 0.2 μm thick blue bronze specimen at 77 K is presented in Fig. 5-1. The spectrum exhibits a sharp fundamental at f_{NBN} = 70 kHz, as well as four higher harmonics at 140, 220, 280, and 360 kHz. This

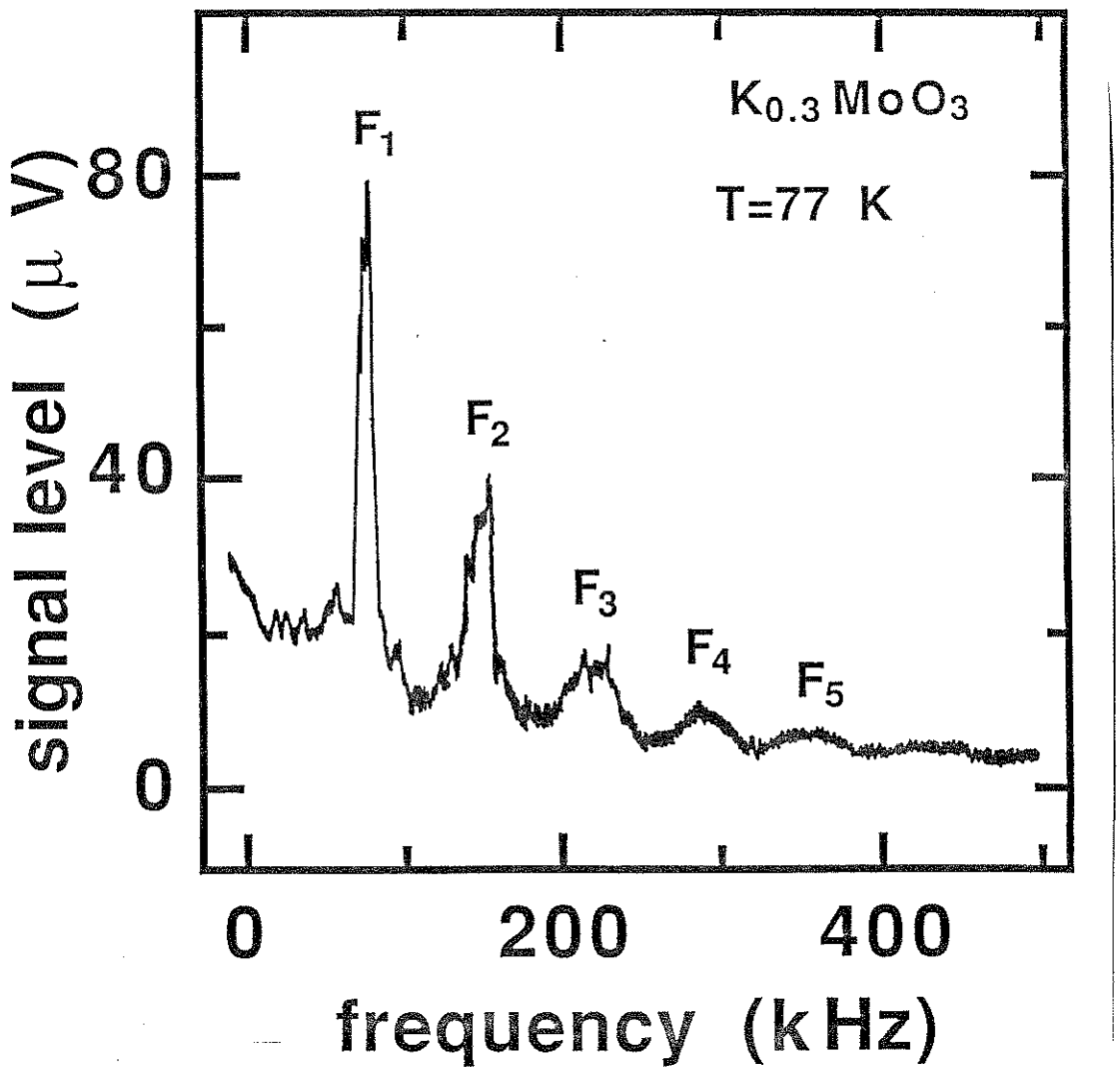

Figure 5-1 Narrow band noise spectrum from a thin sample of $K_{0.3}MoO_3$ at T = 77 K.

sharp spectrum indicates that the sliding CDW state is very coherent. The quality of this NBN spectrum exceeds that of those published previously,[22-24] suggesting that the CDWs in thin blue bronze samples are more coherent than in the large samples (volume~10^{-4} cm^3) usually examined.

The NBN frequency f_{NBN} varies linearly with the excess CDW current I_{CDW}. I_{CDW} is given by

$$I_{CDW} = I - \frac{V_{dc}}{R_o}, \tag{5.4}$$

where I is the total sample current, V_{dc} is the sample dc bias voltage, and R_o is the sample low field ($V_{dc}<V_T$) dc resistance. The linear relationship between I_{CDW} and f_{NBN} was found to hold true for the entire frequency range examined experimentally ($\leq$ 150 kHz). Hence, strongly coherent $K_{0.3}MoO_3$ samples do not exhibit any deviation from a linear CDW current to NBN frequency relationship. The ratio between the NBN frequency and the CDW current density for the sample considered here was found to be f_{NBN}/J_{CDW} = 12 ± 3 kHz cm^2/A.

We have also examined the narrow band noise spectra of blue bronze samples with volumes larger than the one whose NBN spectrum is shown in Fig. 5-1. In general, the NBN quality drops sharply as the volume of the crystal examined varies from that of a transparent sample (volume~10^{-8} cm^3) to

that of a more typical, bulk sample (volume~10^{-4} cm^3). In varying the volume from 10^{-8} cm^3 to 10^{-4} cm^3, the NBN peaks progressively become smaller in size and larger in width. In the large volume limit, the noise spectrum displays no narrow band peaks, but instead exhibits a fairly continuous noise distribution out to a critical frequency f_c.[25] Beyond f_c the noise level drops to zero. We find that this critical frequency varies linearly with the sample bias. These results clearly suggest that NBN generation in $K_{0.3}MoO_3$ is a bulk phenomenon, in agreement with research concerning NBN generation in $NbSe_3$.[5]

The effects of joint ac and dc driving fields on the differential resistance of the 0.2 μm thick $K_{0.3}MoO_3$ sample are shown in Fig. 5-2. The upper trace shows the sample's current driven differential resistance in the absence of any external ac signal. The CDW clearly depins at a threshold current of I_T = 2.5 μA, beyond which dV/dI smoothly decreases as the CDW proceeds to slide. The bottom trace shows the changes in the differential resistance when it is measured with an additional 60 kHz ac signal of magnitude V_{ac} = 80 mV = $4V_T$ applied across the sample. This trace shows a number of partially mode-locked Shapiro steps, each of which is labeled in the figure according to its index n. The fundamental harmonic (n=1) as well as three subharmonic (n=1/3, 1/2, and 2/3) steps are visible in Fig. 5-2. The lower trace also indicates that the mode locking quality

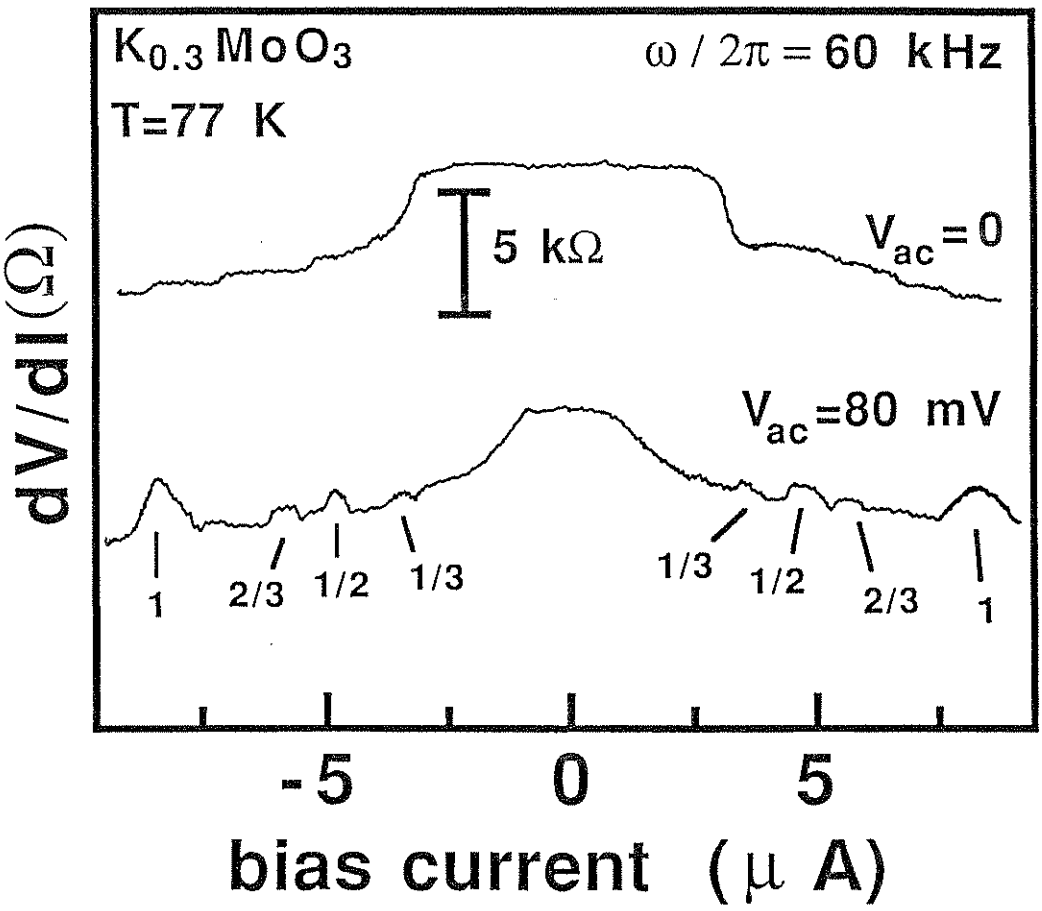

Figure 5-2 Ac-dc interference effects in $K_{0.3}MoO_3$ at 77 K. The top trace is with no ac signal, while the bottom trace shows the differential resistance in the presence of a 60 kHz and 80 mV ac signal. The two traces have been vertically offset for clarity.

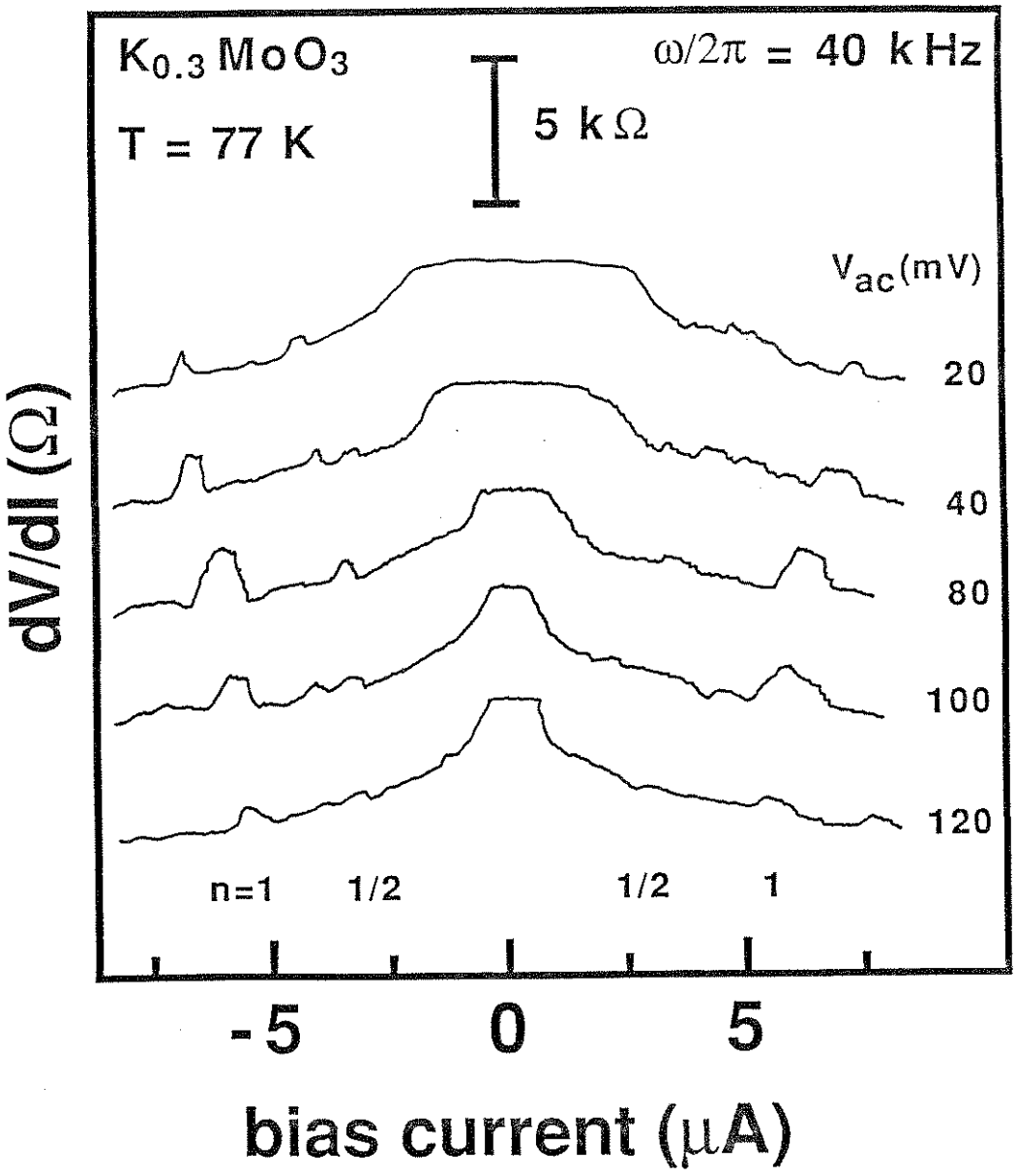

Figure 5-3 Shapiro step spectrum at 77 K with a 40 kHz ac signal. The ac amplitude varies from 20 mV (V_T) to 120 mV ($6V_T$). The traces are vertically offset for clarity.

depends on the direction of the current bias, with the locking quality for negative biases being higher than for positive biases.

The degree to which the CDW becomes locked to the external ac signal is a strong function of the ac amplitude V_{ac}. This is shown in Fig. 5-3, where the Shapiro step spectrum in a 40 kHz ac field is depicted as a function of V_{ac}. V_{ac} varies from 20 mV (V_T) to 120 mV ($6V_T$). The data in Fig. 5-3 indicates that the Shapiro step height increases with increasing V_{ac}, up to roughly 80 mV, beyond which it begins to decrease again. This is more clearly shown in Fig. 5-4 where the Shapiro step magnitude δV, the area under a Shapiro step in a dV/dI vs. I trace, is plotted as a function of V_{ac} for the n=1 Shapiro step. This general step height and step magnitude dependence on V_{ac} appears to hold true for both harmonic and subharmonic Shapiro steps. Increasing V_{ac} also acts to decrease the CDW threshold current, and to move a given Shapiro step to progressively lower total current biases. Effects similar to these have also been observed in mode locking experiments performed on $NbSe_3$ crystals.[7,8,10]

To insure that the mode locking condition as stated in Eqn. 5.3 holds for blue bronze, we have measured the CDW current density on each locked step as a function of the external locking frequency $\omega/2\pi$. The results for n = 2, 1, and 1/2 are presented in Fig. 5-5. We find that the CDW current density on a particular mode-locked step J_{lock} is

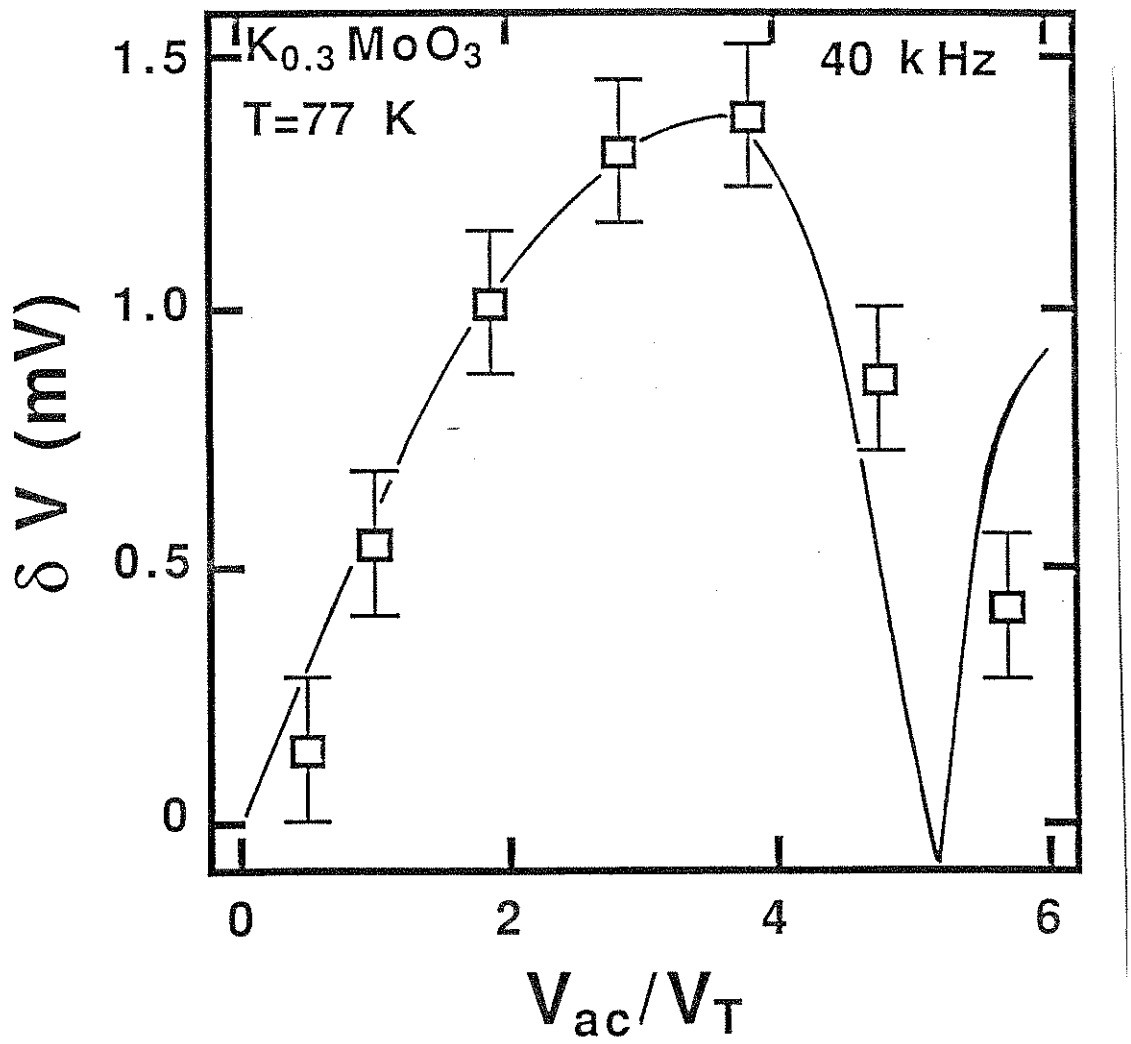

Figure 5-4 Shapiro step magnitude δV plotted as a function of the applied ac driving signal amplitude. The external ac frequency was set at $\omega/2\pi$ = 40 kHz. The solid line is a fit to the data (see text).

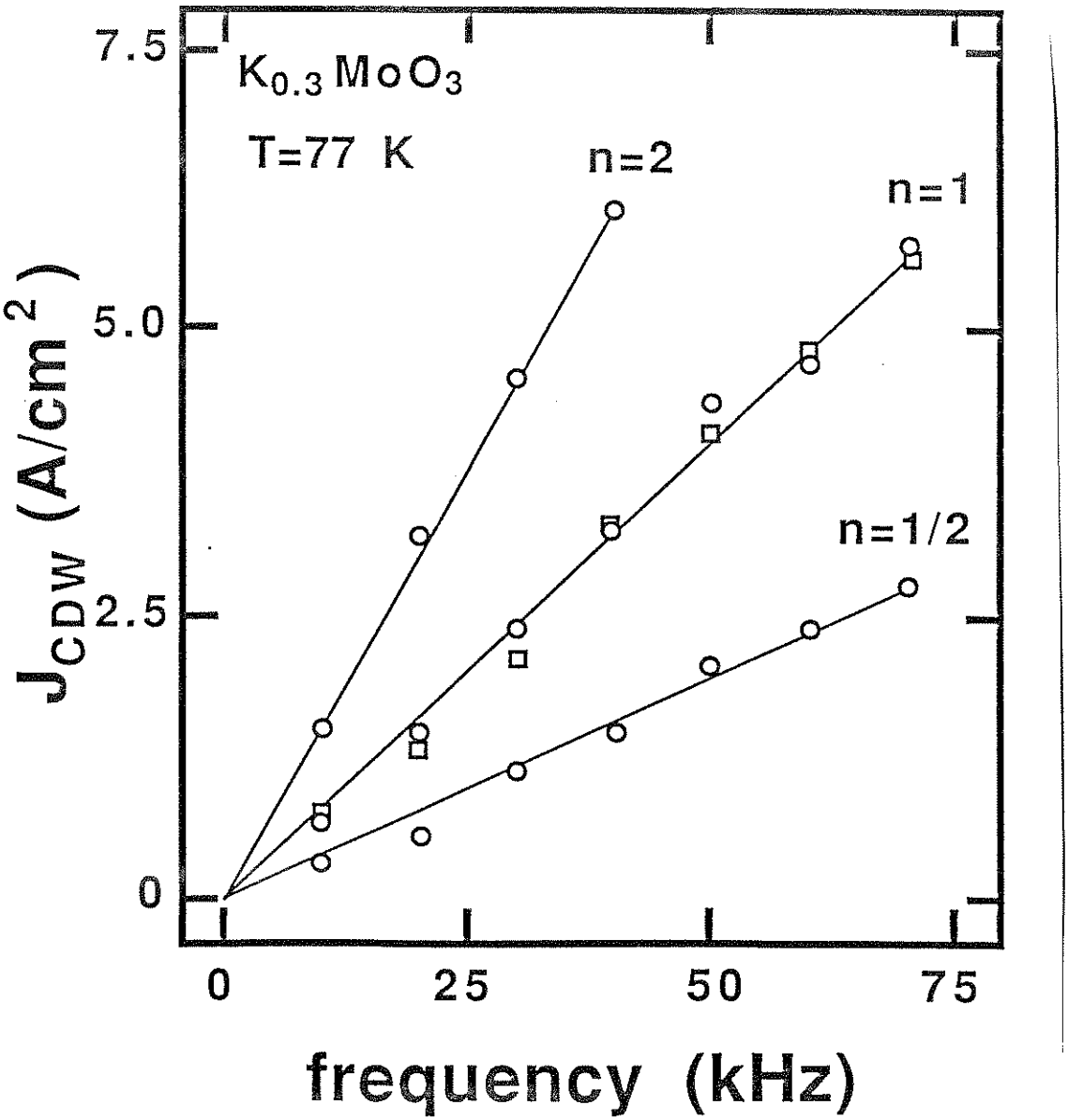

Figure 5-5 CDW current density plotted as a function of external locking frequency for both Shapiro step data (circles) and narrow band noise data (squares).

independent of the ac amplitude for the entire range of measurements ($V_{ac} \leq 6V_T$). The NBN frequency as a function of CDW current density is also plotted in the figure. This data indicates that J_{lock} is linearly related to the locking frequency for all three values of n. The empirical locking CDW current density to locking frequency ratio is $f_{ex}/J_{lock} = \beta/n$, where $\beta = 12 \pm 3$ kHz cm^2/A.

We now turn to an examination of dc bias effects on the complex ac conductivity $\sigma(\omega)$ in $K_{0.3}MoO_3$. In these experiments, a small amplitude ($V_{ac} << V_T$) ac signal $V = V_{ac}\cos(\omega t)$ is applied across the sample and the resulting current I_{ac} flowing through the sample at the same frequency is detected. A bias voltage V_{dc} may also be applied. The complex conductivity, $\sigma(\omega) = \text{Re}\ \sigma(\omega) + i\ \text{Im}\ \sigma(\omega)$, is determined from

$$\sigma(\omega) = \left(\frac{L}{A}\right) \frac{I_{ac}}{V_{ac}} e^{i\theta} , \qquad (5.5)$$

where A is the sample cross sectional area, L is its length, and θ reflects the component of the current response which is out of phase with the input voltage. Our zero-bias complex conductivity measurements on thin samples of $K_{0.3}MoO_3$ at 77K show a rise in Re $\sigma(\omega)$ beginning at roughly 20 kHz; this low frequency mode is the extensively studied dielectric relaxation mode apparently present in all completely gapped

depinnable CDW materials.[14,15] The rise in Re $\sigma(\omega)$ indicates that the characteristic frequency f_{dr} for this mode is roughly 20 kHz.

The effects upon the 50 kHz complex conductivity when a depinning bias field is applied to a thin $K_{0.3}MoO_3$ sample are depicted in Fig. 5-6. The real part of the conductivity is presented in Fig. 5-6a, while the dielectric constant ε, given by

$$\varepsilon(\omega) = \frac{4\pi \text{ Im } \sigma(\omega)}{\omega} , \qquad (5.6)$$

is presented in Fig. 5-6b. There is very little change in Re $\sigma(\omega)$ for $I_{dc} < I_T = 2.5$ μA, while $\varepsilon(\omega)$ does show a slight increase just below threshold. Past threshold, the complex conductivity changes drastically: the real part of the conductivity begins to increase while the dielectric constant decreases towards zero. In addition to this general depinning response, both Re $\sigma(\omega)$ and $\varepsilon(\omega)$ exhibit distinct anomalies for well defined values of the bias current. In particular, $\varepsilon(\omega)$ displays a well defined inductive ($\Delta\varepsilon < 0$) dip at $I_{dc} = 5.7$ μA, and a smaller dip at $I_{dc} = 4.3$ μA. Anomalies at these bias currents also show up in Re $\sigma(\omega)$. The feature in Re $\sigma(\omega)$ centered around $I_{dc} = 5.7$ μA is particularly noticeable. This anomaly is characterized by a *drop* below the background CDW conductivity at a value of I_{dc}

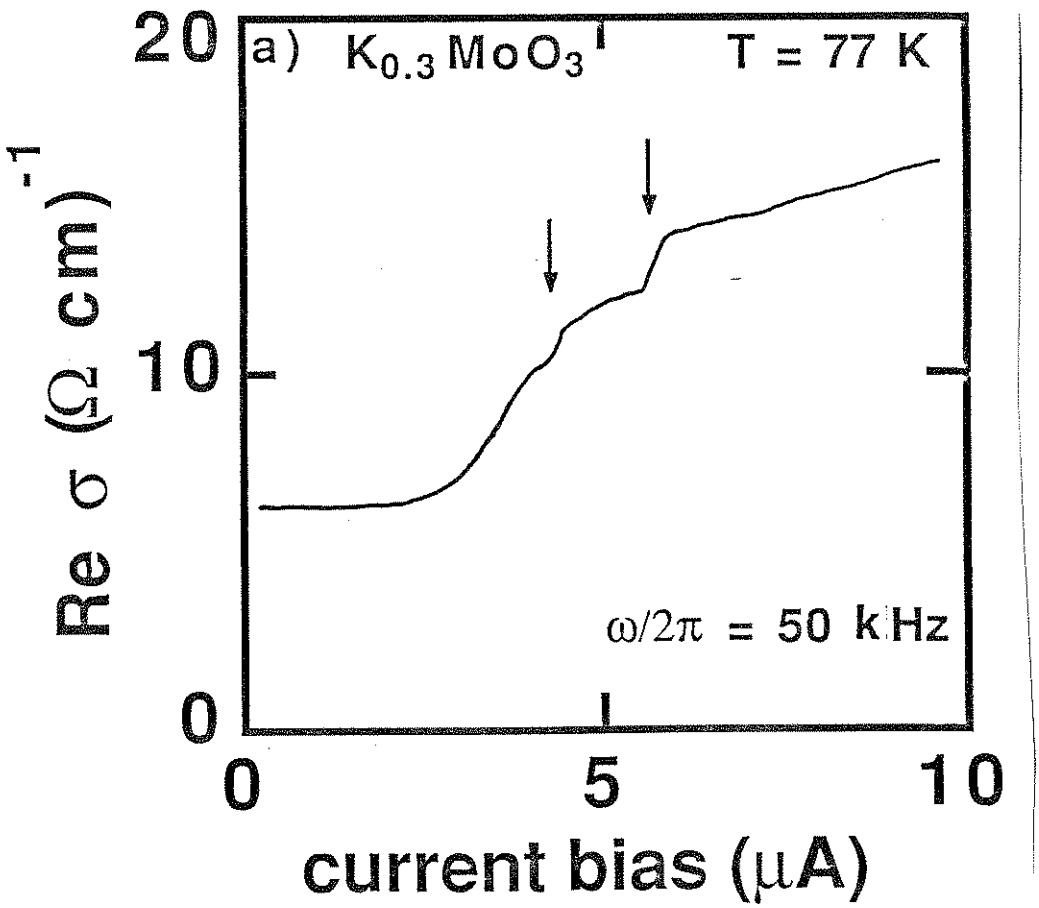

Figure 5-6a The real part of the ac conductivity Re $\sigma(\omega)$ measured at $\omega/2\pi$ = 50 kHz as a function of dc bias current.

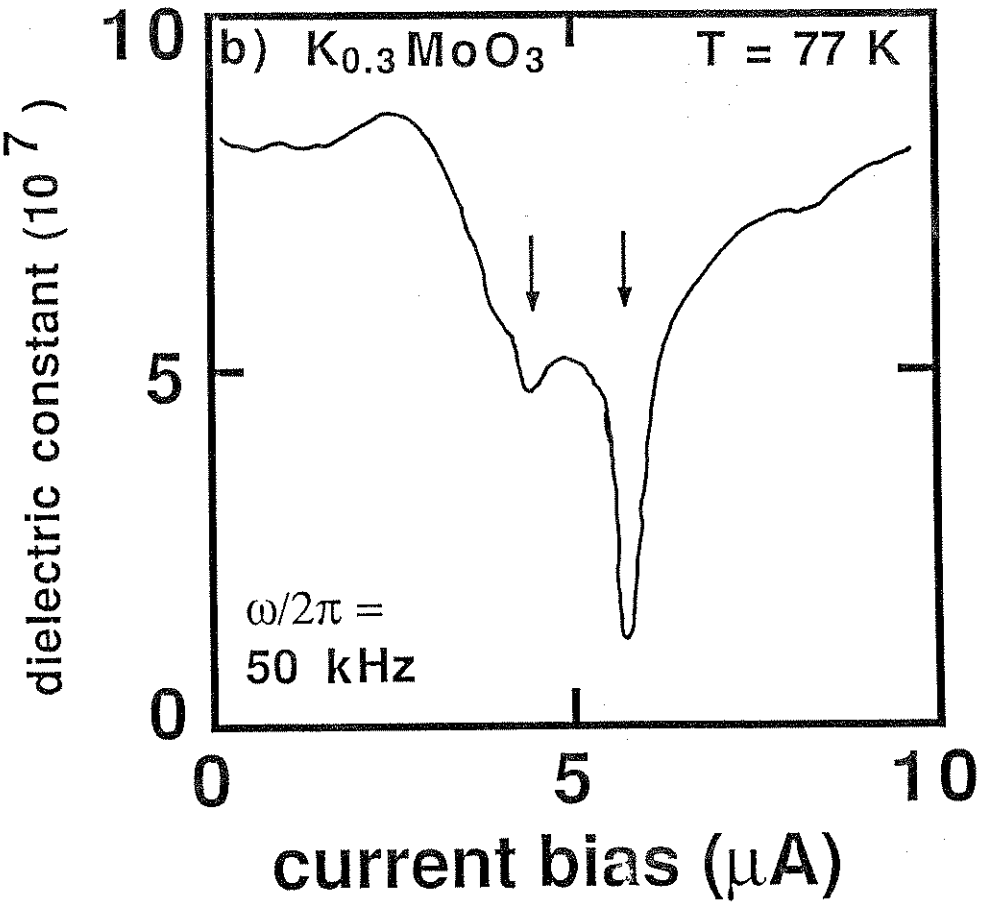

Figure 5-6b The dielectric constant $\varepsilon(\omega)$ measured at $\omega/2\pi$ = 50 kHz as a function of dc bias current.

just below that which gives the large inductive dip in $\varepsilon(\omega)$. A similar *rise* above the background conductivity occurs for values of I_{dc} slightly larger than the inductive dip bias. An examination of the NBN spectrum shows that for I_{dc} = 5.7 μA, f_{NBN} = 50 kHz, while at I_{dc} = 4.3 μA, the second NBN harmonic occurs at 50 kHz. This suggests that the anomalies at 4.3 μA and 5.7 μA are related to resonances between the 50 kHz probing signal and the second NBN harmonic or the NBN fundamental, respectively. Similar well defined anomalies have been extensively studied in $NbSe_3$.[7,10] Very broad anomalies at low frequencies have also been previously reported for $K_{0.3}MoO_3$.[12]

The bias current at which the strong resonance anomalies occur should be a strong function of the probe frequency since they occur when the internal NBN frequency matches the probing frequency. This is shown to be the case in Fig. 5-7, where the dielectric constant $\varepsilon(\omega)$ is plotted as a function of bias current for several ac probing frequencies. The resonance current bias clearly scales linearly with the ac frequency. This is evident in Fig. 5-8, where the CDW current density at resonance is plotted as a function of the resonance frequency. The experimental NBN frequency f_{NBN} to CDW current density relationship is also plotted in the figure. Clearly, both sets of data lie on a line which has a slope of f_{NBN}/J_{CDW} = 12 kHz cm^2/A. This conclusively shows that the anomalies which appear in both

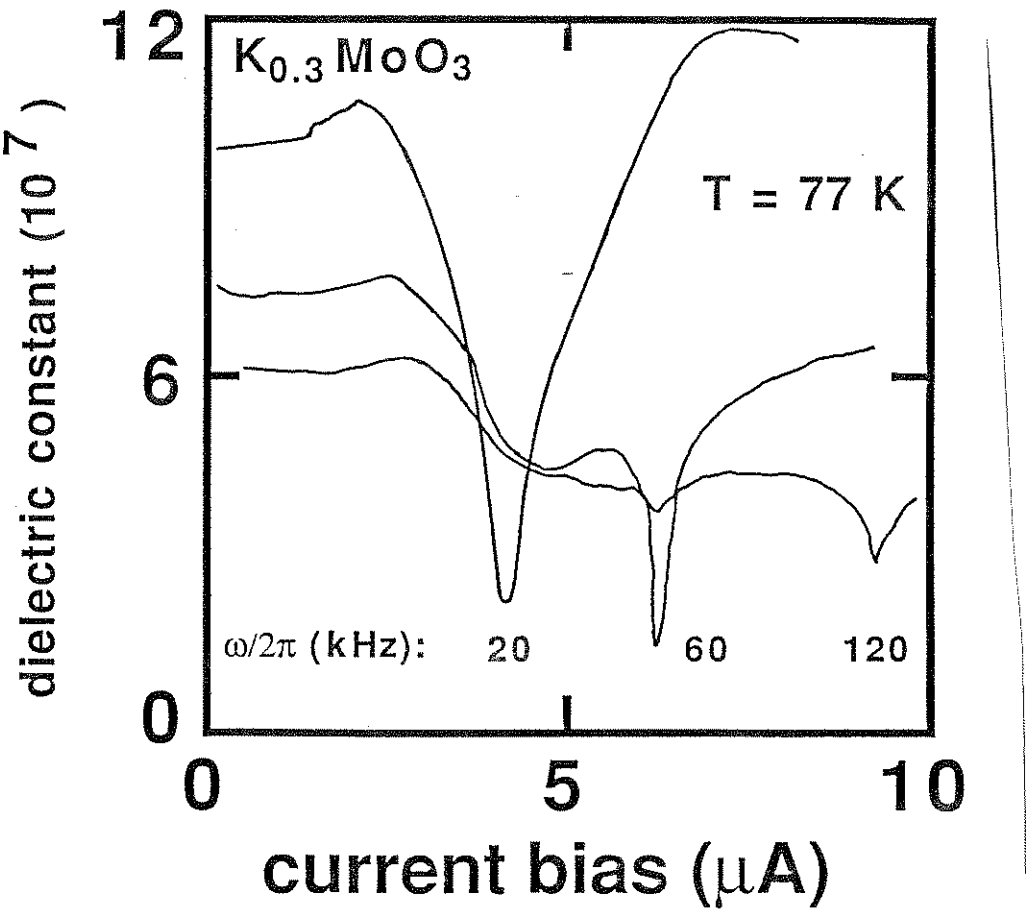

Figure 5-7 The dielectric constant $\varepsilon(\omega)$ measured as a function of dc bias current at three frequencies (20, 60, and 120 kHz).

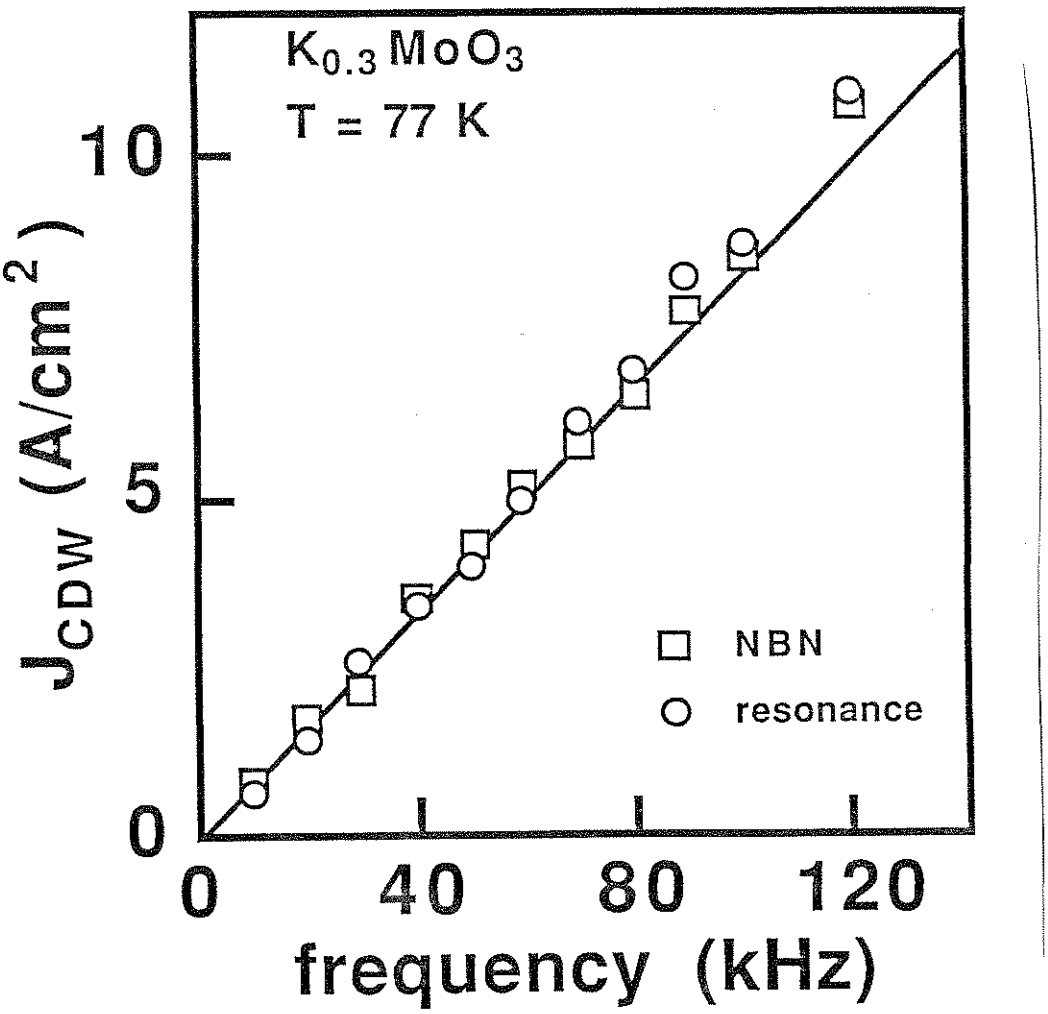

Figure 5-8 The CDW current density at resonance plotted as a function of the resonance frequency (circles). The CDW current density to NBN frequency f_{NBN} is also plotted in the figure (squares).

$\varepsilon(\omega, I_{dc})$ and Re $\sigma(\omega, I_{dc})$ are caused by a direct interference between the internal NBN signal at f_{NBN} and the external signal at $\omega/2\pi$.

Returning to the data in Fig. 5-7, the placement of the inductive dip is not the only frequency dependent aspect of $\varepsilon(\omega, I_{dc})$. The below-threshold dielectric constant appears to decrease with increasing frequency. Additionally, the depth of the inductive dip also decreases with increasing frequency. At 20 kHz, the change in $\varepsilon(\omega)$ due to the dip is $\Delta\varepsilon(20\ \text{kHz}) = -8 \times 10^7$, while at 120 kHz it is only $\Delta\varepsilon(120\ \text{kHz}) = -1.4 \times 10^7$. At frequencies below 20 kHz, the dip continues to increase in size. This is shown in Fig. 5-9, where the bias dependent dielectric constant is plotted at 1, 40, 80, and 120 kHz. The inductive dip measured at 1 kHz clearly dwarfs the anomalies at the higher frequencies; the size of the dip at 1 kHz is $\Delta\varepsilon(1\ \text{kHz}) = -160 \times 10^7$, a factor of 114 higher than the dip at 120 kHz. This indicates that $\Delta\varepsilon$ diverges as $1/\omega$ in the limit that ω goes to zero.

The anomalies in the complex ac conductivity depicted in Figs. 5-6, 5-7, and 5-9 are observed by measuring $\sigma(\omega)$ at a fixed frequency while varying the dc bias. Presumably, the same effects should occur when the dc bias is held fixed and the measurement frequency is swept. The frequency dependent ac conductivity at a depinning bias of $I_{dc} = 7\ \mu A$ is depicted in Fig. 5-10. At this bias, the NBN fundamental occurs at $f_{NBN} = 70$ kHz. Inductive dips are clearly present in the

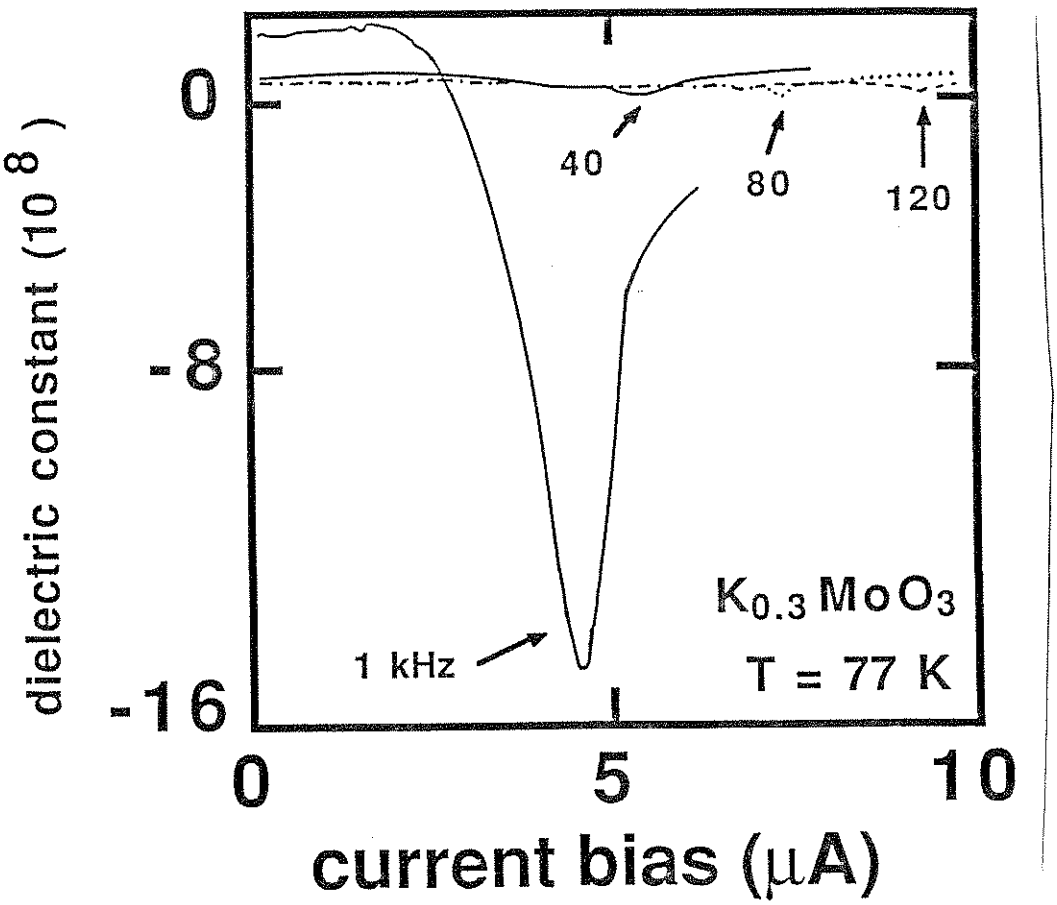

Figure 5-9 $\varepsilon(\omega, I_{dc})$ at low (1 kHz) and high frequencies (40, 80, and 120 kHz). The comparatively small high frequency resonances are indicated by arrows.

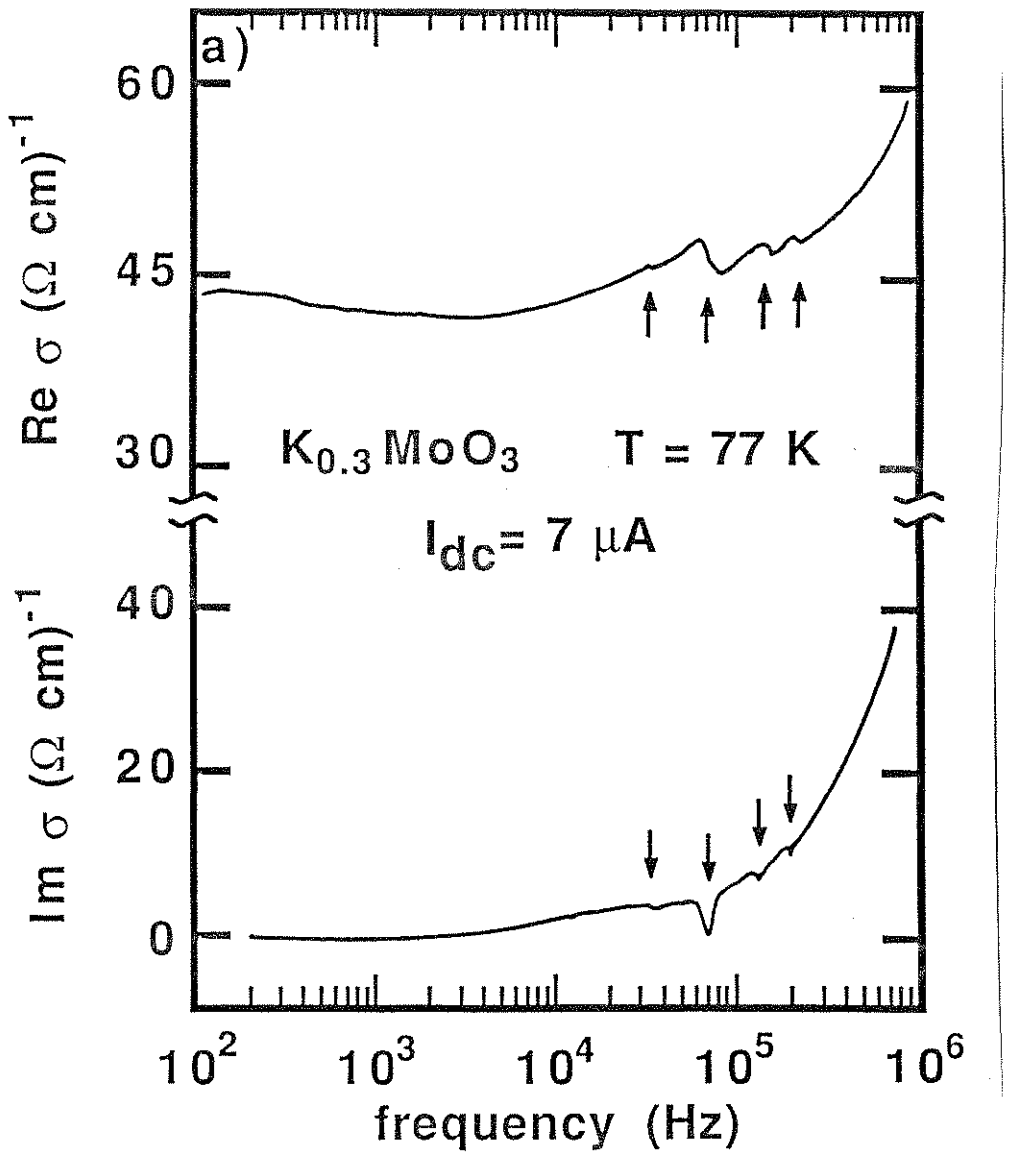

Figure 5-10a Real and Imaginary parts of the conductivity in the presence of a depinning current bias of I_{dc} = 7 μA. At this bias, the NBN fundamental occurs at f_{NBN} = 70 kHz. The harmonic resonances at 35, 70, 140, and 210 kHz are indicated by arrows.

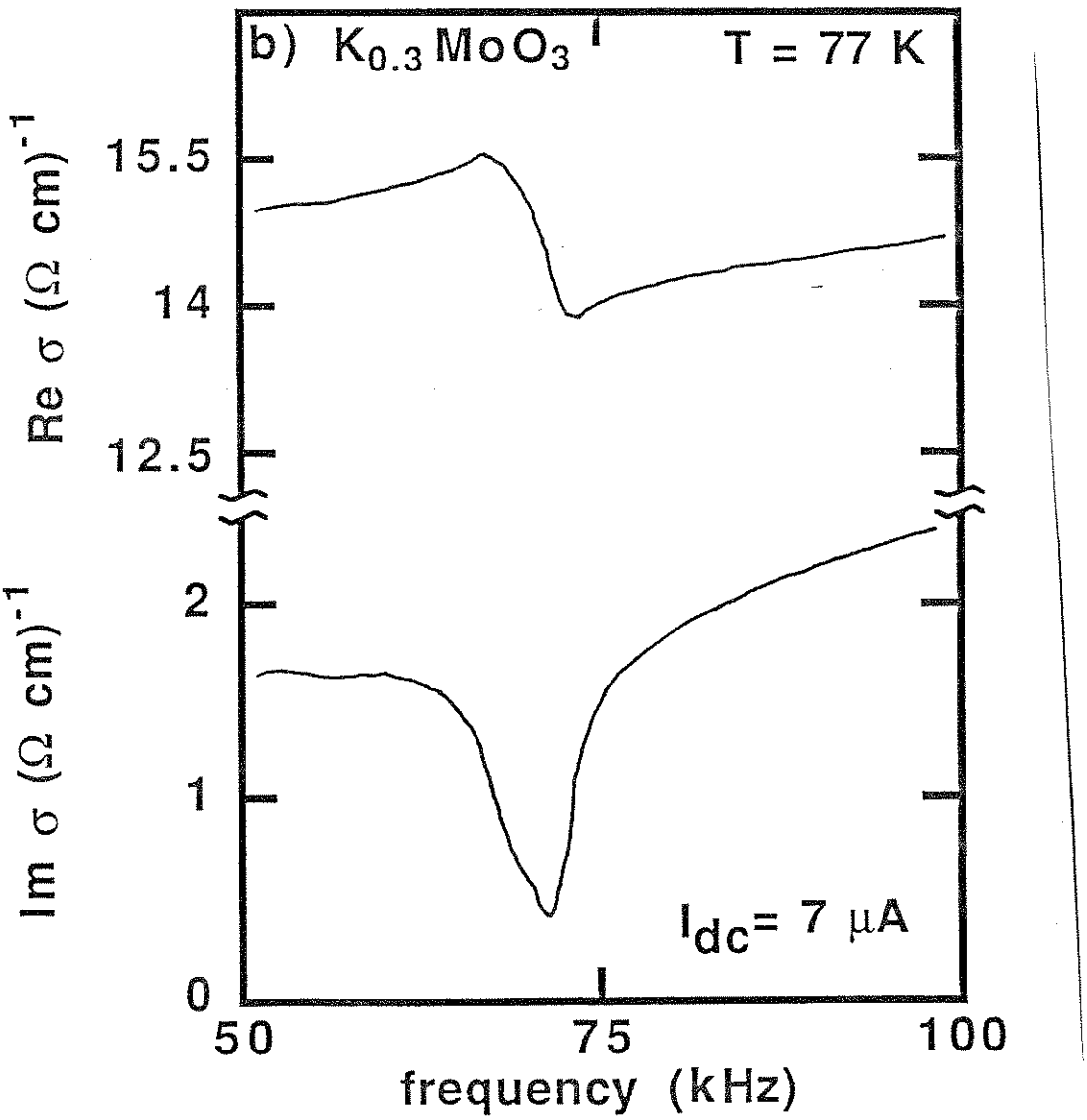

Figure 5-10b A close up around the 70 kHz resonance is shown using a linear frequency scale.

imaginary part of the conductivity at $\omega/2\pi = f_{NBN}/2$ (35 kHz), f_{NBN} (70 kHz), $2f_{NBN}$ (140 kHz), and $3f_{NBN}$ (210 kHz). In addition, anomalies show up in Re $\sigma(\omega)$ centered about these four frequencies. The anomaly at 70 kHz is larger than those at the other frequencies. Details of the resonance around this frequency are shown in Fig. 5-10b, where the ac conductivity is plotted vs. frequency utilizing a linear frequency scale. The imaginary part of the conductivity exhibits an inductive dip with a magnitude of 1.3 $(\Omega\ \text{cm})^{-1}$. Re $\sigma(\omega)$ shows a smaller, less pronounced positive and negative set of peaks above and below 70 kHz, respectively. These two peaks have equal magnitudes of 0.7 $(\Omega\ \text{cm})^{-1}$ above and below the background CDW-plus-normal-electron conductivity of roughly 15 $(\Omega\ \text{cm})^{-1}$. At the 70 kHz resonance frequency, Re $\sigma(\omega)$ appears unchanged from the background conductivity value.

5.4 Analysis

We first examine the relationship between the CDW current density and the NBN frequency in blue bronze. The three sets of experiments discussed in the previous section provide an accurate estimate of the ratio f_{NBN}/J_{CDW}, which can be directly compared to an expression which holds true for NBN phenomena in both $NbSe_3$ and TaS_3. We next use a simple single particle classical model of CDW dynamics to analyze the Shapiro step magnitude dependence on ac signal

amplitude. Lastly, we will discuss the underlying mechanisms which cause the resonance features in the dc biased complex ac conductivity.

5.4.1 CDW current density to NBN frequency relationship

A simple model[3] predicts that the fundamental NBN frequency is linearly related to the CDW current density by

$$\frac{f_{NBN}}{J_{CDW}} = \frac{1}{n_c e \lambda} \qquad (5.7)$$

where λ_{pin} is the intrinsic pinning potential wavelength, and n_c is the CDW electronic carrier concentration. NBN studies indicate that Eqn. 5.7 holds true for both $NbSe_3$ and TaS_3.[3,26] It has been suggested that for CDW conductors the pinning potential wavelength is equal to the CDW wavelength ($\lambda_{pin} = \lambda_{CDW}$). There has been some controversy as to whether or not Eqn. 5.7 holds true for $K_{0.3}MoO_3$.[12,22-24] A large variation exists in the values reported for f_{NBN}/J_{CDW} based on NBN measurements. This is presumably due to the inhomogeneous CDW current densities and low quality NBN spectra typically exhibited by $K_{0.3}MoO_3$ samples.

The difficulty with obtaining estimates of f_{NBN}/J_{CDW} from simple NBN experiments stems from the fact that it is impossible to determine if the CDW current is homogeneous

throughout the sample in these experiments. An estimate of f_{NBN}/J_{CDW} determined from the Shapiro step data, on the other hand, should provide a more direct measure of this quantity because the mode locking condition insures that the CDW current density is uniform throughout the mode-locked sample. The Shapiro step data in Figs. 5-2 and 5-3 show that a substantial portion of the CDW responds coherently in thin blue bronze samples, indicating that the CDW current density within them is homogeneous.

To obtain a value for f_{NBN}/J_{CDW} from the locking frequency $\omega/2\pi$ to locking current density J_{lock} ratio, we combine the ratio f_{ex}/J_{lock} with Eqn. 5.3 and obtain

$$\frac{f_{ex}}{J_{lock}} = \frac{1}{n}\frac{f_{NBN}}{J_{CDW}} \quad , \tag{5.8}$$

where n is the Shapiro step index. The data in Fig. 5-5 give a value for this ratio of $f_{ex}/J_{lock} = \beta/n$, with $\beta = 12 \pm 3$ kHz cm^2/A. Therefore, the Shapiro step data produce a value for the NBN frequency to CDW current density ratio of $f_{NBN}/J_{CDW} = 12 \pm 3$ kHz cm^2/A, in agreement with the ratio determined directly from NBN measurements; a similar value for this ratio has been deduced from NMR measurements.[27,28] Combined with $n_c = 4.95 \times 10^{21}$ cm^{-3}, as determined from structural considerations,[13] and Eqn. 5.7, this value for f_{NBN}/J_{CDW} suggests a pinning potential periodicity of λ_{pin} =

10.6±2 Å. This length is in close agreement with the CDW wavelength in $K_{0.3}MoO_3$ (λ_{CDW} = 9.9 Å). Therefore, Eqn. 5.7 holds true for potassium blue bronze, and the data further suggest that the pinning potential periodicity is equal to the CDW wavelength.

5.4.2 Mode locking

In this section we will examine the quantitative nature of mode locking in blue bronze, in particular the dependence of the Shapiro step magnitude δV on the amplitude of the applied ac locking signal. The data are analyzed within a simple model which qualitatively accounts for Shapiro steps observed in $NbSe_3$.[7,8]

A number of models have been proposed to account for CDW dynamics. Both single degree-of-freedom[8] and many internal degree-of-freedom[29,30] models have been proposed to account for ac-dc interference effects. A simple single degree of freedom phenomenological model,[19] which treats the CDW as an object with charge e and mass m^* moving in a sinusoidal potential, has been surprisingly successful in qualitatively and semi-quantitatively describing the essential frequency and electric field dependent features of CDW transport.[2] The single particle equation of motion is[19]

$$\frac{d^2x}{dt^2} + \Gamma\frac{dx}{dt} + \frac{\omega_o^2}{Q}\sin(Qx) = \frac{eE}{m^*} \quad , \tag{5.9}$$

where x is the CDW center-of-mass coordinate, E is the applied electric field, Q is the periodic pinning potential wavevector, ω_o is the characteristic resonance frequency of the CDW, and $\Gamma = 1/\tau$ is a damping constant with a characteristic relaxation time τ; Eqn. 5.7 follows directly from Eqn. 5.9 with $Q = 2\pi/\lambda_{pin}$. This model accounts for both the narrow band noise oscillations and mode locking observed in CDW materials. In addition, it quantitatively describes the Shapiro step magnitude dependence on ac signal amplitude in $NbSe_3$.[7,8] From our determination that $\lambda_{pin} = \lambda_{CDW}$ in $K_{0.3}MoO_3$, we set $Q = 2\pi/\lambda_{CDW}$ in Eqn. 5.9.

In analogy with the Stewart-McCumber model of Josephson tunneling,[31] Eqn. 5.9 predicts that the magnitude of the n=1 Shapiro step in the high frequency limit ($\omega_{ex} >> \omega_o^2\tau$) should be[8]

$$\delta V = 2\ \alpha\ V_T(\omega=0)\ \left| J_1\left(\frac{\omega_o^2\tau}{\omega}\ \frac{V_{ac}}{V_T(\omega=0)}\right)\right| \quad , \tag{5.10}$$

where α represents the volume fraction locked to the external signal, while ω and V_{ac} are the frequency and amplitude of

the applied signal, respectively. In the low frequency (overdamped) limit ($\omega \leq \omega_o^2\tau$) the inertial term ($d^2x/dt^2$) can be neglected, and a modified Bessel-like solution for δV can be obtained numerically.[32] In the extreme low frequency limit ($\omega << \omega_o^2\tau$), the numerical solution predicts that δV has a maximum at $V_{ac}=V_T$ with an amplitude of $\delta V = (\omega/\omega_o^2\tau)V_T$.

Recently, a seemingly more general derivation for the Shapiro step magnitude was published.[10] That derivation utilized a model independent approach and assumed that the pinning potential was in the form of a cusped-cosine function. Although one might assume that this approach should yield a more general, model independent result, it can be shown[33] that the resulting expression for δV is exactly equivalent to the one produced by a single particle model with a cusped-cosine, rather than a sinusoidal, potential. Nonetheless, this approach clears up two deficiencies of Eqn. 5.10. First, the new result correctly predicts the existence of subharmonic Shapiro steps. Second, because the expression for δV involves a summation of Bessel functions weighted by the pinning potential's Fourier coefficients, the Shapiro step magnitude does not go to zero at the minima (in contrast to the predictions of Eqn. 5.10). Both of these qualitative enhancements are directly related to the inclusion of higher harmonics in the pinning potential. Unfortunately, the model's quantitative prediction [locations of maxima and minima in $\delta V(V_{ac})$] have yet to be compared to experimental

data due to the complexity of the expression. Therefore, it is unclear if the approach of Ref. 10 is quantitatively superior to Eqn. 5.10. For this reason, we shall analyze the blue bronze mode locking data by using the predictions of the single particle classical model, Eqn. 5.9.

A reasonable fit to the data in Fig. 5-4 can be obtained by utilizing the numerical low frequency solution presented in Ref. 32 and considering $\omega_o^2\tau$ to be a fitting parameter. The solid-line fit in Fig. 5-4 was obtained in this way with $f_o = \omega_o^2\tau/2\pi = 25$ kHz. It is noteworthy that this value is roughly *four orders of magnitude* below the characteristic frequency of the high frequency pinned mode seen in $K_{0.3}MoO_3$ (~500 MHz).[17] According to Eqn. 5.9, the contribution to δV from the 500 MHz pinned mode would be negligible at the frequencies where these measurements were performed (40 kHz). Further, low frequency ac conductivity measurements indicate that the dielectric relaxation mode in the sample considered here has a characteristic frequency of $f_{dr} \approx 20$ kHz. Hence, it appears that the ac-dc interference effects seen in $K_{0.3}MoO_3$ at 77K are a result of interactions between the external ac signal and the low frequency dielectric relaxation mode present in this material.

To make certain that the low frequency mode and not the high frequency mode is interacting with the external signals, we must first insure that the characteristic frequency determined from the fit to the Shapiro step data is more than

just a mathematical coincidence. To do this, we calculate the expected classical characteristic frequency $\omega_o{}^2\tau$ in an independent manner by considering in greater detail the low frequency behavior of blue bronze. The narrow band noise typically produced by $K_{0.3}MoO_3$ crystals are relatively low, between 10 and 100 kHz. In addition, dc CDW motion has been shown to be strongly damped below 100K, with the degree of damping growing with decreasing temperature.[34] The damping is such that the CDW conductivity in dc electric fields, far in excess of the threshold field, is limited to the normal carrier ohmic conductivity. The NBN frequency and dc conductivity predicted by Eqn. 5.9 are

$$f_{NBN}(E) = \frac{1}{2\pi}\frac{Q\tau e}{m^*} E\, g(E) , \qquad (5.11)$$

and

$$\sigma_{dc}(E) = \frac{n_c e^2 \tau}{m^*} g(E) , \qquad (5.12)$$

respectively, where $g(E)$ is a function of the applied electric field E with the limiting behavior: $g(E \leq E_T) = 0$, and $g(E >> E_T) = 1$. Eqns. 5.11 and 5.12 indicate that large CDW damping (small τ) is responsible for low dc CDW conductivities and NBN frequencies (small NBN frequencies and CDW conductivities cannot be attributed to variations in Q or

m^* because both are tied to the CDW gap). This suggests that the characteristic frequency $\omega_o^2\tau$ is small in blue bronze because of large CDW damping.

We next calculate an independent estimate of $\omega_o^2\tau$ using other experimental data. From Eqn. 5.9 the threshold dc electric field E_T is

$$E_T = \frac{m^*}{Qe}\,\omega_o^2 \quad . \tag{5.13}$$

This yields an expression for $\omega_o^2\tau$ in terms of E_T and $Qe\tau/m^*$. To obtain $\omega_o^2\tau$ in terms of experimentally determinable quantities, we utilize the high field limit of Eqn. 5.12 ($g(E)=1$), as well as the NBN frequency to CDW current density relation (Eqn. 5.7). By substituting these expressions into Eqn. 5.13, $f_o = \omega_o^2\tau/2\pi$ becomes

$$f_o = \left(\frac{f_{NBN}}{J_{CDW}}\right) \sigma_{dc}(E >> E_T)\; E_T \quad . \tag{5.14}$$

The pertinent experimentally determined parameters for the sample considered here are: f_{NBN}/J_{CDW} = 12 ± 3 kHz cm^2/A, E_T = 320 mV, and $\sigma_{dc}(E >> E_T)$ = 10 $(\Omega\ cm)^{-1}$. Based on these numbers, Eqn. 5.14 yields a value of f_o = 44 ± 11 kHz. This result is in reasonable order-of-magnitude agreement with the frequencies determined from both the fit to the Shapiro step

data (f_o = 25 kHz) and from the ac conductivity measurements ($f_{dr} \approx$ 20 kHz). Hence, it appears that Eqn. 5.9 can account for the fundamental frequency of the low temperature dielectric relaxation mode in blue bronze. Further, the analysis indicates that the low frequency ac-dc interference effects in this material are a direct result of the external signals interacting with the low frequency dielectric relaxation mode.

Because external ac and dc driving fields can interact with the low frequency CDW mode in $K_{0.3}MoO_3$ in the same way that they do with the high frequency pinned phason mode in $NbSe_3$, it would appear that there are actually two qualitatively similar pinned modes in blue bronze. This lends support to the theories concerning screening effects of normal electrons on the CDW as first discussed by Sneddon[30] and more recently by Littlewood.[35] In completely gapped CDW materials, normal electrons act to screen the moving CDW, leading to an enhancement in CDW damping and the creation of an overdamped, low frequency pinned mode. This screening action can only take place in the low frequency($\leq$ 10 MHz) limit. In the high frequency (> 100 MHz) limit, normal electrons are ineffective in damping CDW motion, and an additional unscreened and underdamped, "bare" high frequency pinned phason mode should be realized. The Shapiro step data presented here provides direct evidence that these two modes are qualitatively similar in that external driving fields can

couple to them in the same manner.

5.4.3 Ac conductivity resonances

The data presented in Figs. 5-6 to 5-10 clearly indicate that a resonance-like anomaly occurs in $\sigma(\omega)$ when the internal NBN frequency or one of its harmonics coincides with the frequency at which the ac conductivity is being measured. In this section we examine the detailed nature of these resonant anomalies.

The anomalies appear as sharp inductive dips in either Im $\sigma(\omega)$ or $\varepsilon(\omega)$. The corresponding feature in Re $\sigma(\omega)$ appears as gradual positive and negative peaks located equi-distant above and below the resonance position, respectively. At resonance, Re $\sigma(\omega)$ appears unchanged from its inferred value if no resonance had occurred. A comparison of the anomalies in Re $\sigma(\omega)$ for bias swept data (Fig. 5-6a) and for frequency swept data (Fig. 5-10b) shows that the ordering of the positive and negative peaks relative to the central resonance position are interchanged in the two cases. For bias sweeps, a negative peak occurs just below resonance ($f_{NBN} < \omega/2\pi$), while for frequency sweeps this negative peak occurs above the resonance ($\omega/2\pi > f_{NBN}$). This suggests that the parameter which best characterizes the resonance condition is

$$\Delta f = f_{NBN} - \frac{\omega}{2\pi} . \qquad (5.15)$$

Regardless of which parameter is swept, Re $\sigma(\omega)$ shows a rounded positive peak when Δf approaches zero from above ($\Delta f > 0$), and a negative peak when approaching zero from below ($\Delta f < 0$). In either case, a sharp negative peak occurs in Im $\sigma(\omega)$ centered at $\Delta f = 0$.

The response at resonance is functionally analogous to a resonant harmonic oscillator, but with a phase shift which allows the main resonance at $\Delta f = 0$ to occur as a negative peak in Im $\sigma(\omega)$. To better understand this phenomenon, we consider the response of the sample to a low amplitude ($V_{ac} << V_T$) ac signal in combination with a depinning dc bias $V = V_{dc} + V_{ac}\cos(\omega t)$.[7] The normal carriers will respond with a current $I_n\cos(\omega t)$ completely in phase with the ac signal. The CDW responds with a current $I_{CDW,ac}\cos(\omega t+\theta)$, where the phase angle θ reflects the fact that the CDW conductivity has both a real and an imaginary component ($\theta \neq 0$). In addition to these signals, there is the CDW current produced by the dc bias. This includes both a dc current $I_{CDW,dc}$ and an oscillating current related directly to the narrow band noise, $I_{NBN}\, h(\omega_{NBN}t+\phi)$, where h is a periodic function with a period $1/\omega_{NBN}$. The function $h(\omega t)$ can be well approximated by a complex sinusoidal function $e^{i\omega t}$. The complete current response becomes

$$I = I_{CDW,dc} + e^{i\omega t}\left(I_n + I_{CDW,ac}e^{i\theta} + I_{NBN}e^{i\phi}\right) \quad . \qquad (5.16)$$

The total ac conductivity at the probe frequency ω is

$$\sigma(\omega) = \left\langle \frac{I}{V} \right\rangle = \frac{I_n}{V_{ac}} + \frac{I_{CDW,ac}}{V_{ac}} e^{i\theta} + \frac{I_{NBN}}{V_{ac}} \delta_{\omega\,\omega_{NBN}} e^{i\phi} \quad , \qquad (5.17)$$

where the braces denote a time average, and δ_{ab} is a Kronecker delta. For $\omega \neq \omega_{NBN}$, only the normal and CDW conductivities contribute to the measurement. For $\omega = \omega_{NBN}$, an extra contribution to the conductivity will result from the NBN signal. In order for the resonant conductivity enhancement to appear as a negative dip in the out of phase component, the phase angle at resonance must be $\phi = -\pi/2$.

The size of the inductive dip is predicted by Eqn. 5.17 to be

$$\Delta \mathrm{Im}\ \sigma(\omega = \omega_{NBN}) = \frac{L}{A} \frac{I_{NBN}}{V_{ac}} \quad . \qquad (5.18)$$

This expression makes a number of specific predictions about the inductive dip which can be directly compared to the data presented in Figs. 5-6 to 5-10. First, Eqn. 5.18 suggests that because the size of the NBN oscillations depend only on

the dc bias and not on the ac magnitude or frequency, the magnitude of the inductive dip should be independent of the frequency at which the resonance occurs. The measured dip magnitude ΔIm σ is plotted as a function of the resonance frequency in Fig. 5-11. Clearly, ΔIm σ is independent of the resonance frequency, with a value of ΔIm $\sigma = 1.0 \pm 0.1$ $(\Omega\ \text{cm})^{-1}$. This can be directly compared to experimental parameters; with an ac signal amplitude of $V_{ac} = 1$ mV and a NBN current of $I_{NBN} = 10 \pm 3$ nA (100 μV across 10 kΩ), Eqn. 5.18 predicts a dip magnitude of ΔIm $\sigma = 0.6 \pm 0.2$ $(\Omega\ \text{cm})^{-1}$, in reasonable agreement with the measured value. With ΔIm σ independent of frequency, the ac dielectric constant should be inversely proportional to ω, in agreement with the data presented in Figs. 5-7 and 5-9. The inclusion of I_{NBN} in Eqn. 5.18 also indicates why the resonances involving NBN harmonics are smaller than the resonance involving the fundamental NBN peak. This arises from the fact that magnitude I_{NBN} of a harmonic NBN peak drops as the harmonic order increases. Lastly, Eqn. 5.18 would suggest that for $V_{ac} << V_T$, increasing V_{ac} should in turn decrease the relative size of the resonance anomaly. Although ΔIm σ was not measured as a function of V_{ac} here, a reduction of ΔIm σ with increasing V_{ac} has been observed in $NbSe_3$.[10]

We now consider the resonance anomaly in Re $\sigma(\omega)$. By a simple Kramers-Kronig analysis, positive and negative peaks in Re $\sigma(\omega)$ must occur if a sharp, negative resonant peak

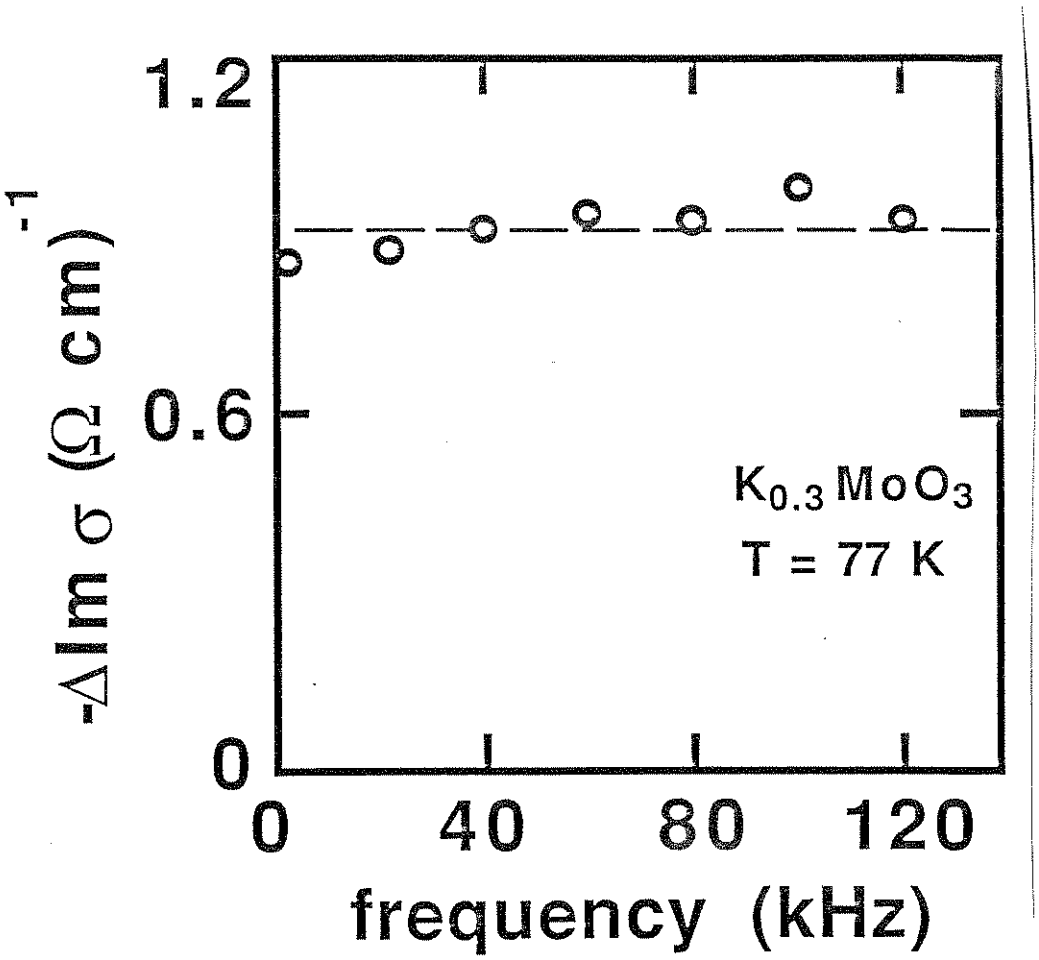

Figure 5-11 The magnitude ΔIm $\sigma(\omega)$ of the inductive dip in the imaginary part of the conductivity at resonance. The dip magnitude is roughly independent of frequency, with an average value of 1.0 ± 0.1 $(\Omega\ \mathrm{cm})^{-1}$ as indicated by the dashed line in the figure.

appears in Im $\sigma(\omega)$. In terms of the harmonic oscillator analogy discussed earlier, it would appear that off (but near) resonance ($\Delta f \neq 0$) the phase ϕ of the NBN signal relative to the ac probing signal must depart from the value at resonance ($\phi = -\pi/2$). In order to correctly account for the signs of the peaks in Re $\sigma(\omega)$ above and below $\Delta f = 0$, this phase angle must have the limiting behavior $\phi \Rightarrow -\pi$ for $\Delta f << 0$, and $\phi \Rightarrow 0$ for $\Delta f >> 0$. Further, the harmonic oscillator analogy would suggest that the inductive dip ΔIm σ should be twice as large as the size ΔRe σ of the peaks in Re σ. The ratio of these magnitudes in Fig. 5-6 is ΔIm σ/ΔRe σ = 1.7, while in Fig. 5-10 it is ΔIm σ/ΔRe σ = 1.9. Both values are in reasonable accord with the factor of two harmonic oscillator prediction.

The ac conductivity resonance effects reported here differ from those previously observed in $NbSe_3$ only in the relative sharpness of the anomalies in Re σ. In $NbSe_3$, the anomaly appears more as a step-like feature than as a pair of positive and negative peaks. The relative sharpness of this feature in a resonant harmonic oscillator is controlled by the damping parameter. With large damping, the resonance is broad and a pair of gradual peaks appear in the out-of-phase conductivity centered about the resonance frequency. As the damping falls to zero, these two features form into a sharp step-like anomaly which occurs exactly at resonance. This suggests that the damping related to the resonance in

$K_{0.3}MoO_3$ is larger that that in $NbSe_3$. As discussed in the previous section, the CDW in blue bronze is highly damped below 100 K,[30,35] whereas the CDWs in $NbSe_3$ are not effectively damped.[35] Hence, it would appear that the differences between the resonant anomalies in these two materials directly reflect the different relative CDW damping that exists within them.

There is still no complete understanding of why the NBN oscillations are $-\pi/2$ out of phase with the probing signal at resonance. The general features of these resonances in $\sigma(\omega)$ have been accounted for by numerical solutions of both a Frenkel-Kontorova model[30] and the tunneling model[10] (as yet, the predictions of the single particle classical model, Eqn. 5.9, have not been numerically calculated). In both cases, no effort was made to understand why the NBN signal is $-\pi/2$ out of phase with respect to the probing signal at resonance. In voltage-driven pulsed mode locking experiments, it has been found that the phase of the NBN oscillations are always $-\pi/2$ out of phase with respect to the start of the pulse.[36] Therefore, whatever the cause, the $-\pi/2$ phase shift between the NBN signal and an external ac signal at resonance appears to be a general feature of CDW response.

5.5 Conclusions

The results presented in this paper indicate that a highly coherent response can be obtained in very thin

$K_{0.3}MoO_3$ samples. Further, this strongly coherent sliding CDW state can couple with combined ac and dc fields to cause a variety of interference effects which are analogous to those seen in $NbSe_3$ and TaS_3. In particular, the CDW can be mode-locked to a large amplitude ac driving signal, resulting in the formation of Shapiro steps in a sample's differential resistance. The relative height of the Shapiro steps observed in blue bronze indicate that upwards of 50% of the CDW becomes locked to the external ac field. In the presence of small amplitude ac probing fields, the dc biased complex ac conductivity shows strong resonance features due to the interactions between the NBN signal and the probing signal. Although a CDW is a many particle system and in general must be described by a many particle Hamiltonian, both of these phenomena can be accounted for by using a simple phenomenological single particle equation of motion. This indicates that the CDW internal degrees of freedom can be neglected when describing, in a simple way, these ac-dc interference effects.

Analysis of the interference features present in the response of the CDW in $K_{0.3}MoO_3$ indicates that these phenomena exhibit evidence for strong damping of the charge density wave. This is evident both in the low frequency Shapiro step data and in the relatively broad resonance features which appear in the real part of the conductivity when $\sigma(\omega)$ is measured in the presence of a depinning bias.

Hence, although ac-dc interference phenomena appear to be universally exhibited by depinnable CDWs, underlying interactions within the CDW (i.e., internal degrees of freedom) manifest themselves as subtle variations in the overall resonant and mode-locked response.

Chapter 6: Transport properties of the heavy Fermion material URu_2Si_2

6.1 Introduction

In this chapter we examine the transport properties of the heavy Fermion compound URu_2Si_2.[1] Amongst the many heavy Fermion materials which show unusual electronic properties, URu_2Si_2 is unique in that it shows evidence for multiple and coexisting Fermi-surface instabilities. Previous work on URu_2Si_2 has demonstrated that, in addition to exhibiting a large effective mass ($m^* \approx 25m_e$) and a superconducting ground state below T_c=1.5K, this material displays anomalous behavior in electrical resistivity, magnetic susceptibility, and specific heat near a "transition" temperature of T_p=17.5K.[2-6] These anomalies are analogous to those seen in materials which undergo charge or spin density wave transitions. For this reason, it has been suggested that the anomalous behavior near T_p results from the formation of a conduction electron charge density wave (CDW) or spin density wave (SDW),[2] or from antiferromagnetic ordering.[4,6] Recent neutron scattering experiments on a single crystal of URu_2Si_2 indicate that antiferromagnetic ordering occurs below T_p with a small ordered moment of $\sim 0.03\mu_B$ and a modulation along the (100) direction.[7] This antiferromagnetically ordered state appears to coexist with the superconducting state below T_c.

The low-field dc electrical resistivity of URu_2Si_2 shows a small peak just below T_p, with a functional form very similar to the resistance anomalies observed below the CDW transition in $ZrTe_3$ and below both CDW transitions in $NbSe_3$.[8,9] The strongest evidence for density wave (either CDW or SDW) formation in URu_2Si_2 comes, however, from specific heat measurements which show a BCS-like anomaly near 17.5K, consistent with a 40% destruction in Fermi surface area.[2]

To better characterize the properties of this material, we present careful thermoelectric power (TEP) and Hall effect measurements on URu_2Si_2 between room temperature and 4.2K. Above T_p, these transport properties are similar to those exhibited by other heavy Fermion systems. Near T_p, both the Hall constant and TEP show anomalous behavior which are consistent with CDW or SDW formation. Our measurements support the notion that the 17.5K transition is a density wave Fermi surface instability; however, we are not able to distinguish clearly between CDW or SDW formation.

6.2 Experimental techniques

Our transport measurements were performed on polycrystalline samples of URu_2Si_2 prepared by the usual arc melting method. The TEP was measured using a slow ac heating technique.[10] Small samples of URu_2Si_2 were suspended in vacuum between a pair of crystalline quartz blocks and 1-mil

gold leads were attached to the sample ends with conductive silver paint. Both quartz blocks were wrapped with independent manganin heater wire which was used to ramp a temperature gradient of varying magnitude and direction across the sample. The temperature gradient was monitored with a chromel-constantan thermocouple. The thermally-induced EMF across the sample was amplified with a low noise amplifier and detected with an X-Y recorder.

The Hall effect was measured via a five-contact method,[11] where a low-frequency ac (200 Hz) current source and three current contacts are used to null the zero magnetic field misalignment voltage. The Hall signal was detected with a low noise impedance matching transformer and a lock-in amplifier. Electrical contacts were made with conventional silver paint techniques. Hall effect measurements were performed on a sample with dimensions of 1.3 mm x 0.6 mm x 0.1 mm, with the H field aligned parallel to the smallest dimension to maximize the Hall signal.

6.3 Experimental results

Figure 6-1 shows the TEP S(T) of URu_2Si_2 measured between 300K and 4.2K. Between room temperature and approximately 120K, the TEP is temperature independent and approximately +2μV/K. Below 150K, the TEP tends towards zero at 70K and then becomes more negative with decreasing temperature. At 18K, the TEP has attained a value of

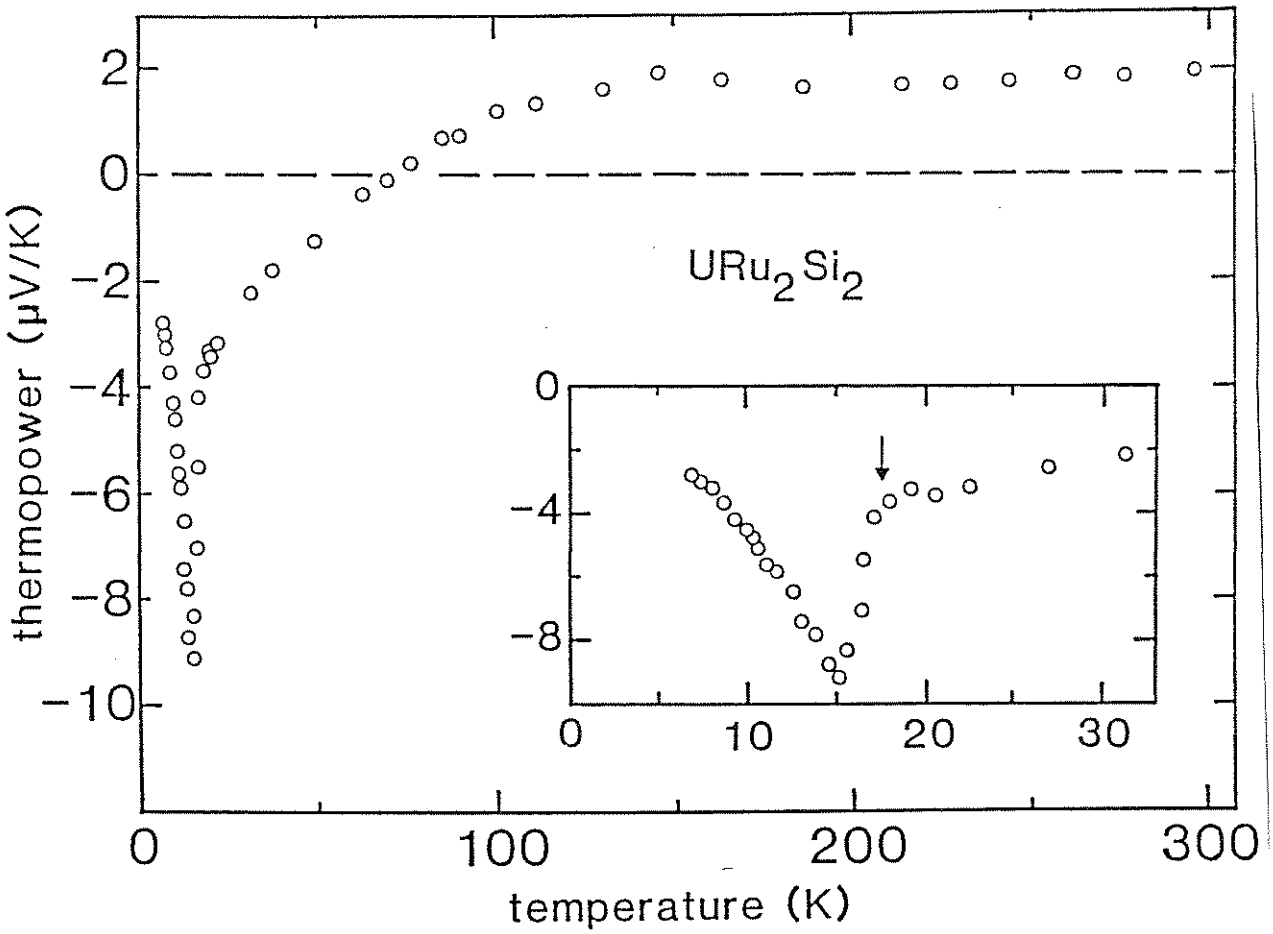

Fig. 6-1 Absolute thermoelectric power of URu_2Si_2 versus temperature. The inset shows in detail the behavior near the transition temperature, indicated by a vertical arrow.

-3.6μV/K. At T=17.5K, there is an abrupt change of slope in the TEP versus temperature curve, from $dS/dT=0.06\mu V/K^2$ at 18K to $dS/dT=2.4\mu V/K^2$ at 17K, signaling a thermodynamic phase transition at T_p=17.5K. Below 17K the TEP continues to increase in magnitude with decreasing temperature, until a dramatic change in direction occurs at T=15K. Below 15K, the TEP appears to smoothly approach zero with decreasing temperature. The inset in Fig. 6-1 shows the TEP behavior near the 17.5K transition in detail. The change in slope in the TEP at 17.5K is good evidence for a Fermi surface instability where free carriers are removed at T_p. The additional sharp reversal at 15K is an apparently independent effect, not associated with any structural transitions.

The results of Hall effect measurements between 300 K and 4.2 K in a magnetic field of 10 kG and a current density of 17 A/cm^2 are shown in Figs. 6-2 and 6-3. The Hall constant R_H is positive and linear in both current density (up to 17 A/cm^2) and field strength (up to 10 kG) at all temperatures examined in this study. The Hall constant at room temperature is $R_H = 1.5\times10^{-9}$ m^3/C. As the temperature is reduced below 300 K, R_H gradually rises until it reaches a maximum value at T_{max} = 50 K of $R_H = 7.4\times10^{-9}$ m^3/C. Below T_{max}, R_H falls until it appears to reach a constant value of $R_H = 4.0\times10^{-9}$ m^3/C below 25 K. At T_p = 17.5 K, the Hall constant abruptly increases and saturates at a value of $R_H = 20.0\times10^{-9}$ m^3/C at temperatures below 12 K. This abrupt

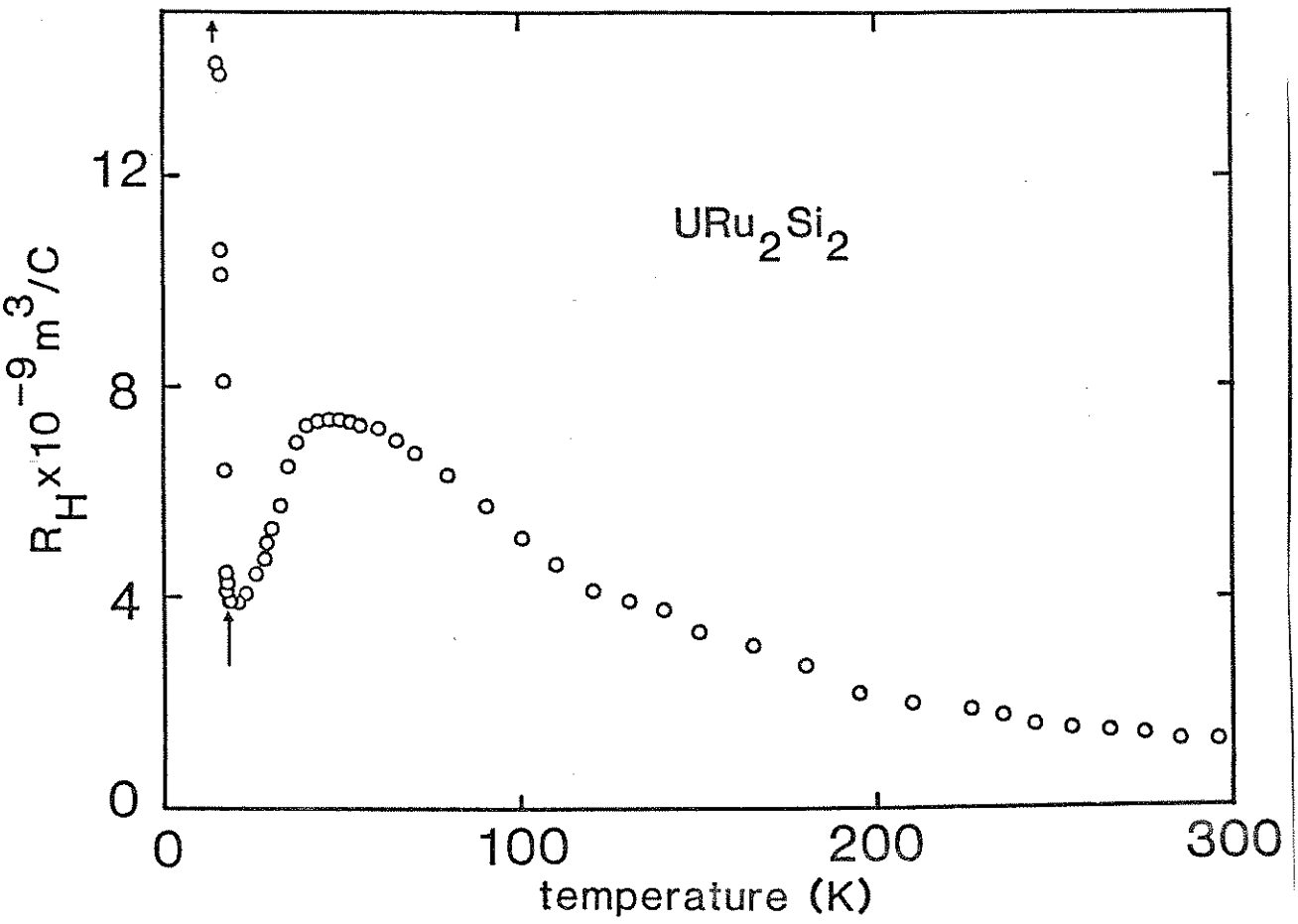

Fig. 6-2 Hall constant of URu_2Si_2 in a magnetic field of 10 kG and at temperatures below 300 K. The arrow indicates the 17.5 K transition temperature.

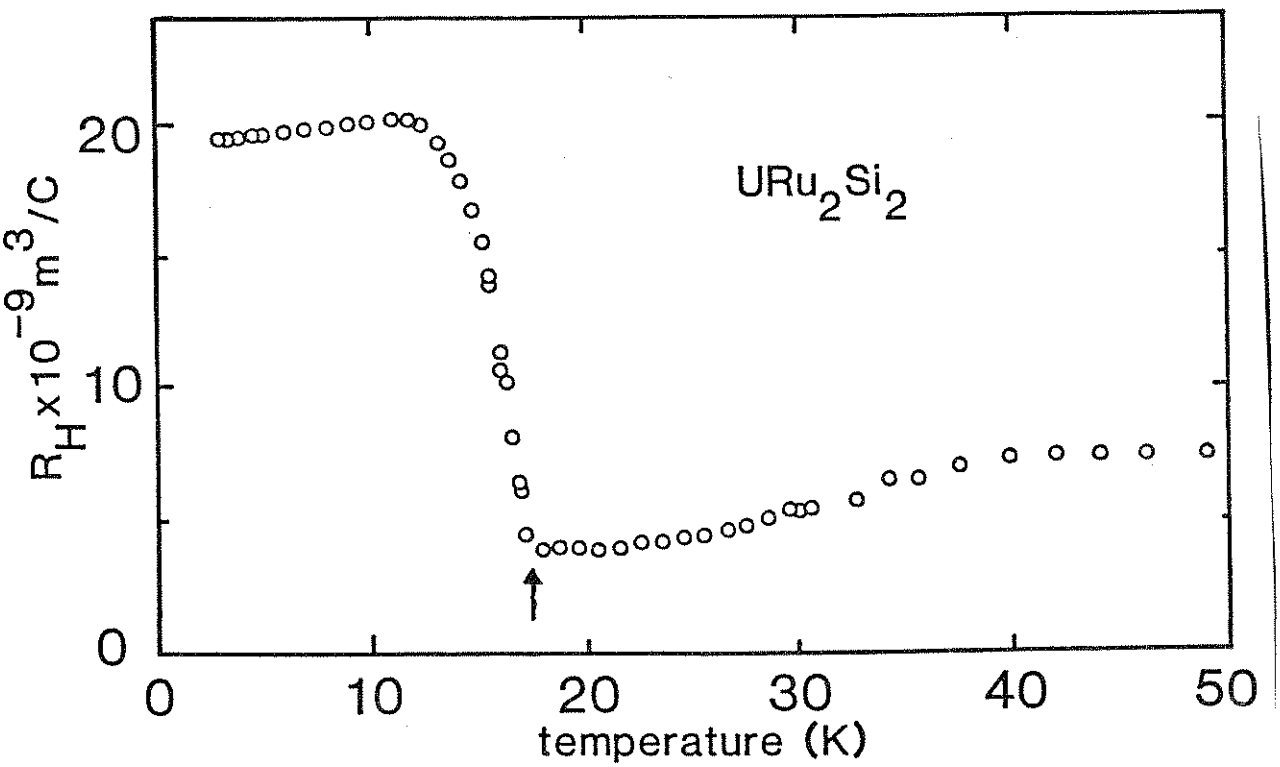

Fig. 6-3 Hall constant of URu_2Si_2 in a magnetic field of 10 kG and at temperatures below 50 K. The 17.5 K transition is indicated by the arrow.

change in R_H at 17.5 K is again solid evidence for a Fermi surface instability wherein a large fraction of the free carriers are removed at T_p. Note that unlike the TEP, the Hall effect data show no additional anomaly at 15K.

6.4 Discussion

The Hall effect in URu_2Si_2 above 17.5 K is quite similar to that exhibited by nearly all other heavy Fermion compounds.[12-21] Generally speaking, heavy Fermion systems all show a broad maximum in R_H centered at a temperature T_{max} which ranges from 1 K ($CeAl_3$) to 100 K (UAl_2).[14] At both high ($T >> T_{max}$) and low ($T << T_{max}$) temperatures, R_H saturates to a constant positive value. A number of theories have been proposed to account for this general temperature dependence.[14,22,23] They all assume that R_H is composed of a temperature independent, residual (normal) Hall constant plus an anomalous temperature dependent Hall constant which reflects the special scattering properties of a heavy Fermion system. The temperature dependence of the anomalous Hall constant stems from the fact that all heavy Fermion systems enter a coherent low temperature state[14] below T_{max}, where charge carrier scattering becomes markedly reduced. Hence, at $T << T_{max}$ the charge carrier mobility reaches a maximum value. This is directly responsible for the minima observed at low temperatures in both the Hall constant and the resistivity.[2] As T approaches T_{max} from

below, intrinsic scattering increases rapidly as fluctuations away from this coherent state begin to develop. The fluctuations reach a maximum near T_{max}, beyond which the system is no longer in a coherent state. Hence, for $T > T_{max}$, these materials enter an incoherent regime where scattering becomes dominated by independent single particle interactions. As T increases above T_{max}, the system acts more and more like a "normal" electronic system, albeit with a large effective mass. At $T >> T_{max}$, the anomalous contribution to the Hall constant drops to zero, leaving only the normal carrier contribution to account for the measured Hall signal.

The data in Figs. 6-2 and 6-3 indicate that the coherence temperature in URu_2Si_2 is roughly 50 K, a fairly typical value for these heavy Fermion systems. The Hall constant appears to saturate at room temperature to a value of $R_H = 1.5 \times 10^{-9}$ m^3/C. Assuming that the anomalous contribution to R_H is negligible at this temperature, the room temperature Hall constant yields a value for the charge carrier concentration of $n = 4.2 \times 10^{21}$ cm^{-3}. URu_2Si_2 forms in a tetragonal lattice with parameters of a = b = 4.13 Å and c = 9.58 Å.[2] With the unit cell volume determined from these lattice parameters (Ω = 163 $Å^3$), the room temperature Hall constant suggests that there are 0.7 holes per unit cell. This value is roughly equivalent to that found in other heavy Fermion materials.[14] Unfortunately, the absence of band

structure calculations for this material makes it impossible to compare this value with theory.

Below 17.5 K, the large increase in the Hall effect is indicative of the occurrence at 17.5 K of a phase transition wherein a large portion of the Fermi surface is destroyed. The change in R_H would suggest that roughly 80% of the Fermi surface was destroyed in this transition, twice what specific heat measurements indicate. Abrupt changes like this have been observed in materials which undergo either a spin or charge density wave transition.[24,25] Hence, although it is clear that URu_2Si_2 undergoes a Fermi surface based transition at 17.5 K, it is impossible to determine, based solely on this Hall effect data, whether the transition leads to the formation of a SDW or CDW.

We now turn to an examination of the thermopower data. The TEP of URu_2Si_2 at temperatures above the 17.5 K transition is similar to that previously observed in other heavy Fermion compounds, in particular cerium based 4f systems.[26,27] In $CeCu_2Si_2$, for example, the TEP is positive at room temperature, gradually decreases with decreasing temperature and becomes negative near 80K, reaches a negative maximum near 20K, and then drops to zero as temperature goes to zero. This behavior has been attributed to the presence of an extremely narrow feature in the density of states N(E) near the Fermi level that is associated with the 4f electrons.[27] The very similar temperature dependence of the

the TEP in URu_2Si_2 for moderate temperatures (T>18K) would suggest that a similar interpretation is in order, i.e. the TEP reflects directly the narrow features in N(E). The existence of these narrow features in the band structure of heavy Fermion materials is closely interrelated with the low temperature coherent state that these materials also exhibit.

In URu_2Si_2 the narrow feature in N(E) is expected to be on the order of 100K, according to transport, thermal, and magnetic measurements that have been previously reported.[2-4] As such, the resulting TEP is quite unlike that observed in conventional metals, where the bandwidth is typically several orders of magnitude larger. In the latter case, temperature changes have little effect on the density of states at the Fermi level.

We analyze the TEP in terms of the semiclassical model where the diffusion TEP S_D is expressed in terms of the dc electrical conductivity σ as[28]

$$S_D = -\frac{\pi}{3}\frac{k_B^2 T}{|e|}\frac{\sigma'(E_F)}{\sigma(E_F)} \qquad (6.1)$$

where the derivative is made with respect to energy and is evaluated at the Fermi level E_F. The conductivity may be expressed in terms of Fermi surface parameters as[29]

$$\sigma = \frac{1}{3} e^2 \tau_F v_F^2 N(E_F) \quad , \qquad (6.2)$$

where τ_F is the relaxation time, v_F the mean Fermi velocity averaged over the Fermi surface, and $N(E_F)$ is the density of states at the Fermi level. In normal metals the band structure terms v_F and $N(E_F)$ are usually taken as independent of temperature, resulting in a TEP linear in temperature (Eqn. 6.1). This neglects the phonon-drag contribution to the TEP, which can be appreciable below 100 K. Any deviation from linearity indicates that scattering mechanisms are coming into play which alter the TEP temperature dependence by way of $\tau_F(T)$ in Eqn. 6.2.

The gradual change in the TEP of URu_2Si_2 between 140K and 20K observed in Fig. 6-1 can be explained in terms of an extremely narrow resonance near E_F. In URu_2Si_2, the origin of the resonance feature is not yet clear, but it is probably tied to the narrow 5f electron band.

We consider the narrow resonance feature superimposed on a wide 6d band. The resonance is characterized by a maximum in the density of states at a characteristic energy E_o ($N(E_o)=N_{max}$). At energies above and below E_o the density of states drops rapidly. Hence, at temperatures above the resonance width, the Fermi level will lie in the 6d band where no temperature dependent effects exist to influence the TEP; any deviation from linearity must be ascribed to a

temperature dependent scattering mechanism. In particular, a temperature independent band structure and a relaxation time inversely proportional to temperature would result in the flat TEP observed in Fig. 6-1 between 300K and 120K.

As the temperature is reduced, the Fermi level will drop into the narrow resonance and the density of states at E_F will be very temperature dependent. With E_F greater than E_o, $N(E_F)$ will increase with decreasing temperature. Hence, $N'(E_F)$ in Eqn. 6.1 will be negative, giving rise to a positive TEP. As the temperature is further reduced, $N(E_F)$ will decrease; $N'(E_F)$ then becomes increasingly positive leading to a negative TEP.

The predicted behavior, i.e., a TEP that is constant and positive at high temperature, gradually falls to zero as T approaches $T_o \equiv E_o/k_B$, gradually becomes more negative as the temperature drops further, is entirely consistent with the observed behavior in URu_2Si_2 at temperatures above 18K. Within the context of this simplified model, we may explicitly deduce the resonance width to be D≈140K and resonance temperature to be T_o = 70 K. This value is quite close to the coherence temperature T_{max} as deduced from Hall effect measurements. This suggests that the low temperature coherent state evident in Hall effect and resistivity measurements is closely related to the narrow resonance in the 5f conduction band.

Below 18K the TEP of URu_2Si_2 is dramatically different

form that observed in other heavy Fermion materials. The abrupt change in slope at T_p=17.5K suggests that a second order phase transition occurs at that temperature. From the anomaly in the specific heat, it has been estimated that 40% of the Fermi surface is destroyed at this transition.[2] The behavior of the TEP just below T_p indicates that a predominantly hole-like part of the Fermi surface is affected; the TEP becomes more negative as the electron-like portion of the Fermi surface becomes less compensated. Similar features in TEP are observed at T_p in materials which undergo CDW or SDW transitions.[30,31] From the behavior of the TEP, it is not possible to distinguish between CDW or SDW formation.

The behavior of the TEP at 15K is even more dramatic than that observed at T_p=17.5K. At 15K the change in slope is extreme: $dS/dT=2.4\mu V/K^2$ just above 15K versus $dS/dT=-0.8\mu V/K^2$ just below 15K. This dramatic reversal is not reflected in any other transport measurement, and we do not associate it with a secondary phase transition. Because URu_2Si_2 is still metallic below 17.5 K, the thermopower must drop to zero as T drops to zero. Hence, it is not unexpected that the TEP shows a turn-around towards zero below 17.5 K. What is surprising though, is the relative abruptness of this turn-around in the TEP of URu_2Si_2. Interestingly enough, the abrupt reversal is very similar to that observed just below the SDW transition in the Bechgaard

salt $(TMTSF)_2PF_6$.[31]

6.5 Conclusions

Above 17.5 K, both the thermopower and the Hall coefficient of URu_2Si_2 are typical of a heavy Fermion system. The overall temperature dependence of both transport properties directly reflects the inherent nature of f-band conduction electrons. At and below 17.5 K, the behavior of both transport properties is consistent with a Fermi surface based phase transition at T_p = 17.5 K wherein a sizable fraction of the charge carriers are removed from the conduction band. Further measurements are required before the precise nature (CDW or SDW?) of the intermediate state (1.5 K < T < 17.5 K) can be determined.

Chapter 7: Temperature and frequency dependent conductivity of thin percolation films

7.1 Introduction

In this chapter we continue with our examination of the transport properties of anisotropic systems. We will here consider the temperature dependent ac conductivity of specially fabricated gold percolation films.[1] The films were made such that gold atoms do not completely cover the insulating substrate. Instead, the gold atoms form interconnecting clusters (networks) which allow percolative electronic transport to occur across the entire film. These networks possess an anisotropy quite unlike those previously considered in this thesis in that they can be characterized by a non-integer dimensionality ($D \approx 1.9$). This stems directly from the fractal, self-similar nature of these percolation clusters. Because of this fractal character, the transport properties of these films will be different from that of a typical two dimensional film. Instead, their transport properties will be determined by their percolative character.

These gold percolation films are best described within the realm of percolation physics. The field of percolation physics, with its close association with fractal geometry, has been actively studied during the past decade.[2] A wide

variety of research methods have been employed to develop an understanding of the many intriguing physical properties that these systems display. These methods have included the use of scaling theories[3] and computer simulations,[4-6] as well as the fabrication and study of physical percolation systems.[7-9] The percolation problem is concerned with the physics of dilute systems which are in the vicinity of a critical point. Both *Metal-insulator* and *metal-superconductor* mixtures are examples of percolation systems. Near the critical point, the system is characterized by a site-filling probability p which is close to the percolation threshold probability p_c. For values of p less than p_c, isolated clusters form which do not allow complete percolation to occur across the entire system; in a metal insulator system $\sigma_{dc} = 0$ for $p < p_c$. With $p > p_c$, a percolation network can form, yielding non-zero electrical conductivity in a metal-insulator mixture.

The scaling theory of percolation is concerned with the way in which physical properties of a system scale with the site-filling probability.[3] Scaling theories suggest that many physical properties of a percolation system should scale with the site-filling probability p. These properties scale as $|p-p_c|^{\alpha}$, where the critical exponent can be positive or negative depending upon the property in question. These critical exponents are theoretically independent of the underlying lattice. Hence, these are *universal* exponents which depend solely upon the dimensionality of the system

involved; only the percolation threshold p_c should depend upon the exact nature of the underlying lattice. For this reason, the properties of percolation systems are said to follow universal scaling laws.

A detailed scaling theory regarding the electrical conductivity of a percolation system indicates that scaling behavior will occur due to the self-similar, fractal nature of the percolation network.[3,10] This theory predicts that the dc conductivity should scale as

$$\sigma_{dc} \sim (p - p_c)^{\mu} \sim \xi^{-\mu/\nu} , \qquad (7.1)$$

where $\xi \sim |p-p_c|^{-\nu}$ is the percolation correlation length; this result holds for $p > p_c$. Because a complete percolation network can exist only for $p > p_c$, the dc conductivity is zero for $p < p_c$. In examining the frequency-dependent conductivity, the self-similar nature of the percolation network will also give rise to scaling between the ac conductivity and the applied frequency. Theories which account for the anomalous diffusion on the fractal network suggest that the resistance and capacitance should scale with frequency as[2]

$$R \sim \omega^{-x} , \qquad (7.2)$$

and

$$C \sim \omega^{-y} , \qquad (7.3)$$

where $x + y = 1$. This scaling behavior will exist for frequencies where the anomalous diffusion length L_d falls within the range $a << L_d << \xi$, where a is the microscopic lattice size.

Studies of extremely thin metal-insulator films indicate that they belong to the same universal class as the idealized percolation systems. These thin films are made by evaporating gold atoms onto an insulating substrate in such a way that a complete coverage of metal does not occur. Digitized transmission electron micrographs of these films have been analyzed using the techniques employed to study simulated percolation networks.[11] This research shows that these films are geometrically equivalent to an idealized percolation system, indicating that the results of scaling theory should apply to their physical properties. Room temperature ac conductivity measurements at frequencies up to 10 MHz were made to test this conjecture.[12] It was found that the resistance and capacitance do scale with frequency in qualitative agreement with the scaling theory, although the critical exponents (x and y) were found to be in disagreement with those predicted by the theory. This discrepancy was presumed to be due to the "non-ideal" nature of the system, perhaps arising from intercluster effects in the form of electron-electron interactions. Because the scaling theory does not take these interactions into account,

it is not surprising that the theory is not entirely successful in predicting the frequency-dependent conductivity of gold percolation networks. The anomalous behavior observed in room temperature ac conductivity data indicates that intriguing results might also be obtained by examining the transport properties of these films below room temperature.

In this chapter we present measurements of the ac conductivity of these thin gold films at frequencies between 100 Hz and 1 GHz and at temperatures between 300 K and 4.2 K. The ac conductivity is found to be very temperature-dependent below 100 K. A "transition" from a high temperature state which displays scaling ac conductivity to a low temperature state which displays highly modified scaling behavior occurs at roughly 35 K. This transition temperature appears to be insensitive to the parameters which characterize the fractal nature of the films. This indicates that the transition may arise from the underlying physical attributes of these films which are not accounted for in the scaling theory.

Both a description of the gold percolation films as well as the techniques used to measure their ac conductivity are presented in Sec. 7.2. The experimental data are presented in Sec. 7.3. The data is analyzed and a brief description of the scaling theory of ac conductivity is given in Sec. 7.4. We summarize our findings and discuss the direction of future research in Sec. 7.5.

7.2 Experimental techniques

The films used in this study were fabricated by researchers at the IBM Research Center in Yorktown Heights, New York. A complete description of the techniques employed to fabricate the films can be found in reference 9. The specimens consist of extremely thin gold films that have been evaporated onto insulating substrates. The nominal coverage of the films was kept very close to the percolation threshold coverage; the typical average film thickness was 6 to 10 nm. Because the substrate is not completely covered by gold atoms, the films are percolation systems with dc resistances in the range of 10 Ω to 1 MΩ. Previous TEM work performed on these films[11] suggests that they are geometrically analogous to a percolation system, with a typical microscopic lattice size of a $\approx$ 10 nm, percolation correlation lengths on the order of 100 nm, and a fractal dimension of D $\approx$ 1.9. Subsequent room temperature ac conductivity measurements at frequencies between 100 Hz and 10 MHz indicate that the films display scaling ac conductivity which qualitatively agrees with the scaling theory.[12] Significant deviations between the theorized critical exponents and those measured were attributed to electron-electron interaction effects.

In the research presented here, the ac conductivity was measured in the frequency range 100 Hz to 1 GHz using two different methods. In the low frequency range (100 Hz to 10

MHz), an HP 4192A low frequency impedance analyzer was used. In the high frequency range (4 MHz to 1 GHz) a computer controlled HP 8754A network analyzer was used to measure the conductivity. In this method, the sample forms the termination on the end of a rigid 50 Ω coaxial cable. The network analyzer reflects an RF signal off of this terminator/sample, and measures the resulting reflection coefficient Γ by comparing the reflecting and incident signals. Γ was corrected via a three point calibration technique; this correction also removed any phase offset due to electrical length mismatch. The ac conductivity was then determined from the corrected reflection coefficient via the relation

$$Z = \frac{1 + \Gamma}{1 - \Gamma}, \qquad (7.4)$$

where Z is the normalized impedance. The resistance is the real part of the impedance (Z=R+iX), while the capacitance is related to the imaginary part of the conductance (Y=G+iB) by $C=B/\omega$. Both methods employed to measure the ac conductivity provide very accurate resistance data at frequencies between 10 Hz and 1 GHz. The capacitance cannot be determined as accurately via these methods because they measure the conductivity ($B = C\omega$) more directly rather than the capacitance. Hence, with a capacitance of 100 pF and a

conductivity sensitivity of ± 1 μS, the capacitance will be measurable only above 10 kHz. For this reason, we report capacitance data only in the high frequency regime, starting at 10 to 100 kHz, with a sensitivity of roughly ± 0.1 pF. In both frequency regimes, care was taken to insure that a low signal level was used so as not to heat or damage the fragile samples. The samples were mounted on the end of a short (14 cm) section of 50Ω coax with a pair of 1 mil gold wires. The samples were surrounded by a copper cap wound with a manganin heater and this assembly was inserted into a gas flow system of our own design. This configuration allowed ac conductivity measurements ranging over seven orders of magnitude in frequency and at temperatures ranging from 300 K down to 4.2 K to be made.

7.3 Experimental results

The ac conductivity of a gold percolation film with a room temperature dc resistance of 380 Ω is shown in Figs. 7-1 to 7-5. The resistance and capacitance are essentially unaffected by changes in temperature above 100 K. The frequency-dependent resistance and capacitance at both 300 K and 100 K are presented in Fig. 7-1. The data is clearly the same at both of these temperatures. Similar measurements were made at 50 K intervals between 300 K and 100 K, and no change in the frequency-dependent behavior was observed. The resistance is independent of frequency below a critical

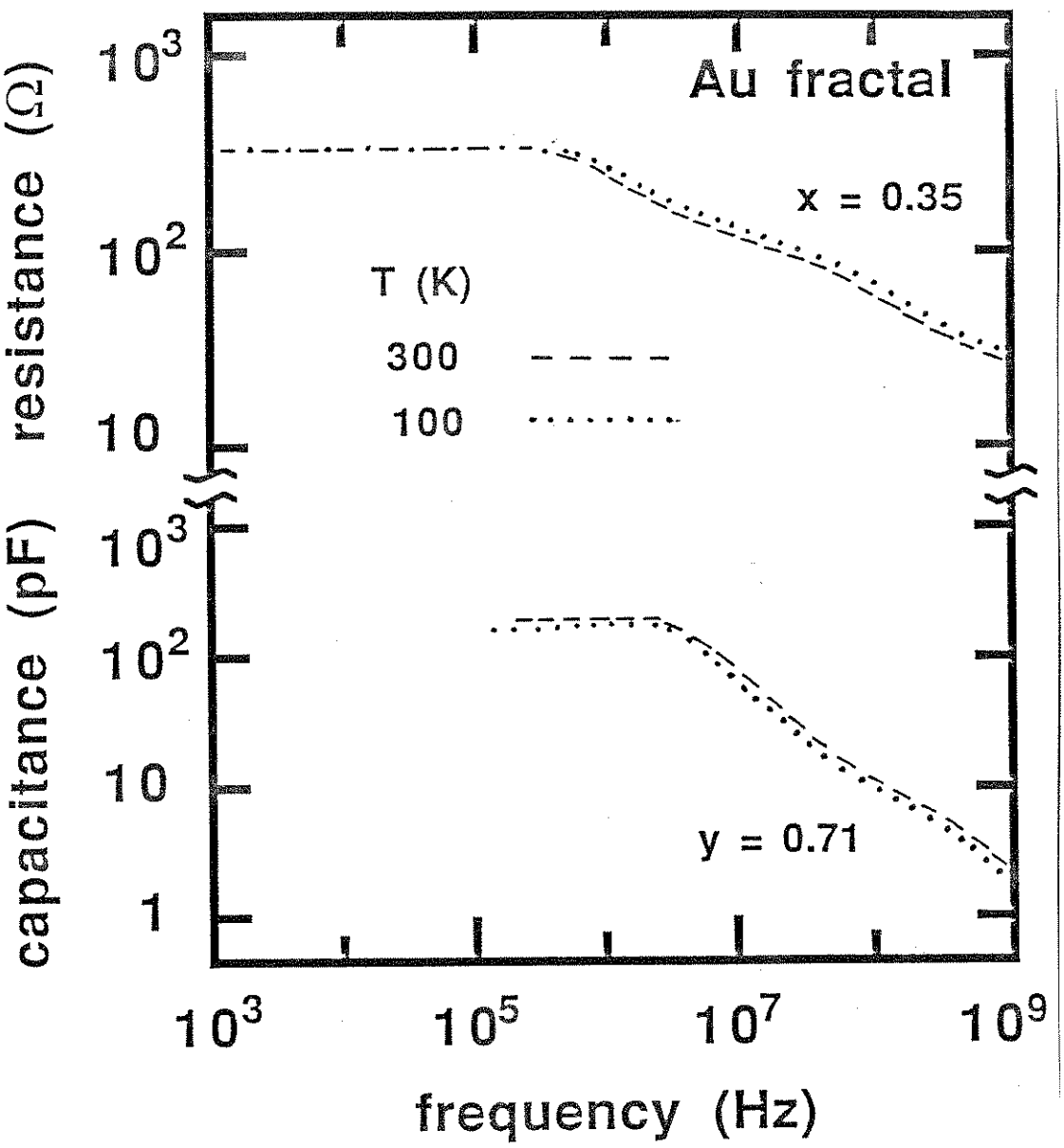

Fig. 7-1: Resistance and Capacitance data at both 300 K (dashed lines) and 100 K (dotted lines). The scaling exponents x ($R \sim \omega^{-x}$) and y ($C \sim \omega^{-y}$) are indicated in the figure.

frequency of $\omega_\xi \approx 300$ kHz, with a low frequency value of $R(\omega < \omega_\xi) = 380\ \Omega$. Similarly, the capacitance appears independent of frequency below roughly 2 MHz, with a low frequency value of $C_o = 200$ pF. Above these critical frequencies, both the resistance and the capacitance decrease with increasing frequency. At 1 GHz the resistance and capacitance have dropped to 25 Ω and 20 pF, respectively. When fit to the simple scaling frequency expressions as given in Eqn. 7.2 and 7.3, the high frequency behavior of the resistance and capacitance give values for the critical exponents of $x = 0.35 \pm .05$ and $y = 0.71 \pm .05$. Hence, above 100 K this gold percolation film displays the expected frequency scaling ac conductivity with no apparent temperature effects upon either the overall scaling behavior, the low frequency resistance, or the low frequency capacitance. In addition, there do not appear to be any effects of temperature upon the critical frequencies ω_ξ above which the ac scaling behavior occurs.

While the high temperature data are unaffected by changes in temperature, the low temperature resistance and capacitance data, as shown in Figs. 7-2 and 7-3, indicate that the ac conductivity changes drastically as the temperature is reduced below 100 K. In particular, the amount by which the resistance changes above ω_ξ decreases as the temperature drops. This is most evident in the data at 23 K where the resistance is constant at all frequencies up to 1 GHz. While the high frequency scaling behavior

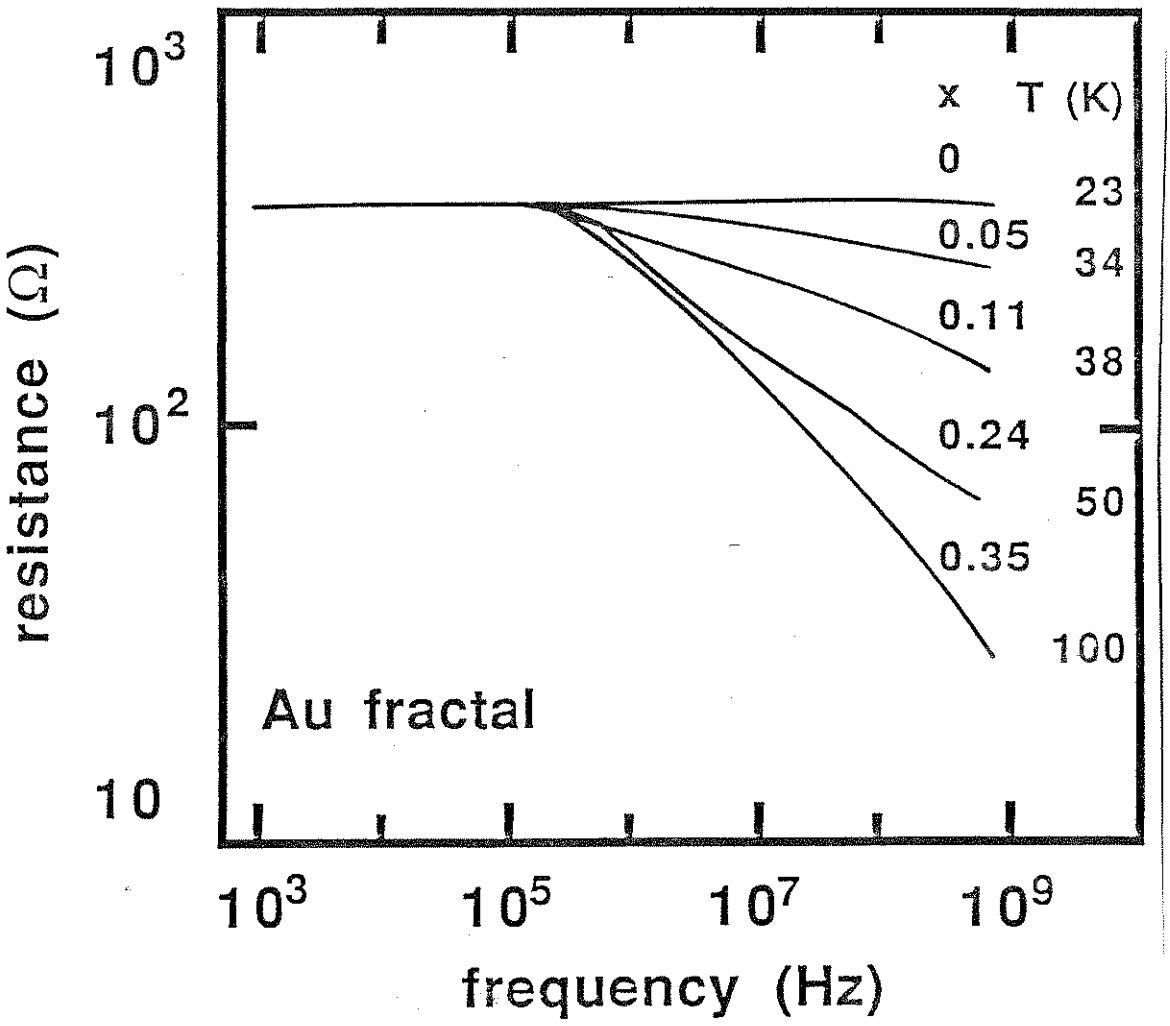

Fig. 7-2: Resistance data in the vicinity of T_c. The critical exponents x(T) are indicated in the figure.

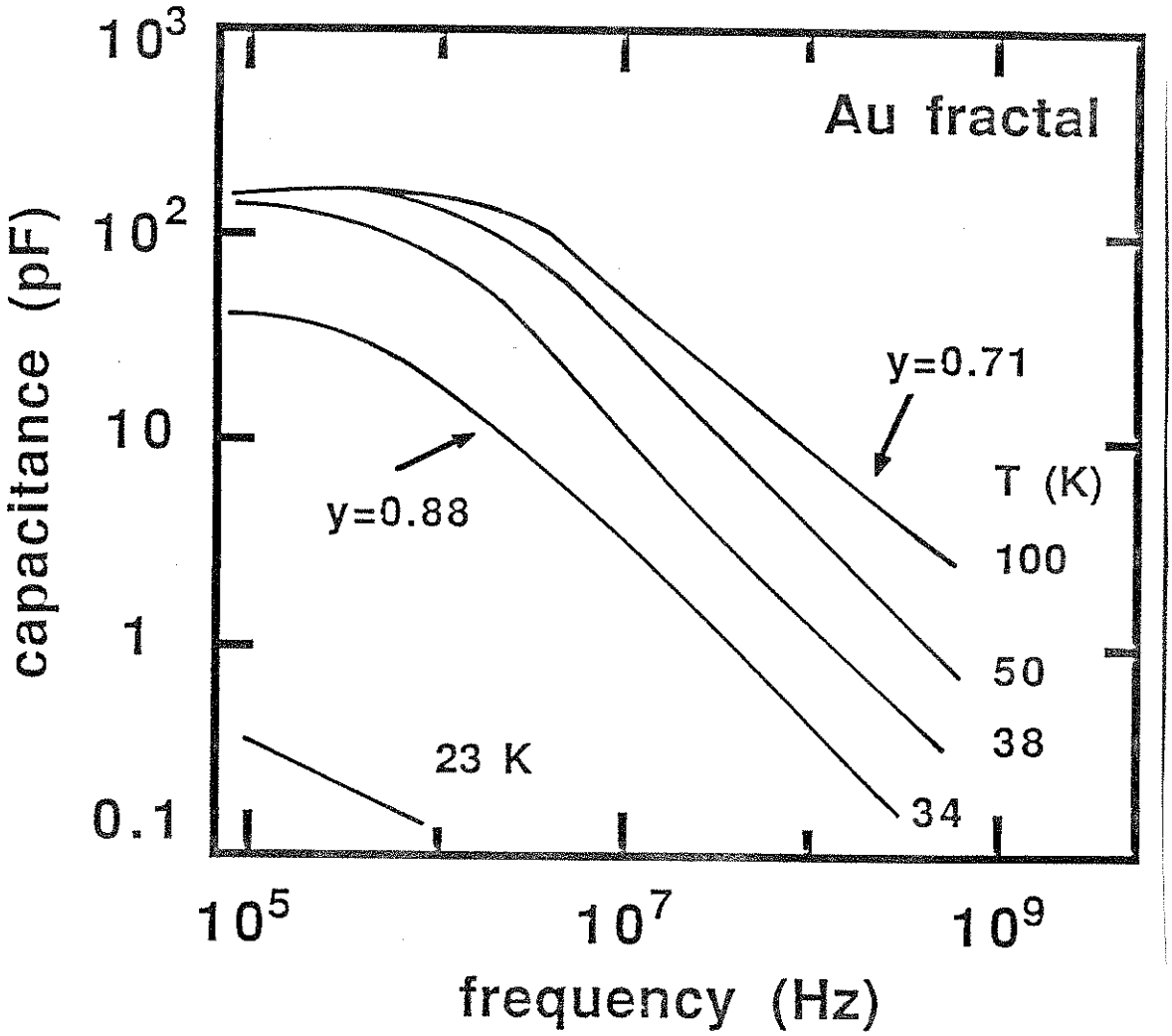

Fig. 7-3: Capacitance data in the vicinity of T_c. The critical exponents y(T) are indicated in the figure.

appears to diminish with dropping temperature, the resistance below the critical scaling frequency is unchanged by a reduction in temperature. In addition, the critical frequency remains independent of temperature. Hence, only the high frequency ac resistance above ω_ξ appears temperature-dependent. Below 23 K the percolation film shows no frequency scaling behavior, acting instead like a homogeneous metal. In terms of the scaling theory, it would appear that the critical exponent x, which controls the resistance at frequency above ω_ξ, drops to zero below 23 K.

The capacitance of the gold percolation film below 100 K is depicted in Fig. 7-3. The data indicate that the capacitance is also very temperature-dependent below 100 K. Between 50 K and 23 K the capacitance drops by roughly 3 orders of magnitude, but it still appears to scale with frequency. The critical capacitance exponent appears to reach a low temperature limit of y = 1. At 23 K the capacitance is less than the experimental sensitivity of 0.1 pF at all frequencies. As a result, it is impossible to determine if the capacitance scales with ω below 23 K.

The resistance and capacitance data are plotted as a function of temperature and grouped by frequency in Figs.7-4 and 7-5, respectively. The data clearly suggest that a "transition" occurs in the percolation film which is characterized by a transition temperature of T_c = 35 K. The effects of the transition begin to show up in the

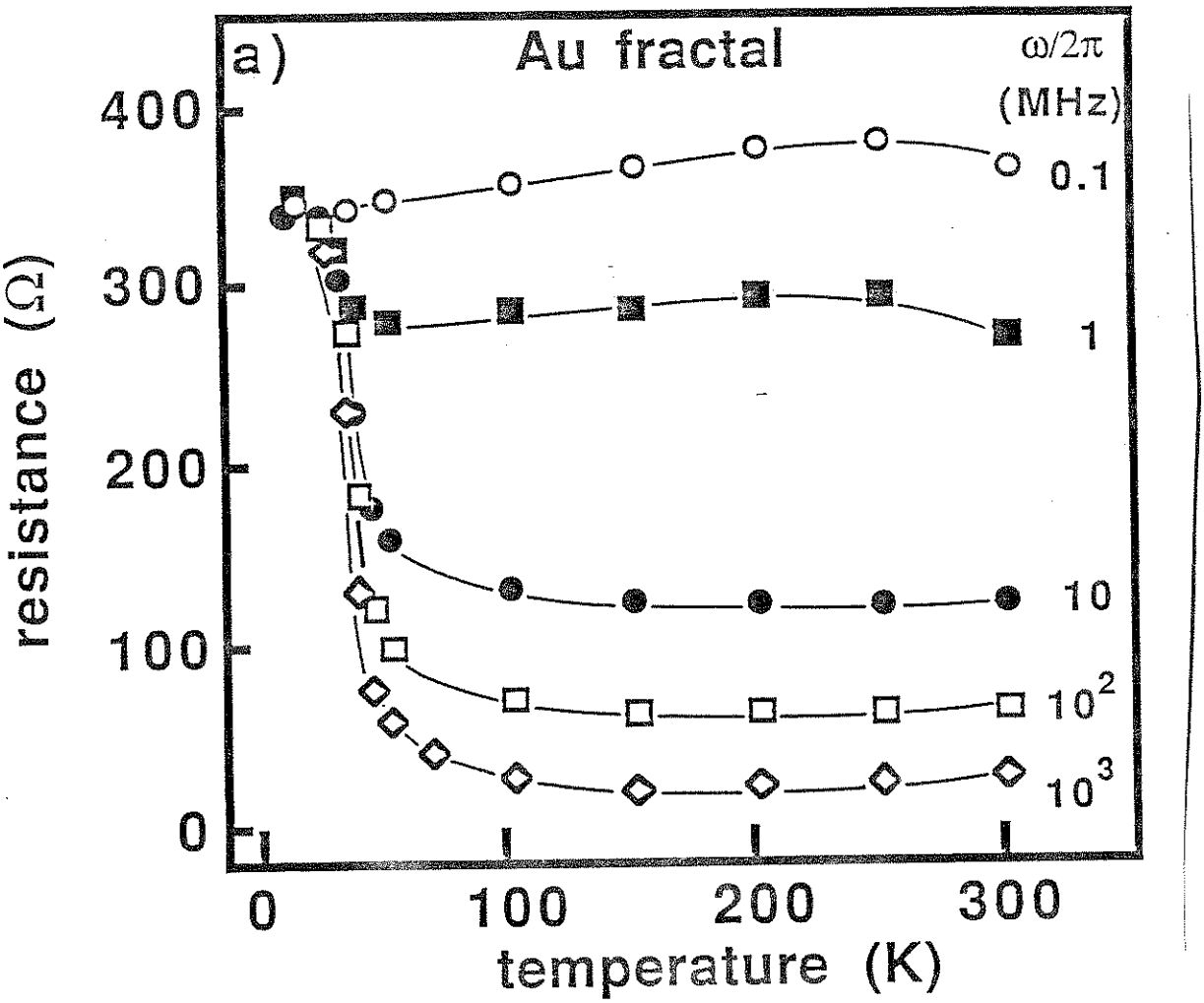

Fig. 7-4a: R(ω) plotted as a function of temperature below 300 K. The solid lines are intended as guides to the eye.

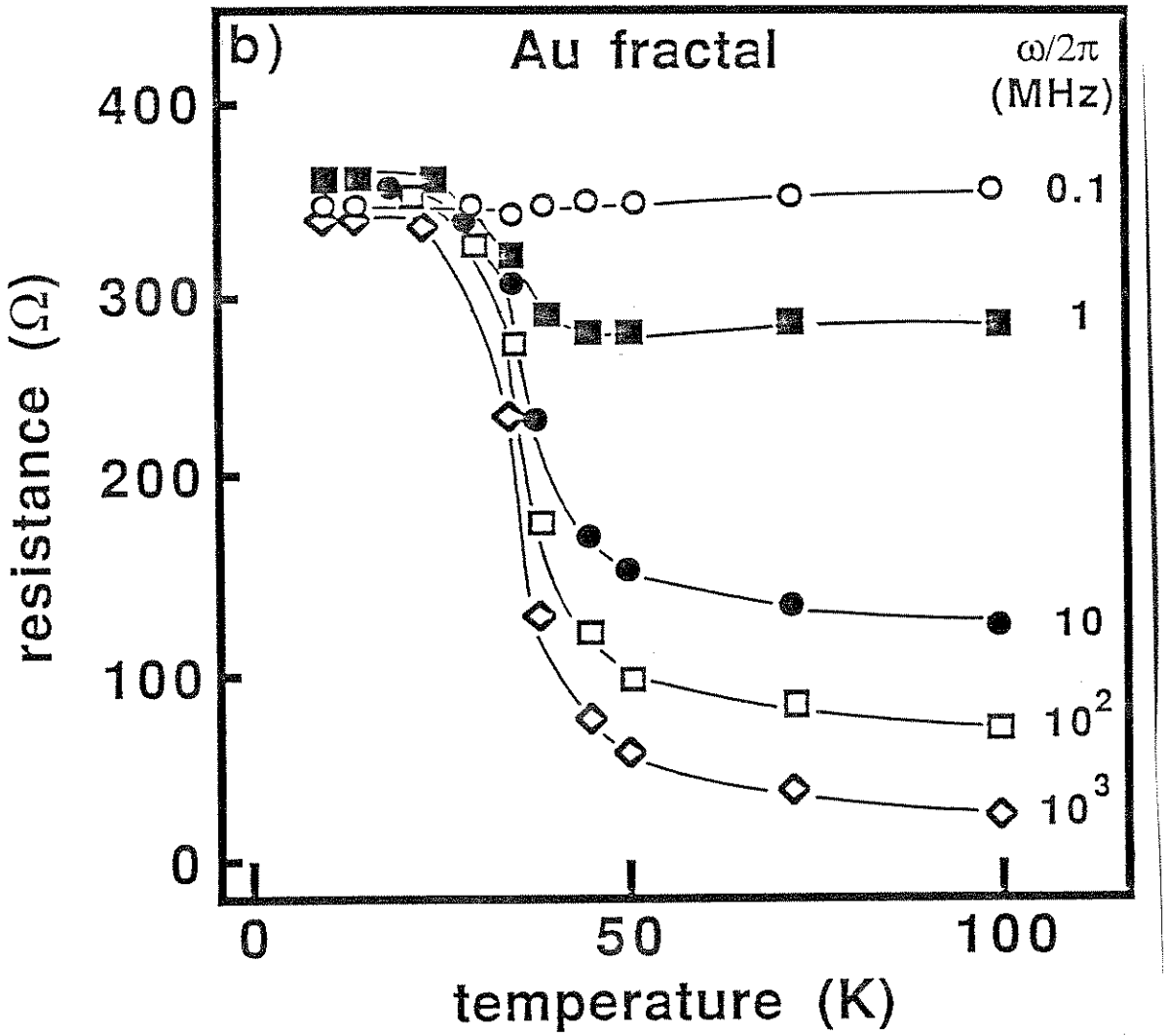

Fig. 7-4b: R(ω) plotted as a function of temperature in the vicinity of the transition. The solid lines are intended as guides to the eye.

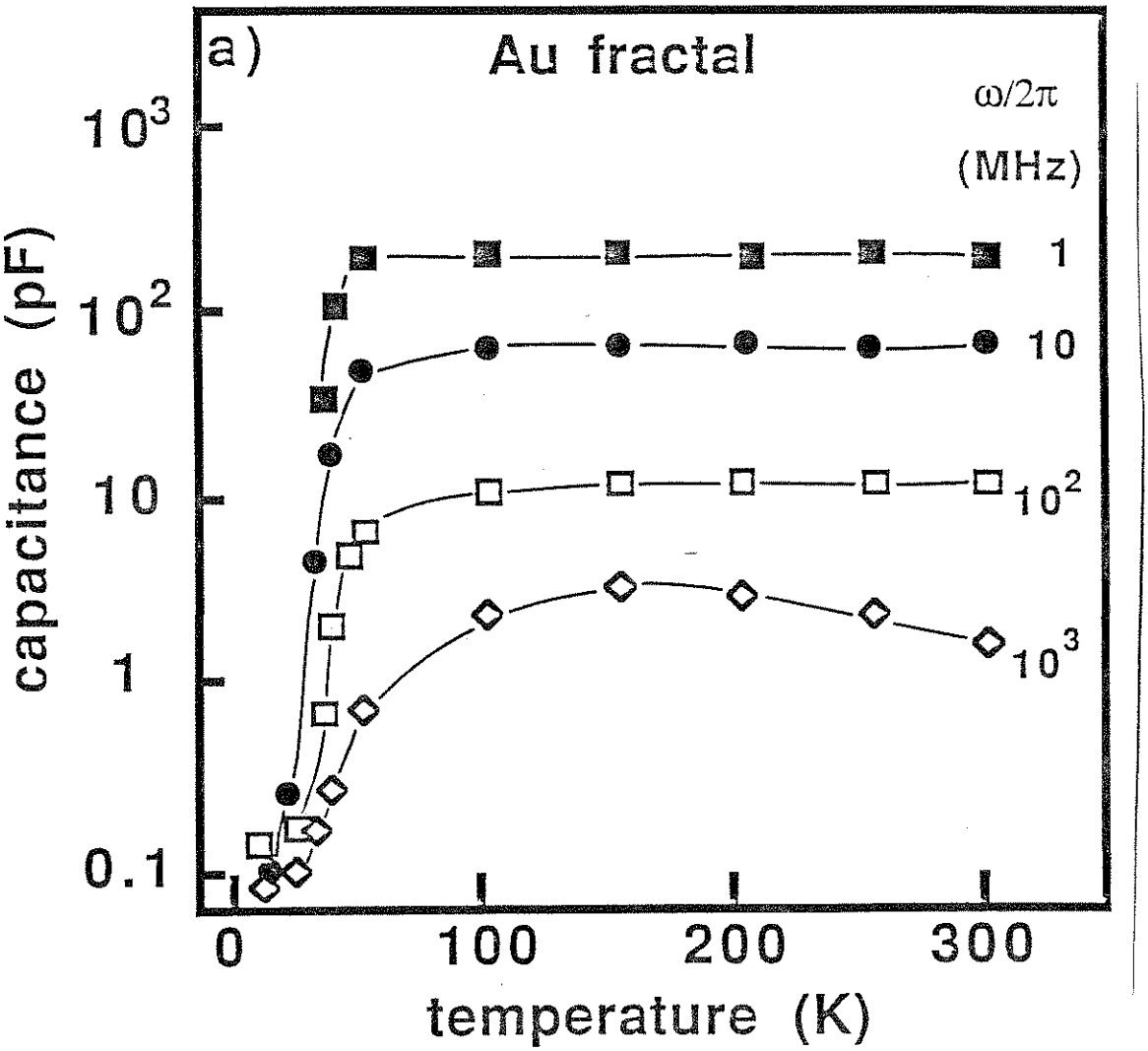

Fig. 7-5a: C(ω) plotted as a function of temperature below 300 K. The solid lines are intended as guides to the eye.

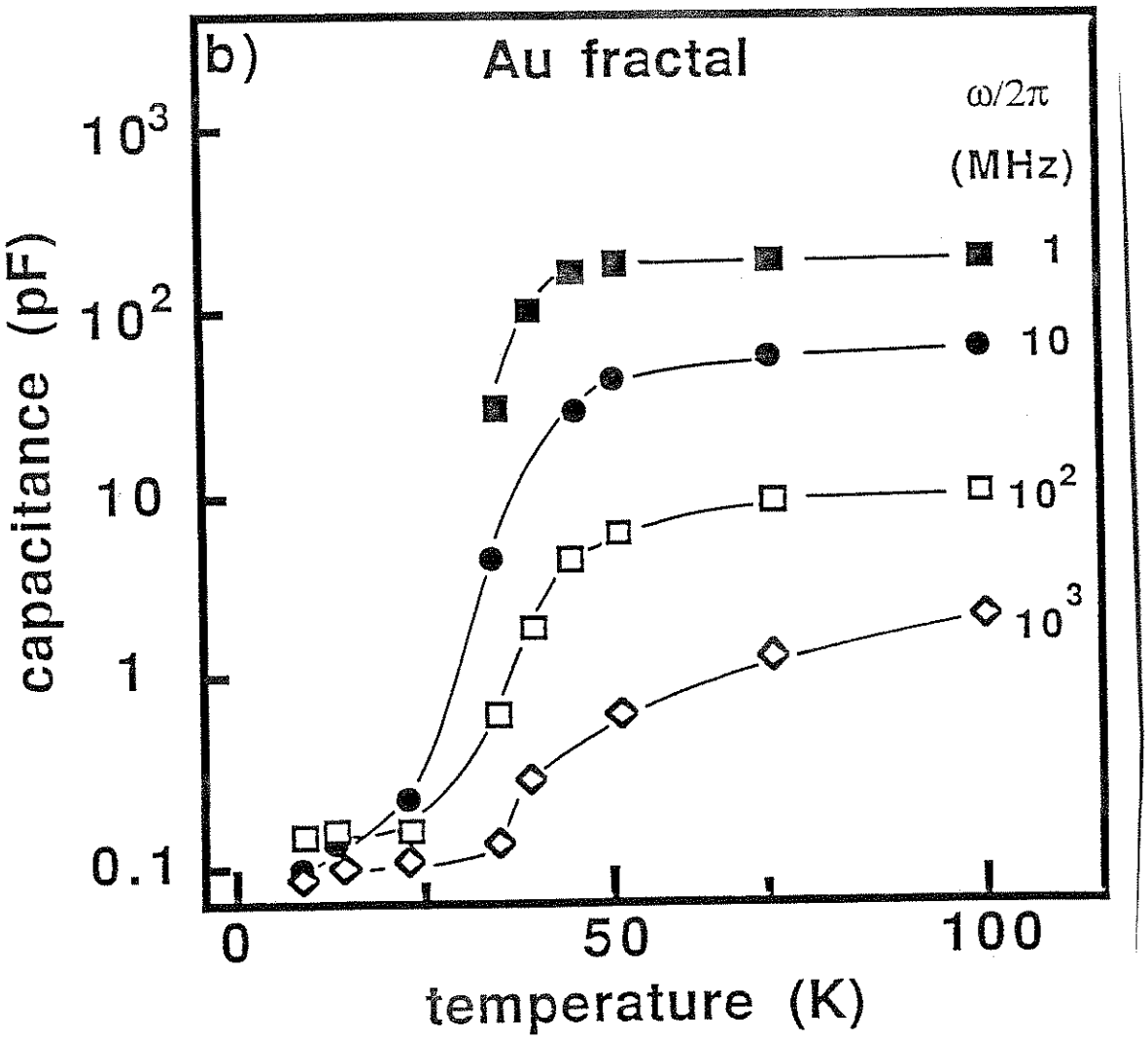

Fig. 7-5b: C(ω) plotted as a function of temperature in the vicinity of the transition. The solid lines are intended as guides to the eye.

frequency-dependent conductivity data at roughly 50 K, and the transition appears to be complete below 20 K. Hence, the transition width T_w is roughly 30 K.

Measurements on a number of other gold percolation samples show the same general temperature-dependent behavior with transition temperatures ranging from 35 K to 40 K. The dc resistances of the samples studied ranged over four orders of magnitude, from 90 Ω to 500 kΩ, with the 500 kΩ sample being very close to the metal-insulator percolation threshold. Because the dc resistance scales with the percolation correlation length, these samples span a wide range of percolation parameters, ranging from being very metallic ($p \approx 1$) to being very nearly non-metallic ($p \approx p_c$). As indicated in Fig. 7-6, the critical frequency ω_ξ (beyond which the ac conductivity scales with frequency) ranged from a low of 100 Hz to a high of 700 kHz. In all cases the temperature dependent ac conductivity is the same, with a transition near 35K to 40K separating a high temperature state which displays *scaling ac conductivity* and a low temperature state which exhibits *no scaling behavior*. Further, both the dc resistance and the critical frequency beyond which scaling behavior occurs are temperature independent. Only the transition width appears to be dependent upon the thin film percolation parameters. A rough correlation exists between the dc resistance, and hence the percolation correlation length, and the transition width.

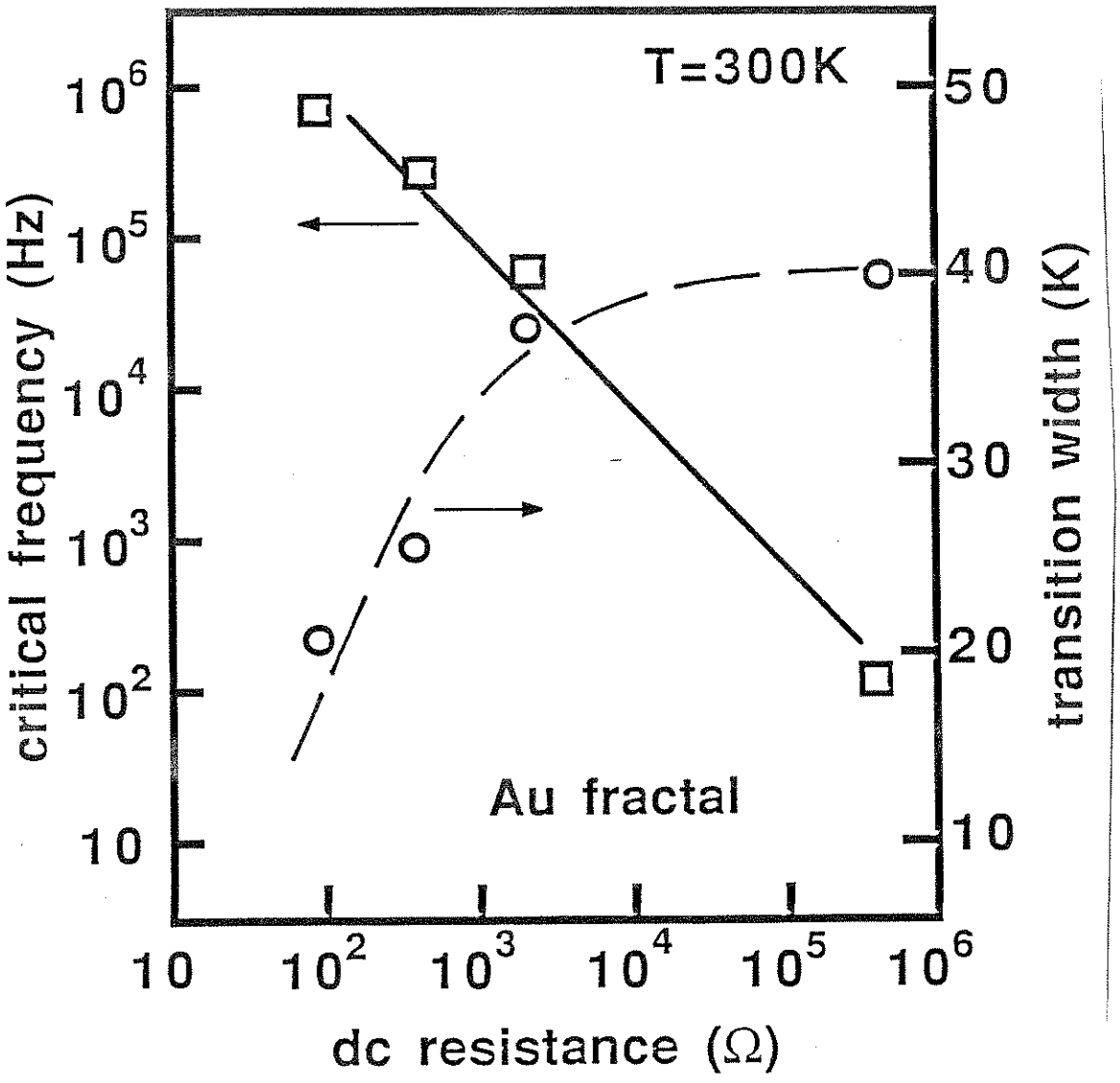

Fig. 7-6: Plots of critical frequency (squares) and transition width (circles) as a function of dc resistance. The dashed line is a guide to the eye. The straight line is a fit to $\omega_\xi \sim R_{dc}^{-.82}$.

As shown in Fig. 7-6, the transition width is an increasing function of the sample dc resistance. Note that the transition width does not appear to rise with increasing dc resistance above R_{dc} = 1 kΩ, where T_w appears to saturate at 40 K. Hence, the transition width does not appear to scale with the dc resistance in as simple a form as does the critical frequency.

The scaling behavior of the high temperature conductivity in the more resistive films appears more complicated than earlier work has suggested.[12] In particular, the low frequency film capacitances appear to be independent of the film parameters. While the four films examined here ranged in dc resistance over four orders of magnitude, the low frequency capacitance ($\omega < \omega_\xi$) for all films was 200 pF. Additionally, the frequency-dependent conductivity in films with low values of ω_ξ suggest that there are two frequency scaling regimes. This is evident in the room temperature ac conductivity of a film with R_{dc}=2.2 kΩ and ω_ξ = 60 kHz presented in Fig. 7-7. At frequencies between ω_ξ and 2 MHz, the resistance scales with a critical exponent of x = 1±.05, while the capacitance does not scale with frequency (y = 0). Above 2 MHz, the resistance exponent drops to x = 0.32±.05 and the capacitance exponent rises to y = 0.8±.05. In both frequency regimes the sum of the critical exponents is always one within the experimental uncertainty.

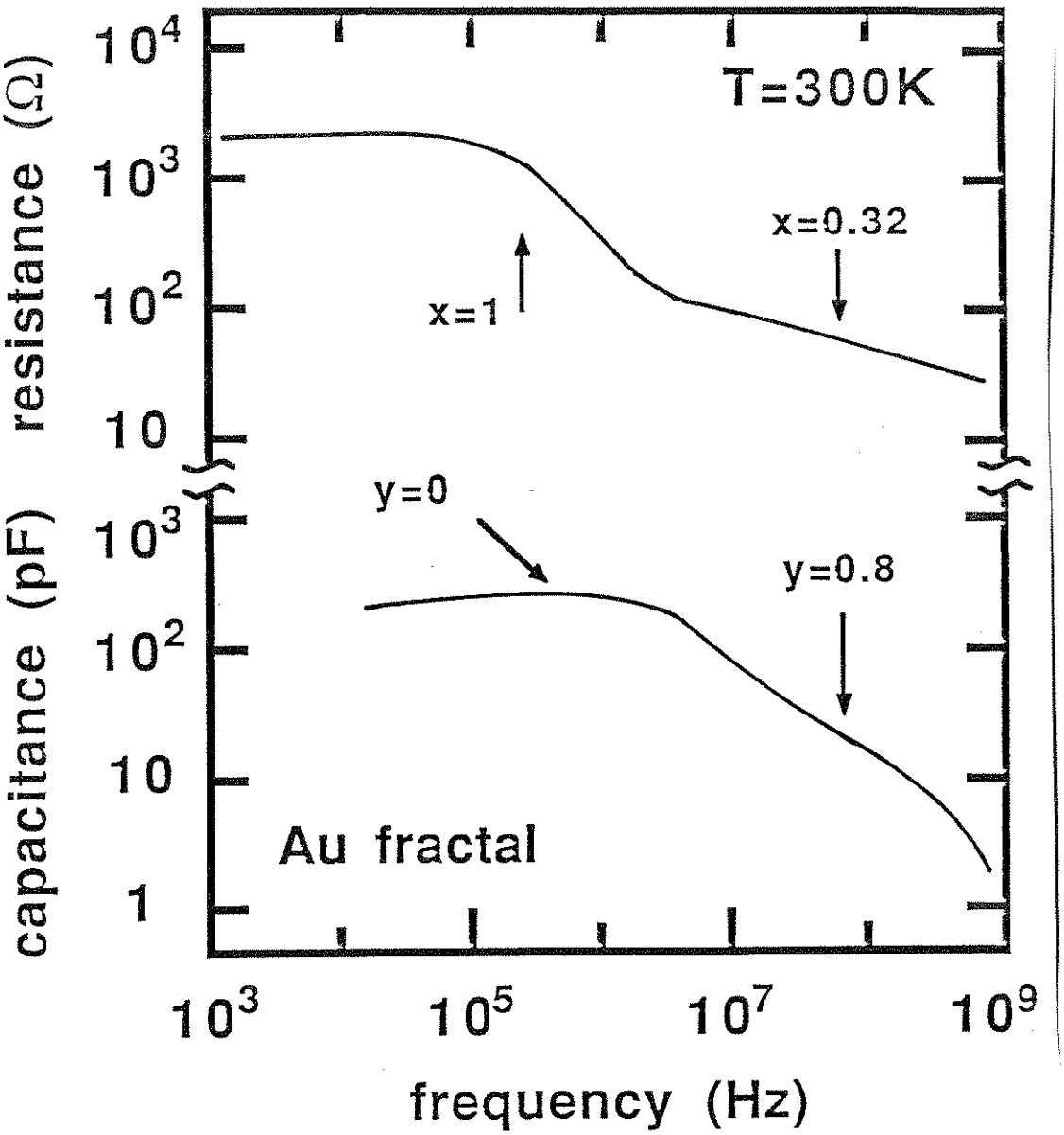

Fig. 7-7: Room temperature conductivity of an Au film with a larger dc resistance. The resistance and capacitance data are plotted as a function of frequency. The critical exponents, x and y, are as indicated in the medium (60 kHz < $\omega/2\pi$ < 2 MHz) and high frequency ($\omega/2\pi$ > 2 MHz) regimes.

7.4 Analysis

We first examine in some detail the theory which predicts that a scaling relationship should exist between the macroscopic properties of a percolation system and its underlying microscopic structure. This scaling theory is based on the premise that the many physical properties of a percolation system will scale with the site-filling probability p in the form $|p-p_c|^{\alpha}$,[3] where α is referred to as a critical exponent. The critical exponents that relate to the work here are: ν, the correlation length exponent, μ, the dc conductivity exponent, and β, the infinite network lattice exponent. The exponent ν determines the percolation correlation length, given by

$$\xi \sim |p - p_c|^{-\nu}, \tag{7.5}$$

where ξ is measured in units of the microscopic lattice length a. Hence, the correlation length is actually $a\xi$. Previous TEM studies[11] indicate that gold percolation films have a microscopic lattice size a $\approx$ 10 nm and a correlation length of roughly 100 nm, yielding $\xi \approx 10$. Computer simulations on two and three dimensional percolation networks suggest $\nu_{2D} = 1.35$ and $\nu_{3D} = 0.88$.[3,13]

For $p > p_c$, the critical exponent β determines the probability for a point in the lattice to belong to the

infinite network, $P_\infty(p)$. This probability is given by

$$P_\infty(p) \sim (p - p_c)^{\beta} \sim \xi^{-\beta/\nu} . \qquad (7.6)$$

The low frequency network capacitance C_o is also related to β by

$$C_o \sim \xi^{2-\beta/\nu} . \qquad (7.7)$$

Computer simulations yield $\beta_{2D} = 0.14$ and $\beta_{3D} = 0.4$.[3] The dc conductivity depends on the exponent μ and ν through the expression

$$\sigma_{dc} \sim (p - p_c)^{\mu} \sim \xi^{-\mu/\nu} . \qquad (7.1)$$

Computer simulations suggest $\mu_{2D} = 1.2$ and $\mu_{3D} = 2.0$.[3,13] The low frequency capacitance and resistance are clearly tied to the percolation correlation length. As a result, the scaling theory directly relates the behavior of R and C at high frequencies to the underlying nature of the percolation system through ξ.

These low frequency results represent averages taken over length scales L_s much larger than ξ. On these length scales, the percolation film appears homogeneous. As the

length scale over which the system is examined is reduced below ξ, its inhomogeneous nature becomes evident. Thus, when measuring the resistance at $L_s > \xi$, the film resistance should take on a constant value which reflects the macroscopic nature of the film (this resistance can be quite high because the infinite cluster is extremely thin). In the opposite extreme, with $L_s \approx a$, the gold film should act like a very perfect metal, because on this length scale, the measurement probes the gold atoms directly. For $a < L_s < \xi$, the fractal nature of the film will become less evident and the resistance should drop as L_s approaches a.

An ac signal at a frequency ω will measure the conductivity over a length $L(\omega) \sim 1/\omega$. Hence, at low frequencies where $L(\omega) >> \xi$, the resistance should be independent of frequency. Above a critical frequency ω_ξ, where $L(\omega_\xi) \approx \xi$, the signal will begin to probe within the percolation cluster and the resistance should drop. The capacitance is expected to behave in a similar fashion. At $\omega < \omega_\xi$ the intercluster capacitance will give rise to a non-zero total capacitance. As the frequency rises above ω_ξ, the signal probes more directly the metallic constituents which form the percolation network, and the capacitance should therefore drop.

Two separate methods have been employed to characterize the high frequency behavior of the resistance and capacitance in percolation systems.[9,13,14-16] Although the two theories

are based on different starting assumptions, they both predict that the resistance and capacitance should scale with frequency in the form

$$R \sim \omega^{-x} , \tag{7.2}$$

and

$$C \sim \omega^{-y} . \tag{7.3}$$

The two theories differ only in their expressions for x and y. In the *non-interacting cluster* approximation it is assumed that anomalous diffusion within a percolation cluster occurs.[9,13] This anomalous diffusion comes about because of the fractal nature of the infinite percolation network. When performing a random walk on the percolation backbone, the mean square distance traveled will scale with the travel time t in the form

$$\langle r^2(t) \rangle \sim t^{2/(2+\theta)} , \tag{7.8}$$

where θ is related to the critical exponents via $\theta = (\mu-\beta)/\nu$. The θ term in Eqn. 7.8 results from the self-similar nature of the infinite cluster; for a non-fractal system, $\theta = 0$, and the mean square displacement scales linearly with t, as expected for a non-fractal, Euclidean system. In two dimensions the values previously quoted for the critical

exponents give $\theta = 0.79$. By performing a Fourier transform and replacing the time in Eqn. 7.8 with frequency ($t \Rightarrow 1/\omega$) the frequency dependent length scale $L(\omega)$ becomes

$$L(\omega) \sim \omega^{-1/(2+\theta)} . \qquad (7.9)$$

The conductivity is calculated by relating this diffusion length to σ via the Einstein diffusion relation. In the non-interacting assumption, the critical exponents of the frequency dependent resistance and capacitance become[9,13]

$$x = \frac{\mu}{\nu(2+\theta)} = \frac{\mu}{2\nu - \beta + \mu} \qquad (7.10)$$

and

$$y = \frac{2\nu - \beta}{\nu(2+\theta)} = \frac{2\nu - \beta}{2\nu - \beta + \mu} , \qquad (7.11)$$

These exponents sum to one ($x + y = 1$) because the frequency dependence of both the resistance and capacitance are characterized by the same time scale.[10,12] These exponents hold in the critical frequency regime where $L(\omega) > \xi$. From Eqn. 7.9, this critical frequency is given by

$$\omega_\xi \sim \xi^{-(2+\theta)} \sim \xi^{-(2\nu + \mu - \beta)/\nu} . \qquad (7.12)$$

In two dimensions the values for μ, ν, and β suggest that the

scaling exponents should be x = 0.32 and y = 0.68.

The *intercluster polarization* approach assumes that scaling conductivity arises solely from intercluster effects.[14-16] In this model the neighboring clusters are linked together with an interaction capacitance. As a result, the critical resistance exponent x is unchanged from the previous result (Eqn. 7.10), while the critical capacitance exponent becomes

$$y = \frac{s}{\nu(2+\theta)} = \frac{s}{2\nu-\beta+\mu} \quad , \qquad (7.13)$$

where s is a critical exponent which characterizes the polarizability of the system. These two expressions for y (Eqns. 7.11 and 7.13) are equivalent only if $s = 2\nu - \beta$. It is theoretically unknown if this equality holds true in all dimensions,[9,17] although it has been suggested that the equality $s = \mu$ may be true in two dimensional space.[18-20] With the accepted values for the critical exponents, this would give x = y = 0.32, which is in disagreement with the requirement that x and y sum to one. By requiring both that x + y = 1 and $\mu = s$, x and y become x = y = 0.5. Clearly, measurements of x and y in real systems will indicate which scaling approach is more correct.

We now compare the high temperature ac conductivity measurements to these scaling theories. The results

presented in this work agree with the scaling theories in that the resistances and capacitances do scale with frequency past a critical frequency which scales inversely with the dc resistance. Throughout the critical frequency region, the critical exponents do roughly sum to one (experimentally $x + y \approx 1.0 \pm .2$). Above 1 MHz the critical exponents are roughly given by $x \approx 0.3 \pm .05$ and $y \approx 0.7 \pm .05$, in excellent agreement with the non-interacting cluster assumption. As the data in Fig. 7-7 indicates, films with $\omega_\xi <$ 1 MHz also display an intermediate frequency region where $x \approx 1$ and $y \approx 0$, in reasonable agreement with the interacting cluster assumption. This compares favorably with earlier low frequency measurements that were performed on these films.[12] That work found $x \approx 0.95 \pm .05$ and $y \approx 0.13 \pm .05$ below 10 MHz. Thus, it would seem that intercluster effects appear important at intermediate frequencies ($\omega_\xi < \omega <$ ~1 MHz), while anomalous diffusion is more important at high frequencies. A scaling theory which unifies these two scaling mechanisms has yet to be developed.

The scaling theory makes a number of other predictions about the physical properties of these films. The theory suggests that ω_ξ should inversely scale with R_{dc}, and this is confirmed by the data shown in Fig. 7-6. While the general scaling relationship appears to hold, the measured exponent (-0.82) disagrees with the predicted exponent (-1.66). The scaling theory also cannot account for the fact that the low

frequency capacitance is completely independent of R_{dc}. Thus, although the predictions of the scaling theory are borne out to some extent by these results, the theory cannot account for all aspects of the high temperature data.

We now discuss the low temperature results. Below 100K the resistance and capacitance become very temperature dependent. A transition from a high temperature state displaying scaling ac conductivity ($x,y \neq 0$) to a low temperature state displaying no apparent scaling behavior occurs near $t_c \approx 35$ K. This low temperature state is characterized by frequency independent resistance ($x = 0$) and zero capacitance (C is certainly less than 0.1 pF). While x and C are very temperature-dependent, the dc resistance and the critical frequency remain unaltered by changes in temperature. It would appear that these results cannot be accounted for by the scaling theory.

Near T_c it appears that scaling may still occur in these films. In the temperature range near T_c ($T_c-T_w/2 < T < T_c+T_w/2$), the resistance exponent drops to zero while the capacitance exponent y appears to rise to one. Hence $x + y \approx 1$ in this temperature regime. This suggests that scaling may still occur in the low temperature state, and it is not observable there only because the capacitance is no longer measurable ($C < 0.1$ pF).

In order for the scaling theory to account for this low temperature behavior, the critical exponents μ, ν, and β must

be altered near and below T_c. The theory can give the proper conductivity exponents ($x = 0$, $y = 1$) if we assume $\mu = 0$. While the changes in x and y can be accounted for in this way, the scaling theory would then suggest that ω_ξ, R_{dc}, and C_o should change in ways that are totally inconsistent with the data. Specifically, with $\mu \Rightarrow 0$, R_{dc} should drop to zero, ω_ξ should increase, and C_o should stay unchanged. In actuality, both R_{dc} and ω_ξ are independent of temperature, while C_o drops from 200 pF at 100K to < 0.1 pF at 23 K. According to Eqn. 7.12, the theory can force ω_ξ to be constant if we assume both that μ goes to zero and β becomes $\beta - \mu$, but the theory then incorrectly predicts that R_{dc} should drop to zero and C_o should increase. Thus, the theory of frequency scaling ac conductivity breaks down at low temperatures. This is somewhat surprising in light of the fact that the theory does not consider temperature effects, and from this it might be assumed that it should work best in the low temperature limit. In actuality, it appears that the theory only holds true in the high temperature limit.

The scaling theory was originally intended to model the behavior of abstract percolation systems that are "created" in computer simulations. In these simulations, the clusters consist of groups of non-physical points lying in a two dimensional lattice. In the gold films, these clusters consist of mounds of gold atoms. Certainly, the gold atoms

are physically far more complicated than the simulated abstract points. Hence, there will be a number of physical attributes of these films which do not exist in computer simulations. In particular, the gold films will not be entirely two dimensional; these films have thicknesses that range from 6 to 10 nm while the percolation correlation lengths are roughly 100 nm. Hence, these clusters are (microscopically) three dimensional objects. In addition, the gold atoms will congregate together within the clusters in an ordered manner. Further, temperature effects will cause phonons to exist throughout the film. There may also be interactions between the substrate and the metallic atoms which may be temperature-dependent (note that the temperature behavior of the ac conductivity cannot be ascribed simply to contractions of the substrate, which might occur with dropping temperature, because this would also necessitate changes in R_{dc} and ω_{ξ}, none of which match the data). All of these many physical aspects of the gold films are not considered in the scaling theory. While these underlying physical attributes may not be important when studying the film's structural nature (TEM work show these films to appear self-similar in exactly the same way that simulated percolation networks do),[11] they may have a profound influence upon the film's dynamical behavior. Hence, the physical, "non-ideal" nature of these gold percolation films presumably must account for the highly temperature-dependent

behavior exhibited by their ac conductivity below 100 K. The fact that some scaling ($x \Rightarrow 0$, $y \Rightarrow 1$) still occurs near T_c suggests that, by carefully taking the physical attributes of the films into account, a properly modified version of the scaling theory may be able to account for this low temperature behavior.

7.5 Conclusions

The temperature dependent ac conductivity of these gold percolation films show that the conventional scaling theory breaks down at low temperatures. In the high temperature regime the theory is in accord with the measured data, indicating that anomalous diffusion gives rise to scaling ac conductivity above 10 MHz. Below 100 K, the resistance and capacitance no longer show conventional scaling behavior. This cannot be accounted for by any of the scaling theories which attempt to describe percolation systems. It is possible that this behavior can be accounted for if the physical attributes of the films are included in a modified scaling theory. The fabrication and study of percolation films made from materials different from those used here could give insights into the exact nature of the physical film properties which control the low temperature behavior.

Chapter 8: Transport Properties of the Superconducting Oxide $La_{1.85}Sr_{0.15}CuO_4$

8.1 Introduction

In this chapter we examine the transport properties (Hall and Seeback effects) of the superconducting lanthanum-copper-oxide material $La_{1.85}Sr_{0.15}CuO_4$.[1] The alloyed conducting lanthanum-copper-oxides $La_{2-x}M_xCuO_4$ (M=Ba, Ca, Sr) were first shown to be high temperature superconductors at T_c ~ 40 K by Bednorz and Müller.[2] In addition to their spectacular high-T_c superconducting properties, these materials also have a highly anisotropic electronic structure. The lanthanum-copper-oxides form in a tetragonal K_2NiF_4 perovskite lattice. The lattice parameters have been found to be a strong function of the dopant concentration x; in the range of interest here ($x \approx 0.15$), the lattice parameters are: a = b = 3.8 Å, and c = 13.3 Å.[3,4] Electronic conduction occurs in the copper-oxide planes. These planes are widely separated from each other by intervening lanthanum (or dopant) atoms. The separation between these conducting planes is roughly c/3 = 4.4 Å. Hence, the electronic structure of this material is strongly two dimensional in character. The yittrium-copper-oxides, which have transition temperatures of up to 100 K, are even more anisotropic than the lanthanum-copper-oxides. This

strongly suggests that the high superconducting transition temperatures exhibited by these materials are critically related to their inherent anisotropic electronic structure.

Since the initial discovery of high-T_c superconductivity in the copper-oxides, a mammoth amount of research has been initiated to fully characterize these materials, and to understand the mechanisms responsible for their relatively high temperature superconducting state. It has been suggested that the materials in this class with the "best" superconducting transition (highest transition temperature and narrowest transition width) are obtained when 7.5% by weight of La in La_2CuO_4 is replaced with Sr.[5,6] Related studies have examined the normal and superconducting states of both La_2CuO_4 and $La_{2-x}M_xCuO_4$. These include investigations of the transition temperature,[7,8] the critical field,[9] the band structure,[10,11] and the energy gap.[12] Although novel mechanisms for the high-T_c superconductivity have been suggested,[13,14] recent oxygen isotope-effect experiments indicate that for $La_{1.85}Sr_{0.15}CuO_4$ normal BCS mechanisms (i.e. phonons) play an important role in the electron pairing responsible for superconductivity.[15]

We have attempted to more fully characterize the normal and superconducting state properties of $La_{1.85}Sr_{0.15}CuO_4$ through electrical-resistivity, Hall-effect, and thermoelectric-power (TEP) measurements, performed between 4.2K and 300K. Below the superconducting transition

temperature T_c=38K, the behavior of the resistivity, Hall effect, and TEP are generally as expected for a superconductor. In the normal state above T_c, the transport coefficients indicate positive charge carriers with a concentration n = $6x10^{21}$ cm^{-3}. The TEP behavior above T_c is unconventional and suggests unusual phonon-drag effects. The Hall constant shows a sharp anomaly near T_c which may be indicative of granular superconductivity.

8.2 Sample preparation and experimental techniques

Samples of $La_{1.85}Sr_{0.15}CuO_4$ were prepared by combining stoichiometric proportions of La_2O_3, CuO, and $SrCO_3$ and heating the mixture to 1100°C for 5 hours. The mixture was then re-ground and pressed into a pellet and sintered at 1100°C for 24 hours. After sintering, the polycrystalline sample was slowly cooled to room temperature. X-ray powder diffraction analysis confirmed that the samples were single phase, with the tetragonal perovskite structure. Magnetic susceptibility measurements performed on a SQUID magnetometer indicated a volume susceptibility of $\chi=-4x10^{-2}=0.5(-1/4\pi)$, suggesting that approximately 50% of the sample behaves as a bulk superconductor.

Electrical-resistivity measurements were performed using an ac four-terminal method with indium current leads and silver-paint voltage probes. The Hall effect was measured via a five-contact method,[16] where a low-frequency

ac (200 Hz) current source and three current contacts are used to null the zero magnetic field misalignment voltage. The small Hall signal was detected with a low noise impedance matching transformer and a lock-in amplifier. The Hall effect was measured on samples with typical dimensions of 5 mm x 2.5 mm x 0.15 mm. Electrical contacts were made by using low melting point indium-tin solder and ultrasonic soldering techniques. The thermoelectric power was measured by using a slow ac heating technique.[17] Small samples, typically 2 mm x 0.5 mm x 0.2 mm, were mounted in a vacuum between a pair of crystalline quartz blocks, and 1-mil gold wires were attached to the sample ends with ultrasonically soldered InSn and Ag paint. Both quartz blocks were wrapped with separate manganin wire heaters which were used to ramp a temperature gradient of varying magnitude and direction across the sample. The temperature gradient was monitored with a chromel-constantan thermocouple. The thermoelectric voltages across both the sample-gold and chromel-constantan thermocouples were amplified with a pair of low-noise amplifiers and then detected with an X-Y chart recorder.

8.3 Experimental results

Figure 8-1 shows the sample resistance measured between 50K and 20K. The initial deviation from the high-temperature behavior occurs at T^{o}_{c}=41 K, the midpoint of the transition is at T_c=38 K, and the resistance is zero below 33 k. The

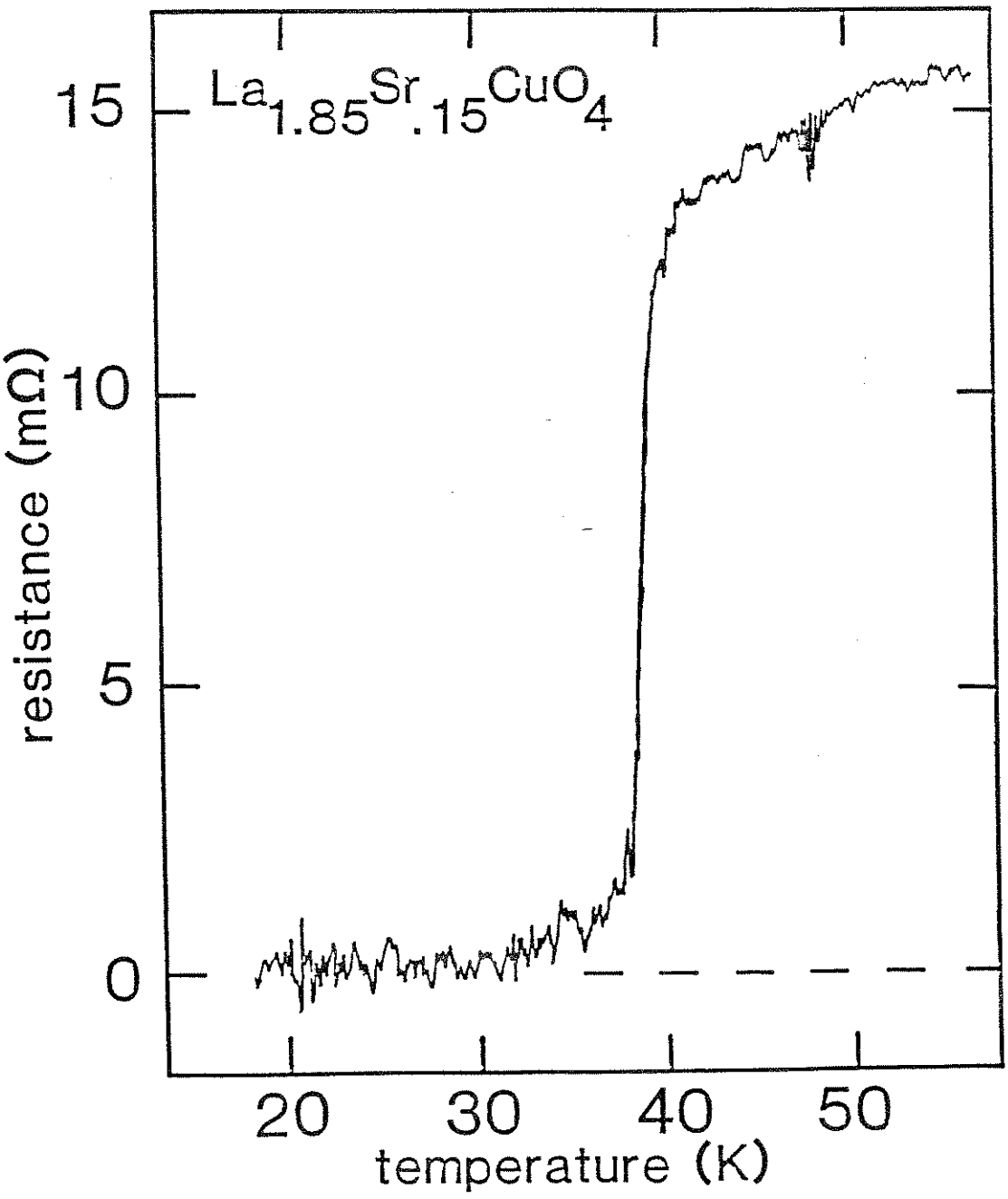

Fig. 8-1. Resistance of $La_{1.85}Sr_{0.15}CuO_4$ near the 38 K superconducting transition.

transition width (90%-10%) is approximately 2 K. These results are in agreement with previous studies on $La_{1.85}Sr_{0.15}CuO_4$.[7]

The results of Hall-effect measurements between 300 and 4.2 K at a magnetic field strength of 10 kG and a current density of 0.23 A/cm^2 are shown in Fig. 8-2. The Hall constant R_H is positive at all temperatures above T_c. R_H was found to be linear both in field strength (up to 10 kG) and current density (up to 0.23 A/cm^2) at all temperatures examined in this study. The Hall constant R_H is 1.0×10^{-9} m^3/C at room temperature, and it rises linearly as the temperature drops towards the superconducting transition temperature, taking on a value of 1.8×10^{-9} m^3/C at 45 K. A large anomaly in the Hall voltage is seen at the temperature where the onset of the superconductivity transition is seen in the resistivity. As shown in the inset to Fig. 8-2, the Hall signal doubles in a span of 2 K, reaching a value of 3.5×10^{-9} m^3/C at T_{max}=38 K. At temperatures below T_{max} the Hall voltage drops towards zero as expected for a superconductor. We note , however, that between 35 and 32 K the Hall voltage appears to overshoot zero slightly, taking on nonnegligible negative values with a maximum of -0.12×10^{-9} m^3/C at 33.8 K. Below 32 K the Hall voltage is zero to within the experimental sensitivity of 0.01×10^{-9} m^3/C.

The thermoelectric power of $La_{1.85}Sr_{0.15}CuO_4$ at temperatures between 4.2 and 300 K is presented in Fig. 8-3.

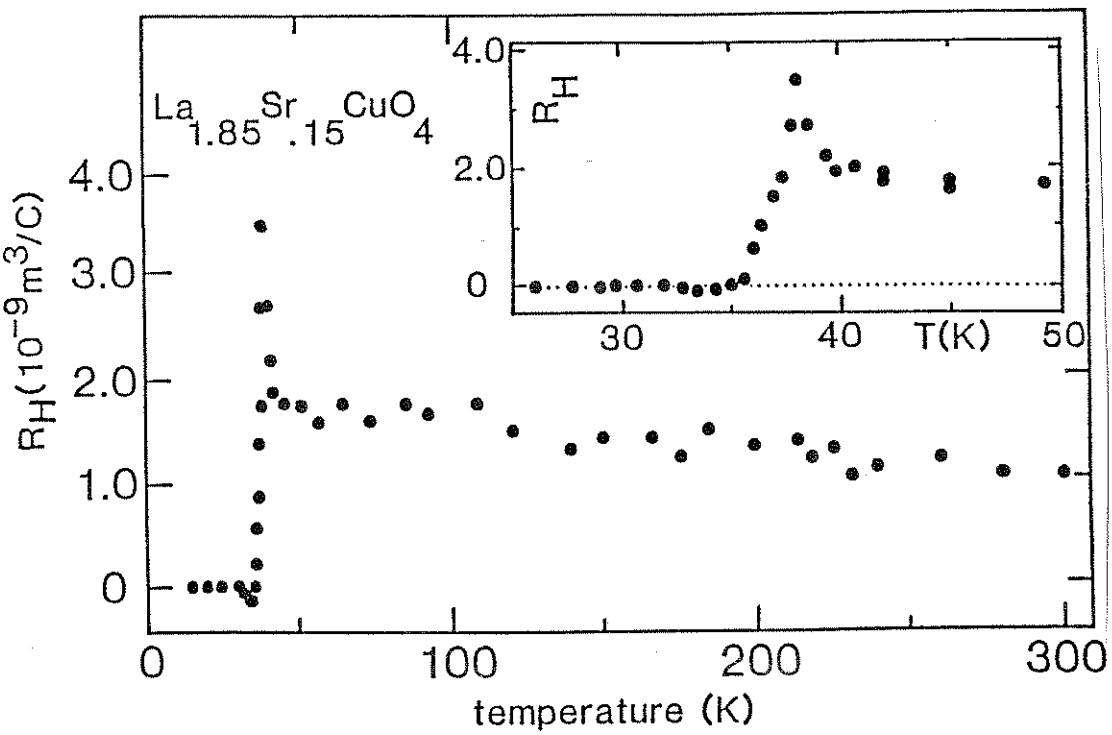

Fig. 8-2. Hall constant in $La_{1.85}Sr_{0.15}CuO_4$. The inset shows the Hall constant in the vicinity of the 38 K superconducting transition.

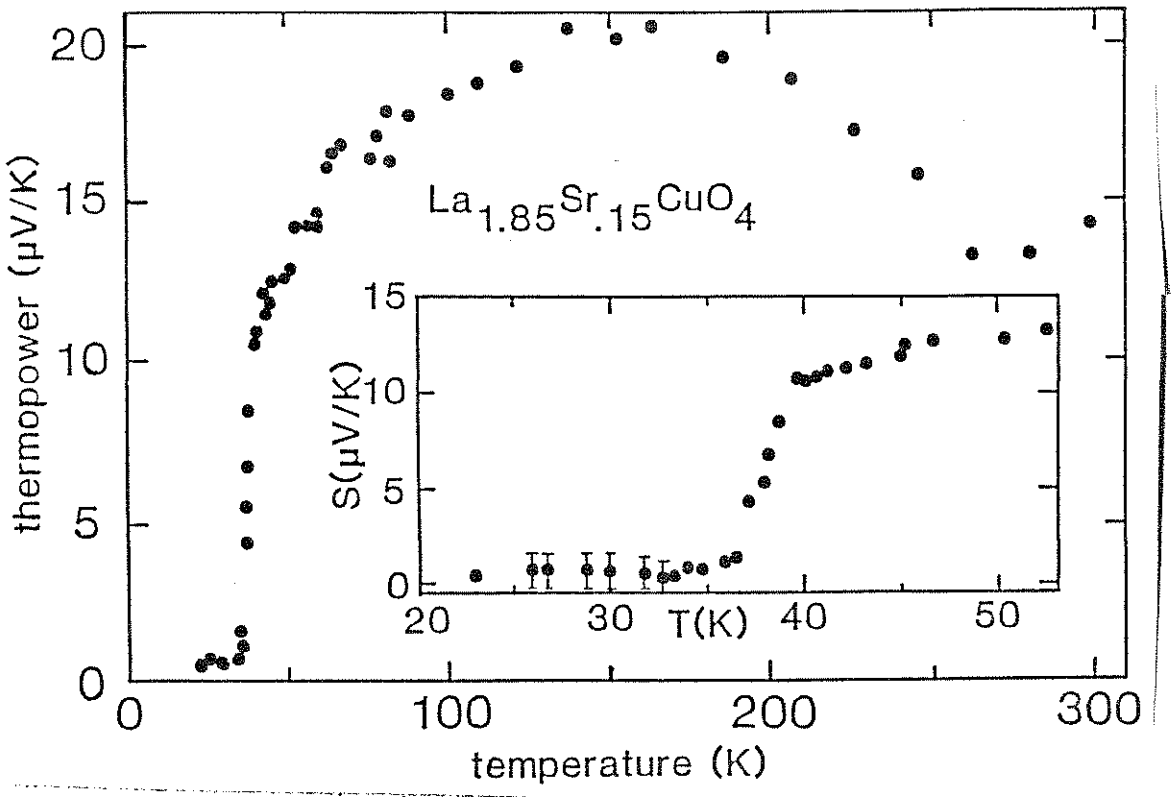

Fig. 8-3. TEP of $La_{1.85}Sr_{0.15}CuO_4$. The inset shows the TEP in the vicinity of the 38 K superconducting transition.

The thermopower is positive at all temperatures, with a room temperature value of +14.2 μV/K. The TEP displays a broad, concave-downward hump centered at 150 K, where the TEP is +20.5 μV/K. Below 150 K the thermopower slowly drops with temperature and reaches a value of +11 μV/K just above the superconducting transition. As shown in the inset to Fig. 8-3, the TEP drops abruptly to zero around T_c. Below 34 K the thermopower is zero to within experimental uncertainty. The large error bars in the low-temperature data are due to the uncertainty in the thermopower of the gold wire used in the measurement apparatus.[18] This uncertainty arises from the large phonon-drag peak which occurs in gold in this temperature region. Because the exact magnitude and location of the peak is quite dependent on impurity levels, manufacturing methods, etc., for the gold wire, and since the majority of the thermopower voltage comes from the gold wire when the sample is in the superconducting state, a large error can result.[19]

8.4 Analysis

We analyze the Hall effect and TEP results above T_c in terms of the semiclassical model with a single band. For a single band with a general, anisotropic relaxation time τ and a local average Fermi-surface radius of curvature $(1/\rho)$ the Hall coefficient will be[20]

$$R_H = \frac{12\pi^3}{ce} \frac{\int \tau^2(\mathbf{k}) v^2 \, (1/\rho) \, d\mathbf{s}}{\left(\int \tau(\mathbf{k}) v \, d\mathbf{s} \right)^2} , \tag{8.1}$$

where v is the Fermi velocity. With isotropic electron scattering and a spherical Fermi surface, this reduces to the familiar 1/nec with a positive value for a hole-like Fermi surface and a negative value for an electron-like surface. Hence, the Hall effect measures both the sign of the carriers and the nature of the electron scattering; any unusual temperature dependence generally signals that unusual electronic scattering is taking place.

The diffusion thermopower is related to the dc electrical conductivity σ in the semiclassical model by[21]

$$S_0 = - \frac{\pi}{3} \frac{k_B^2 T}{|e|} \sigma'(E_F)/\sigma(E_F) , \tag{8.2}$$

where the derivative is made with respect to energy and is evaluated at the Fermi energy E_F. The conductivity can be related to Fermi-surface parameters as[22]

$$\sigma = \frac{e^2}{6\pi^2 h} \tau(E_F) v S_F , \tag{8.3}$$

where S_F is the Fermi-surface area and h is Plank's constant. The sign of the thermopower will indicate the sign of the majority carrier because of the S_F term in Eqs. 8.2 and 8.3. Furthermore, the diffusion thermopower is expected to be linear in temperature; any deviation from linearity indicates that special electronic scattering processes are occurring. In addition to the diffusion thermopower there may exist a phonon-drag thermopower contribution which can give a large enhancement to the total TEP at roughly 1/5th to 1/10th the Debye temperature θ_D. This phonon-drag enhancement usually shows up in the TEP as a large peak in the thermopower voltage at low temperatures. Hence, the thermopower of a "normal" metal will be linear in temperature at high temperatures and may exhibit a phonon-drag peak near $T=\theta_D/10$. In $La_{1.85}Sr_{0.15}CuO_4$, θ_D=413 K.[23]

Within the confines of the semiclassical model, both the Hall effect and thermopower indicate that $La_{1.85}Sr_{0.15}CuO_4$ conducts via holes. The Hall-effect data suggests a hole concentration of 6.0×10^{21} cm^{-3}, or 1.15 holes per unit cell, at room temperature. This value can be compared to the number to be expected based on simple structural arguments. The unit cell for $La_{2-x}Sr_xCuO_4$ has a volume of Ω = 192 $Å^3$. It contains 4-2x lanthanum atoms (valence +3), 2x strontium atoms (valence +2), two copper atoms (predominately valence +2)[24,25], and eight oxygen atoms (valence -2). Therefore, the number of charge carriers per

unit cell will be $N_e = 2x$ (holes), and the predicted charge concentration is

$$n = \frac{2x}{\Omega} \tag{8.4}$$

With $x = 0.15$, the predicted carrier concentration is 1.6×10^{21} cm^{-3} (0.3 holes per unit cell), off by a factor of 3.8 with the measured value of 6.0×10^{21} cm^{-3}. The theoretical prediction was based on the assumption of a simple, spherical Fermi surface. The large discrepancy between the predicted and measured values indicates that this assumption is not valid. Indeed, this is not surprising in light of this material's strongly anisotropic nature.

The lack of features in the temperature dependence of the Hall voltage well above the transition region is typical of metals and appears to indicate that no novel anisotropic temperature-dependent electron scattering occurs in this material. However, the TEP in this temperature region is far different from that expected for a simple metal. In particular, the Seeback voltage is very nonlinear with temperature and the large, broad hump centered about 150 K appears to be both too wide and at too high a temperature to be ascribed to the usual phonon-drag effect. We note that similar unusual TEP results have been seen in such varied materials as the linear chain metal $TaSe_3$ and Uranium

intermetallics,[26,27] but as yet there is no clear explanation as to its cause. The Hall data for $La_{1.85}Sr_{0.15}CuO_4$ clearly show that no unusual electron scattering is occurring above 50 K; hence, the TEP results must be attributed to something other than simple electron scattering effects. It is possible that the broad hump is a manifestation of special phonon-drag scattering that can only occur when a temperature gradient exists across this material. Elasticity measurements[28] on $La_{1.85}Sr_{0.15}CuO_4$ indicate unusual lattice softening effects; it is possible that soft modes could couple to the charge carriers under a temperature gradient through phonon-drag scattering.[29]

The large, distinct anomaly at the onset of the superconducting transition which occurs in the Hall voltage is reminiscent of that seen in materials undergoing a structural phase transition.[30] This is apparently not the case here because no corresponding anomaly appears in the thermopower. The TEP in $La_{1.85}Sr_{0.15}CuO_4$ instead abruptly drops to zero near T_c, whereas the Hall voltage first sharply rises to double its value and then falls to zero as T is lowered through T_c. It is evident that the Hall anomaly must be a result both of the onset of the superconducting transition and the magnetic field. In particular, if superconductivity first occurs in isolated, localized granules, the expelled flux could drastically increase the magnetic field in the normal regions resulting in a large

enhancement of the Hall voltage. As the temperature drops further, these superconducting granules should grow in size until a percolation threshold is surpassed at which point the granules join to form complete sections of "bulk" superconductor. When this occurs the material would act like a conventional superconductor, giving rise to a turn around towards zero in the Hall voltage. This scenario of granular or inhomogeneous superconductivity is particularly plausible in light of the fact that these ceramic oxide materials are somewhat porous in nature; hence, inhomogeneities are likely. Both the thermopower and the Hall voltage drop to zero below the superconducting transition in accord with the behavior expected for a superconducting ground state. The Hall voltage appears to overshoot zero between 32 and 35 K; this could be another result of the inhomogeneous nature of the sample although it could also be due to the type II nature of this superconductor. Below 32 K the Hall voltage is clearly zero.[31]

8.5 Conclusions

The Hall effect and thermopower of $La_{1.85}Sr_{0.15}CuO_4$ show the material to be hole-like in its normal state. The Hall voltage indicates that there may exist granular or inhomogeneous superconductivity in this material. Although a good deal of experimental and theoretical research has been done on granular superconductors[32] we are not aware of any

studies of the Hall effect in these types of materials. The development of a theory to describe the Hall effect near the onset of superconductivity in a granular superconductor would be a fruitful line of research. The thermopower suggests that novel phonon-drag scattering processes occur in the normal state of $La_{1.85}Sr_{0.15}CuO_4$ in the presence of a temperature gradient. The results below T_c are in accord with a superconducting ground state in $La_{1.85}Sr_{0.15}CuO_4$.

Chapter 9: Conclusions and directions for future research

In this report we have examined the electronic transport properties of a number of low dimensional materials. We now briefly summarize the chief findings presented in this report and discuss possible directions for future research.

The narrow band noise (NBN), thermopower, and ac conductivity measurements performed on $NbSe_3$ crystals in externally applied magnetic fields provide strong evidence to support the proposition that magnetic field induced carrier conversion occurs in this material. These experimental findings support the theory concerning magnetic field effects on the electronic structure of density wave systems first proposed by Balseiro and Falicov.[1] The ac conductivity data also indicate that the conventional impurity pinning mechanisms responsible for charge density wave (CDW) dynamics are altered by externally applied magnetic fields.

While the conductivity measurements clearly indicate that CDW dynamical behavior is subtly altered in the presence of external magnetic fields, further work is needed to fully understand this effect. In particular, it would be worthwhile to perform a wide range of dynamical CDW experiments on $NbSe_3$ crystals in an applied magnetic field.

These experiments should include ac conductivity measurements at frequencies above 1 GHz as well as an examination of interference phenomena in the presence of combined ac and dc electric fields. It would also be useful to examine the carrier-conversion process in fields greater than those used here (80 kG) in the hopes of observing a saturation in this effect. More direct measurements of the magnetic field induced enhancement of the CDW order parameter via x-ray diffraction, CDW-insulator-superconductor tunneling, or NMR experiments (analogous to those performed in the absence of a magnetic field)[2-4] would also be informative. Lastly, it would be useful to examine other partially gapped CDW materials for anomalous magnetoresistance behavior to see whether or not $NbSe_3$ is unique in exhibiting these magnetic field induced carrier conversion effects.

The temperature gradient Shapiro step experiments performed on $NbSe_3$ crystals show that applied thermal gradients act to break CDW crystals into multiple phase velocity coherent domains while applied rf signals act to increase CDW coherence. When the mode locked steps are split by a temperature gradient, the structure of the resulting Shapiro step spectrum supports the notion that narrow band noise oscillations are a bulk effect. In addition, the predictions of a simple bulk-based phase slip model of temperature gradient effects on NBN oscillations agree both

qualitatively and semi-quantitatively with the many temperature gradient effects observed in $NbSe_3$.[5] Hence, both the theoretical and experimental results presented in this report support the view that NBN oscillations stem from bulk interactions.

Thus far, $NbSe_3$ is the only CDW material whose NBN response has been examined in an applied temperature gradient. Because $NbSe_3$ is unique amongst the many CDW conductors which display collective effects in that its Fermi surface is only partially gapped by the two Peierls transitions that it undergoes, it would be informative to perform similar temperature gradient experiments on completely gapped CDW materials [TaS_3, the blue bronzes, $(TaSe_4)_2I$, etc.] to see what role normal carrier screening has on charge density wave domain coherence.

The temperature gradient and domain localization experiments performed on switching samples of pure and iron doped $NbSe_3$ indicate that the large variation in switching crystal I-V characteristics originates in differences in the distribution of the switch-causing ultra-strong impurities. The way in which these I-V characteristics evolve in an increasing temperature gradient also suggest that strong coupling can exist between neighboring switching domains. Careful materials research, as well as TEM and microprobe analysis, is needed to determine the microscopic nature of

the impurities which are the underlying cause of CDW switching behavior.

By examining extremely thin samples of $K_{0.3}MoO_3$, we have shown that this material can exhibit strongly coherent sliding charge density wave behavior. This coherent CDW response in turn leads to a variety of interference effects when high quality single crystals are studied in the presence of combined ac and dc driving electric fields. The general features of these interference effects can be described by a simple single degree-of-freedom classical model. The underlying interactions within the CDW (i.e., internal degrees of freedom) manifest themselves as subtle variations in the observed interference response.

It would be worthwhile to extend these measurements by examining the ac-dc interference effects displayed by strongly coherent $K_{0.3}MoO_3$ samples as a function of temperature. Since the CDW damping in $K_{0.3}MoO_3$ is strongly temperature dependent and diverges as T goes to zero,[6] the general features of the ac-dc interference phenomena displayed by this material should also be strongly temperature-dependent. It would also be informative to examine the predictions of the single particle classical model at resonance to see if this simple model can account for the $-\pi/2$ phase shift present in the experimental data at resonance.

The transport properties of polycrystalline URu_2Si_2 samples show strong evidence for both general heavy Fermionic behavior as well as a Fermi surface based transition at T_c = 17.5 K. Above 17.5 K, both the Hall and thermopower coefficients of URu_2Si_2 reflect the unusual nature of f-band conduction electrons. At 17.5 K, both transport properties indicate that a sizable portion of the charge carriers are removed from the conduction band, presumably due to a spin or charge density wave transition.

While these transport measurements clearly indicate that a Fermi surface-based transition occurs at 17.5 K, it is impossible to determine the precise nature of the intermediate state. To do so, good quality URu_2Si_2 single crystals must first be synthesized. X-ray diffraction experiments performed on crystalline samples should be able to determine whether or not the 17.5 K transition leads to the formation of a charge density wave. As a test for the presence of a depinnable CDW, it would also be worthwhile to perform pulsed dc conductivity measurements on single crystals in the hopes of observing non-linear dc conductivity.

The temperature dependent ac conductivity measurements performed on self-similar thin gold percolation films show that the conventional percolative scaling mechanisms break

down at low temperatures in real fractal systems. Regardless of the specific gold film parameters, these films display a transition near 40 K that separates a high temperature state which exhibits scaling ac conductivity and a low temperature state which no longer shows signs of conventional scaling behavior. To determine if this "transition" is due to the physical attributes of the system it would be worthwhile in the future to fabricate and study percolation films made from materials different from those used here.

The Hall effect and thermopower of $La_{1.85}Sr_{0.15}CuO_4$ indicate that this material is hole-like it its normal state. The Hall effect data also shows evidence for granular or inhomogeneous superconductivity in the polycrystalline samples examined here; this possibility is not surprising in light of the porous nature of the ceramic samples which we studied. The thermopower also suggests that unusual phonon-drag scattering occurs in the normal state of $La_{1.85}Sr_{0.15}CuO_4$. Below T_c, the transport properties are in accord with a superconducting ground state in this material. A great deal of materials and physics research is still needed before we can hope to understand the relatively high superconducting transition temperatures exhibited by these ceramic-oxide materials.

In this report we have examined the electronic

transport properties of a number of novel materials. These have included the quasi-one-dimensional materials $NbSe_3$ and $K_{0.3}MoO_3$ which suffer Peierls transitions which lead to the formation of a CDW ground state, display collective mode transport phenomena, and, in the case of $NbSe_3$, undergo unusual magnetic field induced carrier conversion. In addition, we have studied the heavy Fermion compound URu_2Si_2, which undergoes a Fermi surface-based transition at 17.5 K; a class of unusual, sub two-dimensional gold fractal films which display frequency scaling ac conductivity above 40 K; and the planar ceramic-oxide $La_{1.85}Sr_{0.15}CuO_4$ which suffers a superconducting transition at the unusually high temperature of 40 K. Clearly, all these novel materials display very uncommon electronic transport properties, all of which can be directly attributed to the low dimensional electronic and/or spatial structure of these unusual systems.

Chapter 10: References

Chapter 1

1. R.E. Peierls, *Quantum Theory of Solids* (Oxford University Press, London, 1955) p. 108.
2. H. Fröhlich, Proc. Roy. Soc. London, A **223**, 296 (1954).
3. See, for example, *Low-Dimensional Conductors and Superconductors*, D. Jérome and L.G. Caron, eds. (Plenum Press, New York, 1987).
4. G. Grüner and A. Zettl, Physics Reports **119**, 117 (1985).
5. *Electronic Properties of Quasi-One-Dimensional Materials*, P. Monceau, ed. (Reidel, Dordrecht, the Netherlands, 1985).
6. *Low-Dimensional Cooperative Phenomena -- The Possibility of High-Temperature Superconductivity*, H.J. Keller, ed. (Plenum Press, New York, 1974).
7. P. Monceau, N.P. Ong, A.M. Portis, A. Meerschaut, and J. Rouxel, Phys. Rev. Lett. **37**, 602 (1976).
8. R.M. Fleming and C.C. Grimes, Phys. Rev. Lett. **42**, 1423 (1979).
9. R.M. Fleming, D.E. Moncton, and D.B. McWhan, Phys. Rev. B **18**, 5560 (1978).
10. J.H. Ross, Z. Wang, and C.P. Slichter, Phys. Rev. Lett. **56**, 663 (1986).

Chapter 2

1. R.E. Peierls, *Quantum Theory of Solids* (Oxford University Press, 1955), p. 108.
2. H. Fröhlich, Proc. Roy. Soc. London A**223**, 296 (1954).
3. G. Grüner and A. Zettl, Physics Reports **119**, 117 (1985).
4. P. Monceau, in *Electronic Properties of Inorganic Quasi-One-Dimensional Materials*, P. Monceau, ed. (Reidel, Dordrecht, The Netherlands, 1985), Vol. 2, p. 139.
5. *Lecture Notes in Physics*, Vol. 217, Gy. Hutiray and J. Solyom, eds. (Springer-Verlag, Berlin, 1985).
6. *Low Dimensional Conductors and Superconductors*, D. Jerome and L.G. Caron, eds. (Plenum Press, New York, 1987).
7. P. Chaikin, in *Synthesis and Properties of Low-Dimensional Materials*, J.S. Miller and A.J. Epstein, eds., Annals of the New York Academy of Sciences **313**, 128 (1978).
8. J.M. Ziman, *Theory of Solids*, 2nd edition (Cambridge University Press, London, 1972), chapter 5.
9. P.A. Lee, T.M. Rice, and P.W. Anderson, Phys. Rev. Lett **31**, 462 (1973).
10. D. Kuse and H.R. Zeller, Phys. Rev. Lett. **27**, 1060 (1971); B. Renker, H. Rietschel, L. Pintschovius, W.

Gläser, P. Brüesch, D. Kuse, and M.J. Rice, Phys. Rev. Lett. **30**, 1144 (1973).

11. For a review, see A.J. Heeger, in *Highly Conducting One-Dimensional Compounds*, J.T. Devreese, R.P. Evrard, and V.E. Van Doren, eds. (Plenum Press, New York, 1979), p. 69.

12. J.A. Wilson, F.J. DiSalvo, and S. Mahajen, Adv. Phys. **24**, 117 (1975).

13. R.C. Lacoe, H.J. Schulz, D. Jerome, K. Bechgaard, and I. Johannsen, Phys. Rev. Lett **55**, 2351 (1985); see also J.R. Cooper, F. Creuzet, L. Forro, D. Jerome, R.C. Lacoe, and H.J. Schulz in Ref.6, p. 389.

14. P. Lee, T.M. Rice, and P.W. Anderson, Solid State Commun. **14**, 703 (1974).

15. P. Büesch, S. Strässler, and H.R. Zeller, Phys. Rev. B **12**, 219 (1975); D.B. Tanner, C.S. Jacobsen, A.F. Gariot, and A.J. Heeger, Phys. Rev. B **13**, 3381 (1976); D.B. Tanner, K.D. Cummings, and C.S. Jacobsen, Phys. Rev. Lett. **47**, 597 (1981); J.E. Eldrige and F.E. Bates, Phys. Rev. B **28**, 6972 (1983).

16. P. Monceau, N.P. Ong, A.M. Portis, A. Meerschaut, and J. Rouxel, Phys. Rev. Lett. **37**, 602 (1976).

17. R.M. Fleming, D.E. Moncton, and D.B. McWhan, Phys. Rev. B **18**, 5560 (1978).

18. J. Bardeen, Ref. 11, p. 373.

19. R.M. Fleming and C.C. Grimes, Phys. Rev. Lett. **42**, 1423

(1979).

20. R.M. Fleming, Phys. Rev. B **22**, 5606 (1980).

21. J.H. Ross, Z. Wang, and C.P. Slichter, Phys. Rev. Lett. **56**, 663 (1986).

22. P.A. Lee and T.M. Rice, Phys. Rev. B **19**, 3970 (1979).

23. W.W. Fuller, G. Grüner, P.M. Chaikin, and N.P. Ong, Phys. Rev. B **23**, 6259 (1981); Pei-Ling Hsieh, F. de Czito, A. Janossy, and G. Grüner, J. Phys. **44**, C3-1749 (1983).

24. A.H. Thompson, A. Zettl, and G. Grüner, Phys. Rev. Lett. **47**, 64 (1981); M. Ido, K. Kawabata, T. Sambongi, K. Yamaya, and Y. Abe, Mol. Cryst. Liq. Cryst. **81**, 91 (1982).

25. A. Zettl, C.M. Jackson, A. Janossy, G. Grüner, A. Jacobsen, and A.H. Thompson, Solid State Commun. **43**, 345 (1982).

26. J. Dumas, C. Schlenker, J. Marcus, and R. Buder, Phys. Rev. Lett. **50**, 757 (1983).

27. M. Maki, M. Kaiser, A. Zettl, and G. Grüner, Solid State Commun. **46**, 29 (1983); Z.Z. Wang, M.C. Saint-Lager, P. Monceau, M. Renard, P. Gressier, L. Guemas, and A. Meerschaut, Solid State Commun. **46**, 325 (1983).

28. Z.Z. Wang, P. Monceau, M. REnard, P. Gressier, L. Guemas, and A. Meerschaut, Solid State Commun. **47**, 439 (1983).

29. G. Grüner, A. Zettl, and W.G. Clark, Phys. Rev. B **24**, 7247 (1981).

30. S. Sridhar, D. Reagor, and G. Grüner, Phys. Rev. B **34**, 2223 (1986).

31. Wei-yu Wu, A. Janossy, and G. Grüner, Solid State Commun. **49**, 1013 (1984).

32. R.J. Cava, R.M. Fleming, P. Littlewood, E.A. Rietman, L.F. Schneemeyer, and R.G. Dunn, Phys. Rev. B **30**, 3228 (1984).

33. R.J. Cava, P. Littlewood, R.M. Fleming, R.G. Dunn, and E.A. Rietman, Phys. Rev. B **33**, 2439 (1986).

34. P.B. Littlewood, Phys. Rev. **36**, 3108 (1987).

35. G. Grüner, A. Zettl, W.G. Clark, and A.H. Thompson, Phys. Rev. B **23**, 6813 (1981).

36. P. Monceau, J. Richard, and M. Renard, Phys. Rev. Lett. **45**, 43 (1980).

37. N.P. Ong, G. Verma, and K. Maki, Phys. Rev. Lett. **52**, 663 (1984); N.P. Ong and K. Maki, Phys. Rev. B **32**, 6582 (1985).

38. G. Mozurkewich and G. Grüner, Phys. Rev. Lett. **51**, 2206 (1983); S.E. Brown and L. Mihaly, Phys. Rev. Lett. **55**, 742 (1985).

39. S. Shapiro, Phys. Rev. Lett. **11**, 80 (1963).

40. A. Zettl and G. Grüner, Solid State Commun. **46**, 501 (1983).

41. A. Zettl and G. Grüner, Phys. Rev. B **29**, 755 (1984).

42. S.E. Brown, G. Mozurkewich, and G. Grüner, Phys. Rev. Lett. **52**, 2277 (1984); R.P. Hall and A. Zettl, Phys. Rev. B **30**, 2279 (1984); R.E. Thorne, W.G. Lyons, J.W. Lyding, and J.R. Tucker, Phys. Rev. B **35**, 6360 (1987).

43. S.E. Brown, G. Mozurkewich, and G. Grüner, Solid State Commun. **54**, 23 (1985); S.E. Brown and G. Grüner, Phys. Rev. B **31**, 8302 (1985).

44. M.F. Hundley and A. Zettl, Solid State Commun. (to be published).

45. M.F. Hundley and A. Zettl, Phys. Rev. B (to be published).

46. A. Zettl and G. Grüner, Phys. Rev. B **26**, 2298 (1982).

47. L. Mihaly and G. Grüner, Solid State Commun. **50**, 807 (1984).

48. R.P. Hall and A. Zettl, Solid State Commun. **50**, 813 (1984).

49. R.P. Hall and A. Zettl, Solid State Commun. **55**, 307 (1985).

50. R.P. Hall and A. Zettl, Solid State Commun. **57**, 27 (1986).

51. R.P. Hall, M. Sherwin, and A. Zettl, Phys. Rev. Lett. **52**, 2293 (1984).

52. R.P. Hall, M. Sherwin, and A. Zettl, Phys. Rev. B **29**, 7076 (1984).

53. R.P. Hall, M.F. Hundley, and A. Zettl, Phys. Rev. Lett. **56**, 2399 (1986).

54. G. Grüner, A. Zawadowski, and P.M. Chaikin, Phys. Rev. Lett. **46**, 511 (1981).

55. J. Bardeen, Phys. Rev. Lett. **45**, 1978 (1980), and Physica **143**B, 14 (1986).

56. H. Fukuyama and P.A. Lee, Phys. Rev. B **17**, 545 (1978); P.A. Lee and T.M. Rice, Phys. Rev. B **19**, 3970 (1979); L. Sneddon, M.C. Cross, and D.S. Fisher, Phys. Rev. Lett. **49**, 292 (1982); L. Sneddon, Phys. Rev. Lett. **52**, 65 (1983).

57. I. Tütto and A. Zawadowski, Phys. Rev. B **32**, 2449 (1985).

58. For a review, see R.M. Fleming in Ref. 6, p. 433.

59. J.H. Miller, R.E. Thorne, W.G. Lyons, J.R. Tucker, and J. Bardeen, Phys. Rev. B **31**, 5229 (1985).

60. S. Liu and L. Sneddon, Phys. Rev. **35**, 7745 (1987).

61. G. Grüner, A. Zettl, W.G. Clark, and J. Bardeen, Phys. Rev. B **24**, 7247 (1981).

62. A. Meerschaut and J. Rouxel, J. Less Common Metals **39**, 197 (1975).

63. J.L. Hodeau, M. Marezio, C. Roucau, R. Ayroles, A. Meerschaut, J. Rouxel, and P. Monceau, Phys. Stat. Sol. (a) **62**, 483 (1980).

64. J.A. Wilson, Phys. Rev. B **19**, 6456 (1979), and J. Phys. F **12**, 2469 (1982).

65. P. Monceau, J. Richard, and M. Renard, Phys. Rev. B **25**, 931 (1982).

66. P. Haen, P. Monceau, B. Tisser, G. Waysand, A. Meerschaut, P. Molinine, and J. Rouxel, in *Low Temperature Physics Lt-4*, M. Krasius and M. Vuorio, eds. (American Elsevier, New York, 1975).

67. N. Shima and H. Kamimura, in *Theoretical Aspects of Band Structure and Electronic Properties of Psuedo-One-Dimensional Solids*, H. Kamimura, ed. (Reidel, Dordrecht, the Netherlands, 1985), p. 231.

68. D.W. Bullett, J. Phys. C **15**, 3069 (1982).

69. F. Devreux, J. Physique **43**, 1489 (1982).

70. A. Wold, W. Kunnmann, R.J. Arnott, and A. Ferreti, Inorg. Chem. **3**, 545 (1964).

71. G.H. Bouchard, J.H. Perlstein, and M.J. Sienki, Inorg. Chem. **6**, 1682 (1967).

72. R. Brusetti, B.K. Chakroverti, J. Deven yi, J. Dumas, J. Marcus, and C. Schlenker, in *Recent Developments in Condensed Matter Physics*, J.T. Devreese, L.F. Lemmens, V.E. Van Doren, and J. Van Royen, eds. (Plenum Press, New York, 1981), Vol. 2, p. 181.

73. G. Travaglini, P. Wachter, J. Marcus, and C. Schlenker, Solid State Commun. **37**, 599 (1981).

74. J.P. Pouget, S. Kagoshima, C. Schlenker, and J. Marcus, J. Physique Lett. **44**, L113 (1983).

75. C. Schlenker, in Ref. 6, p. 477.

76. M. Ghedira, J. Chenavas, M. Marezio, and J. Marcus, J. Solid State. Chem. **57**, 300 (1985).

77. K. Tsutsumi, T. Tamegai, S. Kagoshima, H. Tomozawa, and M. Sato, J. Phys. Soc. Japan **53**, 3946 (1984).

Chapter 3

1. R.V. Coleman, G. Eiserman, M.P. Everson, A. Johnson, and L.M. Falicov, Phys. Rev. Lett. **55**, 863 (1985).

2. C.A. Balseiro and L.M. Falicov, Phys. Rev. Lett. **55**, 2336 (1985), and Phys. Rev. B **34**, 863 (1986).

3. L. Sneddon, M.C. Cross, and D.S. Fisher, Phys. Rev. Lett **49**, 292 (1982); R.A. Klemm and J.R. Schrieffer, Phys. Rev. Lett **51**, 47 (1983).

4. N.P. Ong, G. Verma, and K. Maki, Phys. Rev. Lett. **52**, 663 (1984); N.P. Ong and K. Maki, Phys. Rev. B **32**, 6582 (1985).

5. X.J. Zhang and N.P. Ong, Phys. Rev. B **30**, 7343 (1984); A. Zettl, M. Kaiser, and G. Grüner, Solid State Commun. **53**, 649 (1985).

6. A. Zettl and G. Grüner, Phys. Rev. B **26**, 2298 (1982).

7. R.P. Hall, M.F. Hundley, and A. Zettl, Phys. Rev. Lett. **56**, 2399 (1986).

8. A. Wold, W. Kunnmann, R.J. Arnott, and A. Ferreti, Inorg. Chem. **3**, 545 (1964).

9. J.P. Pouget, S. Kagoshima, C. Schlenker, and J. Marcus, J. Physique Lett. **44**, L-113 (1983).

10. J. Dumas, C. Schlenker, J. Marcus, and R. Buder, Phys. Rev. Lett. **50**, 757 (1983).

11. C. Schlenker in *Low Dimensional Conductors and*

Superconductors, Series B, Vol. 155, D. Jérome and L.G. Caron, eds. (Plenum Press, New York, 1987) p. 477.

12. M.B. Maple, J.W. Chen, Y. Dalichaouch, T. Kahara, C. Rossel, M.S. Torikachvili, M.W. McElfresh, and J.D. Thompson, Phys. Rev. Lett. **56**, 185 (1986).

13. B.B. Mandelbrot, *The Fractal Geometry of Nature* (W.H. Freeman and Company, San Francisco, 1983).

14. R.F. Voss, R.B. Laibowitz, and E.I. Alessandrini, Phys. Rev. Lett. **49**, 1441 (1982).

15. R.B. Laibowitz and Y. Gefen, Phys. Rev. Lett **53**, 380 (1984).

16. J.G. Bednorz and K.A. Müller, Z. Phys. B **64**, 189 (1986).

Chapter 4

1. For a review, see G. Grüner and A. Zettl, Phys. Rep. 119, 117 (1985); see also P. Monceau in *Electronic Properties of Quasi-One-Dimensional Materials*, Vol. II, P. Monceau, ed. (Reidel, Dordrecht, The Netherlands 1985), p. 139

2. P. Monceau, N.P. Ong, A.M. Portis, A. Meerschaut, and J. Rouxel, Phys. Rev. Lett. **37**, 602 (1976).

3. R.M. Fleming, D.E. Moncton, and D.B. McWhan, Phys. Rev. B **18**, 5560 (1978).

4. R.V. Coleman, G. Eiserman, M.P. Everson, A. Johnson and L.M. Falicov, Phys. Rev. Lett. **55**, 863 (1985).

5. see, for example, N.W. Ashcroft and N.D. Mermin, *Solid State Physics* (Holt, Rinehart, and Winston, Philadelphia 1976), chapter 12.

6. C.A. Balsiero and L.M. Falicov, Phys. Rev. Lett. **55**, 2336 (1985), Phys. Rev. B **34**, 863 (1986).

7. P. Parilla, M.F. Hundley, and A. Zettl, Phys. Rev. Lett. **57**, 619 (1986).

8. M.F. Hundley and A. Zettl, Solid State Commun. **61**, 587 (1987).

9. M.F. Hundley, P. Parilla, and A. Zettl, Phys. Rev. B **34**, 5970 (1986).

10. G. Grüner, A. Zawadowski, and P.M. Chaikin, Phys. Rev.

Lett. **46**, 511 (1981).

11. P. Monceau, J. Richard, and M. Renard, Phys. Rev. Lett. **45**, 43 (1980).
12. J. Bardeen, E. Ben-Jacob, A. Zettl, and G. Grüner, Phys. Rev. Lett. **49**, 493 (1982).
13. A. Zettl and G. Grüner, Phys. Rev. B **29**, 755 (1984).
14. P.A. Lee and T.M. Rice, Phys. Rev. B **19**, 3970 (1979).
15. see for example, D. Allender, J.W. Bray, and J. Bardeen, Phys. Rev. B **9**, 119(1974), and M.J. Rice, in *Low-Dimensional Cooperative Phenomena*, edited by H.J. Keller (Plenum, New York, 1974), p. 23.
16. N.P. Ong and P. Monceau, Phys. Rev. B **16**, 3443 (1977).
17. P.M. Chaikin and J.F. Kwak, Rev. Sci. Instrum. **46**, 218 (1975).
18. H.H. Sample and L.G. Rubin, Cryogenics **17**, 597 (1977).
19. P.M. Chaikin, W.W. Fuller, R. Lacoe, J.F. Kwak, R.L. Greene, J.C. Eckert, and N.P. Ong, Solid State Commun. **39**, 553 (1981).
20. T. Takagaki, M. Ido, and T. Sambongi, J. Phys. Soc. Japan Lett. **45**, 2039 (1978).
21. R.S. Ayerback and D.K. Wagner, Solid State Commun. **11**, 1109 (1972).
22. F.J. Blatt, C.K. Chiang, and L. Smrcka, Phys. Stat. Sol. (a) **24**, 621 (1974).
23. F.J. Blatt, A.D. Caplin, C.K. Chiang, and P.A. Schroeder, Solid State Commun. **15**, 411 (1974).

24. A.D. Caplin, C. Chiang, P.A. Schroeder, and J. Tracy, Phys. Stat. Sol (a) **26**, 497 (1974).

25. J.P. Stokes, A.N. Bloch, A. Janossy, and G. Grüner, Phys. Rev. Lett. **52**, 372 (1984).

26. See, for example, F.J. Blatt, P.A. Schroeder, C.L. Foiles, and D. Greig, in *Thermoelectric Power of Metals* (Plenum Press, New York 1976) p. 27.

27. Ref. 26, p. 19.

28. J.M. Ziman, in *Principles of the Theory of Solids* (Cambridge University Press, London 1972) p. 218.

29. S. Shridar, D. Reagor, and G. Grüner, Phys. Rev. Lett. **55**, 1196 (1985)

30. G. Grüner, L.C. Tippie, J. Sanny, W.G. Clark, and N.P. Ong, Phys. Rev. Lett. **45**, 935 (1980)

31. J. Bardeen, Phys. Rev. Lett. **45**, 1978 (1980); see also G. Grüner, A. Zettl, W.G. Clark, and J. Bardeen, Phys. Rev. B **24**, 7247 (1981)

32. H. Fukuyama and P.A. Lee, Phys. Rev. B **17**, 545 (1978); P.A. Lee and T.M. Rice, Phys. Rev. B **19**, 3970 (1979); L. Sneddon, M.C. Cross, and D.S. Fisher, Phys. Rev. Lett. **49**, 292 (1982)

32. Wei-yu Wu, A. Jánossy, and G. Grüner, Solid State Commun. **49**, 1013 (1984)

34. W.W. Fuller, G. Grüner, P.M. Chaikin, and N.P. Ong, Phys. Rev. B **23**, 6259 (1981); G. Mihály, L. Mihály, and H. Mutka, Solid State Commun. **49**, 1009 (1984)

35. X.J. Zhang and N.P. Ong, Phys. Rev. Lett. **55**, 2919 (1986); N.P. Ong and X.J. Zhang (to be published); R.M. Fleming, R.J. Cava, L.F. Schneemeyer, E.A. Rietman, and R.G. Dunn, Phys. Rev. B **33**, 5450 (1986).

36. A. Zettl and G. Grüner, Phys. Rev. B **28**, 2091 (1983).

37. A. Janossy, C. Berthier, P. Segransan, and P. Butaud, Phys. Rev. Lett. **59**, 2348 (1987).

38. M.F. Hundley and A. Zettl, Solid State Commun. (to be published).

39. S. Sneddon, M.C. Cross, and D.S. Fisher, Phys. Rev. Lett. **49**, 292 (1982).

40. R.A. Klemm and J.R. Schrieffer, Phys. Rev. Lett. **51**, 47 (1983).

41. S.E. Barnes and A. Zawadowski, Phys. Rev. Lett. **51**, 1003 (1983).

42. N.P. Ong, G. Verma, and K. Maki, Phys. Rev. Lett. **52**, 663 (1984).; G. Verma and N.P. Ong, Phys. Rev. B **30**, 2928 (1984).

43. L.P. Gor'kov, JETP Lett. **38**, 87 (1983).

44. G. Mozurkewich and G. Grüner, Phys. Rev. Lett. **51**, 2206 (1983).

45. S.E. Brown and L. Mihaly, Phys. Rev. Lett. **55**, 742 (1985).

46. I. Tütto and A. Zawadowski, Phys. Rev. B **32**, 2449 (1985).

47. P. Monceau, M. Renard, M.C. Saint-Lager, H. Salva, and

Z.Z. Wang, Phys. Rev. B **28**, 1646 (1983).

48. M.F. Hundley and P. Parilla (unpublished).

49. S.E. Brown and G. Grüner, Phys. Rev. B **31**, 8302 (1985).

50. A. Zettl, M. Kaiser, and G. Grüner, Solid State Commun. **53**, 649 (1985).

51. X.J. Zhang and N.P. Ong, Phys. Rev. B **30**, 7343 (1984).

52. S.E. Brown, A. Janossy, and G. Grüner, Phys. Rev. B **31**, 6869 (1985).

53. J.W. Lyding, J.S. Hubacek, G. Gammie, and R.F. Thorne, Phys. Rev. B **33**, 4341 (1986).

54. M.F. Hundley and A. Zettl, Phys. Rev. B **33**, 2883 (1986).

55. M.F. Hundley, P. Parilla, and A. Zettl, Solid State Commun. (to be published).

56. A. Zettl and G. Grüner, Solid State Commun. **46**, 501 (1983).

57. S.E. Brown, G. Mozurkewich, and G. Grüner, Phys. Rev. Lett. **52**, 2277 (1984).

58. R.P. Hall and A. Zettl, Phys. Rev. B. **30**, 2279 (1984).

59. M.S. Sherwin and A. Zettl, Phys. Rev. B **32**, 5536 (1985).

60. R.M. Fleming, Phys. Rev. B **22**, 5606 (1980).

61. D. Reagor, S. Sridhar, and G. Grüner, Phys. Rev. B **34**, 2212 (1986).

62. A.J. Berlinsky, Rep. Prog. Phys. **42**, 1243 (1979).

63. N.P. Ong and G. Verma, in *Nonlinear transport and*

related phenomena in inorganic quasi one dimensional conductors, Proceedings of the international symposium, Sapporo, Japan, 1983, p. 115.

64. K. Maki, in Ref. 63, p. 17.

65. R.M. Fleming, D.E. Moncton, and D.B. McWhan, Phys. Rev. B **18**, 5560 (1978).

66. A. Fournel, J.P. Sorbier, M. Konczykowski, and P. Monceau, Phys. Rev. Lett. **57**, 2199 (1986).

67. A. Zettl and G. Grüner, Phys. Rev. B **26**, 2298 (1982).

68. R.P. Hall and A. Zettl, Solid State Commun. **50**, 813 (1984).

69. R.P. Hall and A. Zettl, Solid State Commun. **57**, 27 (1986).

70. R.P. Hall, M. Sherwin, and A. Zettl, Phys. Rev. Lett. **52**, 2293 (1984).

71. R.P. Hall, M. Sherwin, and A. Zettl, Phys. Rev. B **29**, 7076 (1984).

72. R.P. Hall and A. Zettl, Solid State Commun. **55**, 307 (1985).

73. L. Mihaly and G. Grüner, Solid State Commun. **50**, 807 (1984).

74. J. Dumas, C. Schlenker, J. Marcus, and R. Buder, Phys. Rev. Lett. **50**, 757 (1983).

75. Z.Z. Wang, P. Monceau, M. Renard, P. Gressier, L. Guemas, and A. Meerschaut, Solid State Commun. **47**, 439 (1983).

76. M.P. Everson and R.V. Coleman, Phys. Rev. B **28**, 6659 (1983).

77. H. Mutka, S. Bouffard, J. Dumas, and C. Schlenker, J. Phys. (Paris) Lett. **45**, L729 (1985).

78. R.P. Hall, M.F. Hundley, and A. Zettl, Phys. Rev. Lett. **56**, 2399 (1986).

79. R.P. Hall, M.F. Hundley, and A. Zettl, Phys. Rev. B (to be published).

80. M. Inui, R.P. Hall, S. Doniach, and A. Zettl (to be published).

81. R.P. Hall, M.F. Hundley, and A. Zettl, Physica **143**B, 152 (1986).

82. M.F. Hundley and A. Zettl, Solid State Commun. **65**, 791 (1988).

83. M.F. Hundley and A. Zettl, Phys. Rev. B (in press).

84. Other models of switching have been proposed. See B. Joos and D. Murray, Phys. Rev. B **29**, 1094 (1984), and W. Wonneberger and H.J. Breymayer, Z. Phys. B **56**, 241 (1984); also A. Janossy, G. Mihaly, and L. Mihaly in *Charge Density Waves in Solids*, edited by Gy. Hutiray and J. Solyom (Springer, New York, 1985), p.412, and L. Mihaly, Ting Chen, and G. Grüner, Solid State Commun. **61**, 751 (1987).

85. It is interesting to note that the concept of domain coupling and avalanche depinning is similar to a model first proposed in B. Joos and D. Murray, Phys. Rev. B

29, 1094 (1984).

86. J.L. Hodeau, M. Marezio, C. Roucau, R. Ayroles, A. Meerschaut, J. Rouxel, and P. Monceau, J. Phys. C **11**, 4117 (1978).

Chapter 5

1. P. Monceau, N.P. Ong, A.M. Portis, A. Meerschaut, and J. Rouxel, Phys. Rev. Lett. **37**, 602 (1976).

2. For a review see G. Grüner and A. Zettl, Physics Reports **119**, 117 (1985); see also P. Monceau in *Electronic Properties of Quasi-One-Dimensional Materials*, Vol. II, P. Monceau, ed. (Reidel, Dordrecht, The Netherlands, 1985) p. 139.

3. P. Monceau, J. Richard, and M. Renard, Phys. Rev. Lett. **45**, 43 (1980).

4. N.P. Ong, G. Verma, and K. Maki, Phys. Rev. Lett. **52**, 663 (1984); N.P. Ong and K. Maki, Phys. Rev. B **32**, 6582 (1985).

5. G. Mozurkewich and G. Grüner, Phys. Rev. Lett. **51**, 2206 (1983), and S.E. Brown and L. Mihaly, Phys. Rev. Lett. **55**, 742 (1985).

6. P. Monceau, J. Richard, and M. Renard, Phys. Rev. B **25**, 931 (1982).

7. A. Zettl and G. Grüner, Phys. Rev. B **29**, 755 (1984).

8. A. Zettl and G. Grüner, Solid State Commun. **46**, 501 (1983).

9. S.E. Brown, G. Mozurkewich, and G. Grüner, Phys. Rev. Lett. **52**, 2277 (1984).

10. R.E. Thorne, W.G. Lyons, J.W. Lyding, and J.R. Tucker, Phys. Rev. B **35**, 6360 (1987).

11. S.E. Brown, G. Mozurkewich, and G. Grüner, Solid State Commun. **54**, 23 (1985), and S.E. Brown and G. Grüner, Phys. Rev. B **31**, 8302 (1985).

12. R.M. Fleming, L.F. Schneemeyer, and R.J. Cava, Phys. Rev. B **31**, 1181 (1985).

13. C. Schlenker in *Low Dimensional Conductors and Superconductors*, Series B, Vol. 155, D. Jérome and L.G. Caron, eds. (Plenum Press, New York, 1987) p. 477.

14. R.J. Cava, R.M. Fleming, P. Littlewood, E.A. Rietman, L.F. Schneemeyer, and R.G. Dunn, Phys. Rev. B **30**, 3228 (1984).

15. R.P. Hall, M.S. Sherwin, and A. Zettl, Solid State Commun. **54**, 683 (1985).

16. For a review of metastable effects in $K_{0.3}MoO_3$ see R.M. Fleming in Ref. 14, p. 433.

17. G. Mihály, J. Dumas, and A. Jánossy, Solid State Commun. **60**, 785 (1986); also D. Reagor and G. Mozurkewich (unpublished).

18. M.F. Hundley and A. Zettl, Solid State Commun. (submitted).

19. M.F. Hundley and A. Zettl, Phys. Rev. B (submitted).

20. G. Grüner, A. Zawadowski, and P.M. Chaikin, Phys. Rev. Lett. **46**, 511 (1981).

21. A. Wold, W. Kunnmann, R.J. Arnott, and A. Ferreti, Inorg. Chem. **3**, 545 (1964).

22. J. Dumas, C. Schlenker, J. Marcus, and R. Buder, Phys.

Rev. Lett. **50**, 757 (1983), and J. Dumas and C. Schlenker, Solid State Commun. **45**, 885 (1983).

23. A. Jánossy, G. Kriza, S. Pekker, and K. Kamarús, Europhys. Lett. **3**, 1027 (1987).

24. G. Mihály and P. Beauchêne, Solid State Commun. **63**, 911 (1987).

25. J.P. Stokes, M.O. Robbins, and S. Bhattacharya, Bull. Am. Phys. Soc. **30**, 214 (1985).

26. A. Zettl and G. Grüner, Phys. Rev. B **28**, 2091 (1983).

27. P. Ségransan, A. Jánossy, C. Berthier, J. Marcus, and P. Butaud, Phys. Rev. Lett. **56**, 1854 (1986).

28. A. Jánossy, C. Berthier, P. Ségransan, and P. Butaud, Phys. Rev. Lett. **59**, 2348 (1987).

29. L. Sneddon, M.C. Cross, and D.S. Fisher, Phys. Rev. Lett. **49**, 292 (1982).

30. L. Sneddon, Phys. Rev. Lett. **52**, 65 (1984), Phys. Rev. B **29**, 719 (1984), Phys. Rev. B **29**, 725 (1984).

31. D.E. McCumber, J. Appl. Phys. **39**, 3113 (1968); W.C. Stewart, Appl. Lett. **12**, 277 (1968).

32. H. Fack and V. Kose, J. Appl. Phys. **42**, 320 (1971).

33. M.F. Hundley (unpublished).

34. R.M. Fleming, R.J. Cava, L.F. Schneemeyer, E.A. Rietman, and R.G. Dunn, Phys. Rev. B **33**, 5450 (1986).

35. P.B. Littlewood, Phys. Rev. B **36**, 3108 (1987).

36. John Bardeen, E. Ben-Jacob, A. Zettl, And G. Grüner, Phys. Rev. Lett. **49**, 493 (1982).

Chapter 6

1. M.F. Hundley, L.C. Bourne, A. Zettl, C. Rossel, and M.B. Mapel, Solid State Commun. **62**, 603 (1987).

2. M.B. Maple, J.W. Chen, Y. Dalichaouch, T. Kohara, C. Rossel, M.S. Torikachvili, M.W. McElfresh, and J.D. Thompson, Phys. Rev. Lett. **56**, 185 (1986).

3. T.T.M. Palstra, A.A. Menovsky, J. van den Berg, A.J. Dirkmaat, P.H. Kes, G.J. Nieuwenhuys, and J.A. Mydosh, Phys. Rev. Lett. **55**, 2727 (1985).

4. W. Schlabitz, J. Baumann, B. Pollit, U. Rauchschwalbe, H.M. Mayer, U. Ahlheim, and C.D. Bredl, Z. Phys. B**62**, 171 (1986).

5. F.R. Boer, J.J.M. Franse, E. Louis, A.A. Menovsky, J.A. Mydosh, T.T.M. Palstra, U. Rauchschwalbe, W. Schlabitz, F. Steglich, and A. de Visser (unpublished).

6. T.T.M. Palstra, A.A. Menovsky, and J.A. Mydosh, (to be published).

7. C. Brosholm, J.K. Kjems, W.J.L. Buyers, P. Matthews, T.T.M. Palstra, A.A. Menovsky, and J.A. Mydosh (to be published).

8. S. Takahashi, T. Sambongi, J.W. Brill, and W. Roark, Solid State Commun. **49**, 1031 (1984).

9. P. Monceau, N.P. Ong, A.M. Portis, A. Meerschaut, and J. Rouxel, Phys. Rev. Lett. **37**, 602 (1976).

10. P.M. Chaikin and J.F. Kwak, Rev. Sci. Instrum. **46**, 218

(1975).

11. R.H. Friend and N. Bett, J. Phys. E **13**, 294 (1980).

12. M. Christen and M. Godet, Phys. Lett. **63A**, 125 (1981).

13. N.B. Brandt and V.V. Moshchalkov, Adv. Phys. **33**, 373 (1984).

14. M. Hadzic-Leroux, A. Hamzic, A. Fert, P. Haen, F. Lapierre, and O. Laborde, Europhys. Lett. **1**, 579 (1986).

15. E. Cattaneo, Z. Phys. **64**, 305 (1986); **64**, 317 (1986).

16. T. Penney, J. Stankiewicz, S. Von Molnar, Z. Fisk, J.L Smith, and H.R. Ott, J. Magn. Magn. Mater. **54-57**, 370 (1986).

17. K. Winzer, Z. Phys. B **64**, 159 (1986).

18. J. Schoenes and J.J.M. Franse, Phys. Rev. B **33**, 5138 (1986).

19. W.R. Datars, K. Kadowaki, N. Ali, and S.B. Woods, J. Phys. F L63 (1986).

20. T. Siegrist, M. Olivier, S.P. McAlister, and R.W. Cochrane, Phys. Rev. B **33**, 4370 (1986).

21. J. Schoenes, C. Schonenberger, J.J.M. Franse, and A.A. Menovsky, Phys. Rev. B **35**, 5375 (1987).

22. A. Fert and P.M. Levy, Phys. Rev. B **36**, 1907 (1987).

23. P. Coleman, P.W. Anderson, and T.V. Ramakrishnan, Phys. Rev. Lett. **55**, 414 (1985).

24. N.P. Ong and P. Monceau, Solid State Commun. **26**, 487 (1978).

25. E. Bervas, Ph.D. Thesis, Université Scientifique et Médicale de Grenoble (1984).

26. E. Gratz, E. Bauer, B. Barbara, S. Zermirli, F. Steglich, C.D. Bredl, and W. Lieke, J. Phys. F: Met. Phys. **15**, 1975 (1985).

27. D. Jaccard, J. Flouquet, and J. Sierro (to be published).

28. N.F. Mott, Proc. Roy. Soc. London A **156**, 368 (1936).

29. J.M. Ziman, in *Principles of the Theory of Solids*, (Cambridge University Press, London, 1972) p. 218.

30. P.M. Chaikin, W.W. Fuller, R. Lacoe, J.F. Kwak, R.L. Greene, J.C. Eckert, and N.P. Ong, Solid State Commun. **39**, 553 (1981).

31. K. Mortensen, Solid State Commun. **44**, 643 (1982).

Chapter 7

1. M.F. Hundley and A. Zettl (to be published).

2. For a review see S.H. Liu (to be published).

3. D. Stauffer, Phys. Rep. **54**, 3 (1979).

4. H.E. Stanley, J. Phys. A **10**, L211 (1977).

5. P.L. Leath, Phys. Rev. B **14**, 5046 (1976).

6. R.J. Harrison, G.H. Bishop, and G.D. Quinn, J. Stat. Phys. **19**, 53 (1978).

7. B.A. Ables, H.L. Pinsh, and J.I. Gittleman, Phys. Rev. Lett. **35**, 247 (1976).

8. C.J. Lobb, M. Tinkham, and W.J. Skocpol, Solid State Commun. **27**, 1253 (1978).

9. R.B. Laibowitz, E.I. Alessandrini, C.R. Guarnieri , and R.F. Voss, J. Vac. Sci. Technol. A **1**, 438 (1983).

10. Y. Gefen, A. Aharnoy, and S. Alexander, Phys. Rev. Lett. **50**, 77 (1983).

11. R.F. Voss, R.B. Laibowitz, and E.I. Alessandrini, Phys. Rev. Lett. **49**, 1441 (1982).

12. R.B. Laibowitz and Y. Gefen, Phys. Rev. Lett. **53**, 380 (1984).

13. R.B. Pandey and D. Stauffer, Phys. Rev. Lett. **51**, 527 (1982).

14. D. Ben Arraham and S. Harlin, J. Phys. A **15**, L691 (1982).

15. A.L. Efros and B.I. Shklovski, Phys. Status Solidi(b)

76, 475 (1976).

16. J.P. Straley, Phys. Rev. B **15**, 5733 (1977).

17. D.J. Bergmann and Y. Imry, Phys. Rev. Lett. **39**, 1222 (1977).

18. M.J. Stephen, Phys. Rev. B **17**, 4444 (1978).

19. A.M. Dykhne, Sov. Phys. JETP **32**, 63 (1971).

20. J. Marchunt and R. Gallibard, C.R. Acad. Sci. Ser. B **281**, 261 (1975).

21. J.P. Straley, J. Phys. C **9**, 783 (1976).

Chapter 8

1. M.F. Hundley, A. Zettl, A. Stacy, and M.L. Cohen, Phys. Rev. B **35**, 8800 (1987).

2. J.G. Bednorz and K.A. Müller, Z. Phys. B **64**, 189 (1986).

3. N. Nguyen, J. Choisnet, M. Hervieu, and B. Raveau, J. Solid State Chem. **39**, 120 (1981).

4. N. Nguyen, F. Studer, and B. Raveau, J. Phys. Chem. Solids. **44**, 389 (1983).

5. R.B. van Dover, R.J. Cava, B. Batlogg, and E.A. Rietman, Phys. Rev. B **35**, 5337 (1987).

6. K. Kishio, K. Kitazawa, S. Kanbe, I. Yasuda, N. Sugii, H. Takagi, S. Uchida, K. Fueki, and S. Tanaka, Chem Lett. (1987).

7. R.J. Cava, R.B. van Dover, B. Batlogg, and E.A. Rietman, Phys. Rev. Lett. **58**, 408 (1987).

8. C.W. Chu, P.H. Hor, R.L. Meng, L. Gao, Z.J. Huang, and Y.Q. Wang, Phys. Rev. Lett. **58**, 405 (1987).

9. D.W. Capone II, D.G. Hinks, J.D. Jorgensen, and K. Zhang (unpublished).

10. J.J. Yu, A.J. Freeman, and J.H. Xu, Phys. Rev. Lett. **58**, 1035 (1987) .

11. L.F. Mattheiss, Phys. Rev. Lett. **58**, 1028 (1987).

12. U. Walter, M.S. Sherwin, A. Stacy, P.L. Richards, and A. Zettl, Phys. Rev. B **35**, 5327 (1987).

13. P.W. Anderson, Science **235**, 1196 (1987).

14. V. Kresin, Phys. Rev. B (to be published).

15. T.A. Faltens, W.K. Ham, S.W. Keller, K.J. Leary, J.N. Michaels, A.M. Stacy, H.C. Loye, D.E. Morris, T.W. Barbee III, L.C. Bourne, M.L. Cohen, S. Hoen, and A. Zettl, Phys. Rev. Lett. **59**, 915 (1987).

16. R.H. Friend and N. Bett, J. Phys. E **13**, 294 (1980).

17. P.M. Chaikin and J.F. Kwak, Rev. Sci. Instrum. **46**, 218 (1975).

18. The experiment measures only the difference in TEP between the sample and the gold wire. Hence, any uncertainty in the absolute TEP of the gold leads to an uncertainty in the TEP of the sample.

19. R.L. Crisp, Philos. Mag. **10**, 533 (1964).

20. C.M. Hurd, *The Hall Effect in Metal and Alloys* (Plenum, New York, 1972), p. 75.

21. N.F. Mott, Proc. R. Soc. London, Ser. A **156**, 368 (1936).

22. J.M. Ziman, *Principles of the Theory of Solids* (Cambridge Univ. Press, London, 1972), p. 218.

23. N. Phillips (private communication).

24. N.P. Ong, Z.Z. Wang, J. Claybold, J.M. Tarascon, L.H. Greene, and W.R. Mckinnon, Phys. Rev. B **35**, 8807 (1987).

25. J.R. Cooper, B. Alavi, L-W. Zhou, W.P. Beyermann, and G. Grüner, Phys. Rev. B **35**, 8794 (1987).

26. M.F. Hundley and J.C. Eckert (unpublished).

27. F.J. Blatt and P.A. Schroeder, *Thermoelectricity in Metallic Conductors* (Plenum, New York, 1978).

28. L.C. Bourne, A. Zettl, K.J. Chang, M.L. Cohen, A.M. Stacy, and W.K. Ham, Phys. Rev. B **35**, 8785 (1987).

29. L.C. Bourne and A. Zettl (unpublished).

30. N.P. Ong and P. Monceau, Solid State Commun. **26**, 487 (1978).

31. Note that the Hall angle, $\tan\theta = R_H \sigma H$, need not be zero in a superconductor since $\sigma \rightarrow \infty$ while $R_H \rightarrow 0$.

32. For a review, see D.U. Gubser, T.L. Francavilla, S.A. Wolf, and J.R. Leibowitz, *Inhomogeneous Superconductors - 1979* (AIP, New York, 1980).

Chapter 9

1. C.A. Balseiro and L.M. Falicov, Phys. Rev. Lett. **55**, 2336 (1985), and Phys. Rev. B **34**, 863 (1986).

2. R.M. Fleming, D.E. Moncton, and D.B. McWhan, Phys. Rev. B **18**, 5560 (1978).

3. A. Fournel, J.P. Sorbier, M. Konczykowski, and P. Monceau, Phys. Rev. Lett. **57**, 2199 (1986).

4. F. Devreux, J. Physique **43**, 1489 (1982); J.H. Ross, Z. Wang, and C.P. Slichter, Phys. Rev. Lett. **56**, 663 (1986).

5. X.J. Zhang and N.P. Ong, Phys. Rev. B **30**, 7343 (1984); A. Zettl, M. Kaiser, and G. Grüner, Solid State Commun. **53**, 649 (1985); S.E. Brown, A. Janossy, and G. Grüner, Phys. Rev. B **31**, 6869 (1985); M.F. Hundley and A. Zettl, Phys. Rev. B **33**, 2883 (1986); J.W. Lyding, J.S. Hubacek, G. Gammie, and R.F. Thorne, Phys. Rev. B **33**, 4341 (1986).

6. R.M. Fleming, R.J. Cava, L.F. Schneemeyer, E.A. Rietman, and R.G. Dunn, Phys. Rev. B **33**, 5450 (1986).